INTRODUCTION

The characterization of the behavior of soil under loading is a complex task. The finite element method has in recent years been a useful tool in analyzing structures, structures on soil and soil-structures. An emphasis has been placed on use of nonlinear plasticity soil models to more accurately capture the soil response. Recent work has focused on effective stress analysis, the ability to not only calculate the soil stress but also to calculate the pore fluid pressure.

The use of an effective stress model has application in analysis of ocean floor soils, nearshore and offshore structures, and in seismic analysis. Oscillations in loading, whether from wave action or seismic shaking, produce a dynamic loading that can induce significant increases in pore pressure. The increase in pore pressure can reduce allowable capacities and increase deformations from a reduction in effective confining stress. Under extreme conditions flow slides and liquefaction occur. Although liquefaction has been identified as a phenomenon for 20 years, soil-mechanics is just beginning to understand the interaction of stress confinement and drainage path, which occurs in the field such as under a foundation or around a pile. For example, common engineering practice in the evaluation of seismically induced soil liquefaction considers level ground conditions away from the structure. Shear stresses from the structure are not considered. Present design guidelines for pile foundations are based on static load considerations.

Recent earthquakes, particularly those in Alaska, Japan, and Chile, have emphasized the high damage threat the soil liquefaction phenomenon poses to waterfront structures. In the 1960 Chilean earthquake (magnitude 7) quay walls, sheet piles, and sea walls were damaged by liquefaction of loose, fine, sandy soils. In the 1964 Alaskan earthquake (magnitude 8.4) severe damage to Anchorage, Cordova, and Valdez occurred including large-scale land slides as a result of liquefaction. Japanese earthquakes (Niigata, 1964, magnitude 7.5; Tokachi-Oki, 1968, magnitude 7.8; Nemuro-Hanto-Oki, 1973, magnitude 7.3; Miyagi-Ken-Oki, 1978, magnitude 7.4) experienced severe waterfront damage to wharfs, bulkheads, quay walls, piers, and conventional structures. The majority of the damage sustained in waterfront areas was primarily from liquefaction of loose, cohesionless sands.

Effective stress techniques are of interest in understanding pile behavior. Pore pressure builds up during the driving process and then dissipates gradually.

This report will document work performed during FY82 investigating use of the effective stress soil model. Funding for this task was obtained jointly from the Navy and the Department of the Interior. Tasks performed include:

1. Development of cyclic degradation function (Contract with Professor Prevost, Princeton University).

2. Soil testing program basic soil behavior, drained/undrained behavior (Contract with Professor Lade, UCLA (Appendix A), and Norwegian Geotechnical Institute data exchange).

3. Program DYNAFLO conversion to Prime and CDC computers.

4. Evaluation of DYNAFLO and Prevost soil model (Appendix B).

5. Example case studies as demonstration of the methodology.

PREVOST SOIL MODEL

The soil is viewed as a multiphase medium consisting of an inelastic porous skeleton and viscous fluids. The model (Ref 1 and 2) is a general analytical model that describes the nonlinear, anisotropic, elasto-plastic, stress and strain dependents, and strength properties of the skeleton when subjected to a three-dimensional loading. Prevost (Ref 1) developed the coupled field tensor equations for a saturated soil consisting of a perfect fluid and a piecewise-linear, time -independent porous skeleton where the pore fluid and the solid grains are incompressible.

$$\text{div}\left(\overset{\nabla}{\underset{\sim}{\sigma}}{}'^{s} + \underset{\sim}{\sigma}'^{s}\ \text{div}\ \underset{\sim}{v}^{s}\right) - \text{div}\left[\left(\dot{p}_w + p_w\ \text{div}\ \underset{\sim}{v}^{s}\right)\left[\underset{\sim}{1}\right]\right]$$

$$+ \text{div}\left[\underset{\sim}{D}:\underset{\sim}{L}^{s}\right] + \rho_w\ \text{div}\ v^{s}\left(b - a^{w}\right) + \rho\ \underset{\sim}{b}' = \rho^{s}\ \underset{\sim}{a}^{s} + \rho^{w}\ \underset{\sim}{a}^{w}$$

$$- \text{div}\left[\frac{n^{w}}{\rho}\ \underset{\sim}{k}^{ws}\left(\text{grad}\ p_w - \rho_w\ \underset{\sim}{b} + \rho_w\ \underset{\sim}{a}^{w}\right)\right] + \text{div}\ \underset{\sim}{v}^{s} = 0$$

in which

$$\underset{\sim}{D} = D_{abcd} = \frac{1}{2}\left[\sigma_{bd}\ \delta_{ac} - \sigma_{ad}\ \delta_{bc} - \delta_{ac}\ \delta_{bd} - \sigma_{bc}\ \delta_{ad}\right]$$

is a tensor arising from geometric changes,

$$\underset{\sim}{\sigma} = \underset{\sim}{\sigma}'^{s} - p_w\ \underset{\sim}{1}$$

is the total stress tensor,

$$\dot{p}_w = \frac{\partial p_w}{\partial_t} + \underset{\sim}{v}^{s} \cdot \text{grad}\ p_w$$

$$\dot{n}^w = (1 - n^w) \operatorname{div} v^s$$

$$\rho^s = (1 - n^w) \rho_s$$

$$\rho = \rho^s + n^w \rho_w$$

where

s = subscript solid phase

w = subscript fluid phase

σ'^s = effective Cauchy stress tensor

p_w = pore fluid pressure

$\underset{\sim}{v}^\alpha$ = velocity of α-phase where α refers to solid or fluid

a^α = acceleration of α-phase

d^α = symmetric part of velocity gradient

w^α = skew symmetric part of velocity gradient

L^α = velocity gradient

d^{ws} = permeability tensor

ρ_α = microscopic mass density of α-phase

n^w = porosity

b = body force density per unit mass

σ^{∇}'s = Jaumann derivative

The elastic and plastic components of deformation are separated, and it is assumed the elasticity of the material is isotropic and linear in shear. Shear nonlinearity and anisotropy result from their material's plasticity. The elastic components are related by a generalized Hooke's law in which the shear modulus is constant and the bulk modulus is assumed to be a function of the effective mean normal stress.

The model uses a series of yield surfaces with a normality flow rule of plasticity. The rule of isotropic plastic hardening is not adequate for soils in general since under unloading and loading reversals it implies elastic behavior exclusively until the stress is fully reversed.

Test data show both elastic and plastic deformations occur well before the stress is fully reversed. To account for this combination, an isotropic and kinematic plastic hardening rule is used to allow the yield surfaces to be translated in stress space as well as to change in size. The yield surfaces initial position and size reflect the past stress-strain history. The yield functions (Figure 1) are represented by:

$$\frac{3}{2}\left[s_{ij} - \alpha_{ij}^{(m)}\right]\left[s_{ij} - \alpha_{ij}^{(m)}\right] + \frac{9}{2}\left[p - \beta^{(m)}\right] - \left[k^{(m)}\right]^2 = 0$$

where $\alpha_{ij}^{(m)}$ and $\beta^{(m)}$ = coordinates of center of yield surface

s_{ij} = deviatoric stress tensor

p = effective mean normal stress

The outermost "boundary" surface is a "volumetric" yield surface whose size, position, and movement are functions of material density. Points C and E (Figure 1) define the critical state conditions for triaxial compression and extension, and the slopes of lines OC and OE remain constant. An associative flow rule is used on the yield surface, f_p, to compute plastic strain rate vector components. The plastic modulus associated with the f_p surface is

$$H'_p = \left[\frac{3}{2} kp - \beta^{(p)}\right] \frac{\left(\sigma_{ij}\ \xi_{ij}^{(p)}\right)\sigma_{ij}}{k^{(p)^2}}$$

where k is the material parameter equal to the slope of the virgin consolidation curve.

A plastic modulus is associated with the inner yield surfaces and varies along the yield surface, f_n. Projections of the yield surface, f_n, onto the deviatoric subspace define regions of constant plastic shear moduli. A nonassociative flow rule is used on the yield surface, f_n. The plastic deviatoric strain rate vector, however, remains normal to the projection of the yield surface, f_n onto the deviatoric subspace. All the yield surfaces may translate in stress space, touch and push each other, but they cannot intersect. When the stress loading point reaches yield surface f_n, all the yield surfaces, f_1, f_2, ... f_n, are tangent to each other at the contact point, f_n (Figure 1). If a stress rate is then applied such that the stress rate vector points out of f_n, the plastic strain rate vectors are given by the nonassociative flow rule. The yield surfaces translate together and remain together based on the stress path. Overlapping of the yield surfaces is prevented by restricting contact to points only having the same outward normal. The pore pressure is related through the bulk modulus to the plastic potential.

FITTING THE PREVOST MODEL

Specification of the model parameters requires:

1. The initial size and positions of the yield surfaces and the associated plastic moduli
2. Size and change of plastic moduli as a function of load
3. The elastic shear and bulk moduli

The model parameters required can be derived from results of conventional monotonic axial and cyclic strain-controlled simple shear tests. The stress-strain curves in compression and extension are approximated by linear segments along which a tangent modulus is constructed. In general, the modulus is not to be found equal for the same value of shear stress in compression and extension.

The following is based on Prevost (Ref 2):

Since during both triaxial compression and extension tests, the stress point travels along the $\sigma_{y\text{-axis}}$ (Figure 2), $(\sigma_v - \sigma_x) = \alpha_1^{(m)} + k^{(m)}$ when it reaches f_m in compression whereas $(\sigma_v - \sigma_x) = \alpha_1^{(m)} - k^{(m)}$ in extension. At this same moment, the incremental vertical strain is defined. The yield circles in Figures 2c and 2e thus define the regions of constant shear moduli in stress space. The elastic shear modulus is calculated from the steepest slope at the origin since f_o is chosen of size 0 and $h_o' = \infty$. It is thus apparent that by comparing experimental stress-strain curves obtained in both monotonic triaxial compression and extension tests, the initial positions $\alpha_1^{(m)}$, sizes $k_o^{(m)}$, and associated shear moduli H_m of the yield surfaces may be determined. This is illustrated schematically in Figure 2.

Figure 2 presents the situation upon reaching point P in compression. Upon loading reversal, the stress point leaves point P, inverse plastic flow occurs, and the stress point translates the surfaces downwards. The reserve loading curve is shown in Figure 1 for the case when $k^{(m)} = k_o^{(m)} = \text{constant}$. Both $k^{(m)}$ and h_m' are, in general, functions of λ. In a triaxial soil test $\dot{\lambda} = \dot{\varepsilon}_y^p$. Variations in $h_m'(\lambda)$ usually occur only once large values of λ have been reached, whereas the $k^{(m)}(\lambda)$ functions usually start to vary upon the first loading reversal.

Prevost has developed a program to determine the failure surfaces based directly on the tabulated data from axial compression, axial extension, hydrostatic, and simple shear tests.

The nonassociativity parameters are determined relative to the (initial) elastic bulk modulus. Volumetric strain is directly dependent on the nonassociativity parameter.

SCALING DATA

Based on limited data, it has been found reasonable to scale by the ratio of average confining stress levels. The elastic shear modulus, the initial elasto-plastic shear modulus, and the elastic bulk modulus are scaled by the square root of the stress ratio. The bulk exponent is not scaled. Initial stress components are scaled by the ratio. The softening parameters, delta, delta ultimate, and the yield surface axis ratio, are scaled by the stress ratio. The size of the yield surface is scaled by the stress ratio. The elasto-plastic shear and plastic bulk moduli are scaled by the square root of the stress ratio; the degree of nonassociativity is not scaled. Typical results for Cook's sand are shown in Figures 3 and 4.

Anisotropic consolidation can also be treated by shifting the ellipses. It is assumed that isotropic data are used and the J_1 value is maintained constant.

$$J_1 = \sigma_v + 2\,\sigma_H$$

$$J_1 = (1 + 2\,k_o)\,\sigma_v$$

$$\text{Shift } \sqrt{J_2} = \frac{\sigma_v - \sigma_H}{\sqrt{3}}$$

$$\text{Shift } \sqrt{J_2} = \frac{(1 - k_o)}{\sqrt{3}}\,\sigma_v$$

$$\text{Shift } \sqrt{J_2} = \left(\frac{1 - k_o}{\sqrt{3}}\right)\left(\frac{J_1}{1 + 2\,k_o}\right)$$

The new values for σ_v and σ_H are

$$\sigma_v = \frac{J_1}{1 + 2\,k_o}$$

$$F(\sigma', \eta) = 0$$

where J_1 is from the isotropic test.

It is suggested that data be first scaled to the correct J_1 and then shifted to anisotropic conditions.

DYNAFLO PROGRAM

The DYNAFLO Program (Ref 3) is a finite element program intended for the static and transient analysis of linear and nonlinear two- and three-dimensional problems. The analysis capabilities include the following:

Static - Nonlinear elliptic boundary value problems with two degrees of freedom per 2D node and three degrees of freedom per 3D node.

Diffusion - Nonlinear parabolic boundary value problems with one additional degree of freedom for the phase porous fluid pore pressure.

Dynamic - Nonlinear hyperbolic boundary value problems with two additional degrees of freedom for the phase porous fluid.

The program incorporates the full Prevost model for nonlinear effective stress analysis. The material model produces a nonsymmetric stiffness matrix. Solution techniques employed allow for implicit, explicit, and implicit/explicit matrix solution.

For static analysis an incremental predictor-corrector load step procedure is utilized. Alpha equal to 1/2 is utilized and associates the midpoint of the load (time) interval to the predictor phase and achieves second-order accuracy. Iteration is not performed and each load step must remain small to preserve accuracy.

For parabolic analysis, diffusion problems, a Newton-Raphson iterative procedure is utilized. Unconditional stability is achieved for $\alpha \geq 1/2$, and a value of $\alpha = 1$ is recommended to maximize high frequency numerical dissipation. For explicit elements a time step restriction occurs:

$$\Delta t < \frac{2}{(1 - 2\alpha)} \lambda$$

where λ = largest eigenvalue associated with problem

For hyperbolic analysis an implicit-explicit predictor-multicorrector algorithm is used. Stability is achieved when $\alpha \geq 1/2$. Implicit elements are unconditionally stable if $\beta \geq \alpha/2$. Explicit elements have a time step restriction:

$$\Omega < 2 (1 - \xi) / (\alpha + 1/2)$$

where $\Omega = w\Delta t$

ξ = model viscous damping

when $\sigma = 3/2$ and $\beta = 1$ the dissipative properties of the algorithm damp all dynamic transient phenomena and permit static solution.

Solution of the porous media problem requires defining boundary conditions for the fluid as would occur in a conventional seepage analysis. This is accomplished by defining the third and fourth degrees of freedom.

A standard 4-node element is used. It is suggested that one-point Gaussian quadrature be used for the initial stress stiffness integration, that one-point Gaussian quadrature be used for the volumetric stiffness numerical integration, and that two-by-two Gaussian quadrature be used for the deviatoric stiffness numerical integration.

CLARIFICATION OF USERS GUIDE

The following section is intended to clarify usage of the Program DYNAFLO. The program, card 1, has the option of the following modes:

0	Elliptic	Static solution with pore pressure, no fluid flow
1	Hyperbolic	Dynamic problem with pore pressure with fluid flow and inertia
2	Parabolic	Static problem with pore pressure with fluid flow

The code may be run explicitly with equilibrium iteration for such applications as studying wave propagation problems, implicitly for stiff components, or implicit-explicitly. Elliptic problems must be implicit or implicit-explicit. Parabolic problems require very short time steps so it is not practical to run them explicitly. In the implicit-explicit scheme the linear portions of an element are solved implicitly and the nonlinear explicitly. The parameter ISYMM on the first control card defines the treatment of the stiffness matrix as symmetric or nonsymmetric. Implicit formulations require treatment as nonsymmetric. However, implicit-explicit formulations are symmetric since only linear portions are included in the stiffness matrix. The term "load cases" is used on card 1; this is equivalent to indicating the number of time functions. All of the time functions or load cases must have the same number of points. This is termed as "load steps". The number of computational time iterations to be performed in the solution is specified by the number of time steps, card 1.

The program, card 2, allows for specification of time step multiplier. This allows for a graduated time increment up to a specified maximum. Use of this parameter allows for small time steps during pore pressure buildup and large steps during the diffusion state.

Specification of the plot code is accomplished on card 3. Use of the codes IP2, IP3, IP4, IP5, and IP6 allows plotting at specified steps. Normally, plotting is desired for all points after the last step; therefore, the variables should be specified as the last step number.

As with seepage analysis codes, the specification of pore pressures requires definition of the third degree of freedom in a two-dimensional problem and the fourth degree of freedom in a three-dimensional problem. Specification of a value of 1 must be made along the free surface. This sets the surface pore pressure to 0.0. Failure to define the pore pressure leads to gross errors.

Generation of omitted nodal points and boundary points requires specification of a 1 on the first and a 0 on the second card set of nodes. Generation will occur between nodes at the same boundary conditions specified on the first card. Generation may take place over several specified nodes defining a surface in which case an isoparametric data generation sequence will be initiated.

Section 7 specifies the nodes at which either forces or displacements are specified. The values specified in Section 7 will be forces unless that degree of freedom is specified as a displacement in Section 5. Values prescribed in Section 5 as displacements and not set in Section 7 are set to 0.0. The value of force or displacement set in Section 7 is multiplied by the time function in Section 8. There are a number of sets of Section 7 and Section 8 cards as specified in the number of load cases.

Each element group specified must start with the first element being numbered as 1. For material having pore pressure, an NTYPE of 4 must be used. This specifies the specific two-dimensional element with porous media formulation. The following values are recommended for Gaussian quadrature:

1 point	Initial stress stiffness integration
1 point	Volumetric stiffness integration
2 x 2	Deviatoric stiffness integration

When incompatible modes are included to improve an element in bending and in application to incompressible materials, two-by-two Gaussian quadrature in both volumetric and deviatoric terms should be employed.

The weight density of the solid phase is calculated as

dry density

(1 - porosity)

The permeability matrix at the element level requires K_{12} and K_{21} to be set to values different from K_{11} and K_{22}, or a singularity will develop. Values of K_{12} and K_{21} of 0.0 have been used specifying only K_{11} and K_{22}. The horizontal permeability is normally substantially greater than the vertical permeability (10 to 1 in stratified materials).

The gravity load multiplier is set to the first time function specified.

The contact element allows for specification of a tension gap such that when a structure pulls away from soil a break in stress transfer occurs. This is accomplished by specifying two nodes, A and B, initially at the same location and a vector, n, in the direction of travel. The component of motion in the direction n specifies contact or separation as follows:

$$\ell = (X_B + d_B) - (X_A + d_A)$$

$$\xi = \ell_n$$

where $X_{A,\ B}$ = initial position

$d_{A,\ B}$ = displacement induced

n = prescribed vector

Displacement	Condition	Contact Force
$\xi > 0$	separation	0
$\xi \leq 0$	contact	$K\ \xi$

Perpendicular to the n vector, a condition of slip (0 friction) or stick (K friction) can occur depending on what the user specifies. The value of K should be specified as large to minimize the physical movement between nodal pores, A and B, when in contact.

It is important to study the intended use and the correct direction to specify the direction vector. The contact/separatum depends on the net displacement difference between A and B. A displacement difference must consider the direction of the vector and the order of the nodes A and B.

The following sections require termination by a blank card:

3.0	7.1	9.2.5
4.1	9.1.4	9.3.3
5.0	9.1.5	9.5
6.1	9.2.4	

CONVERSION OF THE PROGRAM

The original DYNAFLO program was written for an IBM computer using the G-compiler. The program was installed on the FACSO IBM 370 computer. Minimal changes were made consisting of changing unformatted read statements to formatted ones and satisfying externals for plotting.

Changes for the CDC version of the program were more extensive. The program was installed in a CDC 175 machine using the NOS operating system with a FORTRAN V compiler. This compiler was required since the code incorporated dimension statements with variable sizes passed through common statements. The program was changed to single precision. Dimension and common statements had to be reordered. Graphics subroutines were added to make the program compatible with standard CalComp using CDC UNIPLOT. The size of the blank common was reduced to 50,000 from the original 100,000 to fit on the CDC 175 computer. This should not limit the use of the program since the original version used double precision for most variables, which was not needed on CDC.

The program was also converted for use on the PRIME 550 computer using the F77 compiler without optimization with the long integer option. The program was run in the double precision mode. Minor modifications similar to CDC were made. The program ran correctly for small jobs when the core utilized was within one segment. Large jobs had errors caused by the computer's inability to bridge segments. This paging problem is being investigated by PRIME. It appears to be resolved by using full dimension statements, such as DIMENSION A(100000), rather than DIMENSION A(1).

EXPERIMENTAL TEST PROGRAM

To evaluate the behavior of the Prevost model under drained and undrained conditions, a series of soil tests were planned. The test program, described in Appendix A, included:

1. Consolidated-drained triaxial compression tests
2. Consolidated-drained triaxial extension tests
3. Consolidated undrained triaxial compression tests
4. K_o tests
5. Consolidated-undrained slow cyclic triaxial tests
6. Proportional loading tests

The program was designed to provide data to fit the Prevost model based on drained characteristics and then to predict undrained tests. A fine sand was used for all the tests. The void ratio for the test was 0.76, a relatively loose condition to allow generation of pore pressures during the undrained loading.

SOIL PARAMETER FIT OF TEST DATA

The data presented in Appendix A were used to obtain soil parameters for the model. Tables 1 and 2 present the results where

A = stress tensor
ALPHA = compressional stress to center ellipse
BETA = shear stress to center ellipse
KM = size of yield surface
HC = compressional plastic modulus
HE = extensional plastic modulus
SC = coefficient
SE = coefficient
AMC = nonassociativity in compression
AME = nonassociativity in extension

Figure 5 shows the yield surfaces for the soil in Appendix A. Figures 5b, 5c, and 5d show stress strain data. Figure 6 shows the yield surfaces for Cook's sand whose data were fit previously.

A recent modification to the model formulation provides for variation of the plastic modulus along the surfaces. With the inclusion of this, the surfaces can be treated as circles (ellipses with an eccentricity of 1.0). The model provides for characterization of the plastic modulus and nonassociativity in compression and extension. The last surface representing yield behavior should have a plastic modulus of 0.0 and a large nonassociativity constant (typically increase the value determined from data by 10). Softening of a material is a demonstration of nonhomogeneous behavior of the soil. This may be included in the model but is not provided in the data fitting procedure. Additional surfaces are required in which the modulus is determined based on $h/2g = 0.01$; problems which exhibit this behavior must be run implicitly.

Figures 7a, 7b, and 7c show the results of the model in reproducing the drained compression test for the soil described in Appendix A. The results show a satisfactory agreement of stress-strain behavior; however, strain-strain behavior is not as good. This is caused by the lack of data points in the initial loading segment to define the region in sufficient detail to establish the yield surfaces.

Figure 8 shows the volumetric soil data in compression and extension. The data are unusual in two respects. First, the curvature of the loading portion of the data is inverted (Ref 4). Second, and more significant, the magnitude of the volumetric strain in extension is greater than that in compression. This indicates the soil compresses more in extension than in compression which, according to Prevost (Ref 4), appears abnormal. Figure 8 illustrates the expected results.

Figure 9 shows results for the K_o compression test showing test data and three simulations using different numbers of load steps. It is significant that the correct shape behavior (stiffening), which is a stress path dependent variable, is shown. Note that the soil exhibits softening under a triaxial stress path but stiffening in a K_o stress path. This test is predicted based on triaxial data indicating good model performance.

Figures 10a and 10b shows simulated behavior in simple shear. Note the hysteresis loop for three different tests using different numbers of load steps.

Figure 11 shows the results of an undrained compression test and model simulation. Initially the test data indicate greater dilation than the simulation. The model behavior is based on the yield surfaces determined from drained triaxial compression and extension tests. Figure 12 illustrates that only two surfaces are in the region where the dilation occurs. This results in a poor definition of volumetric behavior in that region. The material model simulation indicates flow along the critical state line correctly predicting the compressive post dilation phase. Note that the model in unloading experiences severe loss of mean stress. This is caused by the extension data, which control the unloading of the soil. The extension data shows large volume strains as noted in Figure 8 discussed above. This behavior illustrates the "abnormal" behavior of the test data (Ref 4).

It is the opinion of the authors that volumetric data in extension can indeed be greater than that in compression. This phenomenon is clearly demonstrated by Poisson's ratios in unloading being greater than those in loading. Pyke (Ref 5) shows that the range of Poisson's ratio in unloading can vary from 0.2 to 2.0. The question is whether this represents true soil behavior or is a condition at which the material fails to behave as a homogeneous continuum.

Figure 13 shows the stress-strain data for the choice of initial elastic parameters B, = 338 kg/cm^2 and G1 = 66 kg/cm^2. Figure 13b shows the undrained cyclic stress-strain results and Figure 13c shows the undrained stress path. The volume strain in extension was reduced and the cyclic test repeated. Figure 14 presents the results. Figure 14c shows the stress path showing the number of cycles to liquefaction, reduction of effective confining stress. Figure 14c shows the cyclic degradation effects. Figure 15 repeats the same type test for slightly different reduction in volume strain with a different load level.

DEMONSTRATION EXAMPLE PROBLEMS

Four example problems are presented to illustrate a few of the capabilities of the DYNAFLO program. These problems are:

1. A 4-element test case with a Δt parameter study
2. A 10-element soil column consolidation problem
3. A 90-element soil field, which includes a pile
4. A 100-element soil field, loaded with foundation pressure

Each of the four example problems had the following control options:

1. Two dimensions with a third degree of freedom for pore fluid pressure
2. A nonsymmetric stiffness matrix
3. A parabolic case (static problem with pore pressure)
4. The Gaussian quadrature recommended previously
5. Plane strain analysis
6. Variable time steps with $\Delta t_{mult} = 3.0$
7. Initial $\Delta t = 0.001$ sec, except for example 1
8. A load-time function
9. Implicit solution

Typical material properties were used for the example problems, and in general, each was used to illustrate various aspects in the generation and dissipation of pore fluid pressure.

Figure 16 shows the four-element test case with pore pressure history plots for initial $\Delta t = 0.0001$, 0.01, and 1 second. The initial Δt was varied, keeping all other parameters and options constant. The pore pressure history plots show that variation of the initial Δt used in this case has minimal effects on the generation and dissipation of pore

fluid pressure. The initial Δt must be small enough to ensure that the peak pore fluid pressure is obtained. In this problem, the peak fluid pressure of 1.0 psi is seen from time 0.001 second to 0.1 second.

Figure 17 shows the 10-element soil column with pore pressure history plots for elements 1, 5, and 10. In this study, the pore fluid pressure was allowed to drain at the top of the soil column. The pore pressures drain fastest at the top and slowest at the bottom. Drainage is a function of the length over which the pore fluid must flow. In this case, the total height of the column is 1,000 inch; therefore, dissipation is slow.

Figure 18 shows the undeformed finite element mesh for the pile problem. Drainage of pore fluid pressure was allowed at the top. Finer elements were used near the lower tip of the pile because the highest stresses would occur there. Half of the soil field and the pile was analyzed due to symmetry. Figures 19 and 20 show the deformed mesh and the displacement vectors at step 10 or time = 29.5 second. The plots are very exaggerated, so they must be interpreted in relative terms. Figure 20 is especially useful in visualizing the movement of the soil field relative to the pile. Pore pressure contours plots are shown in Figures 21 to 23. In this case, the generation and dissipation of pore fluid pressure is fairly rapid. Dissipation is a function of the drainage characteristics of the soil. The permeability values $k_{11} = k_{22} =$ 0.0004 in./sec are typical.

Figure 24 shows the undeformed mesh of the 100-element soil field with finer elements at the upper right corner. Drainage of pore fluid is allowed at the top, and the soil was loaded with a 15-psi-bearing pressure on the upper right. The deformed mesh and displacement vector plots at step = 10 (29.5 second) for the soil field are shown in Figures 25 and 26. Vertical displacements at nodes 121 and 73 are shown in Figures 27 and 28. These figures indicate that the displacements level off at t = 10 seconds (step 9 of 10), showing the usefulness of the variable time step. Pore pressure contour plots for the soil problem are shown in Figures 29 to 35. Gravity is included for the problem in Figures 29 to 31. These latter figures show that the pore pressures have completely dissipated at step = 8 (t = 3.28 seconds). Comparatively, it was seen that the displacements leveled off at step 9 in Figures 27 and 28. The contour plots in Figures 24 to 27 show in more detail the dissipation of pore pressure. At step = 3 (t = 0.0013 seconds) in Figure 33, the pore pressures are near their maximum because the load-time function attains its maximum at t = 0.001 second.

SUMMARY

Basic soil tests have been conducted to evaluate the behavior of loose sands. These data have been used to evaluate and validate the Prevost soil model. The model can successfully represent the drained behavior of the soil under arbitrary loading based on compression and extension test data. Further, the model can predict undrained behavior, although clearly not to the same accuracy. Additional test data are required to more fully evaluate undrained stress-strain behavior. The model does exhibit cyclic strain phenomenon showing buildup of pore pressure under constant strain amplitude cyclic loading.

REFERENCES

1. J. Prevost and T. Hughes. "Finite element solution of boundary value problems in soil mechanics," in Proceedings of International Conference on Soils Under Cyclic and Transient Loading, Swansea, United Kingdom, Jan 1980.

2. J. Prevost and T. Hughes. "Mathematical modeling of cyclic soil behavior," Earthquake Engineering and Soil Dynamics. New York, N.Y., American Society of Civil Engineering, Jun 1979.

3. Princeton University, Department of Civil Engineering. DYNAFLO: A nonlinear transient finite element analysis program. Princeton, N.J., 1981.

4. J. Prevost. "DYNAFLO: A nonlinear transient finite element analysis program," Princeton Department of Civil Engineering, Princeton Universtiy, Princeton, J.J., 1981.

5. Private communication between J. Ferritto, NCEL, and J. Prevost, Princeton Department of Civil Engineering, Jul 1982.

6. R. Pyke. "A scheme for following soil properties under computer cyclic loadings," presented at the International Workshop on the Constitutive Behavior of Soils, Zurich, Switzerland, Sep 1982.

Table 1. Soil Parameters Based on Appendix A

M	ALPHA	BETA	XKM	HPC	HPE	SC	SE	AMC	AME
1	0.000E-01	2.000E+00	2.533E+02	5.066E+02	6.754E+02	5.000E-01	0.000E-01	0.000E-01	0.000E-01
2	4.683E-01	1.933E+00	6.686E-01	4.606E+02	4.956E+02	7.997E-01	1.000E+00	-1.638E-01	-2.220E+00
3	8.873E-01	1.902E+00	1.182E+00	1.718E+02	1.913E+02	7.998E-01	1.000E+00	-9.692E-02	-8.521E-01
4	1.198E+00	1.822E+00	1.731E+00	6.525E+01	7.580E+01	7.999E-01	1.000E+00	-2.274E-01	-7.282E-01
5	1.525E+00	1.763E+00	2.237E+00	2.906E+01	3.531E+01	8.000E-01	1.000E+00	-3.371E-01	-8.958E-01
6	1.668E+00	1.695E+00	2.583E+00	1.417E+01	1.782E+01	8.000E-01	1.000E+00	-4.246E-01	-7.182E-01
7	1.802E+00	1.643E+00	2.872E+00	7.385E+00	9.563E+00	7.999E-01	1.000E+00	-4.828E-01	-0.000E-01
8	1.873E+00	1.587E+00	3.113E+00	5.282E+00	7.051E+00	8.000E-01	1.000E+00	-5.339E-01	-3.395E-01
9	1.997E+00	1.583E+00	3.228E+00	3.231E+00	4.344E+00	7.999E-01	1.000E+00	-5.685E-01	-2.091E-01
10	2.009E+00	1.531E+00	3.415E+00	1.223E+00	1.685E+00	7.999E-01	1.000E+00	-5.530E-01	-1.316E-02
11	2.004E+00	1.499E+00	3.508E+00	1.734E-10	2.427E-10	8.000E-01	1.000E+00	-5.022E+00	4.282E-02

Table 2. Soil Parameters for Computer Soil Model

A11	A22	A33	A12	A23	A31	KM	HC	HE	SC	AMC	AME
-2.00E+00	-2.00E+00	-2.00E+00	0.00E-01	0.00E-01	0.00E-01	2.53E+02	5.07E+02	6.75E+02	5.00E-01	0.00E-01	0.00E-01
-1.78E+00	-2.25E+00	-1.78E+00	0.00E-01	0.00E-01	0.00E-01	6.69E-01	4.61E+02	4.96E+02	8.00E-01	-1.64E-01	-2.22E+00
-1.61E+00	-2.49E+00	-1.61E+00	0.00E-01	0.00E-01	0.00E-01	1.18E+00	1.72E+02	1.91E+02	8.00E-01	-9.69E-02	-8.52E-01
-1.42E+00	-2.62E+00	-1.42E+00	0.00E-01	0.00E-01	0.00E-01	1.73E+00	6.52E+01	7.58E+01	8.00E-01	-2.27E-01	-7.28E-01
-1.25E+00	-2.78E+00	-1.25E+00	0.00E-01	0.00E-01	0.00E-01	2.24E+00	2.91E+01	3.53E+01	8.00E-01	-3.37E-01	-8.96E-01
-1.14E+00	-2.81E+00	-1.14E+00	0.00E-01	0.00E-01	0.00E-01	2.58E+00	1.42E+01	1.78E+01	8.00E-01	-4.25E-01	-7.18E-01
-1.04E+00	-2.84E+00	-1.04E+00	0.00E-01	0.00E-01	0.00E-01	2.87E+00	7.39E+00	9.56E+00	8.00E-01	-4.83E-01	-0.00E-01
-9.62E-01	-2.84E+00	-9.62E-01	0.00E-01	0.00E-01	0.00E-01	3.11E+00	5.28E+00	7.05E+00	8.00E-01	-5.34E-01	-3.40E-01
-9.24E-01	-2.90E+00	-9.24E-01	0.00E-01	0.00E-01	0.00E-01	3.23E+00	3.23E+00	4.34E+00	8.00E-01	-5.69E-01	-2.09E-01
-8.62E-01	-2.87E+00	-8.62E-01	0.00E-01	0.00E-01	0.00E-01	3.41E+00	1.22E+00	1.68E+00	8.00E-01	-5.53E-01	-1.32E-02
-8.31E-01	-2.83E+00	-8.31E-01	0.00E-01	0.00E-01	0.00E-01	3.51E+00	1.73E-10	2.43E-10	8.00E-01	-5.02E+00	4.28E-02

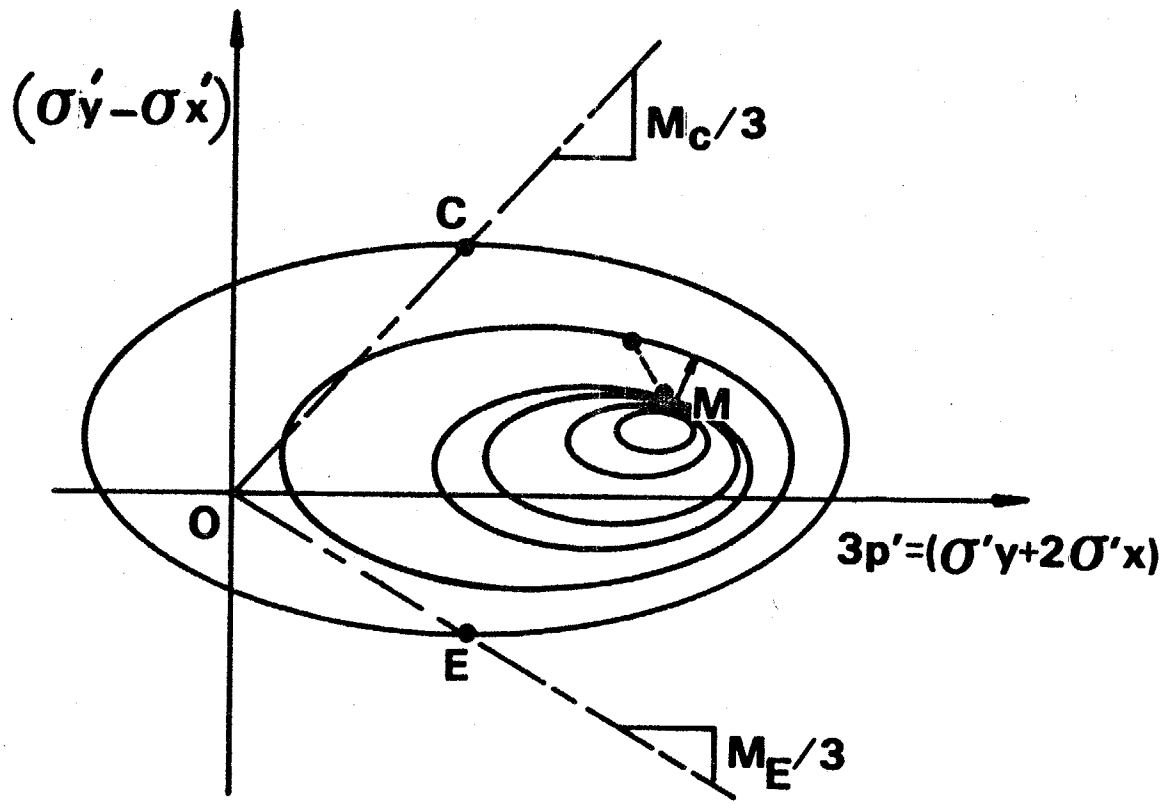

PREVOST SOIL MODEL

FIGURE 1.

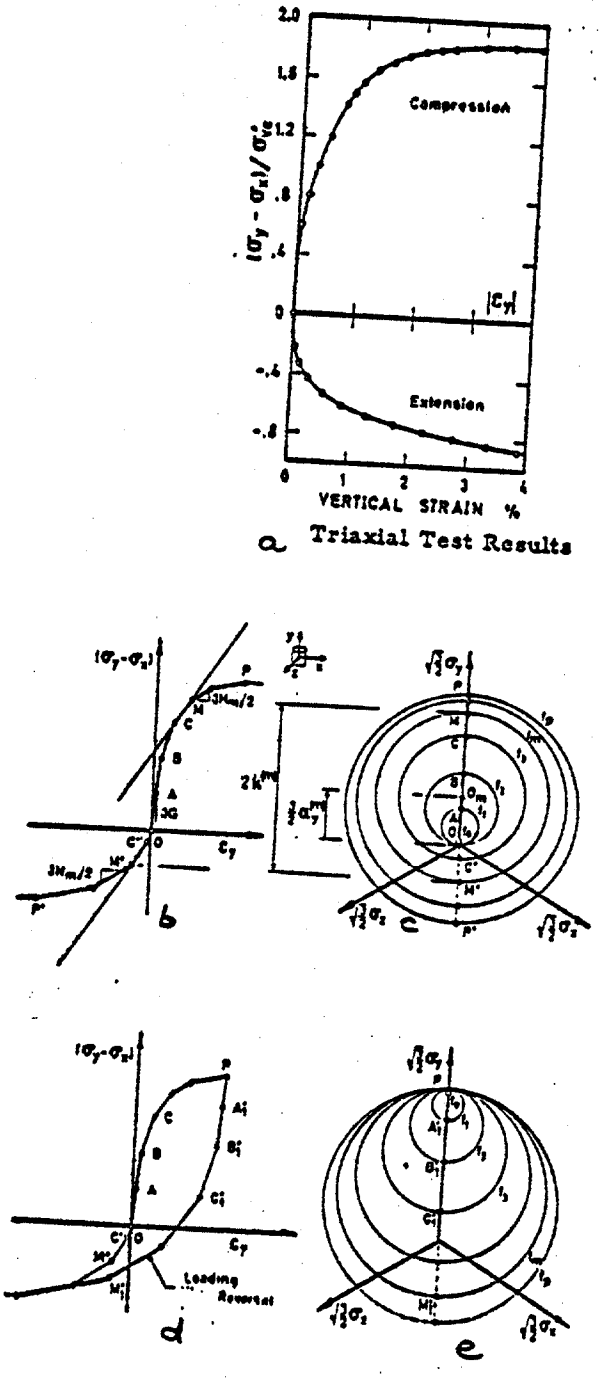

Figure 2. Fitting model parameters

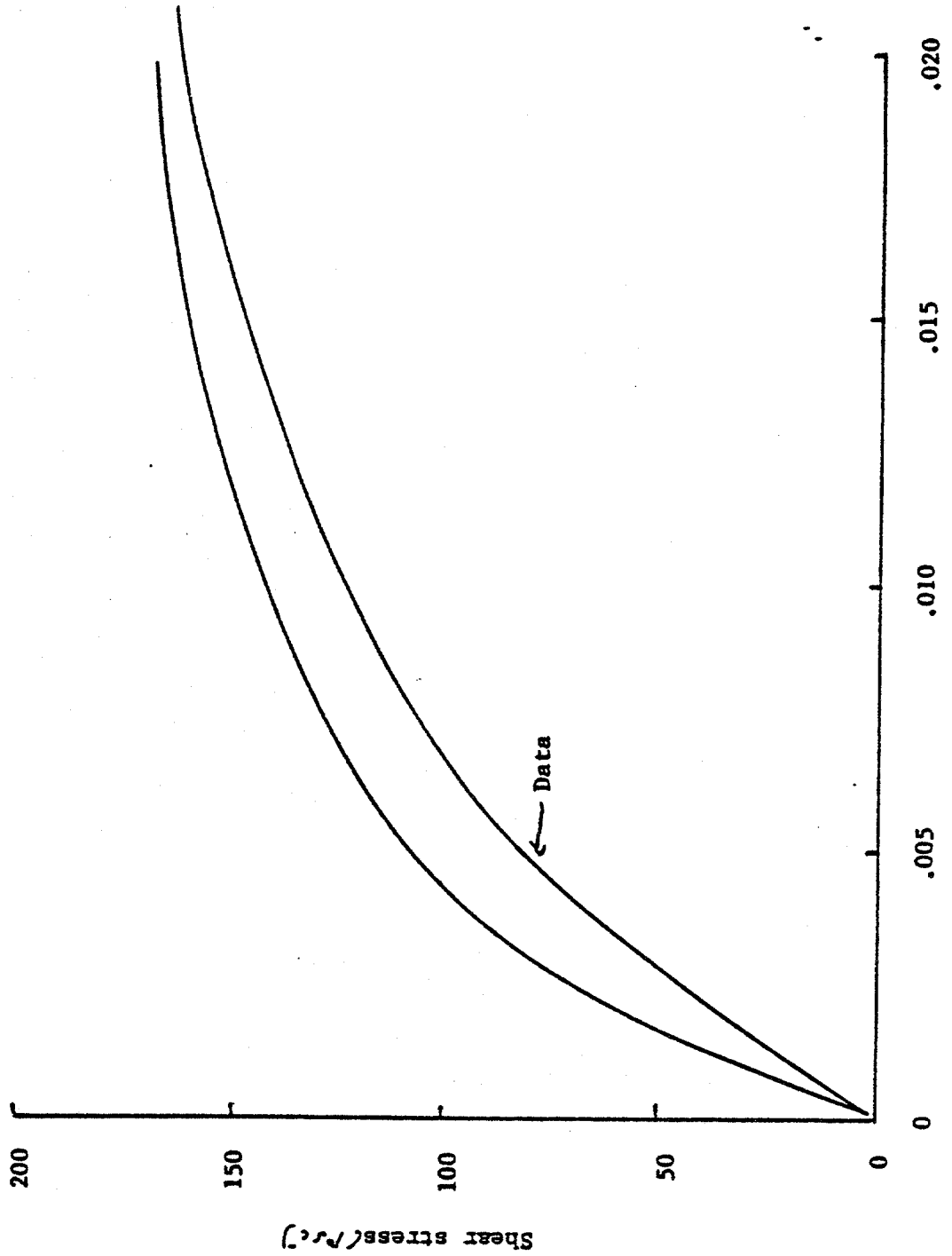

Figure 3a. Scaled data 50psi to 100psi, isotropic.

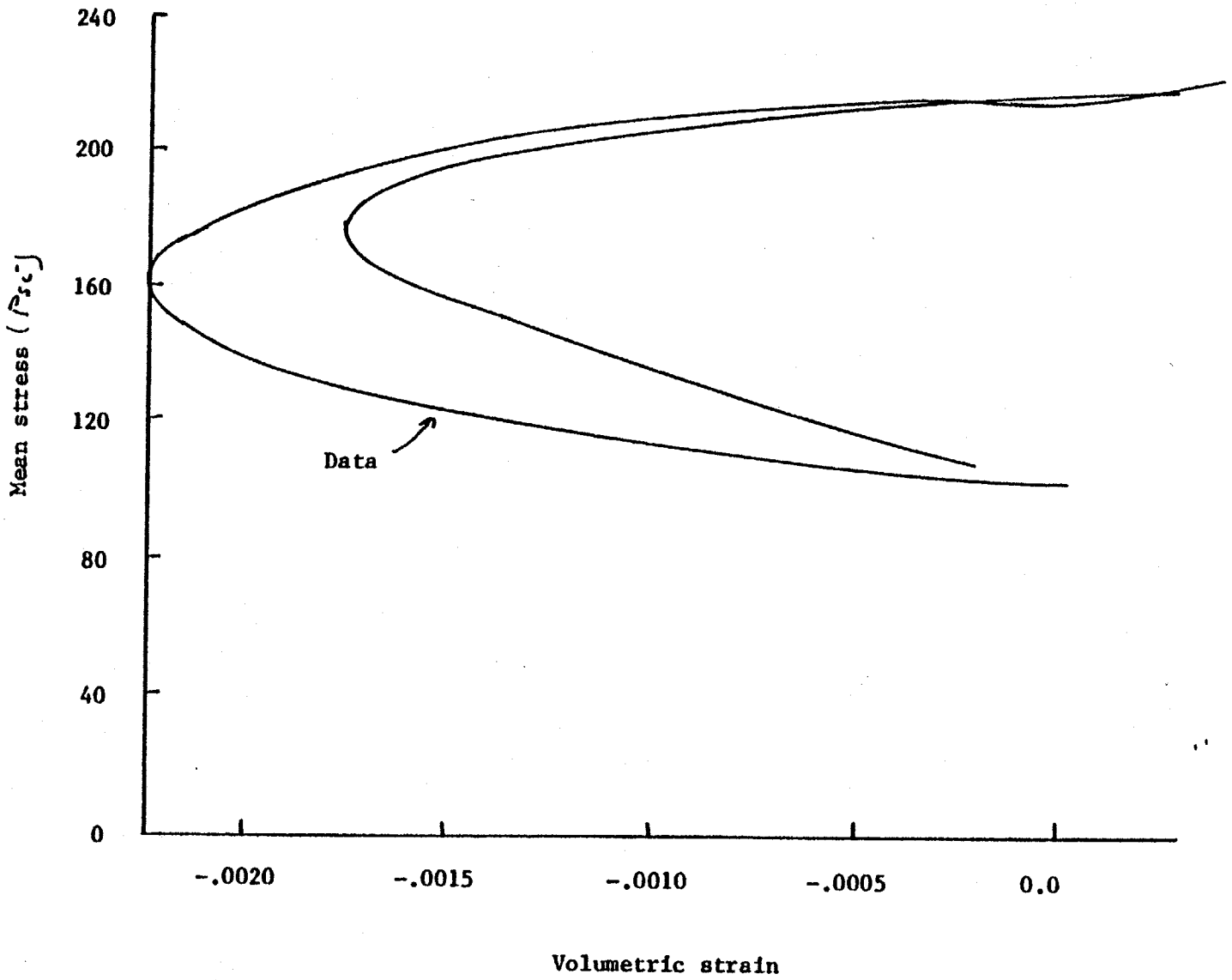

Figure 3b. Scaled data 50psi to 100psi, isotropic.

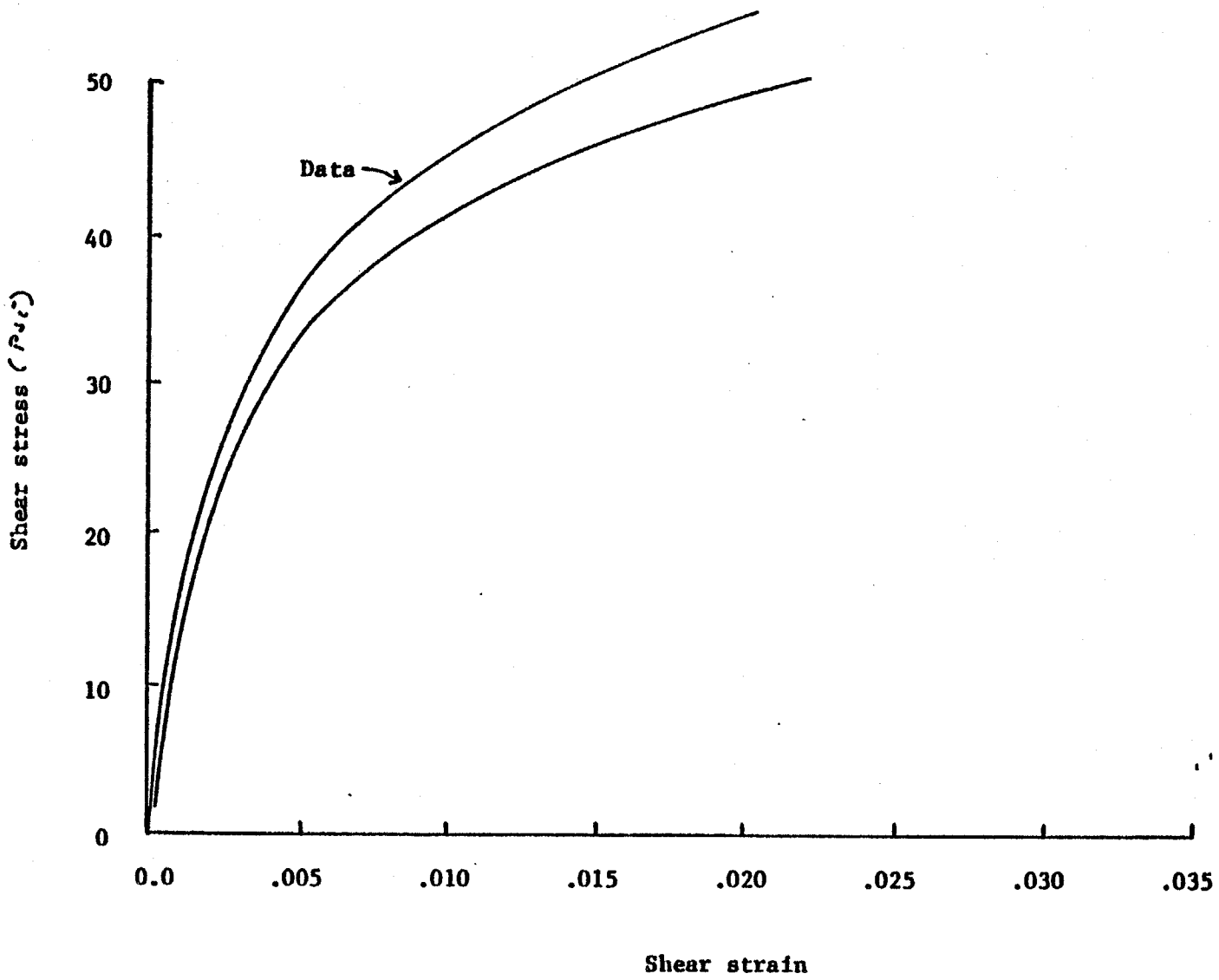

Figure 4a. Scaled data 50psi to 25psi, isotropic.

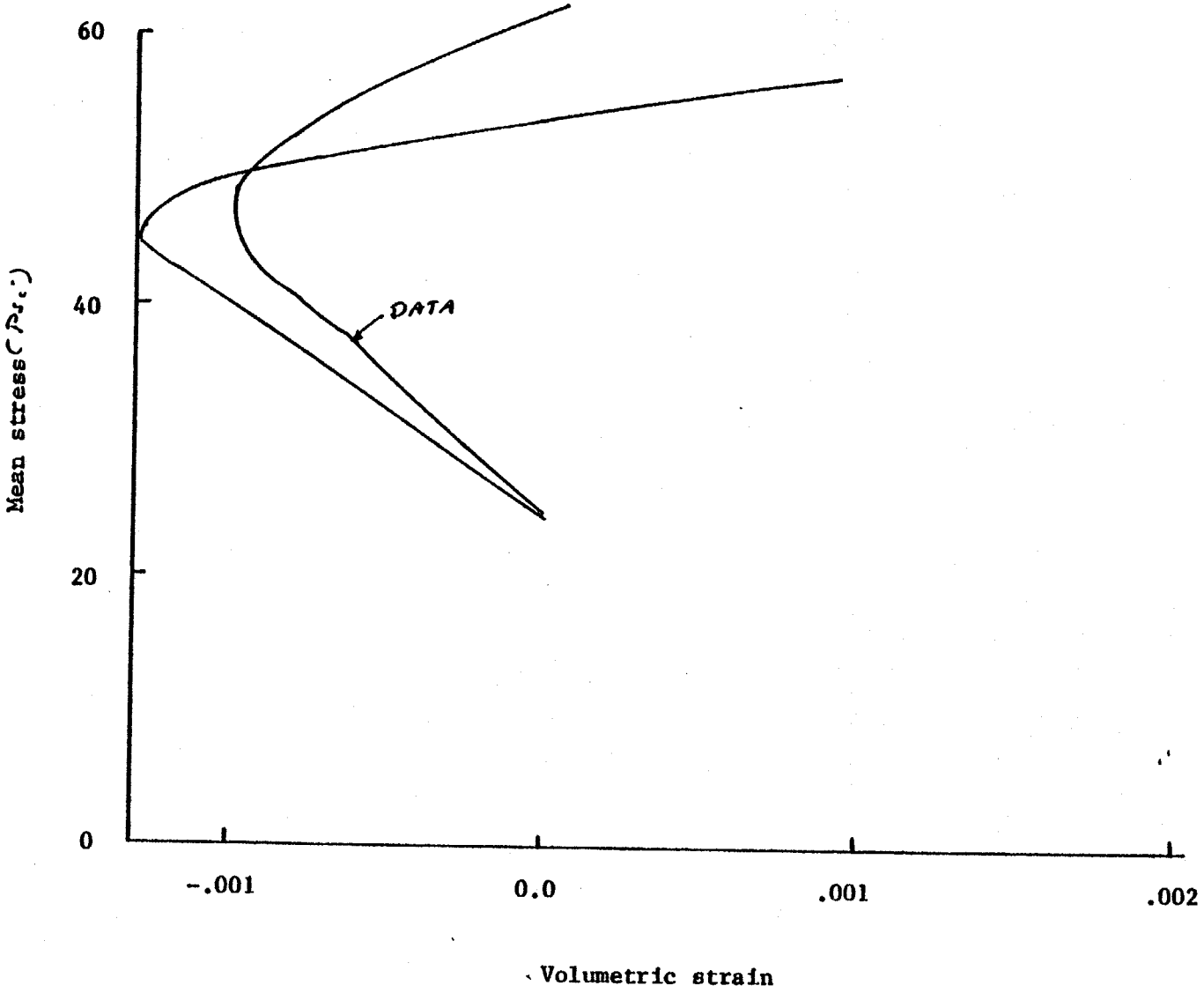

Figure 4b. Scaled data 50psi to 25psi, isotropic.

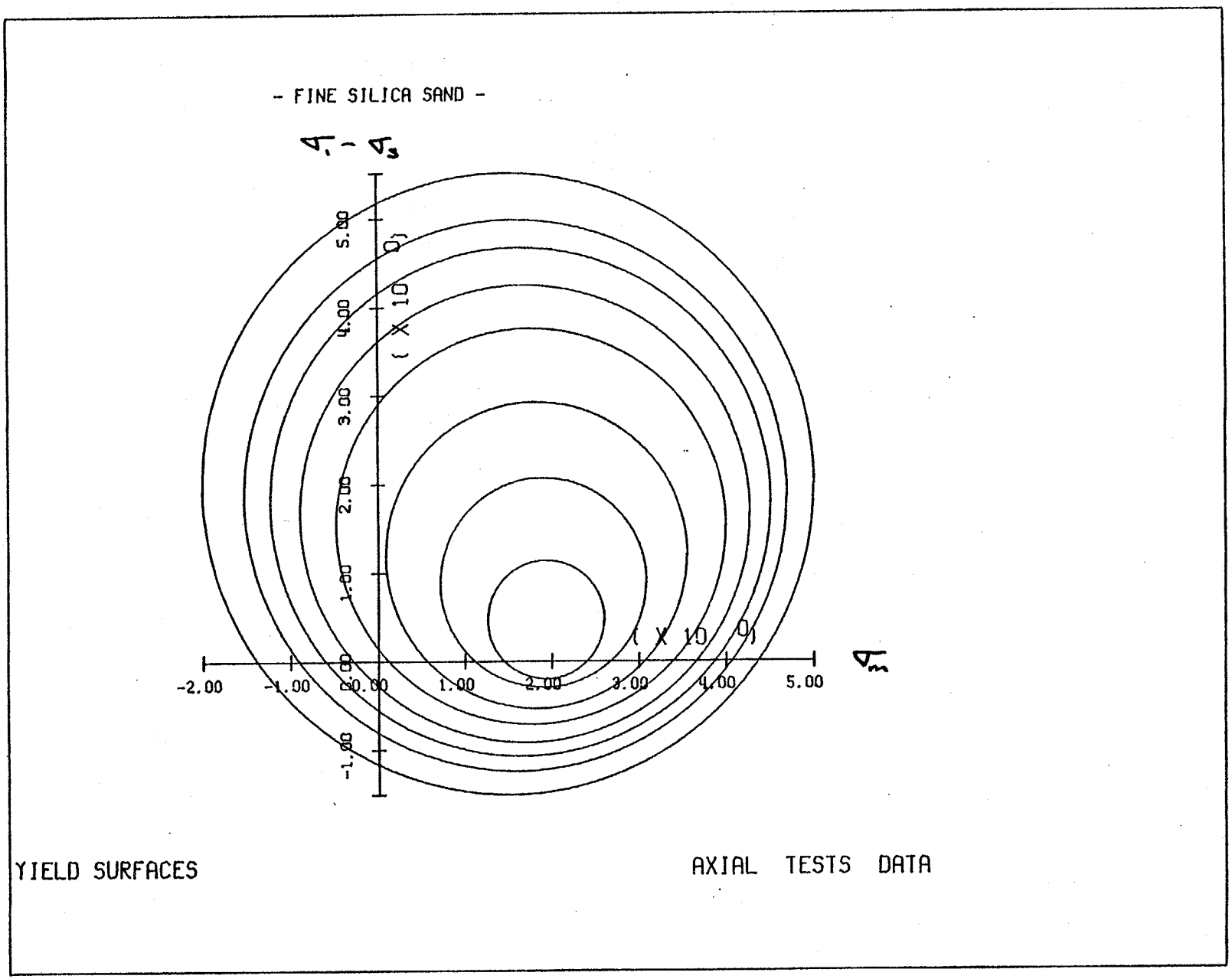

Figure 5a. Yield surfaces for soil described in Appendix A.

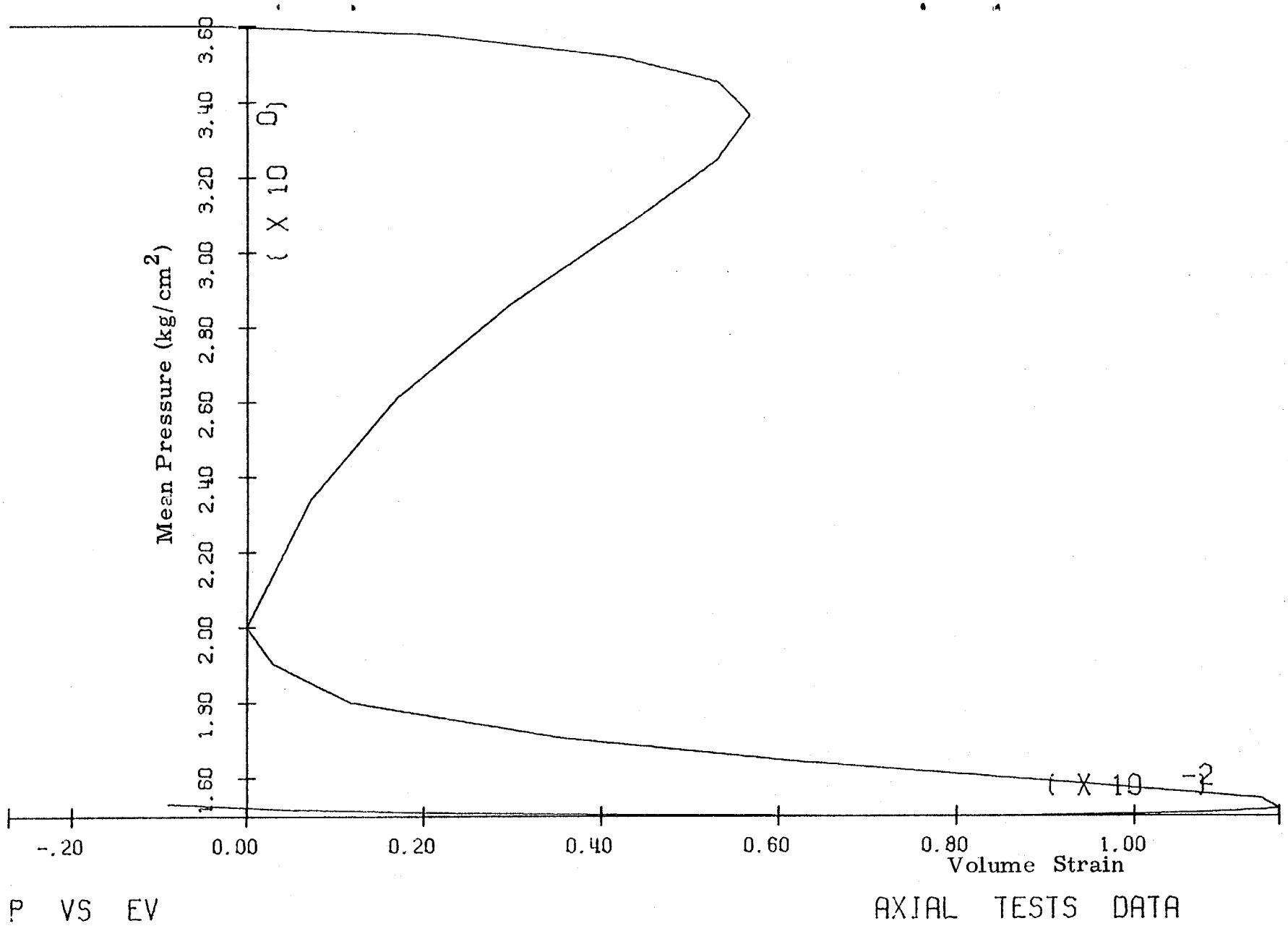

Figure 5b. Mean stress volume strain plot.

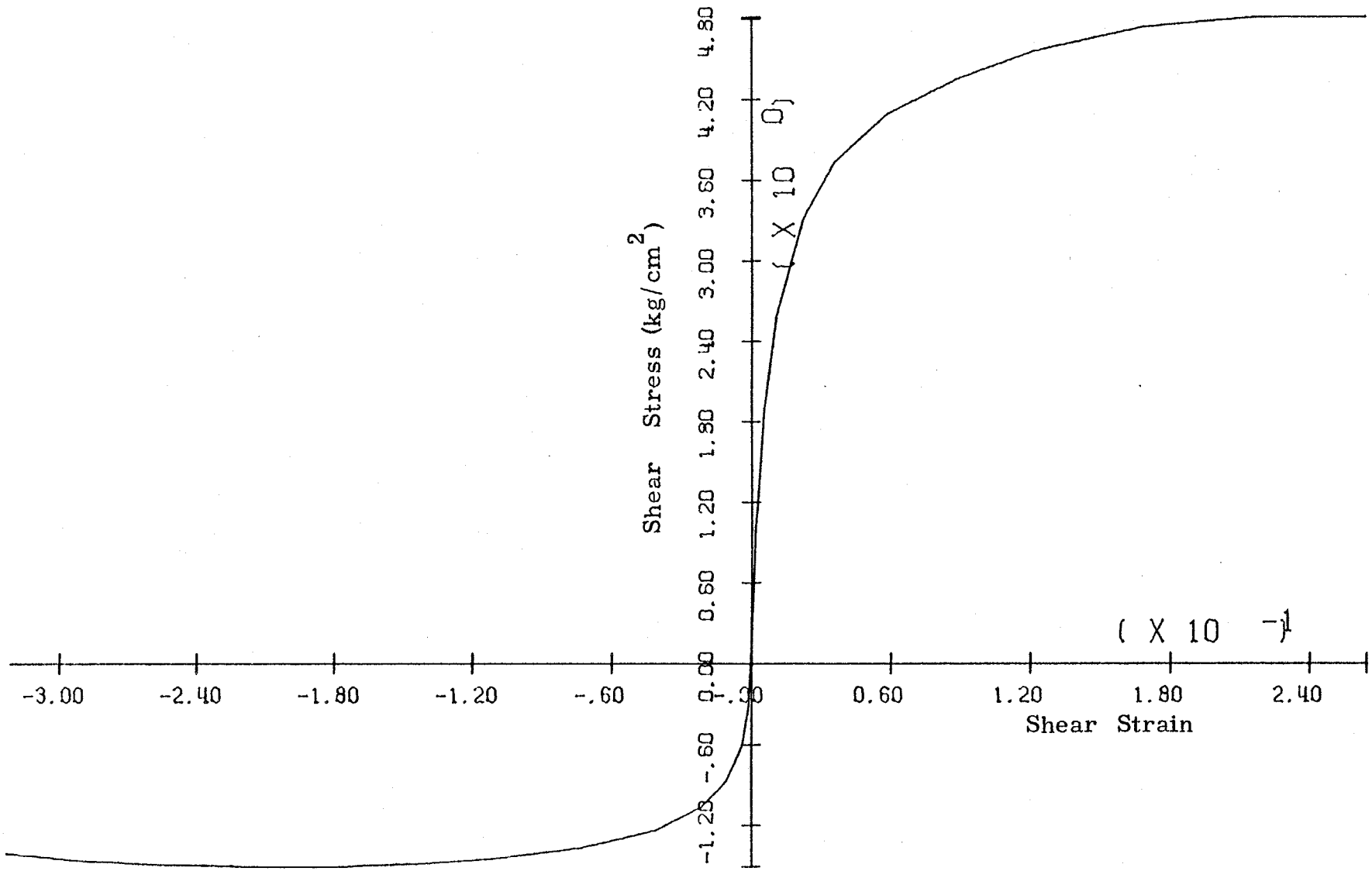

Figure 5c. Shear stress Shear strain plot.

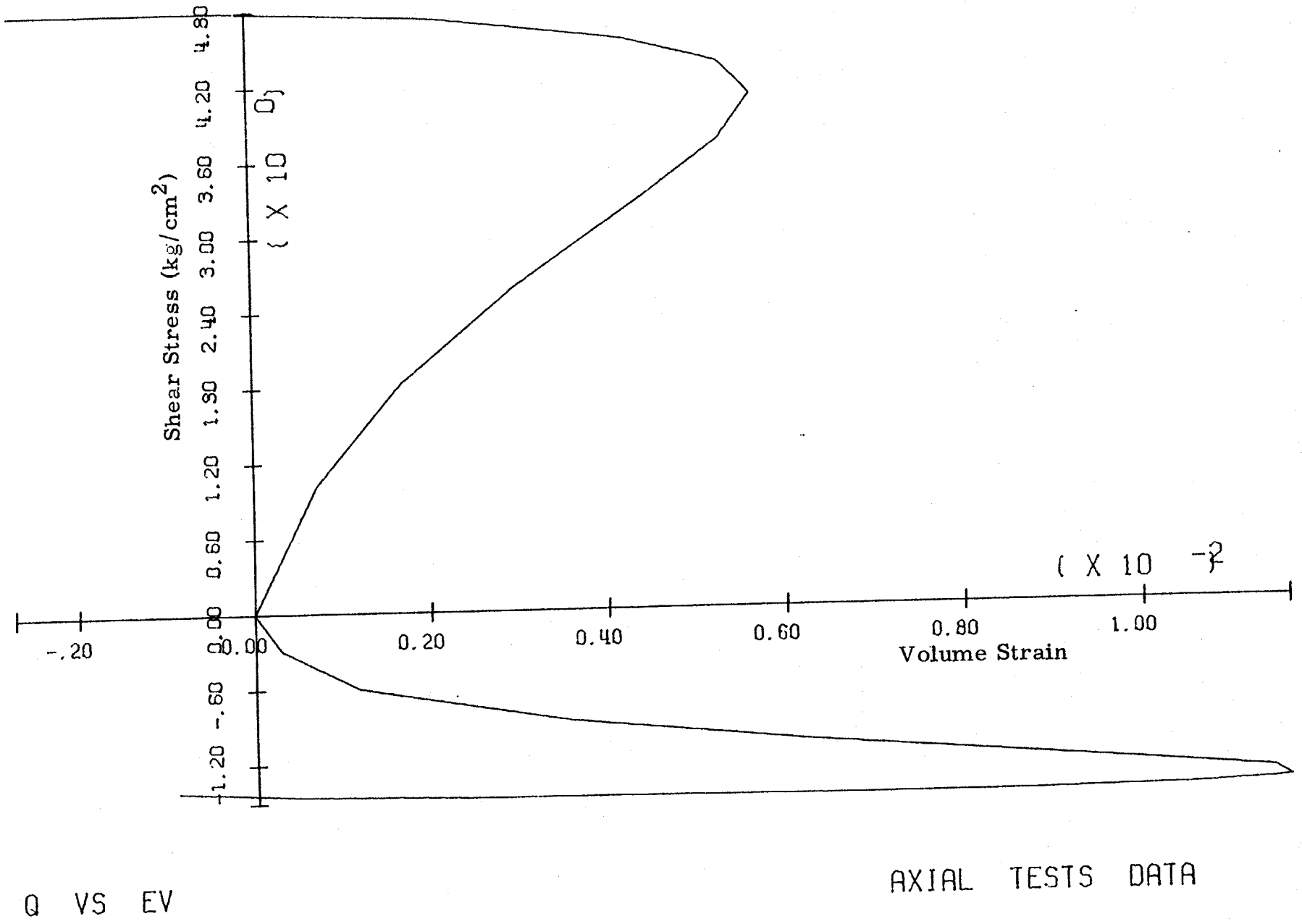

Figure 5d. Shear stress volume strain plot.

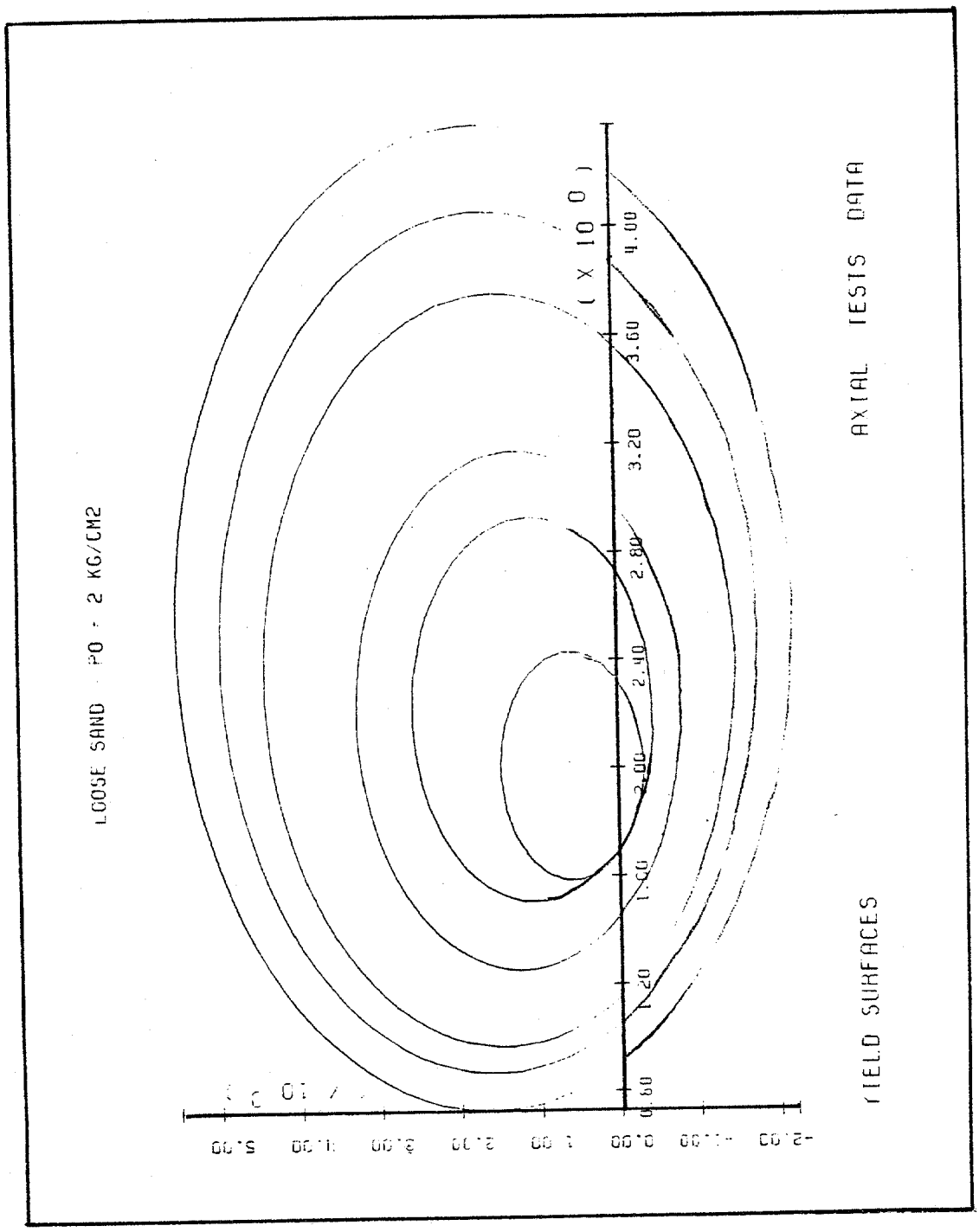

Figure 6. Cook's Sand yield surfaces.

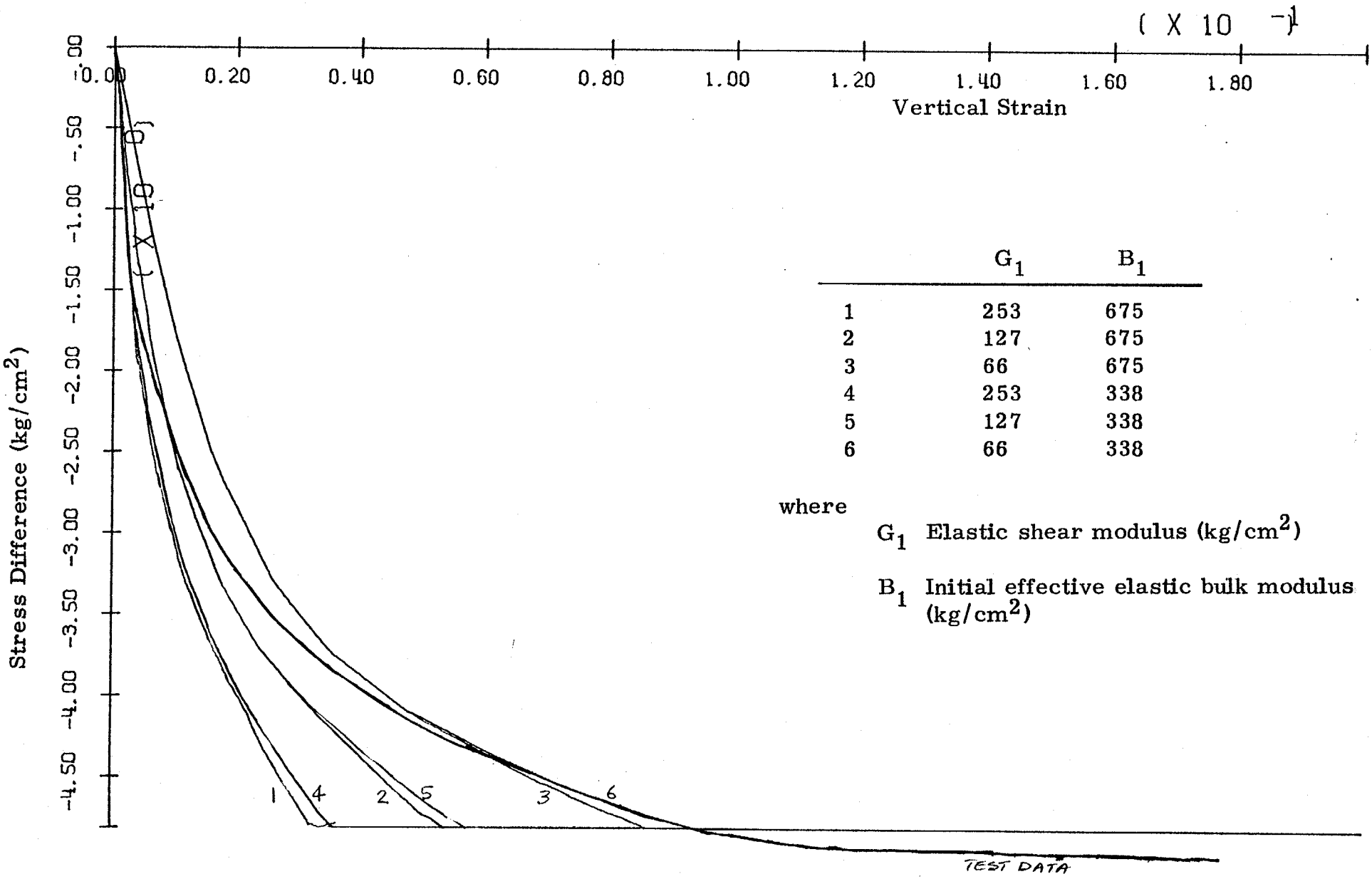

	G_1	B_1
1	253	675
2	127	675
3	66	675
4	253	338
5	127	338
6	66	338

where

G_1 Elastic shear modulus (kg/cm^2)

B_1 Initial effective elastic bulk modulus (kg/cm^2)

Figure 7a. Shear stress - vertical strain compression test showing the effect of variation of moduli.

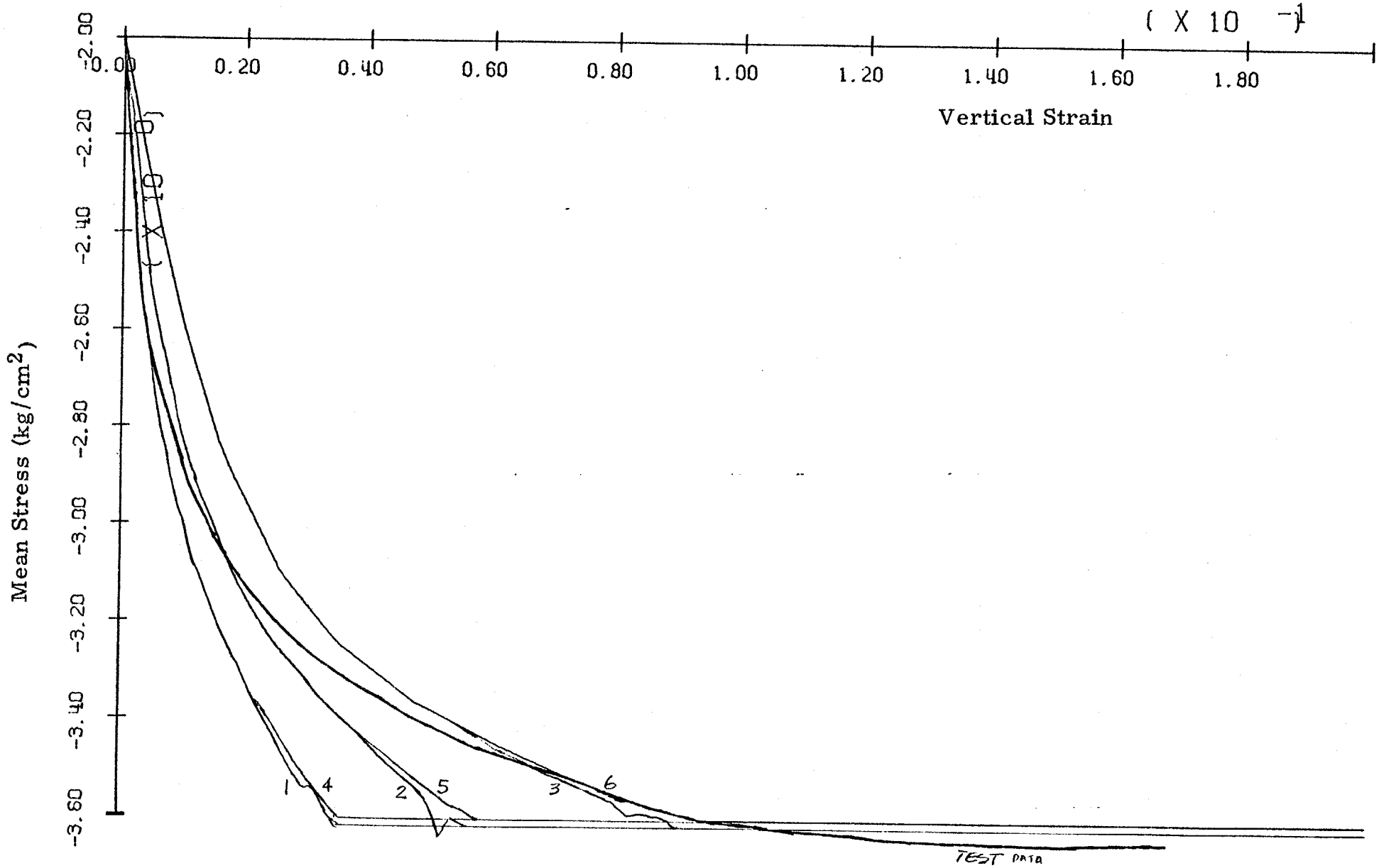

Figure 7b. Mean stress - vertical strain, compression test.

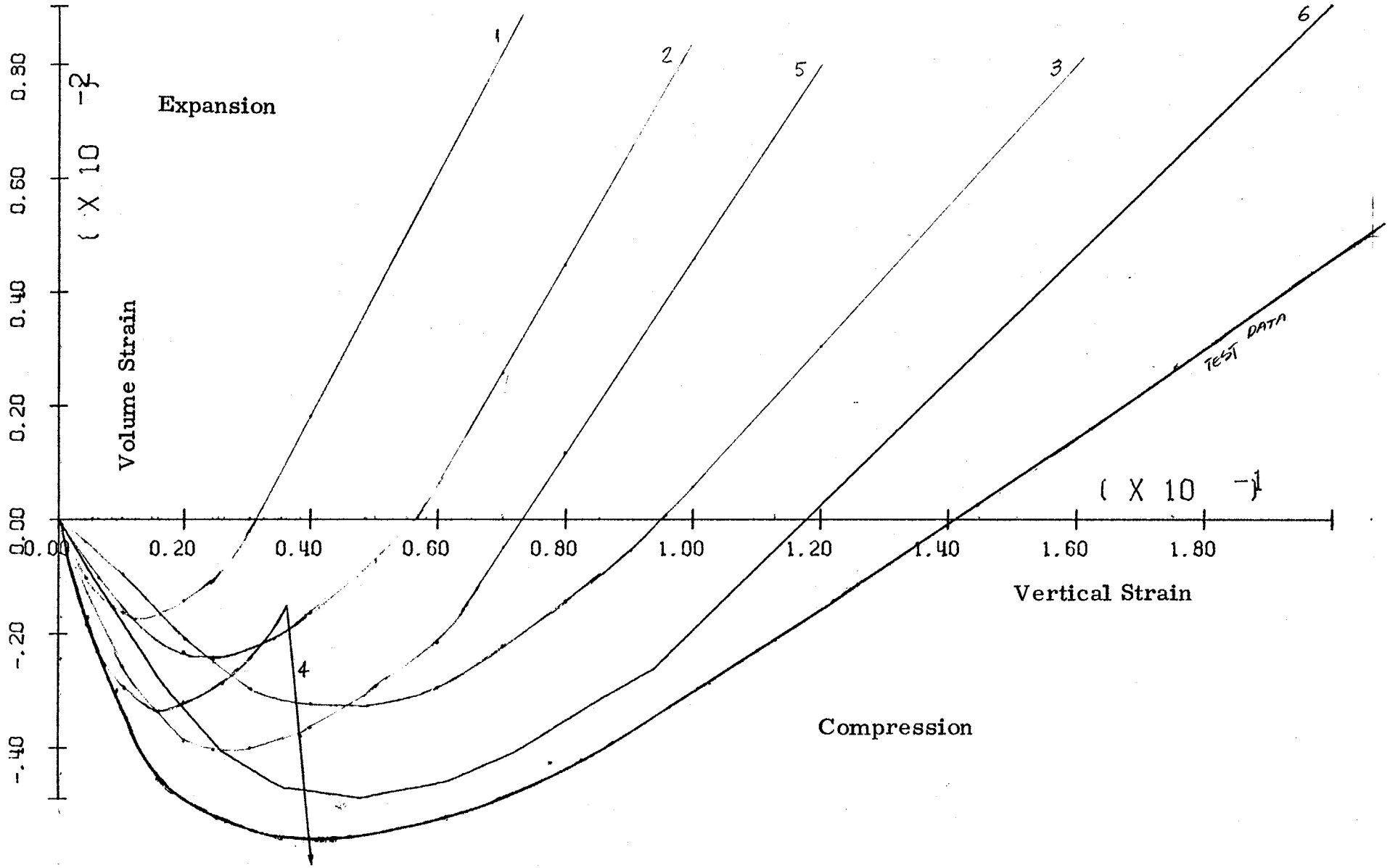

Figure 7c. Volume strain - vertical strain, compression test.

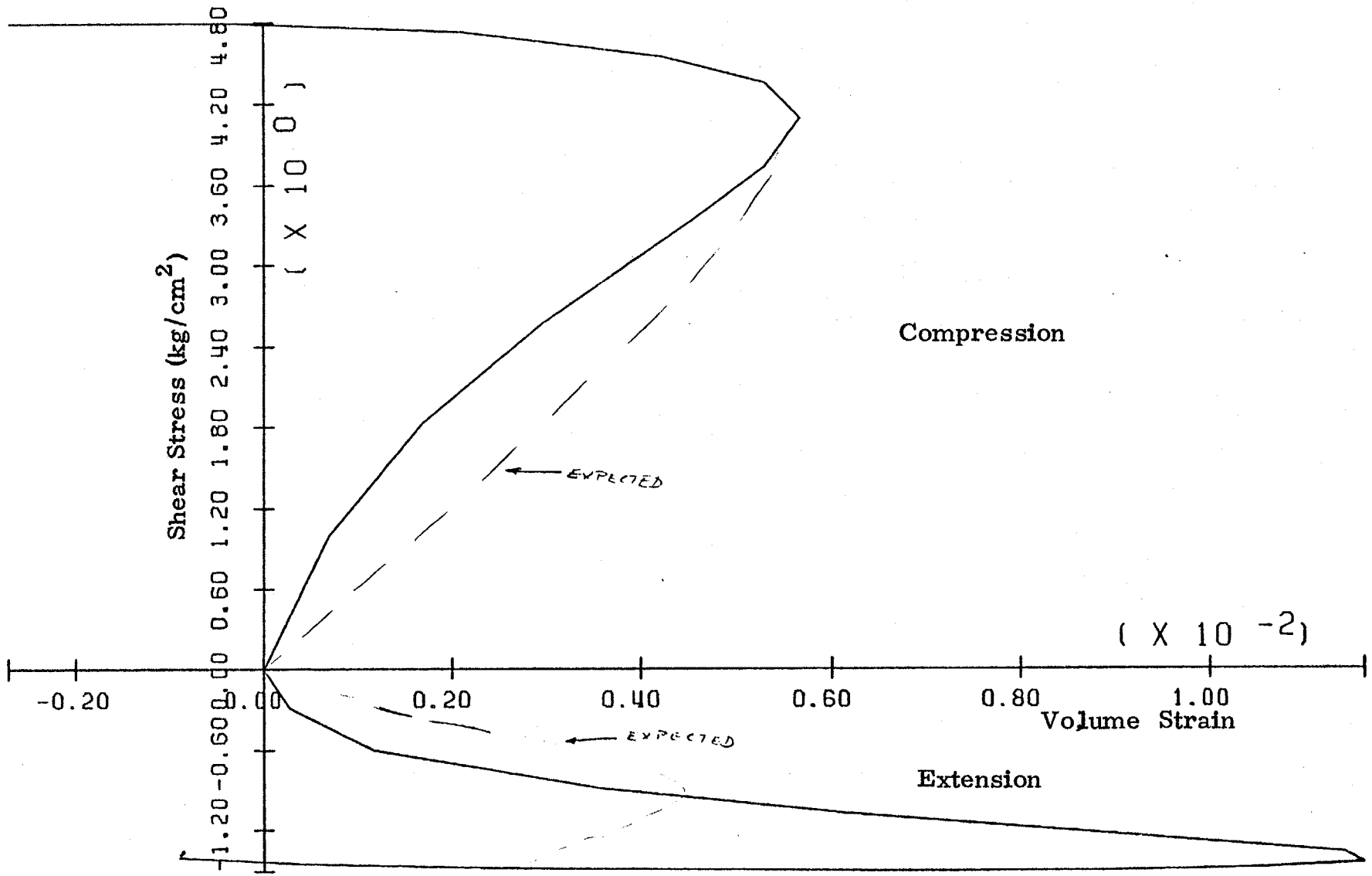

Figure 8. Shear stress volume strain in compression and extension.

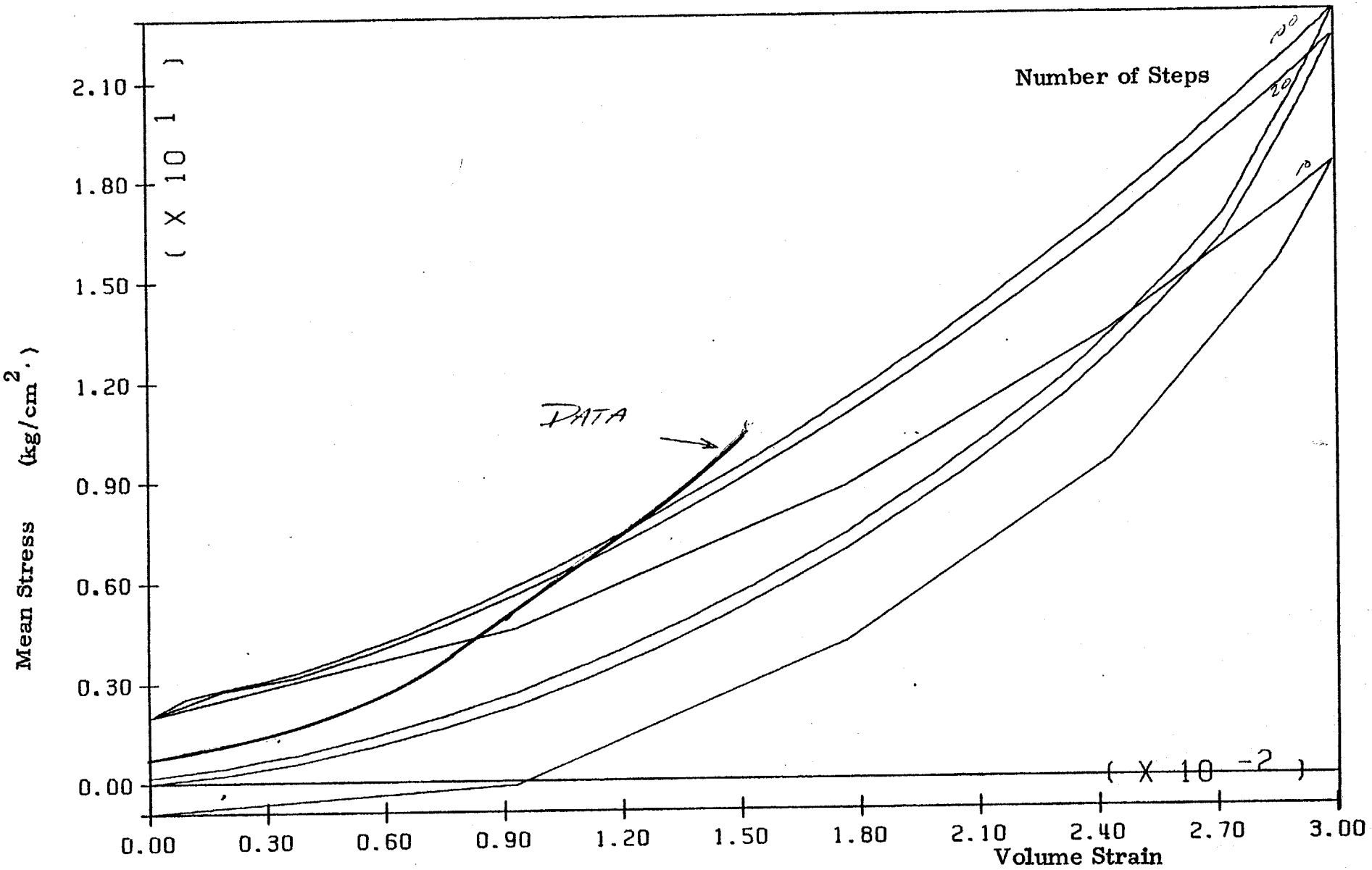

Figure 9a. K_o compression test , B1 =675 kg/cm^2, G_1 = 253 kg/cm^2.

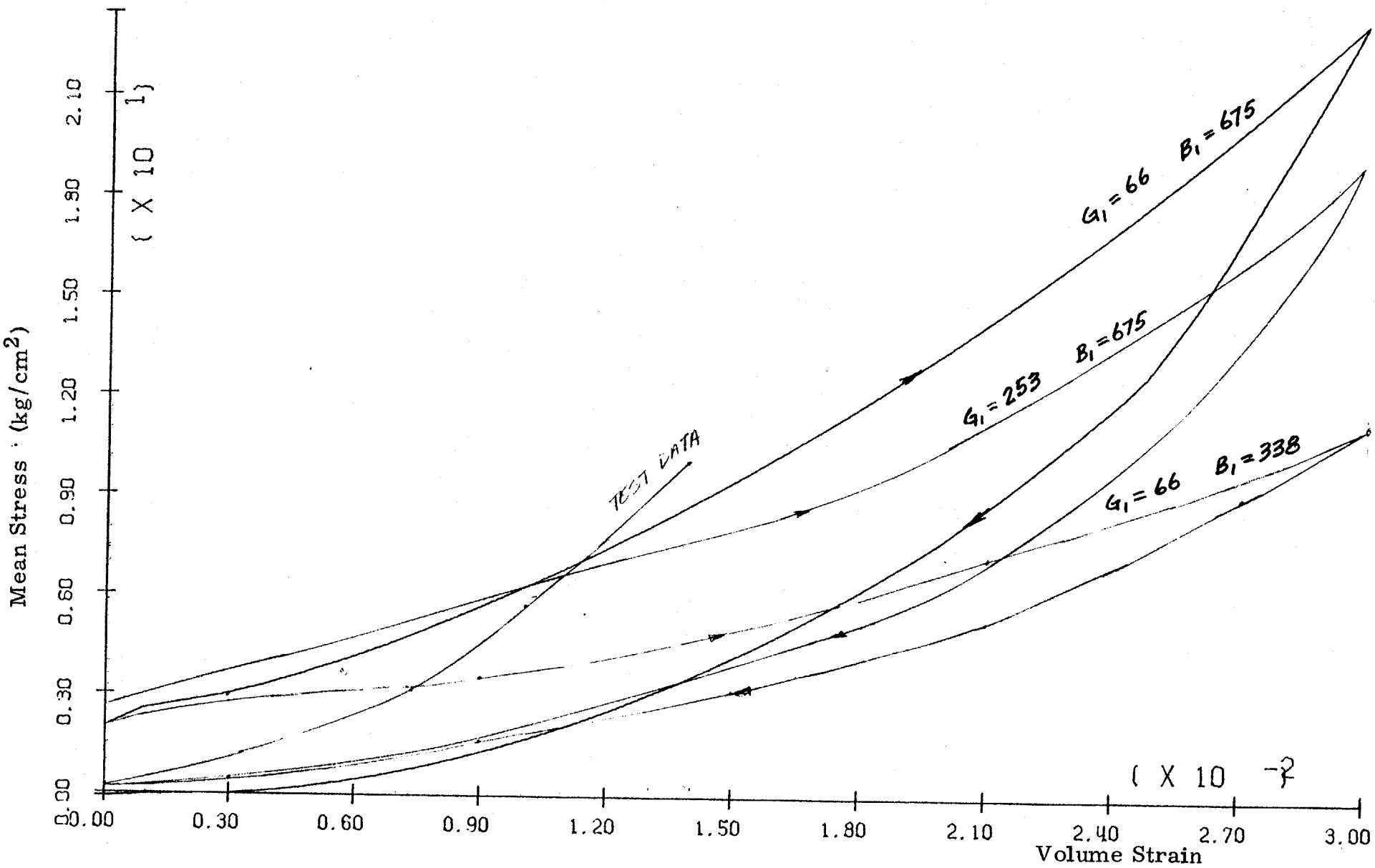

Figure 9b. K_0 compression test for various B_1 and G_1

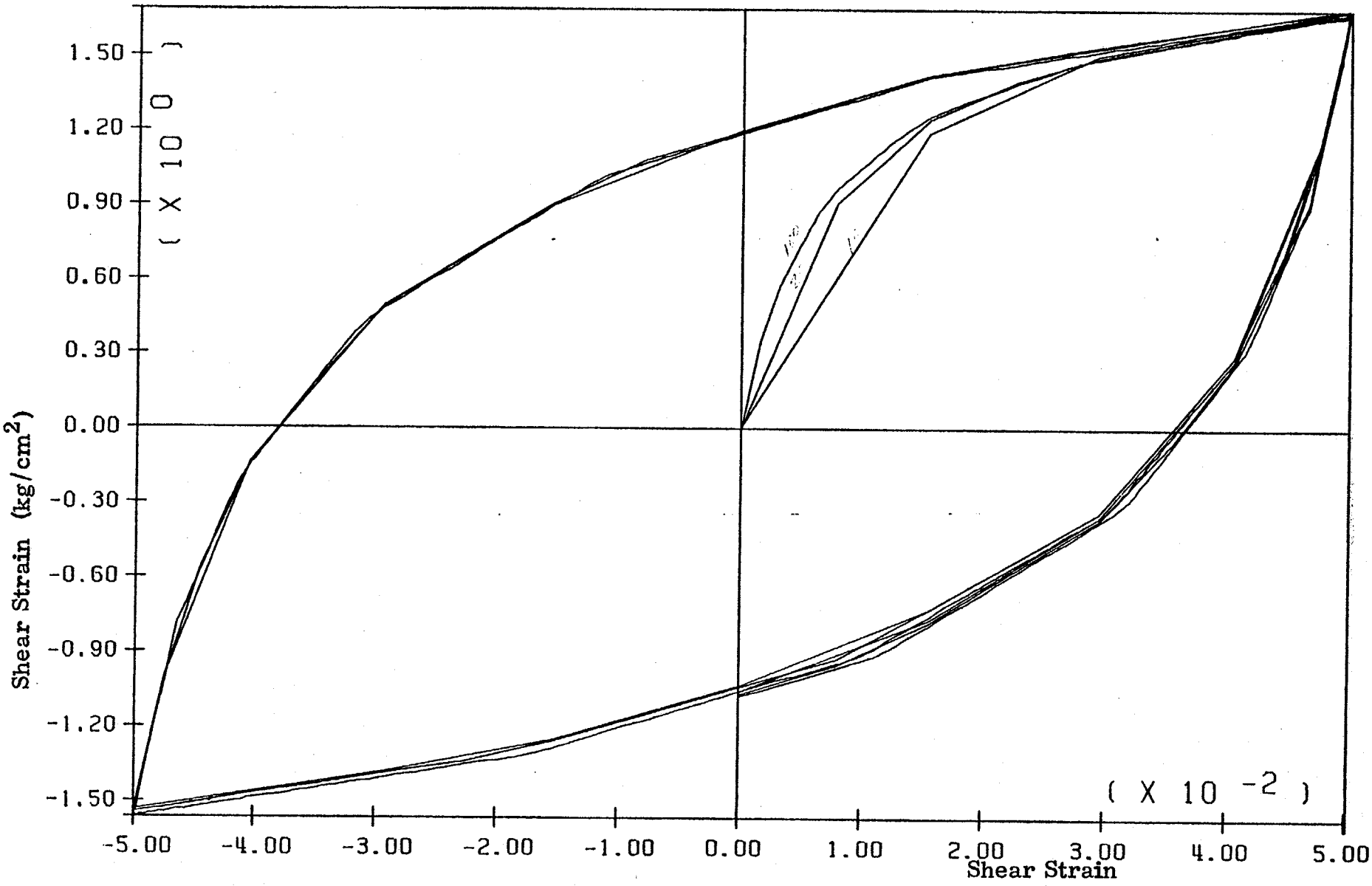

Figure 10 a. Shear Stress shear strain in simple shear test simulation.

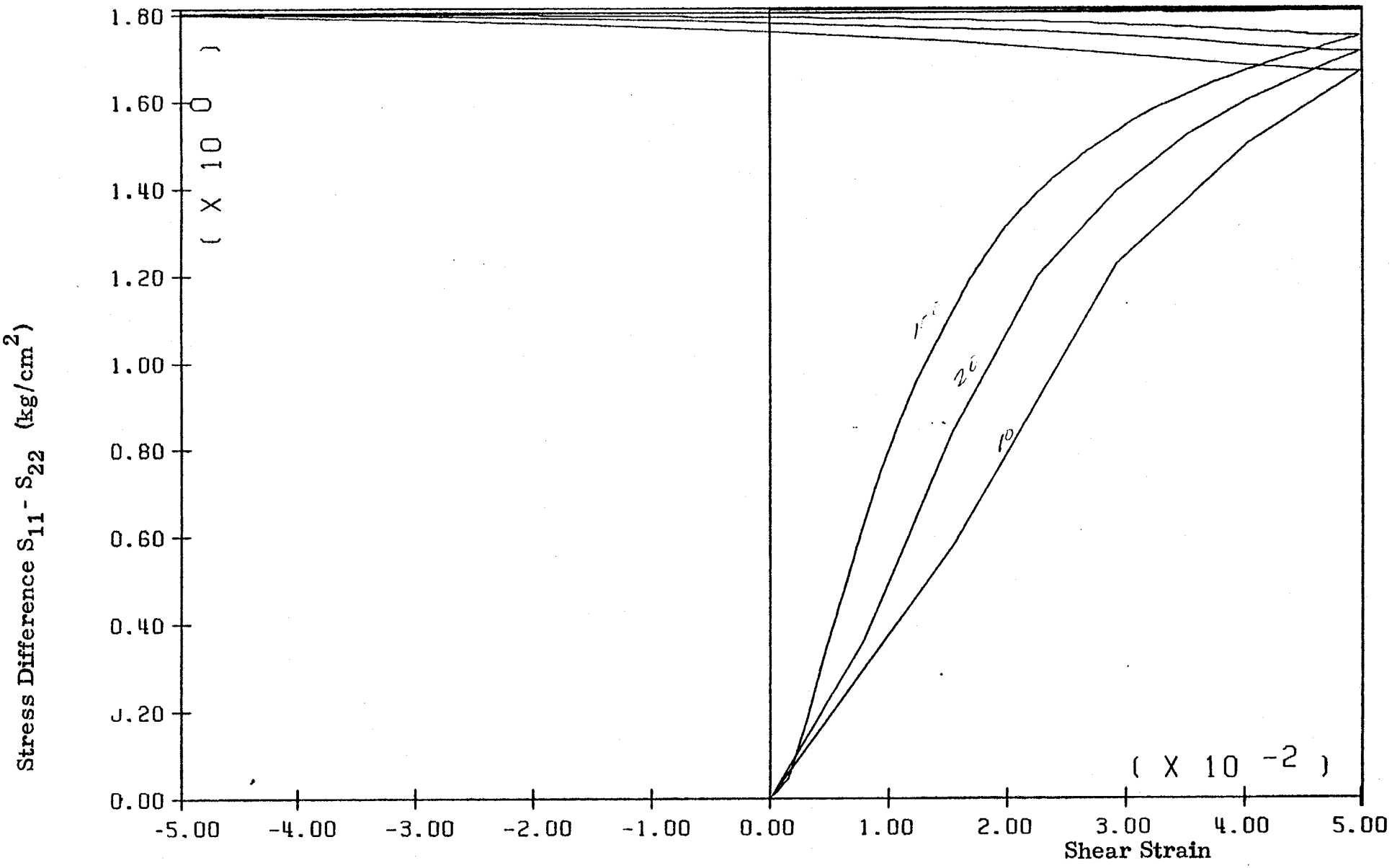

Figure 10b Stress difference - shear strain , simple shear test simulation.

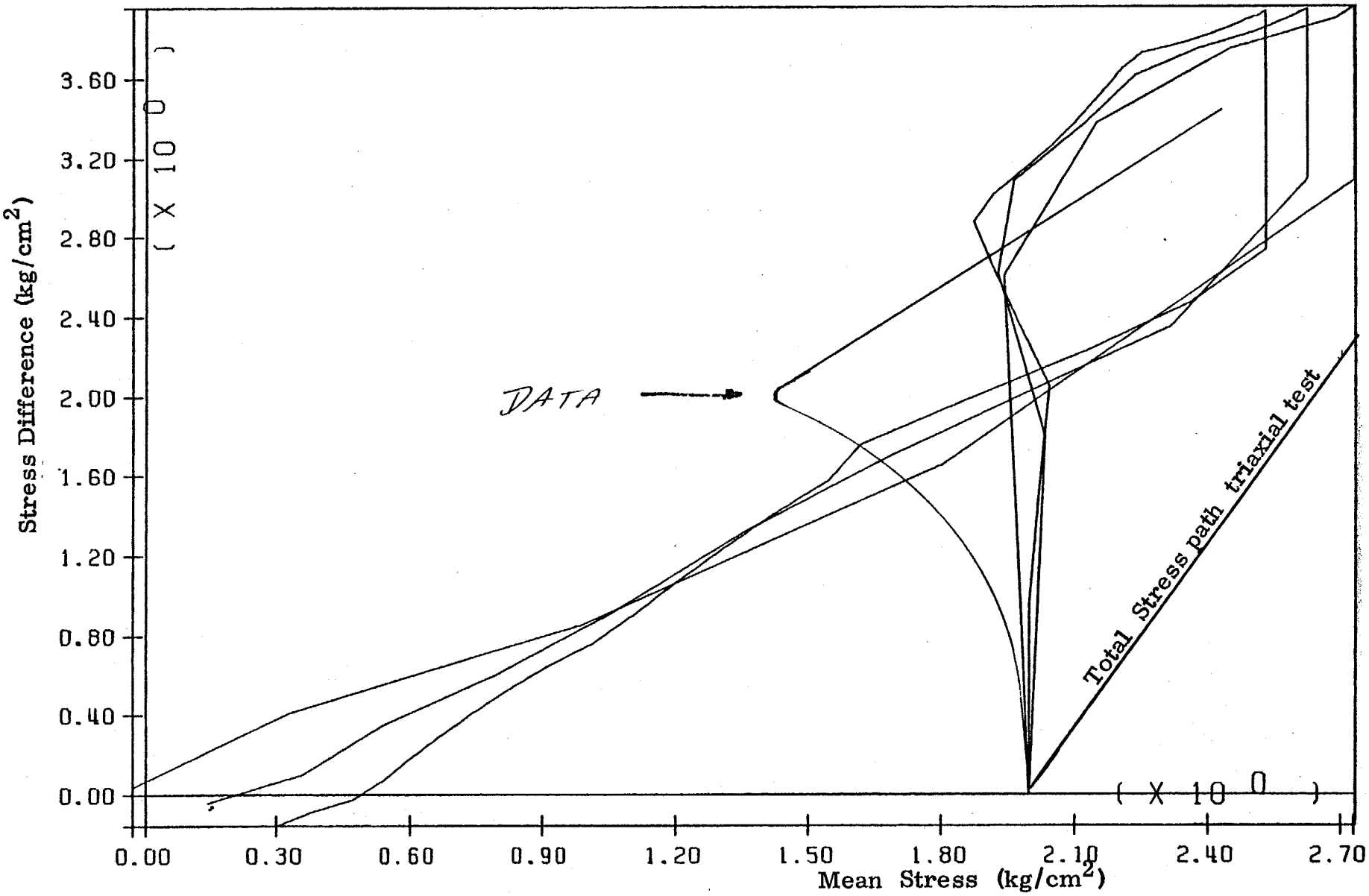

Figure 11. Stress difference - mean stress, stress path undrained test.

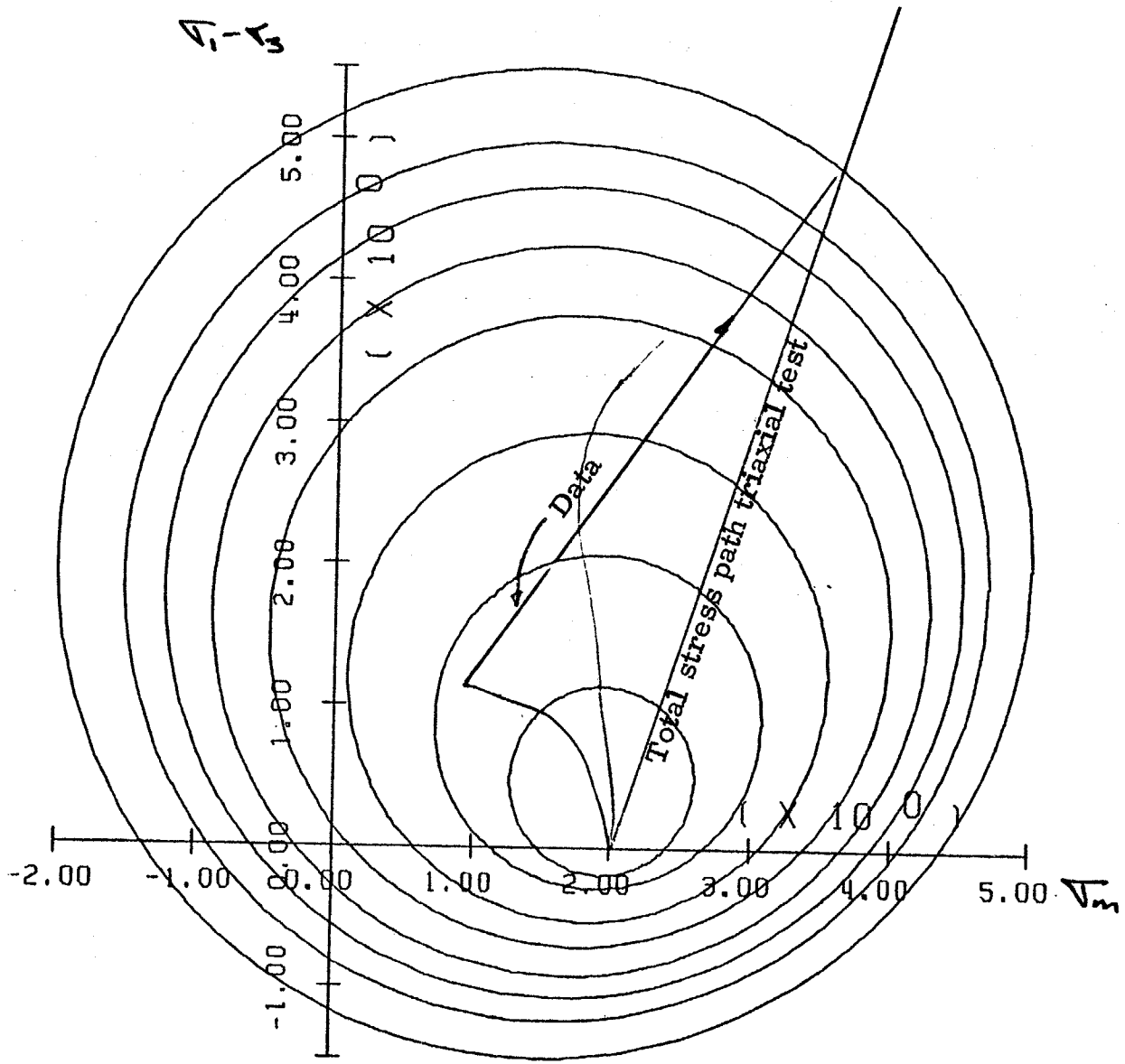

Figure 12. Yield surfaces and stress path.

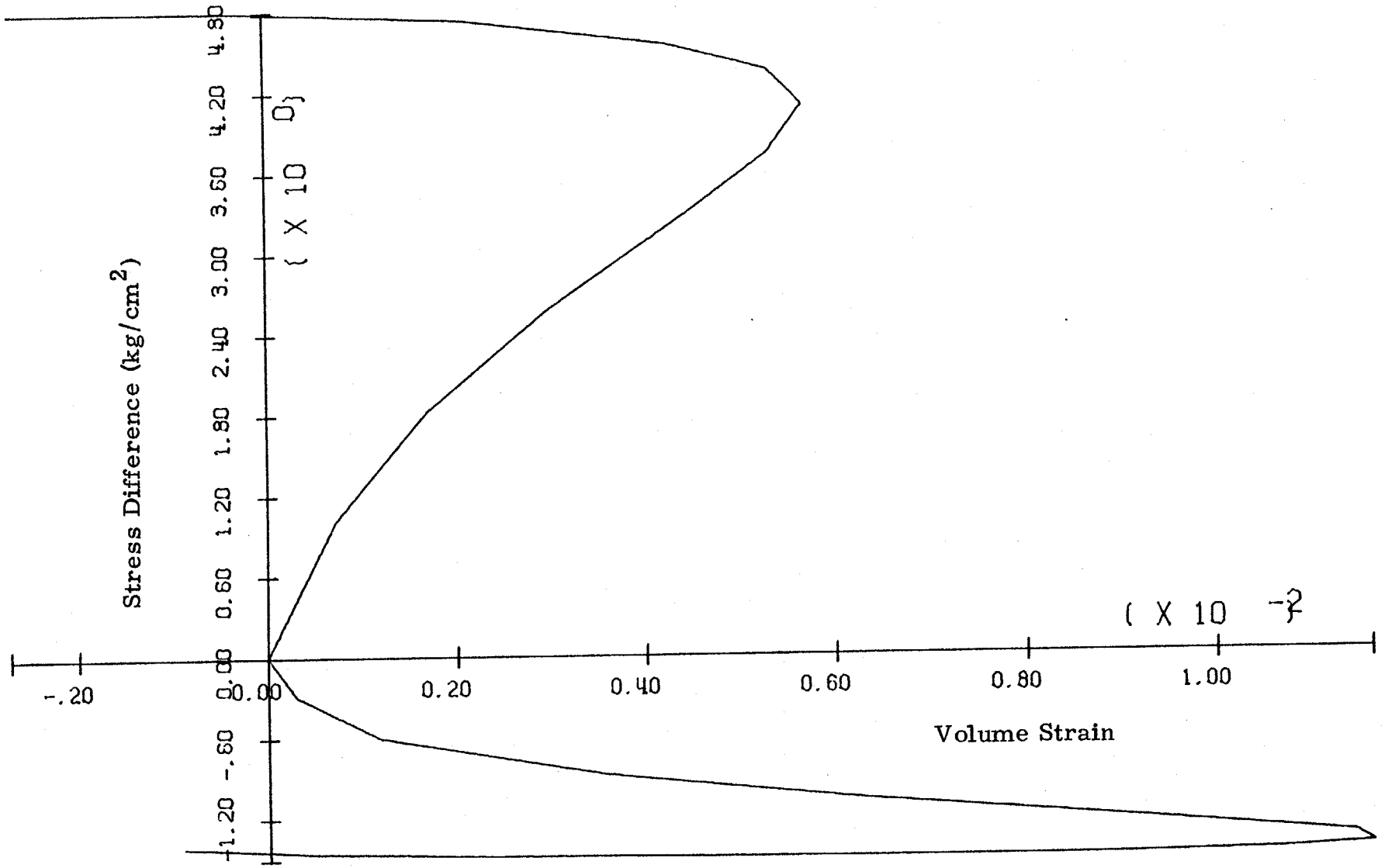

Figure 13a. Original volume data, B1= 338 kg/cm^2, G_1=66 kg/cm^2.

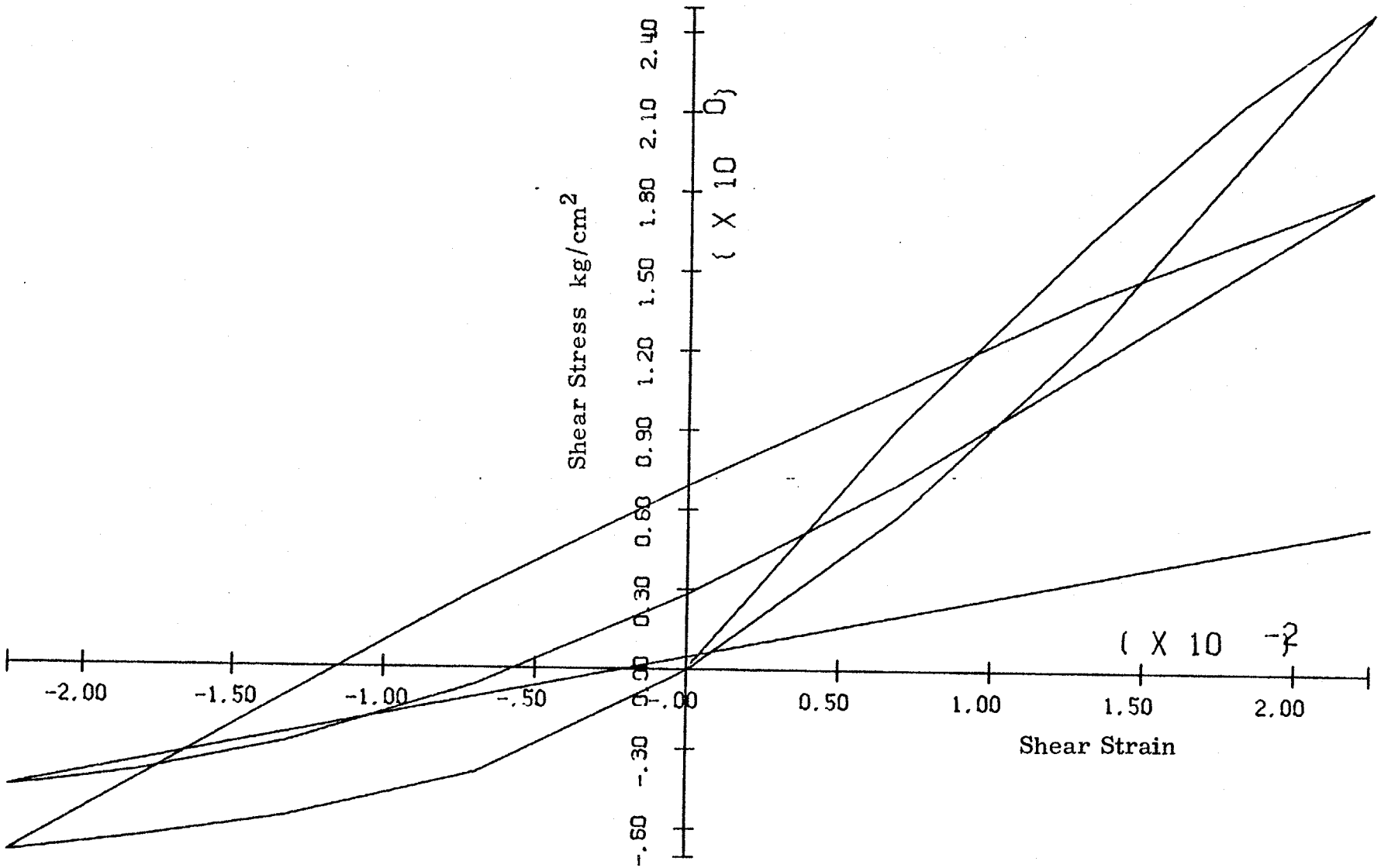

Figure 13b. Shear stress- shear strain B_1=338 kg/cm^2, G_1=66 kg/cm^2.

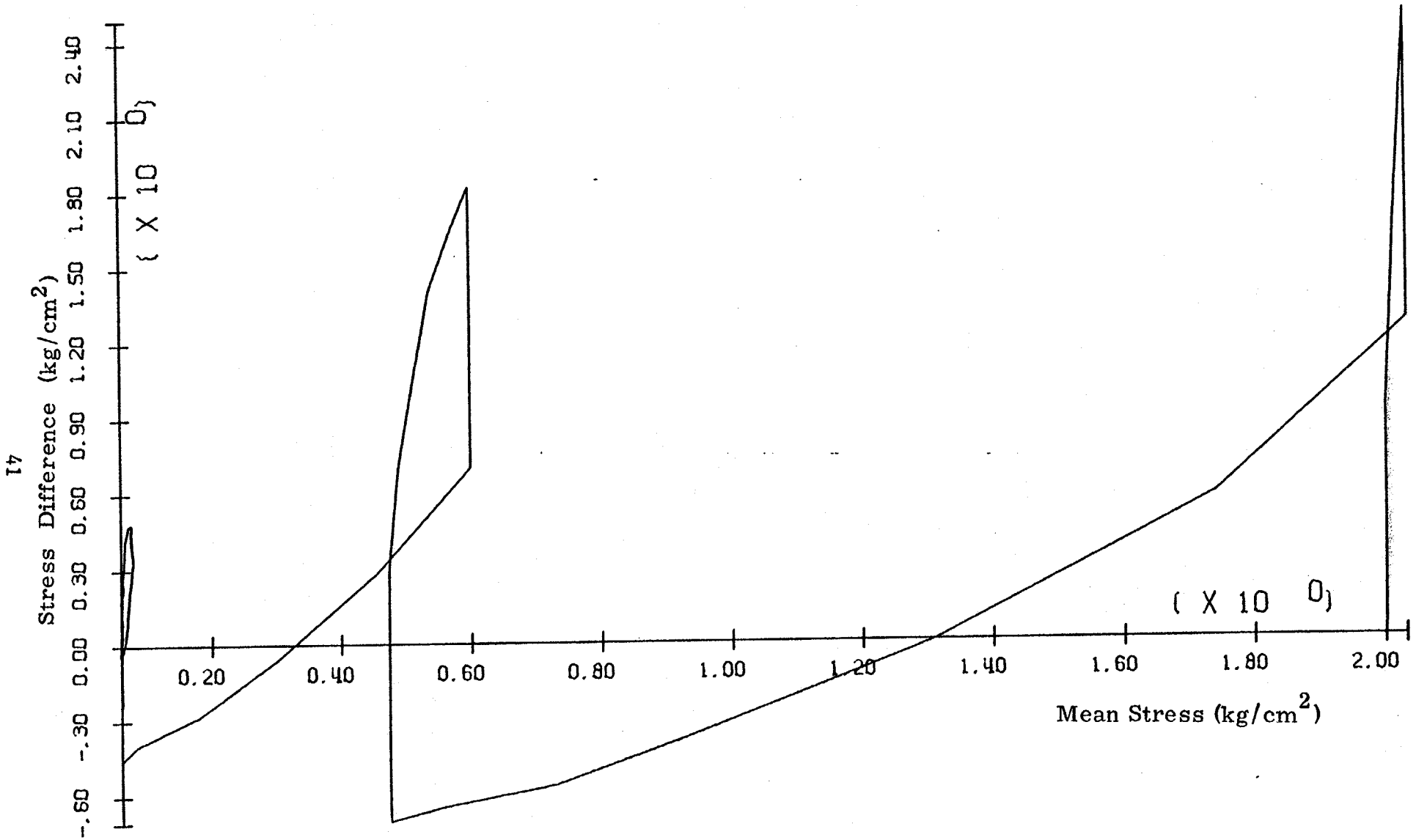

Figure 13c. Stress path B_1= 338 kg/cm^2, G_1= 66 kg/cm^2.

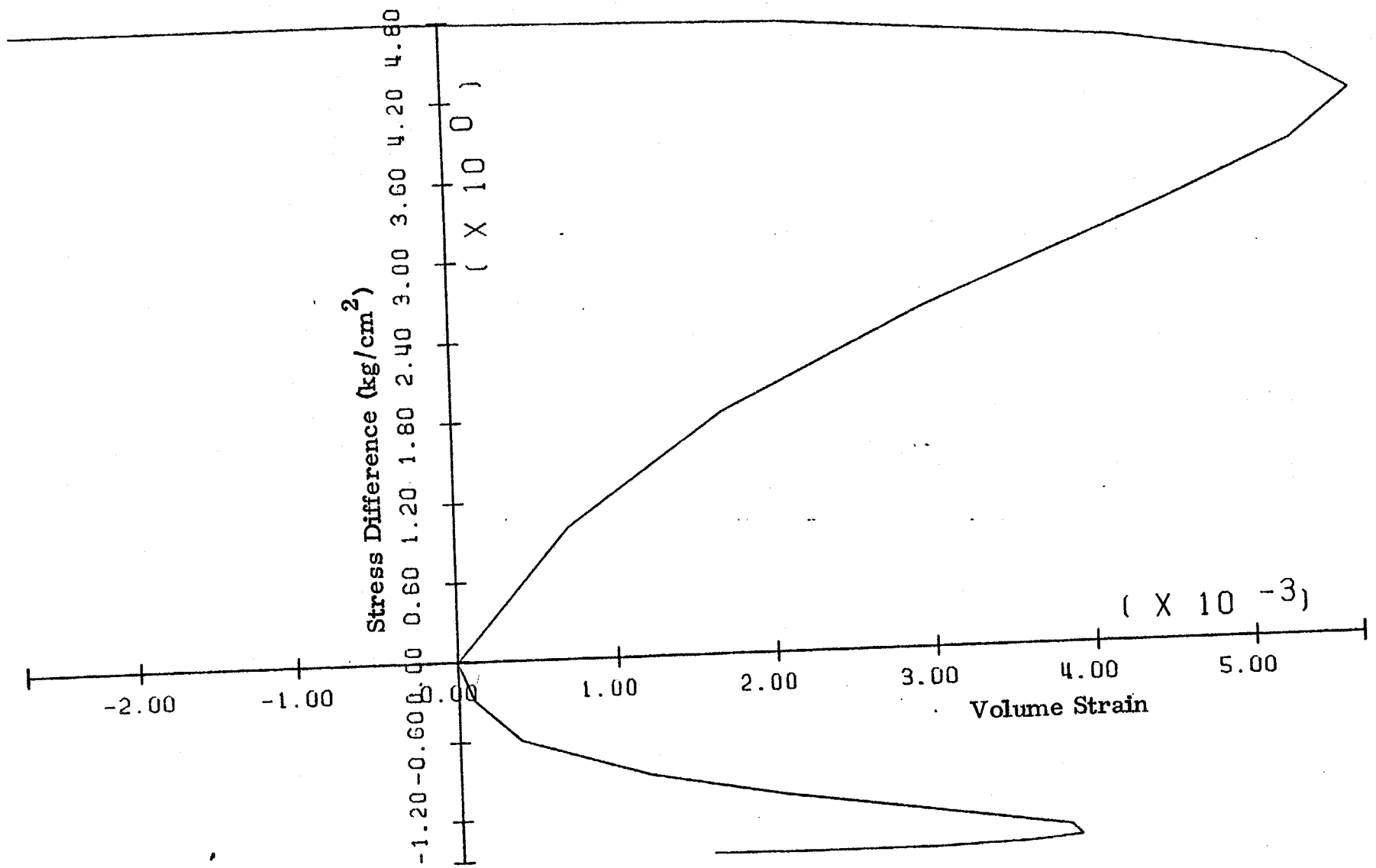

Figure 14a. Revised volumetric data in extension .

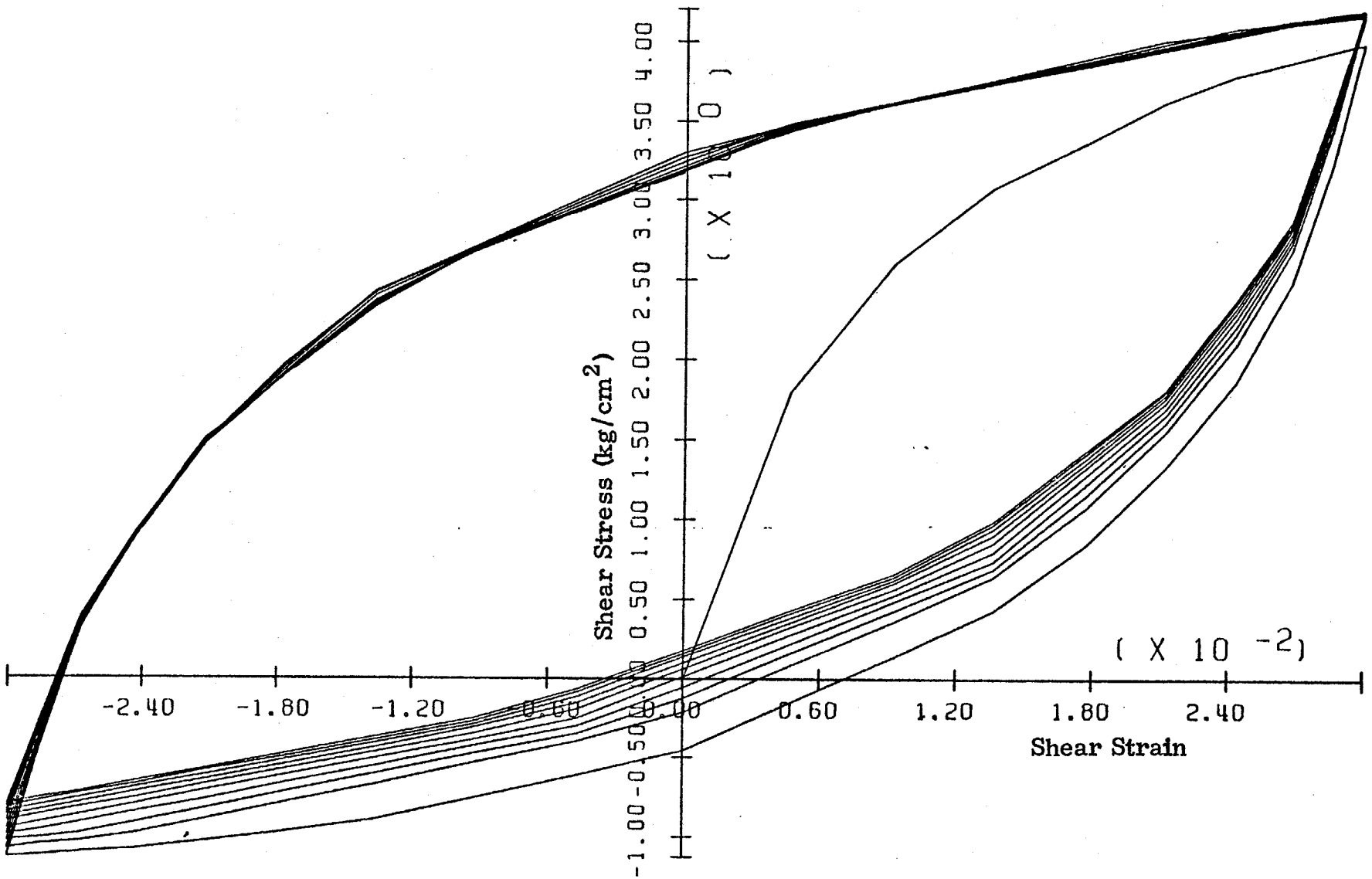

Figure 14b.Shear stress - shear strain modified data.

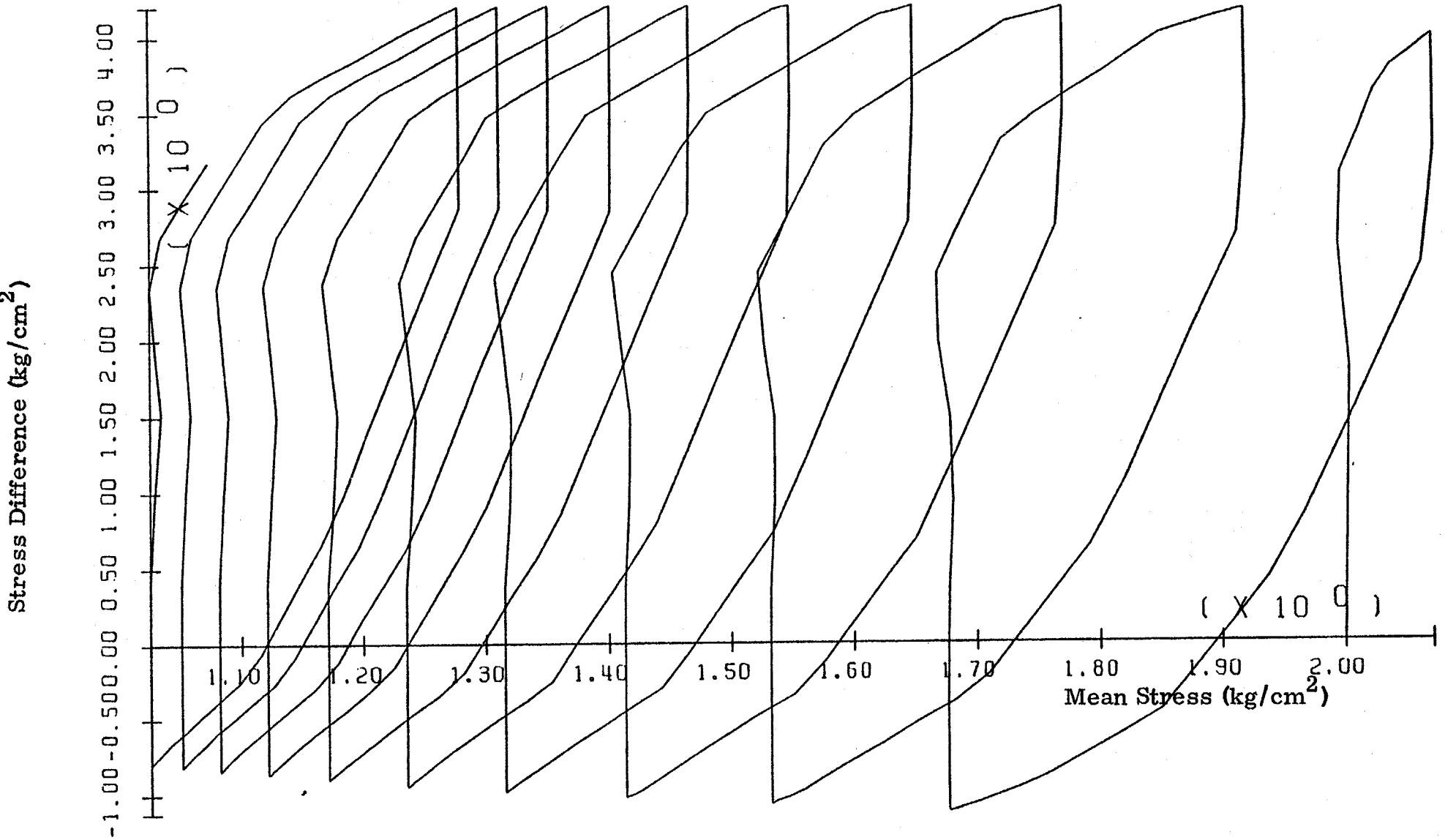

Figure 14c. Stress path modified soil data.

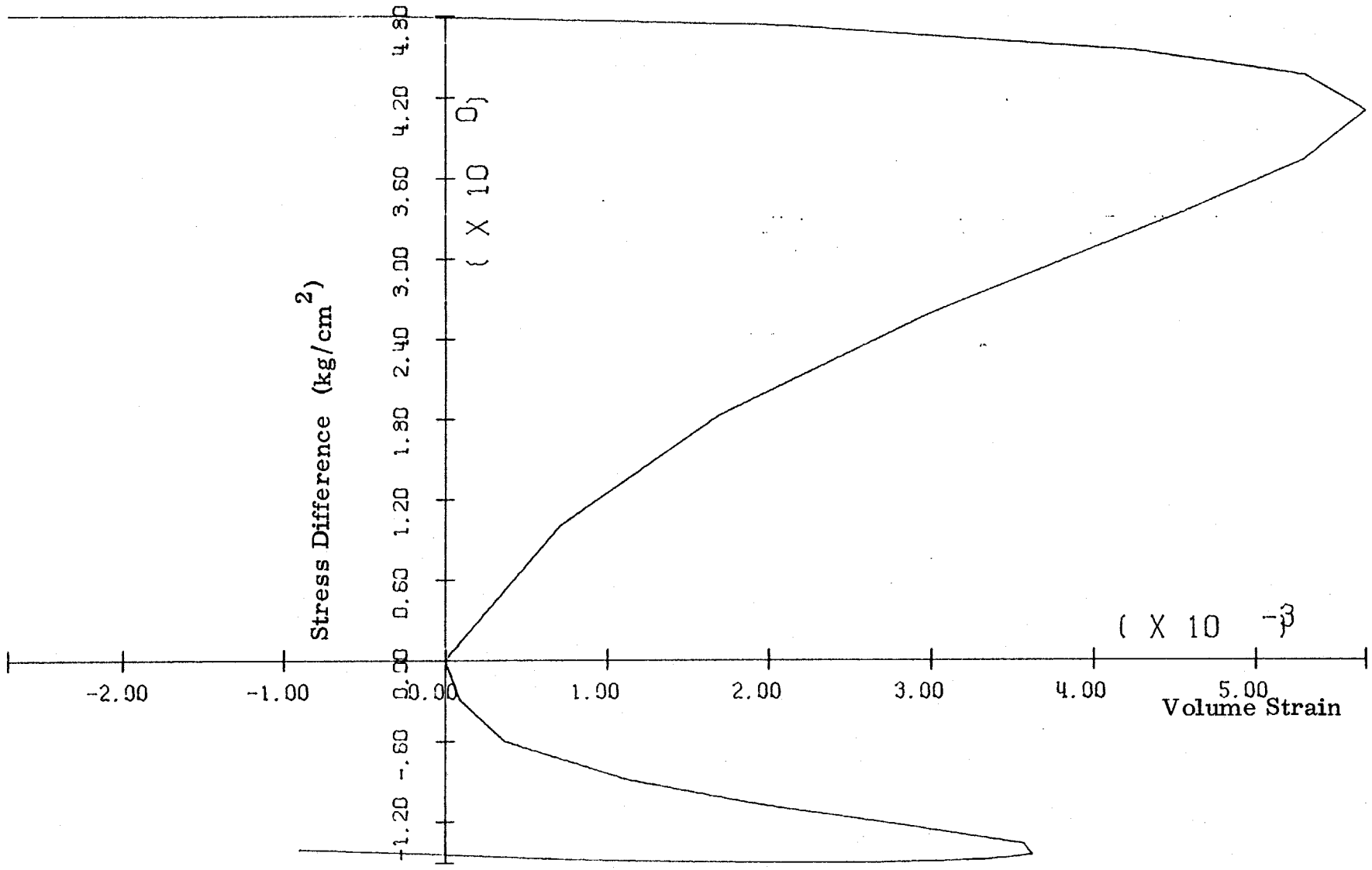

Figure 15a. Stress - strain data for soil modified in extension.

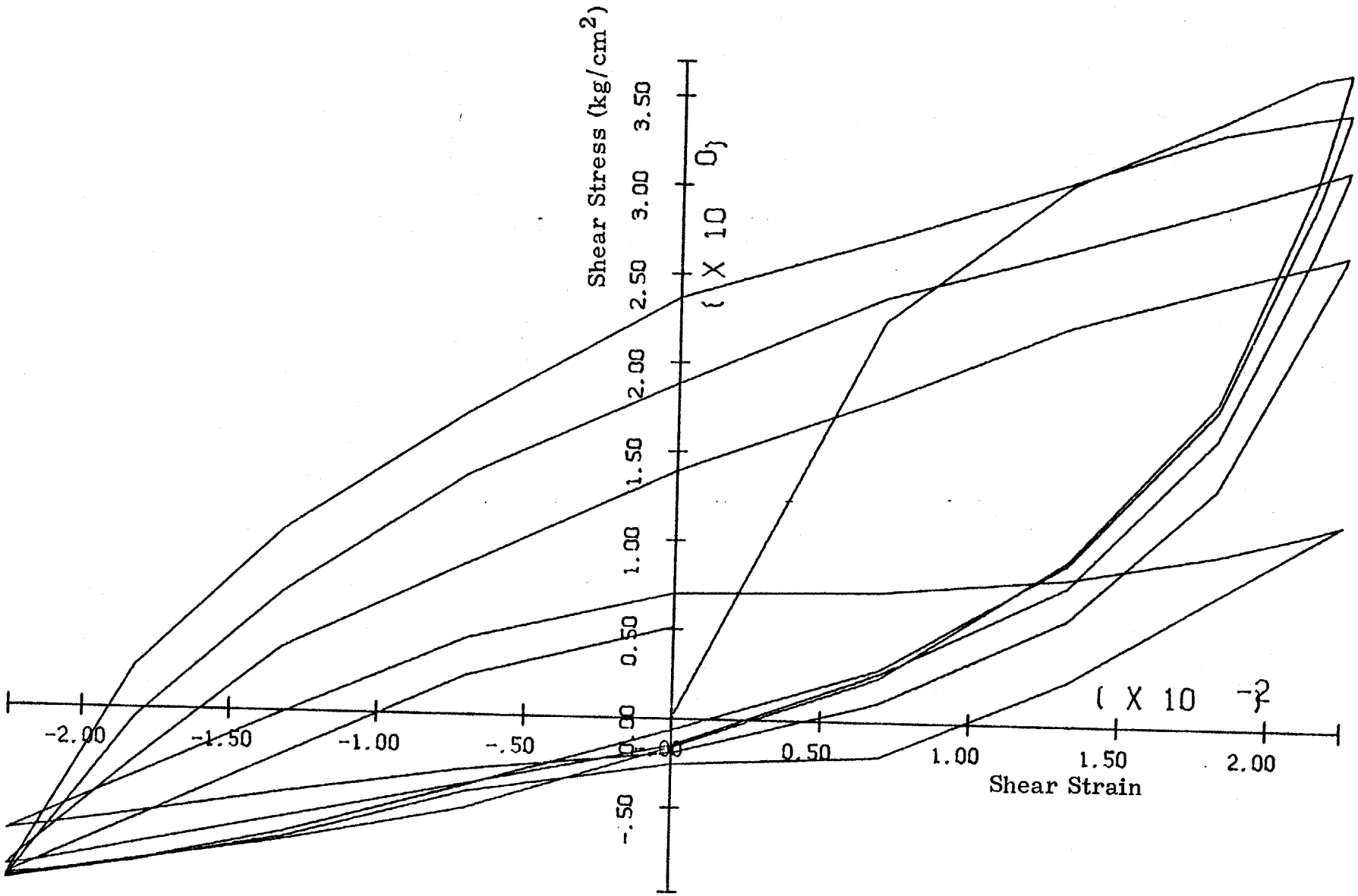

Figure 15b. Shear stress- shear strain modified data.

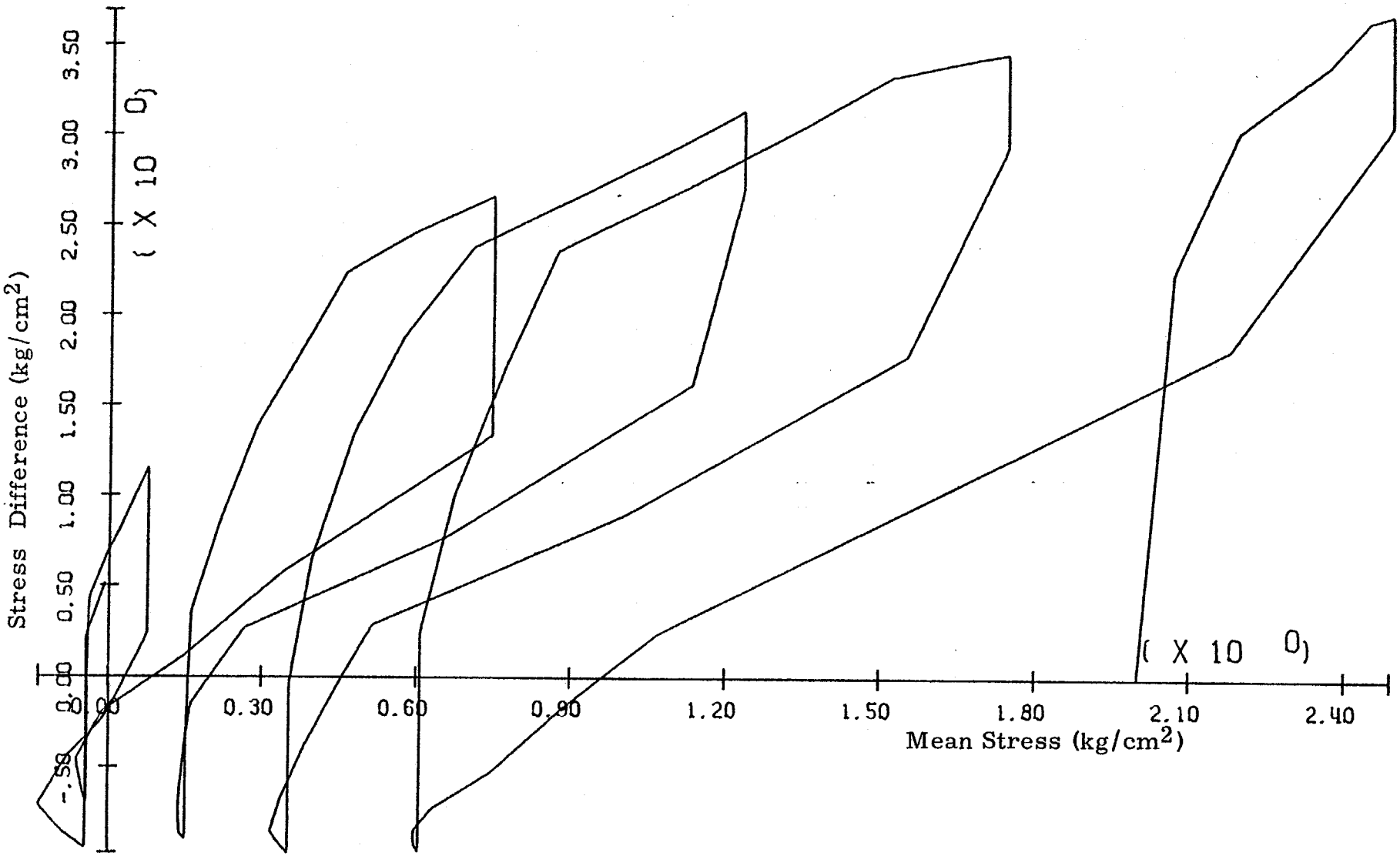

Figure 15c. Stress path modified data.

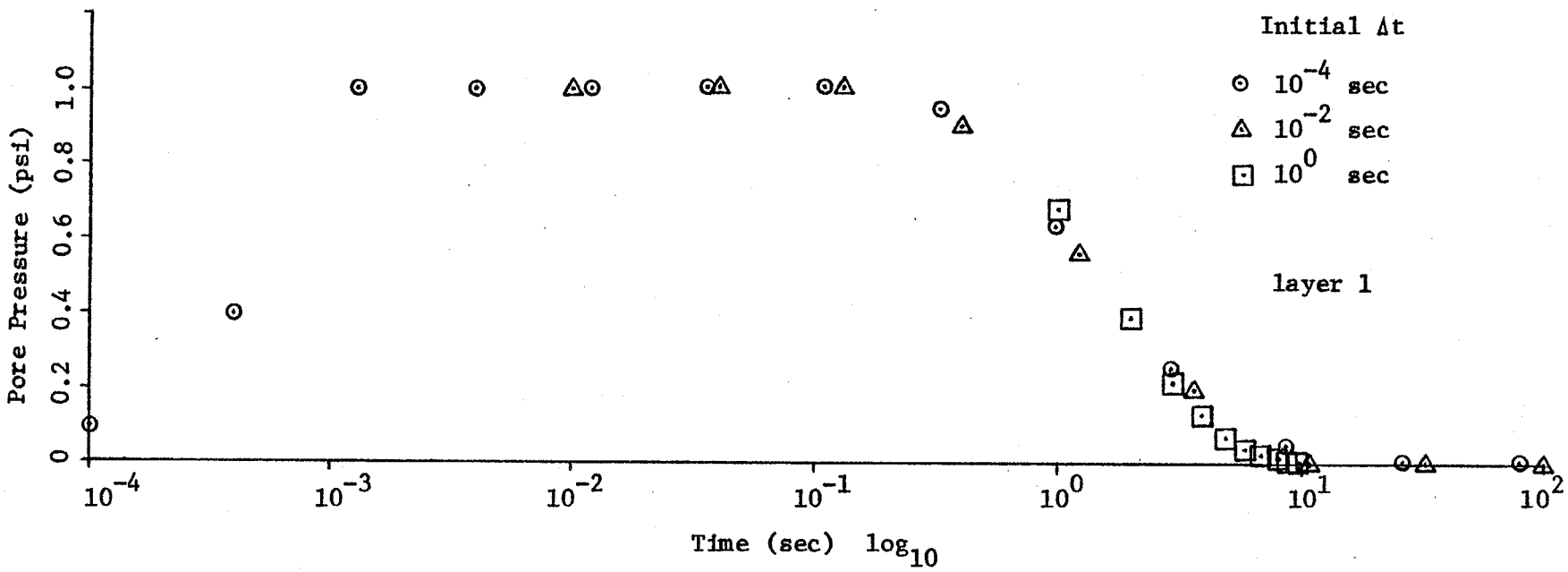

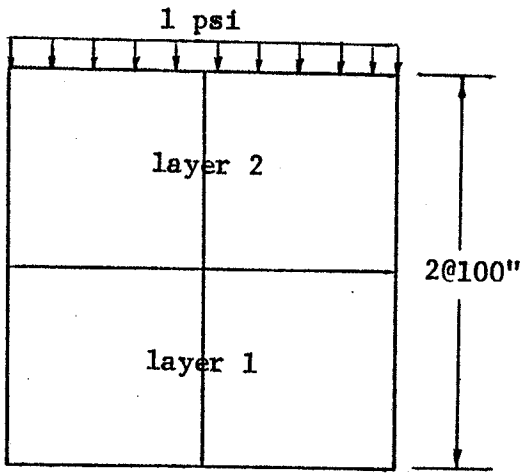

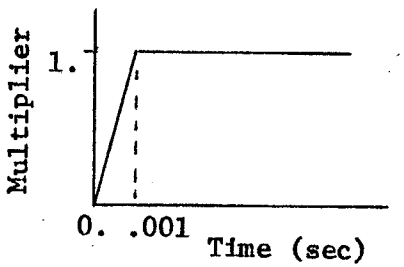

$K_{11}=K_{22}=0.0001$ in/sec

Figure 16. Pore Pressure History

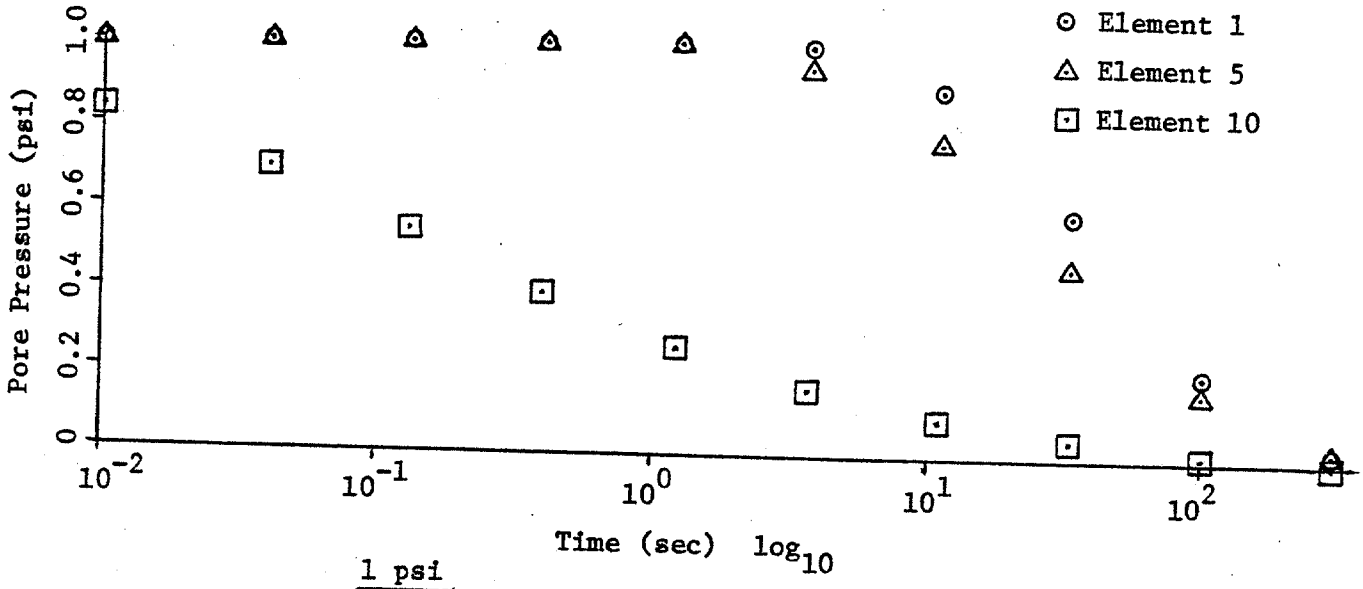

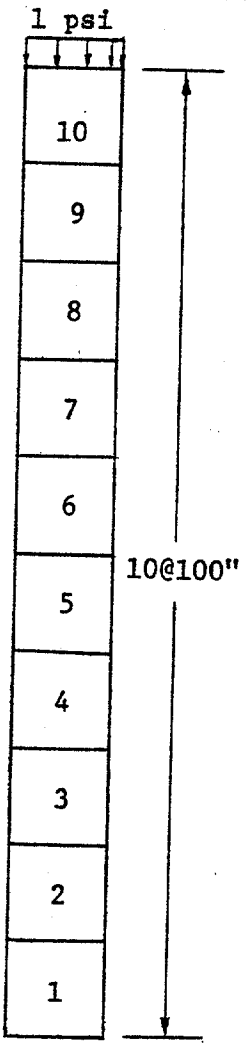

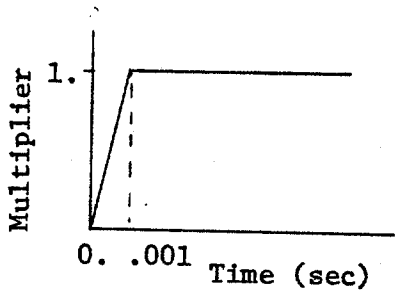

$K_{11}=K_{22}=0.0001$ in/sec

Figure 17. Soil Column Study

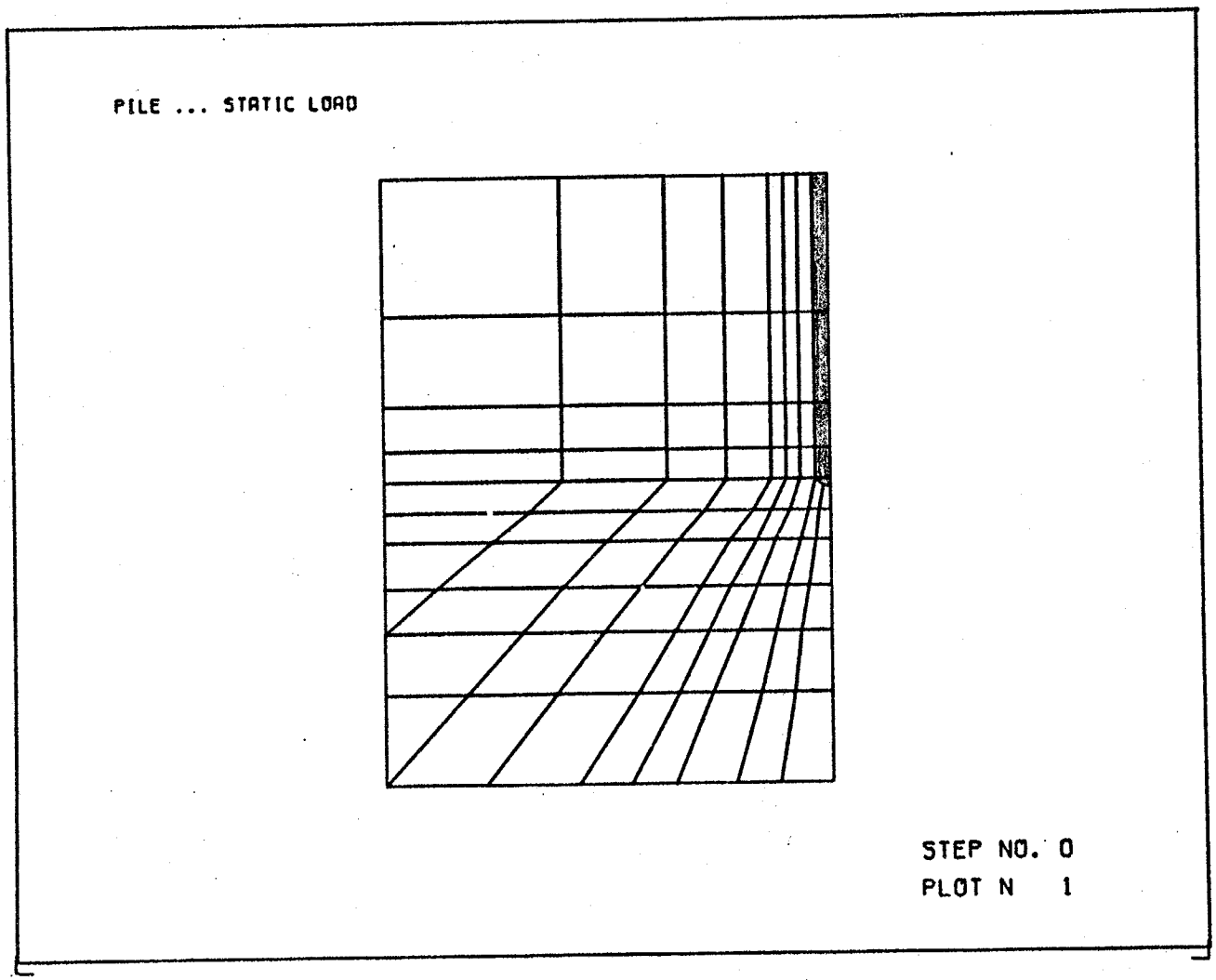

Figure 18. Undeformed mesh.

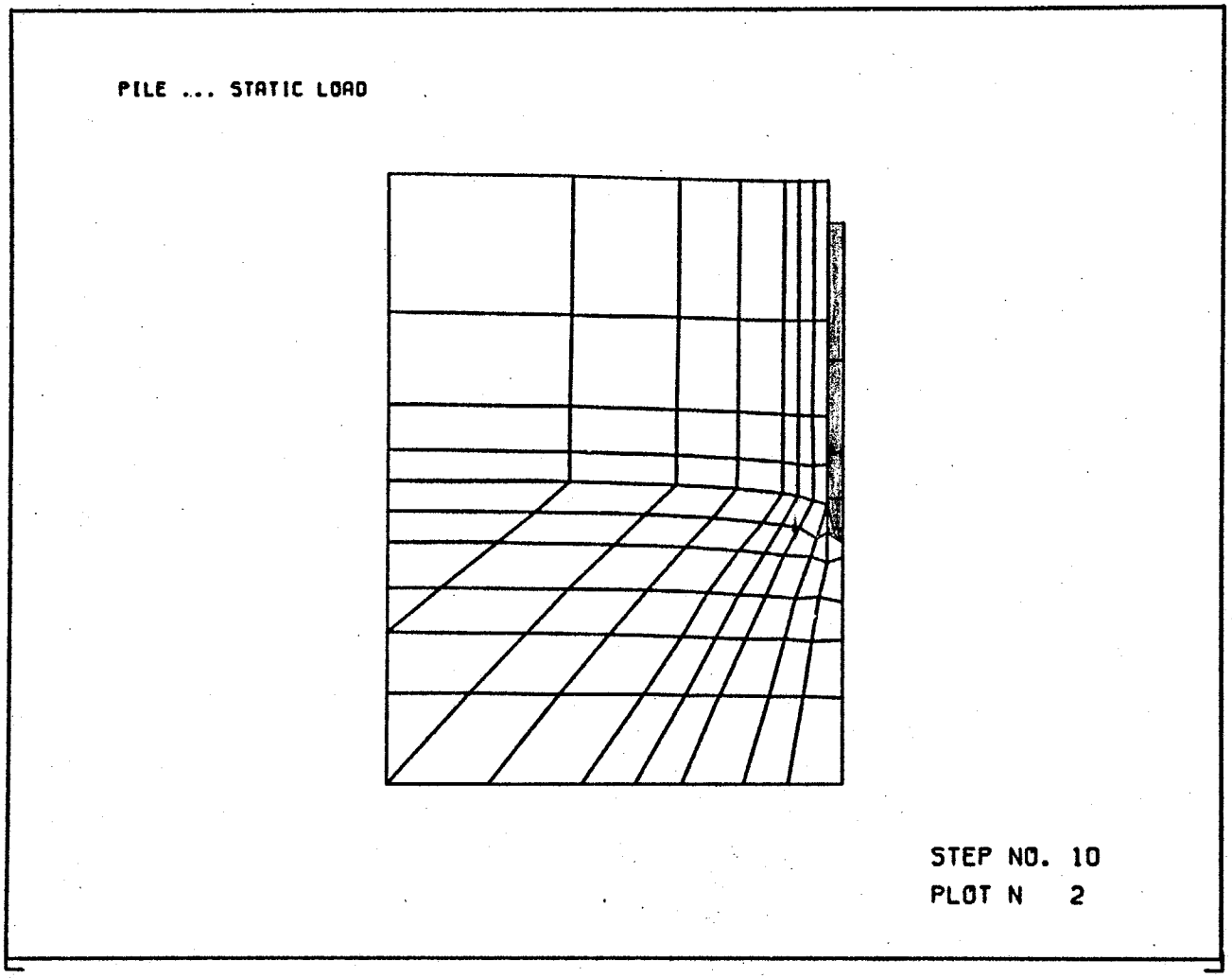

Figure 19. Deformed Mesh.

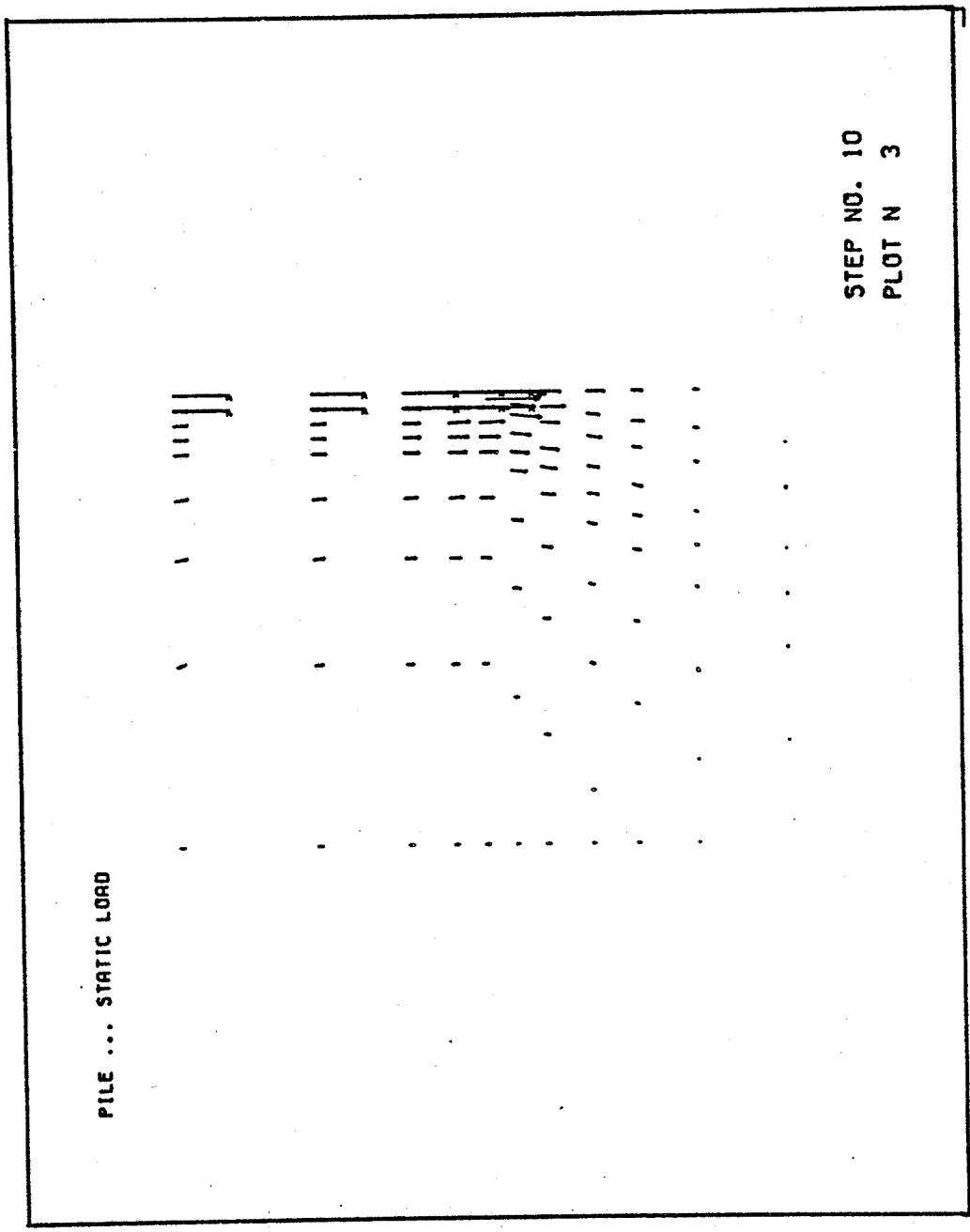

Figure 20. Displacement Vectors.

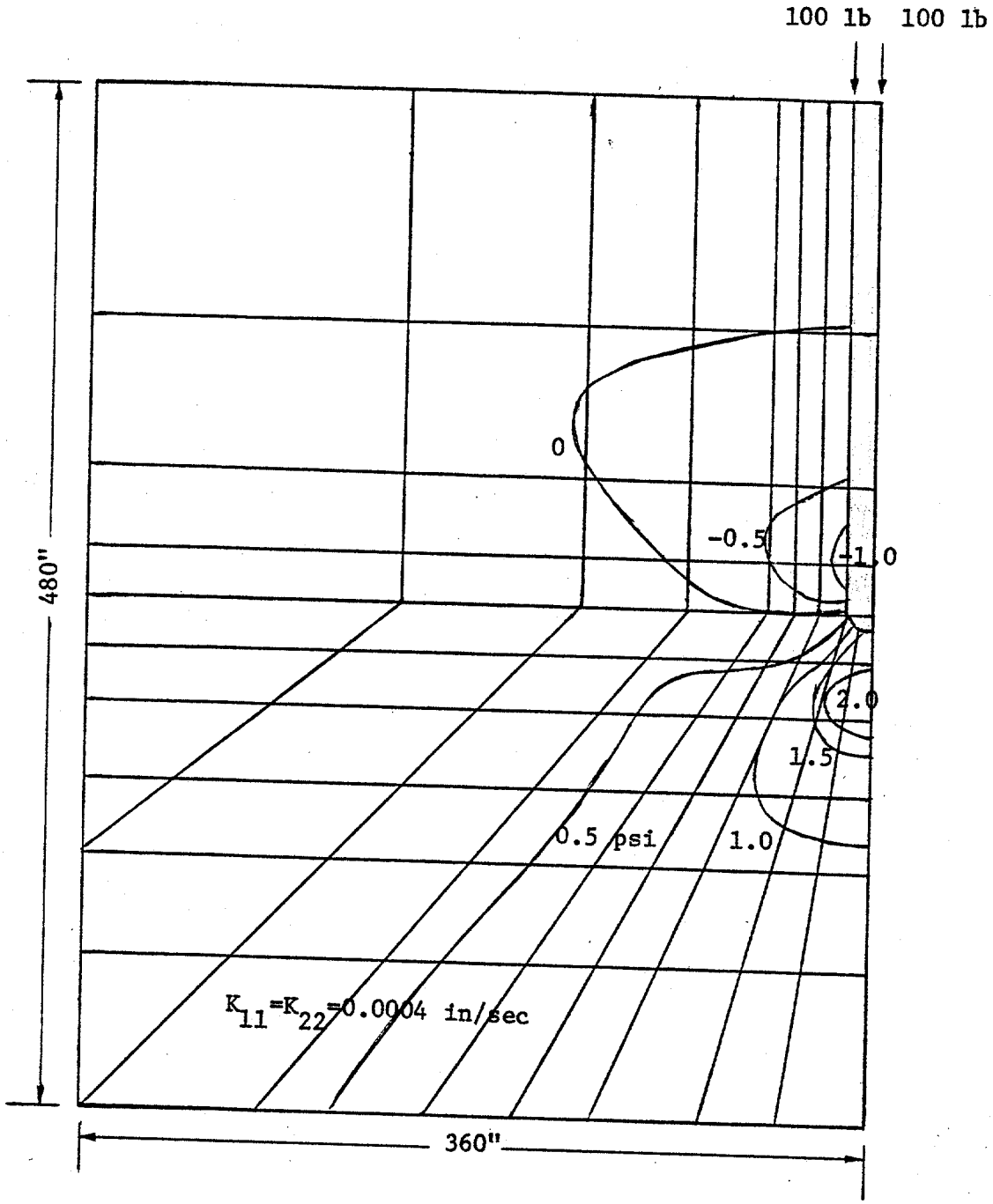

Figure 21. Pile Problem Pore Pressure Contours: Step=1, time=0.001 sec

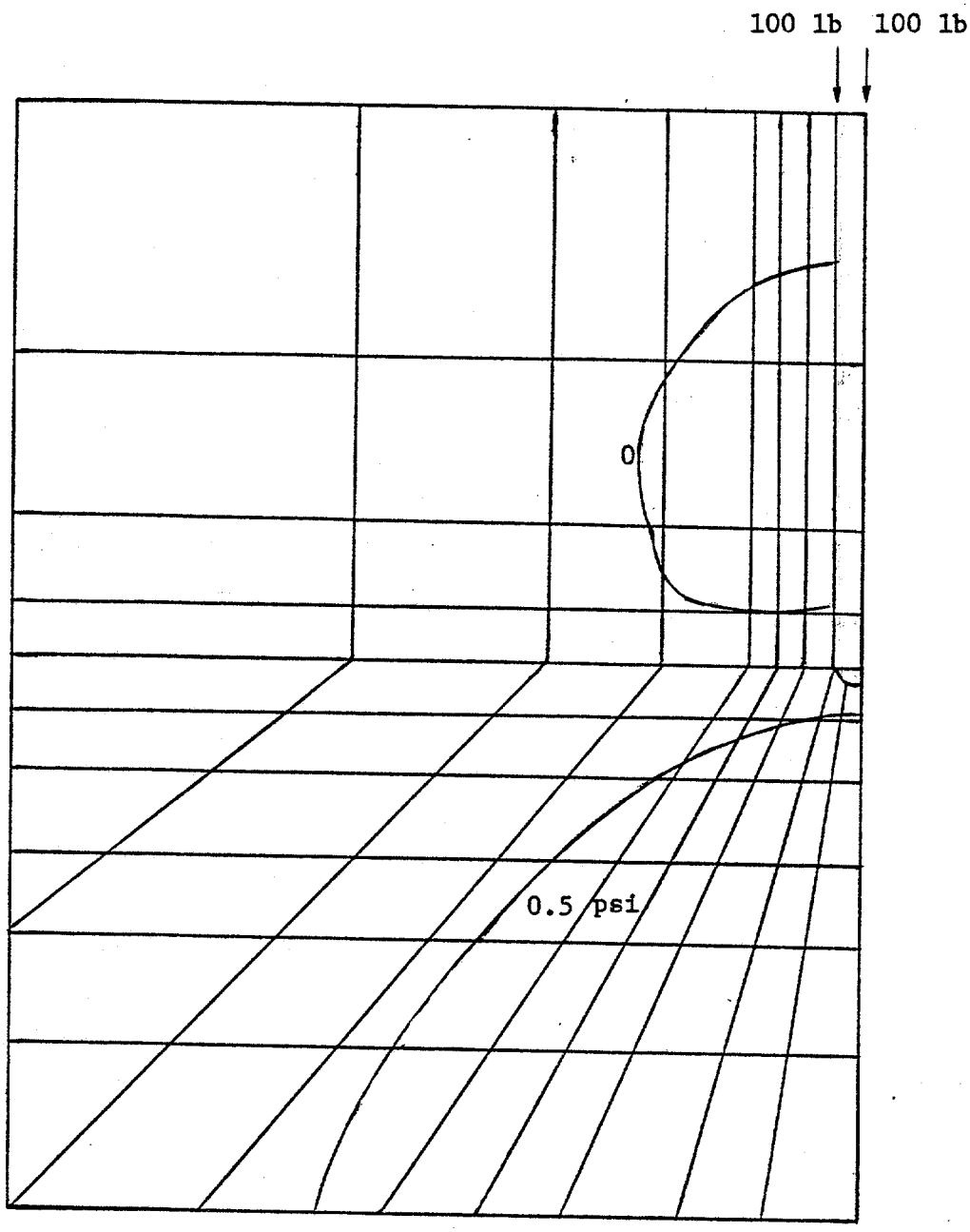

Figure 22. Pile Problem Pore Pressure Contours:
Step=3, time=0.013 sec

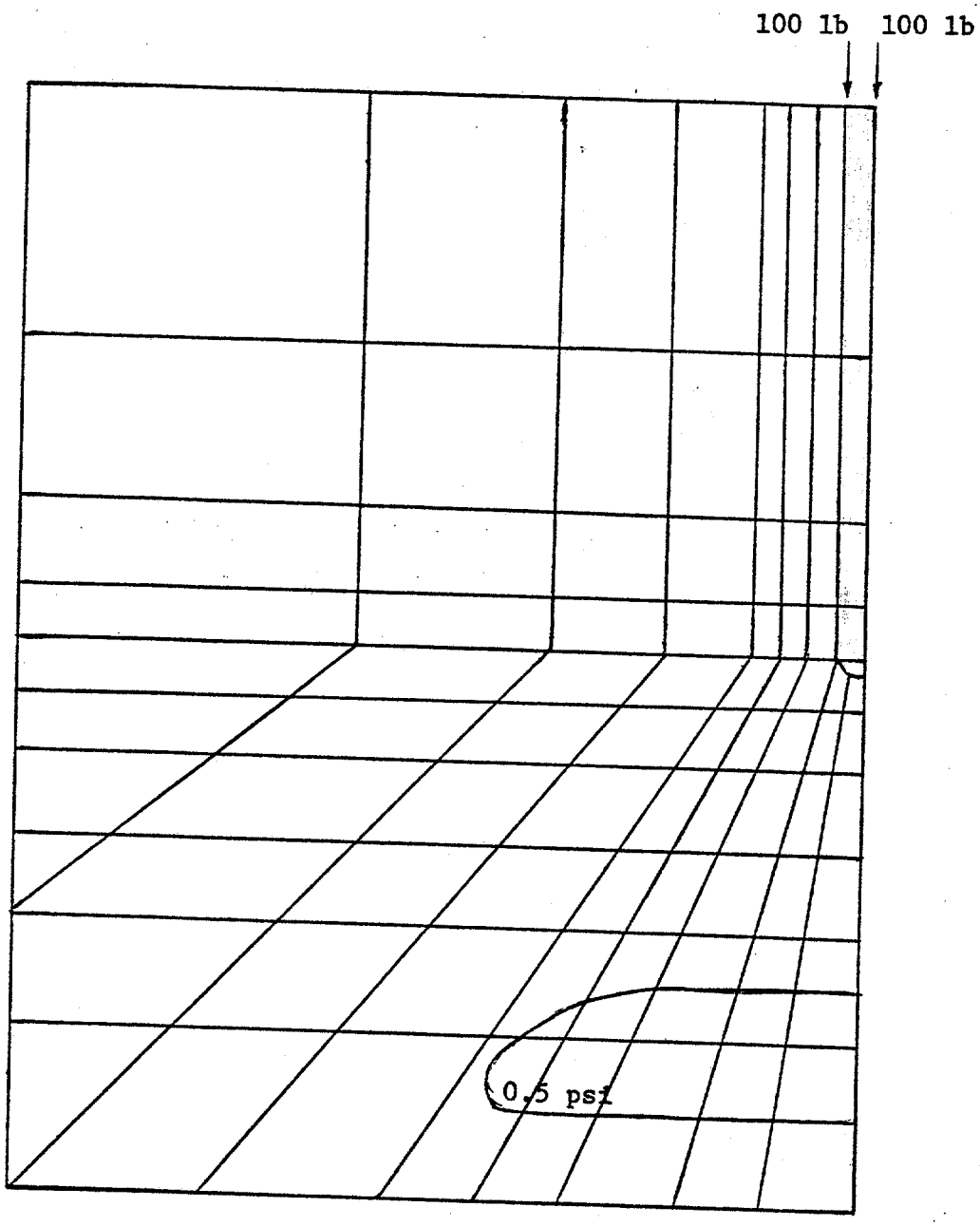

Figure 23. Pile Problem Pore Pressure Contours: Step=5, time=0.121 sec

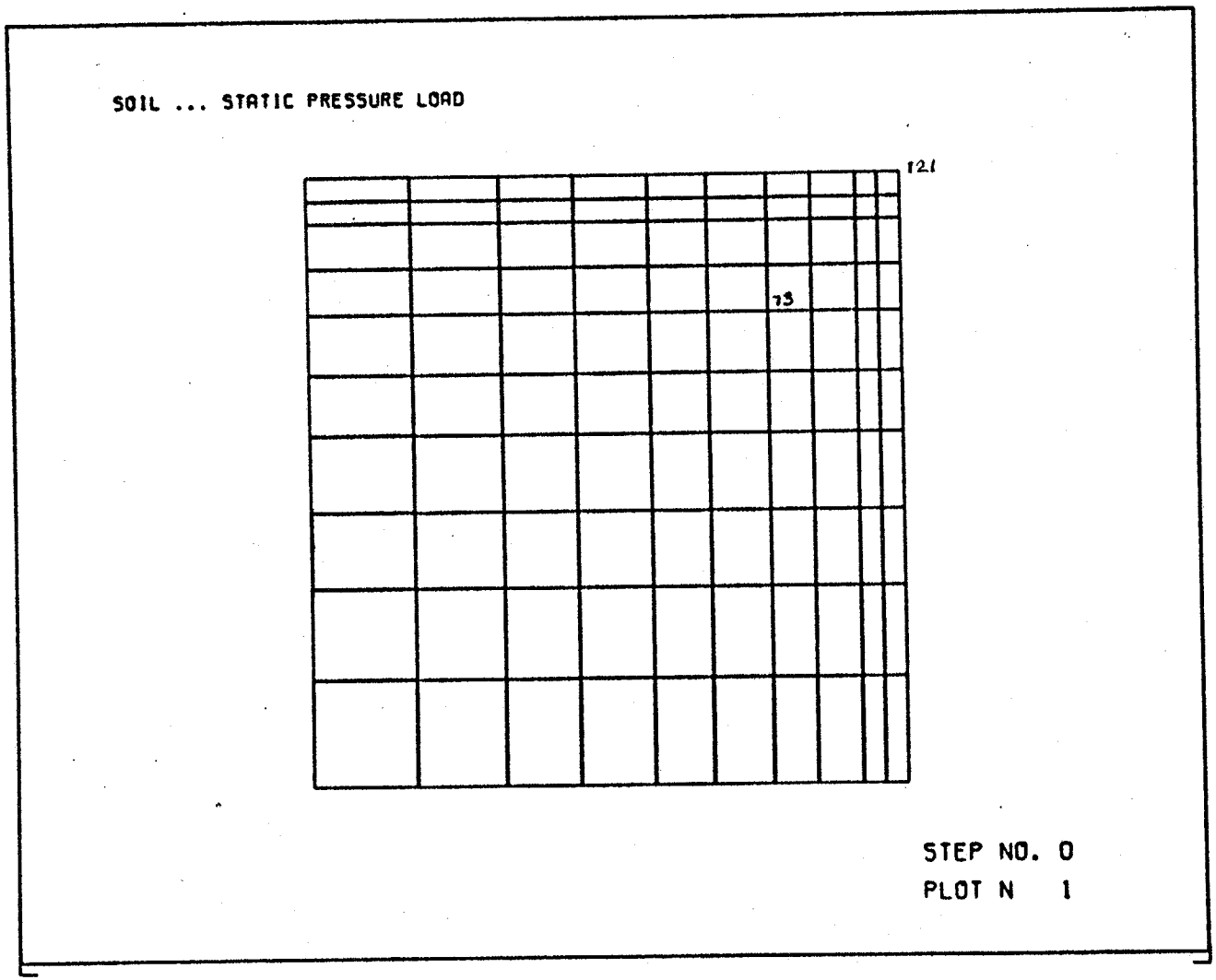

Figure 24. Undeformed Mesh.

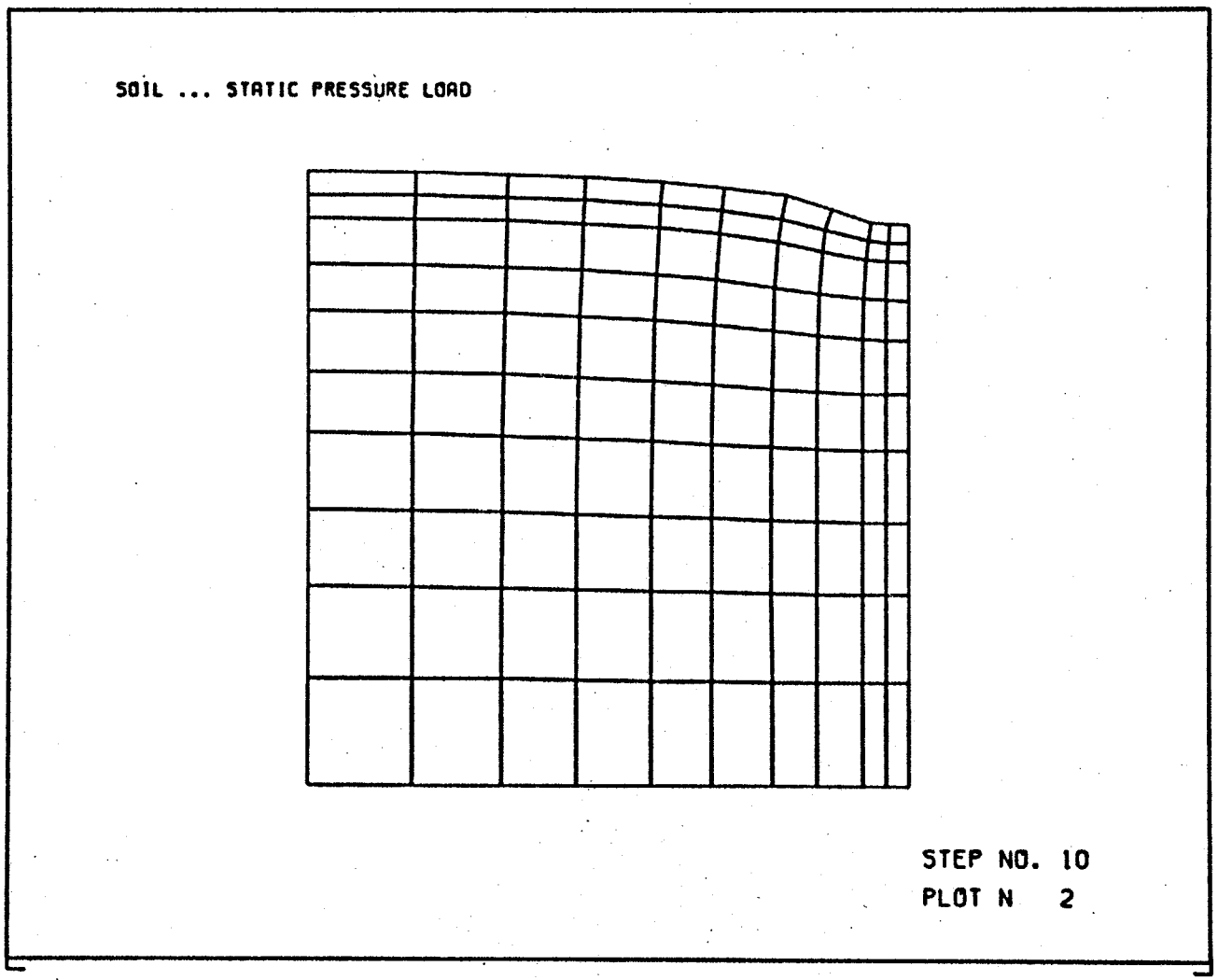

Figure 25. Deformed Mesh.

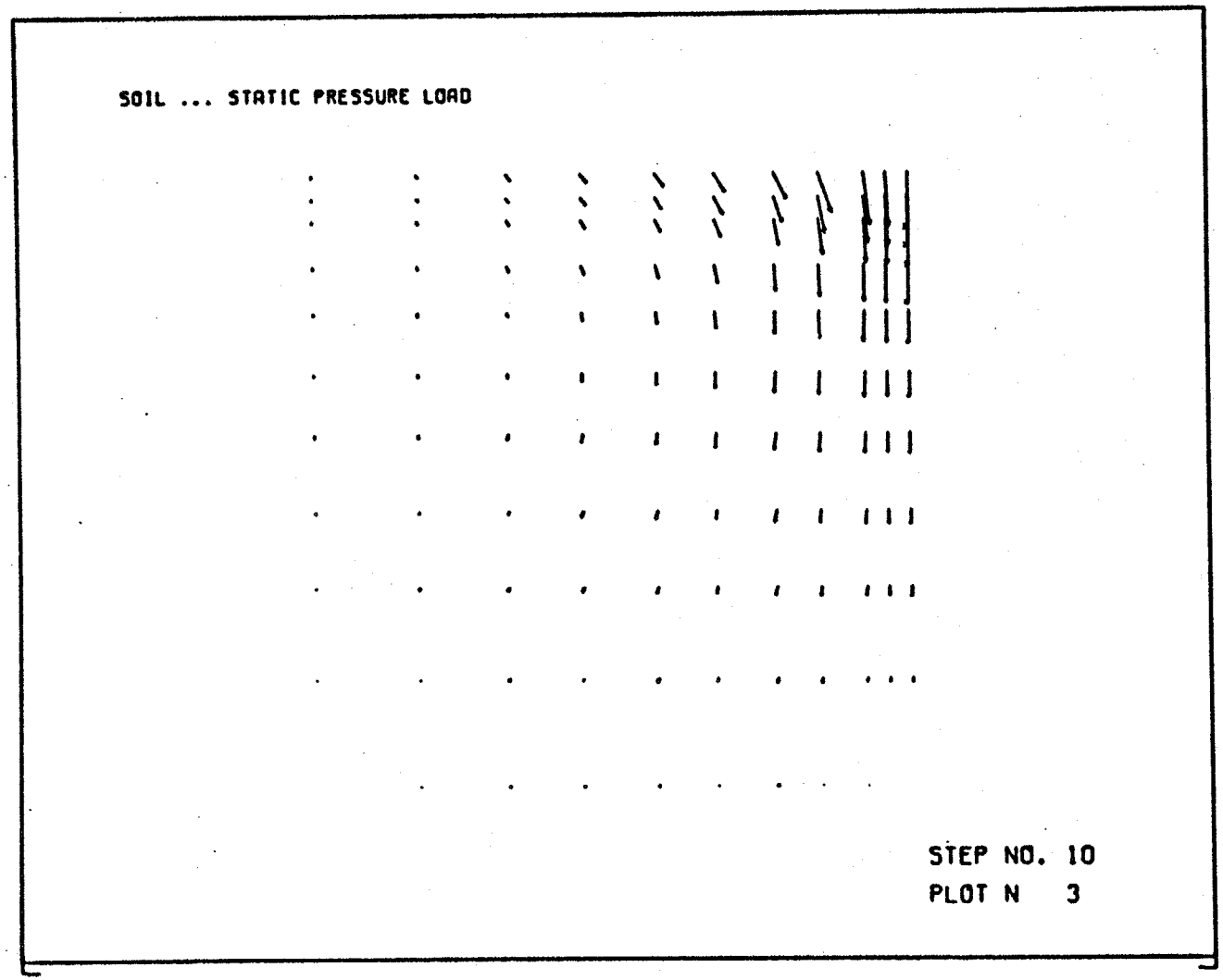

Figure 26. Displacement Vectors.

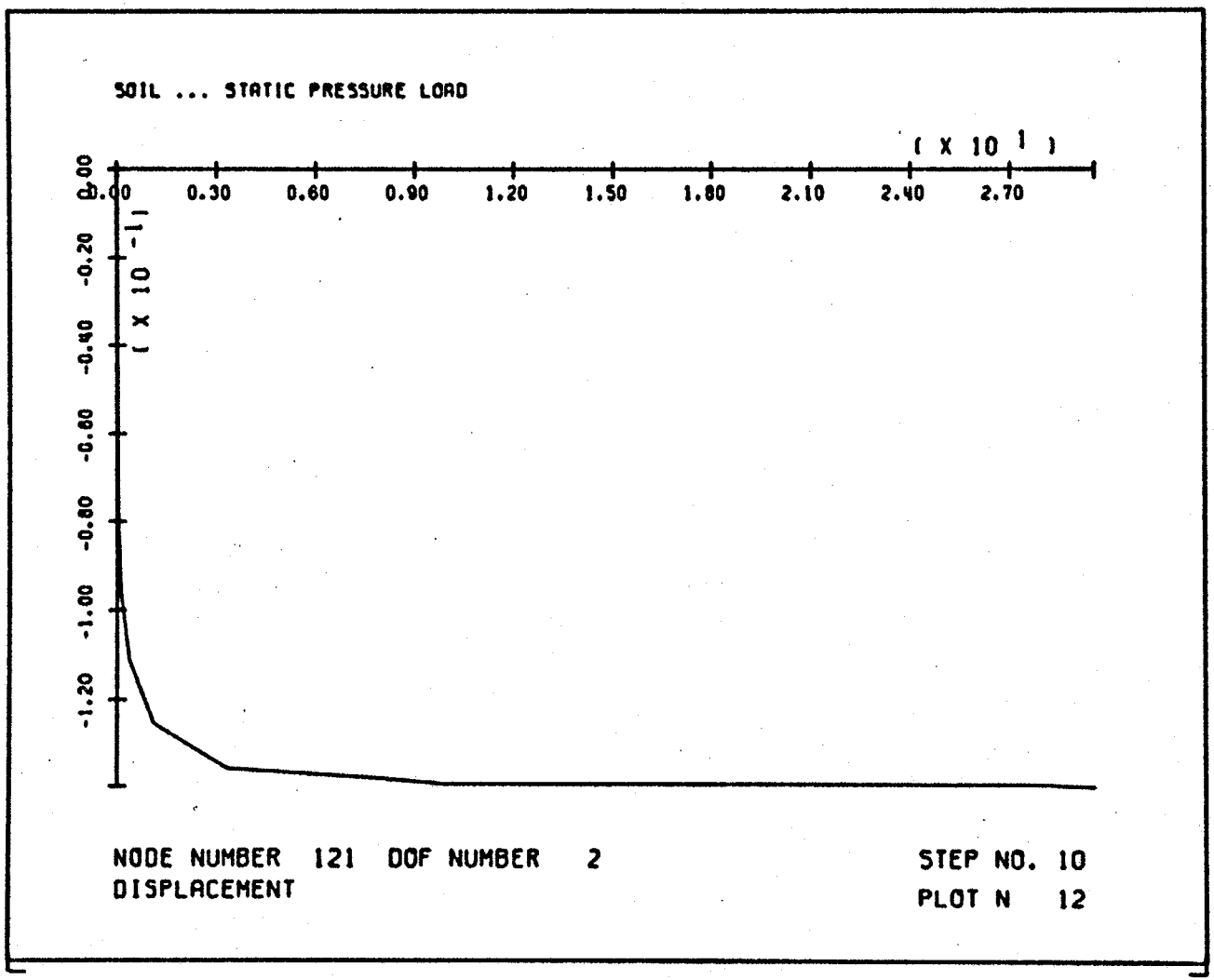

Figure 27. Displacement node 121.

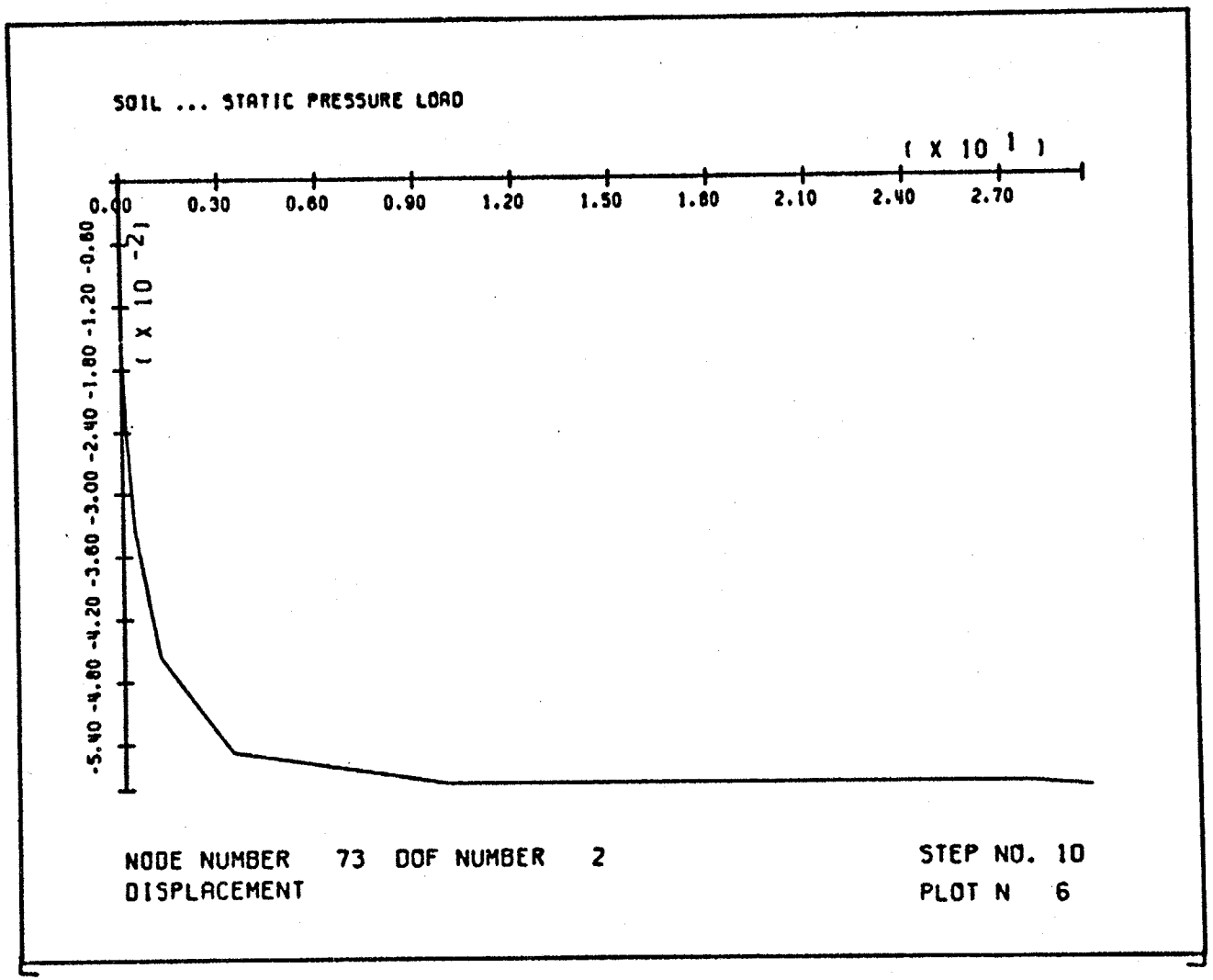

Figure 28. Displacement node 73.

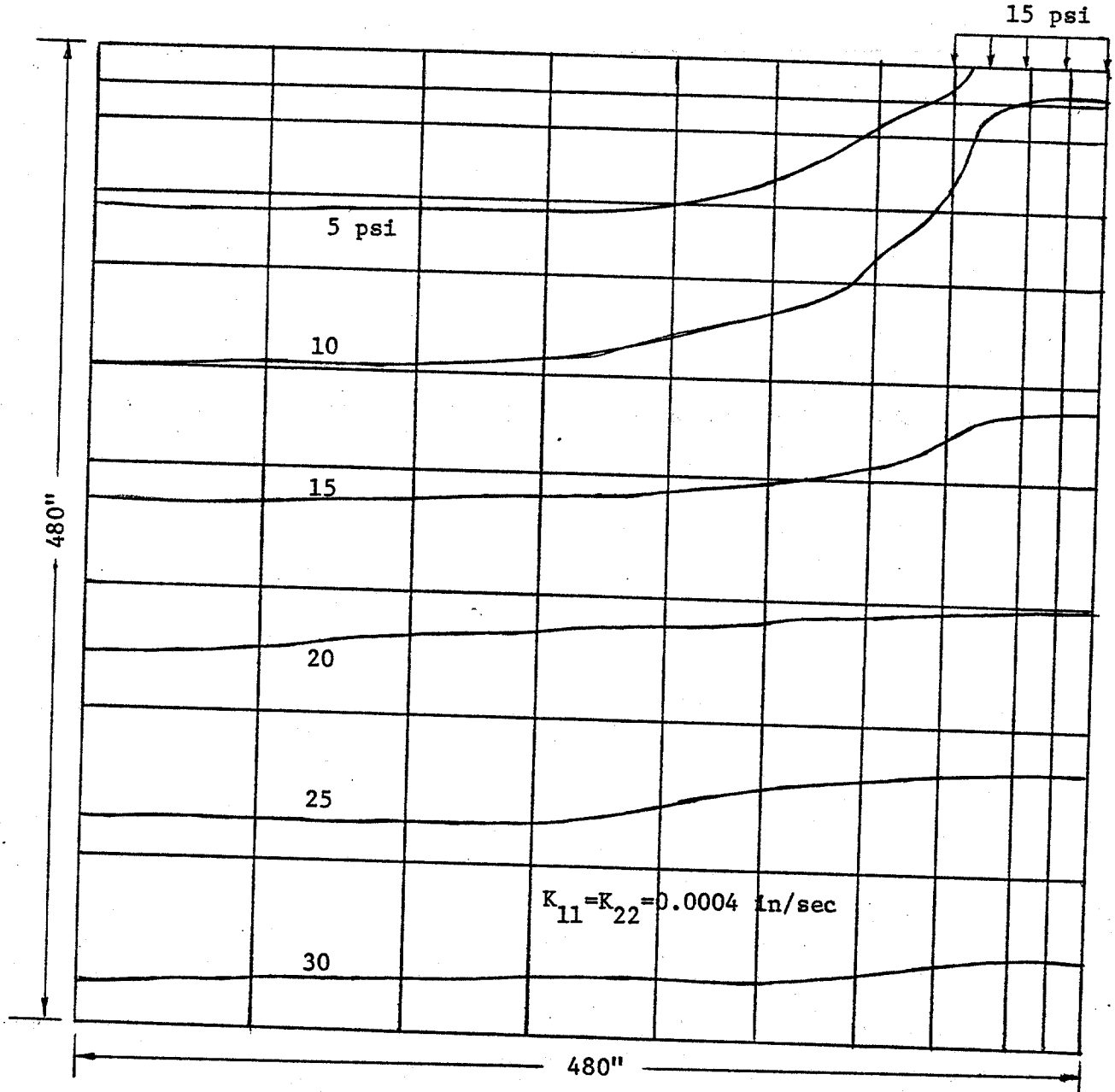

Figure 29. Pore Pressure Contours: Step=1, time=0.001 sec (Gravity included)

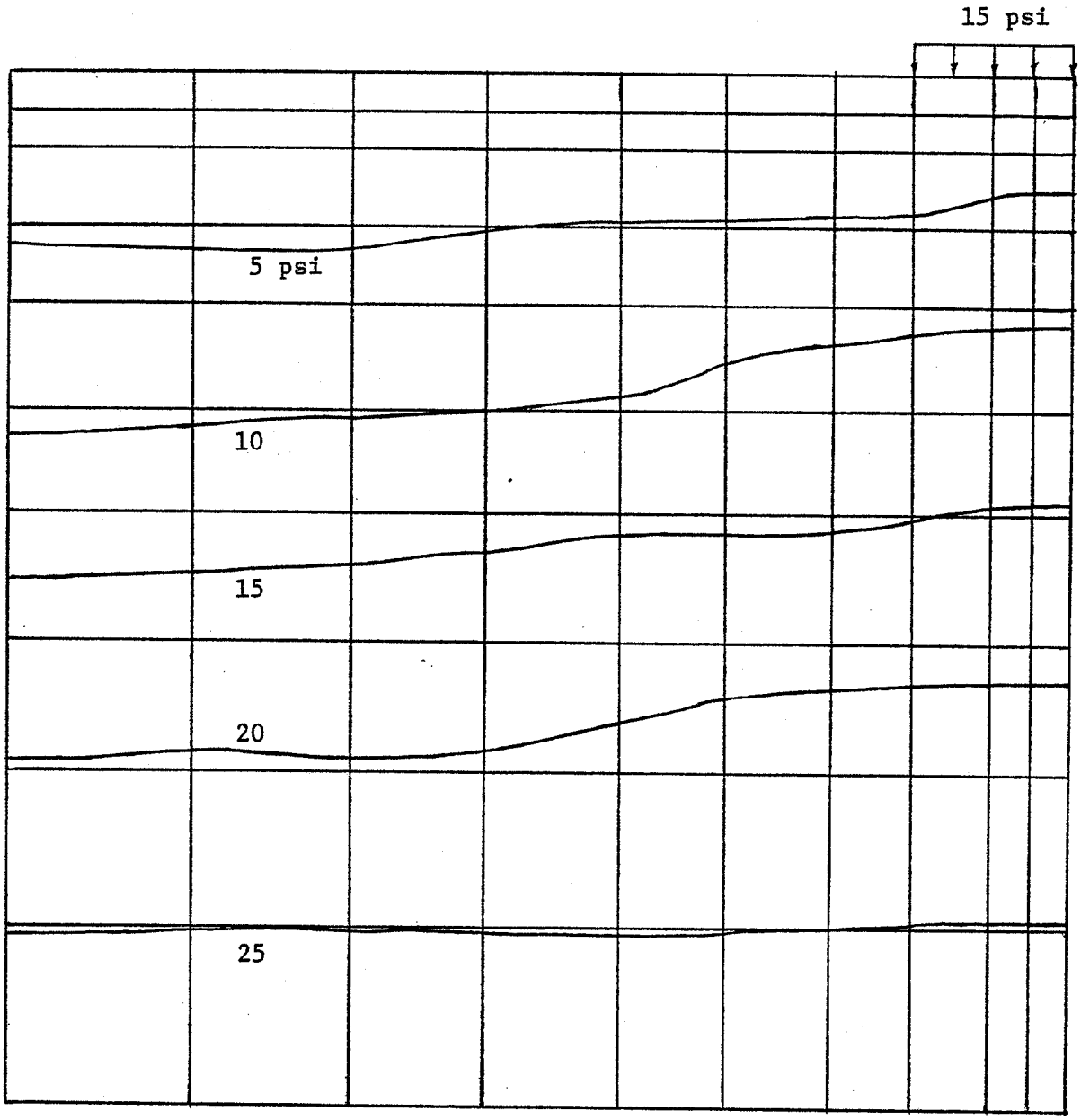

Figure 30. Pore Pressure Contours: Step=5, time=0.121 sec (Gravity included)

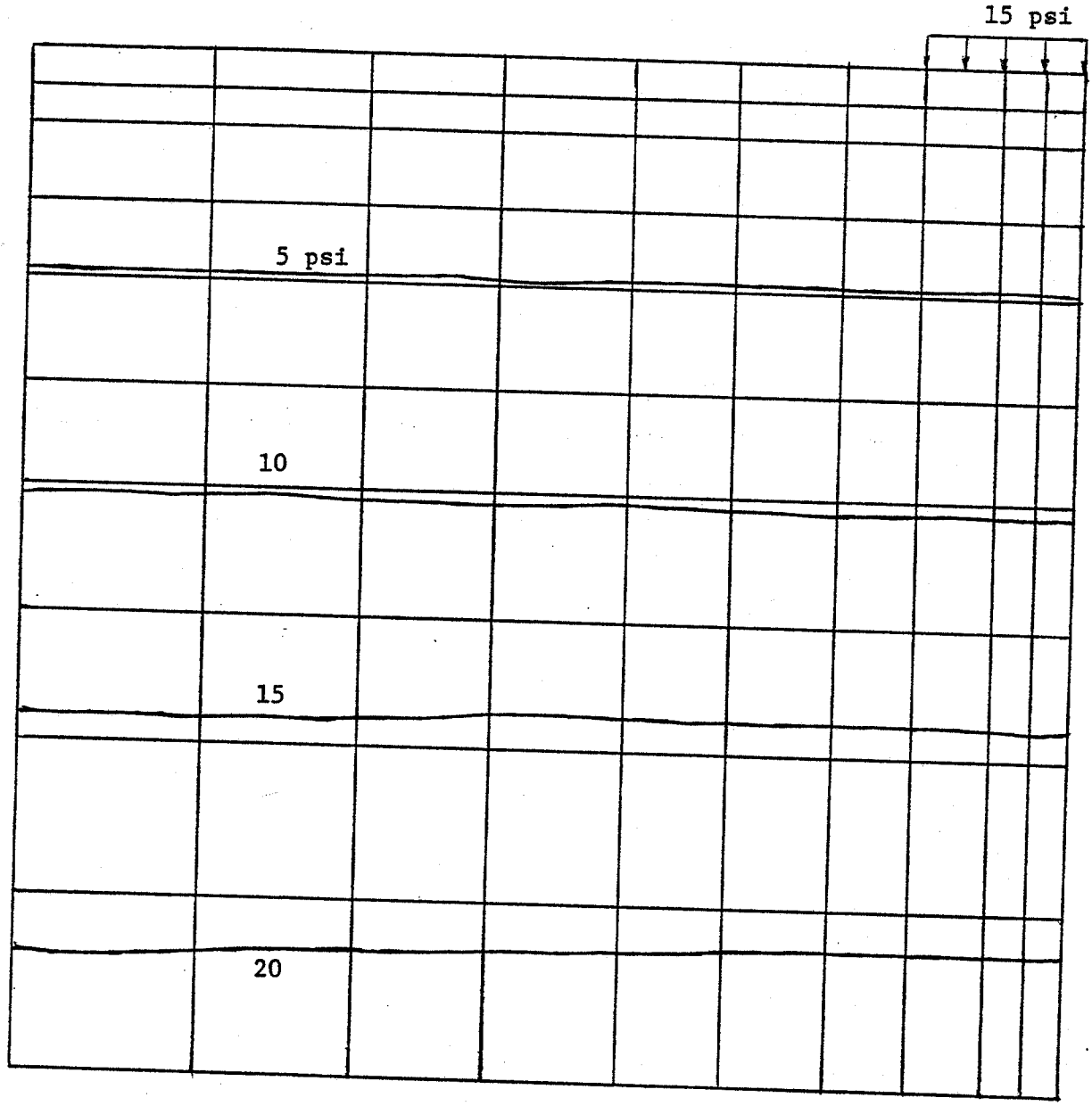

Figure 31. Pore Pressure Contours: Step=8, time=3.28 sec (Gravity Included)

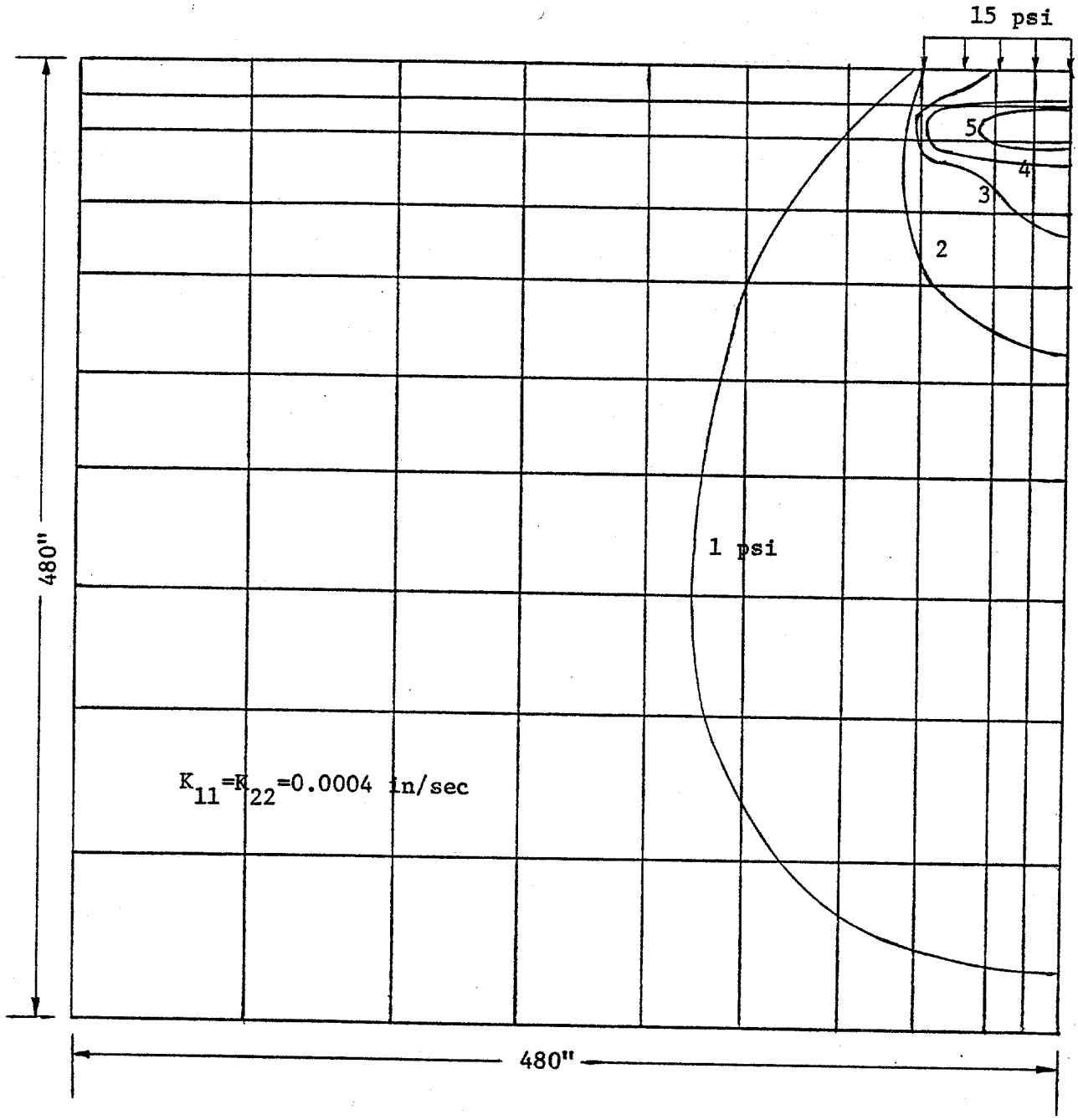

Figure 32. Pore Pressure Contours: Step=2, time=0.0004 sec

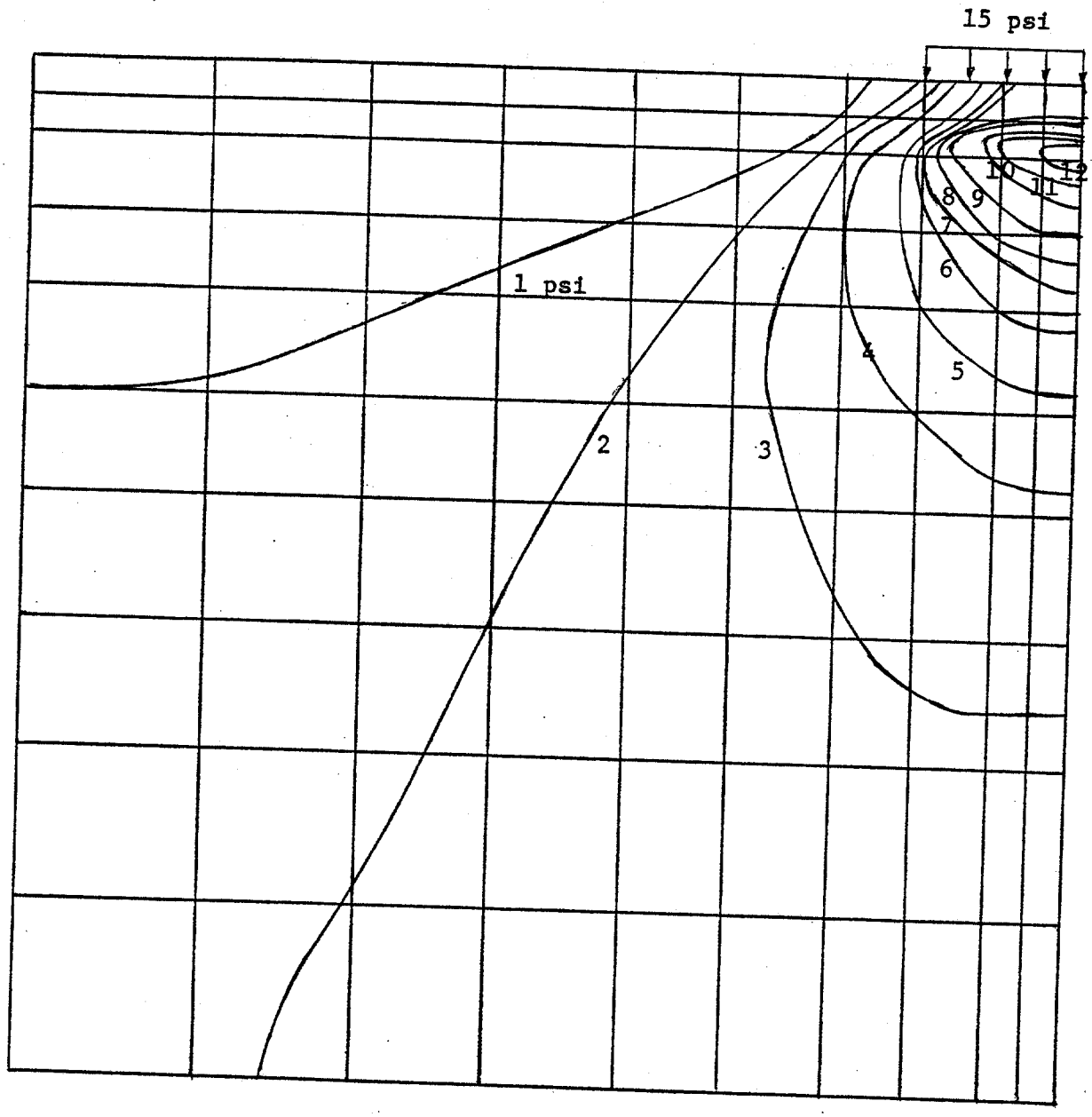

Figure 33. Pore Pressure Contours: Step=3, time=0.0013 sec

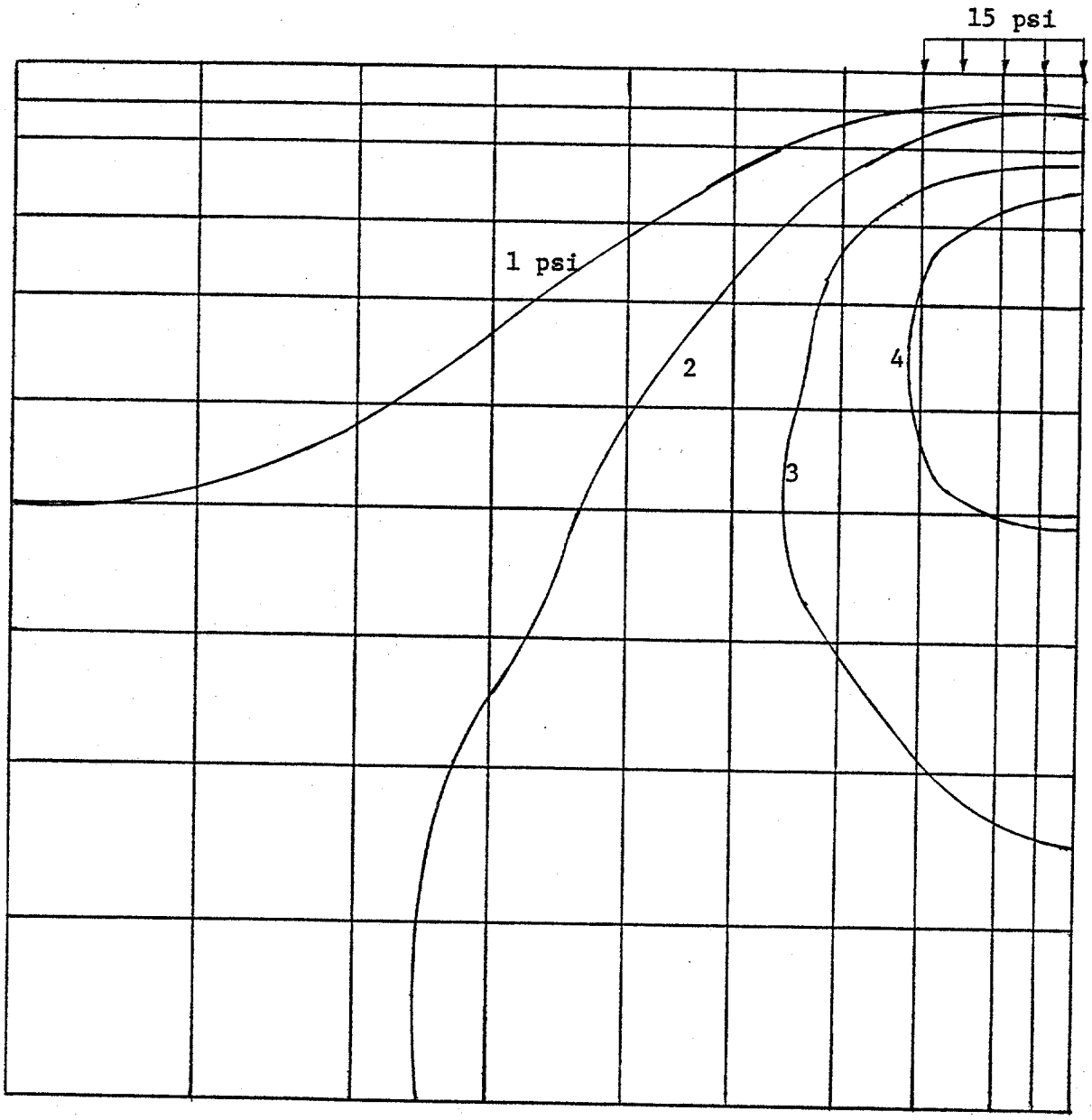

Figure 34. Pore Pressure Contours: Step=6, time=0.0364 sec

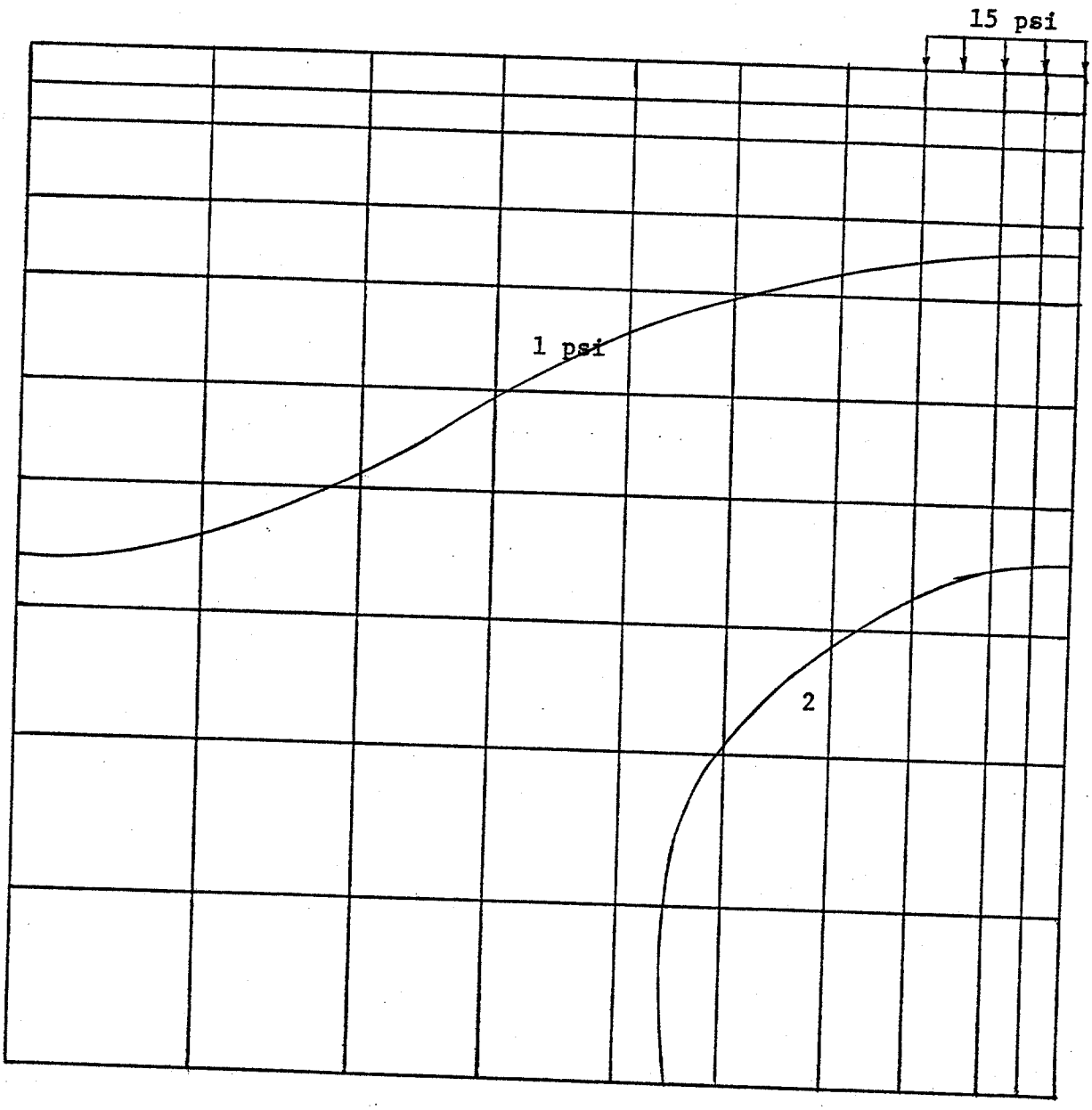

Figure 35. Pore Pressure Contours: Step=8, time=0.328 sec

Appendix A

Select Tests on Fine Silica Sand

by

Poul V. Lade

Report to

Department of the Navy
Civil Engineering Laboratory
Naval Construction Battalion Center
Port Hueneme, California 93043

Under Contract No. N62583/81 M R543

December, 1981

Report On

Select Tests on Fine Silica Sand

by Poul V. Lade

Introduction

A series of static tests were performed on triaxial specimens of fine Silica Sand. These tests were conducted to establish the stress-strain behavior of a granular material for various types of test conditions and stress paths. All specimens were prepared with the same constant density, and the following tests were included in the experimental program:

4 Consolidated-Drained Triaxial Compression Tests

2 Consolidated-Drained Triaxial Extension Tests

2 Consolidated-Undrained Triaxial Compression Tests

1 K_o-Test

1 Consolidated-Undrained, Slow Cyclic Triaxial Test (5 cycles)

In addition to these tests, sieve analyses, specific gravity tests and maximum and minimum void ratio tests were performed in order to establish the gradation curve, the specific gravity, and the relative density for the sand employed in the experimental program.

The sand, specimen preparation, test procedures, measurements, and test results are presented and discussed below.

Description of Sand Tested

Composition. - In order to avoid experimental problems due

to excessive effects of membrane penetration in the undrained tests (Lade and Hernandez, 1977; Martin et al., 1978), all tests were performed on a fine sand. Membrane penetration into the pores of granular soils is small to negligible when the average diameter of the soil grains is smaller than 0.1-0.2 mm (Frydman et al., 1973).

A portion of a Silica No. 90 Sand commercially available from the Ottawa Silica Company was employed. The portion finer than the No. 60 U.S. Sieve (0.246 mm) was separated from the Silica No. 90 Sand, and the grain size distribution for this portion was determined by sieve analyses. The grain size distribution for the sand used in all tests is shown on Fig. 1. The average diameter and the coefficient of uniformity were determined and are listed in Table 1.

The particle shapes were determined from an inspection of a group of grains under a microscope. The particle shapes were found to be angular. The grains consisted mainly of quartz with a few grains of black minerals.

Specific Gravity. - Two specific gravity tests were performed according to ASTM Standard Method of Test for Specific Gravity of Soils (D854-58). The results of these tests are also given in Table 1.

Maximum and Minimum Void Ratios. - The maximum void ratio was determined according to the method proposed by Kolbuszewsky (1948) in which the loosest packing is obtained by tilting a graduated cylinder (2000 cm^3, 3.0 inches diameter) containing

dry sand (2000 g) through 180° from one vertical position to the other. This procedure was repeated several times and the volume of the sand was measured for determination of the maximum void ratio.

The minimum void ratio was determined by slowly raining dry sand through a sieve into a 2000 cm^3 graduated cylinder from approximately 50 cm above the sand surface. Corresponding values of volume and dry weight were used for calculation of the minimum void ratio for the fine sand.

The void ratios and dry densities obtained from these tests are given in Table 1.

Relative Density. - It was desirable to use a sand density for which pore pressure increases would be observed in consecutive cycles in the consolidated-undrained slow cyclic triaxial test to be performed with relatively low consolidation pressure (2.00 kg/cm^2). In order to obtain an indication of the approximate conditions in terms of void ratio (or dry density) and consolidation pressure for which increasing pore pressures would be observed in consecutive cycles of an undrained cyclic loading test, a preliminary consolidated-undrained triaxial compression test was performed with high back pressure. The specimen employed for this test was prepared with a relative density of 65%, and a consolidation pressure of 2.00 kg/cm^2. The results of this test (Test No. CU-2.0-1; detailed results not given in this report) indicated that the fine sand would tend to dilate at low values of stress difference ($\sigma_1-\sigma_3$),

thus resulting in decreasing pore pressures under undrained conditions.

The relative density was consequently decreased to 30% (corresponding to a void ratio of 0.760 and a dry density of 1.511 g/cm^3 = 94.3 lb/ft^3) and following another consolidated-undrained triaxial compression test, it was decided to use this relative density in all tests included in the experimental program.

Specimen Preparation and Testing Procedures

General. - All triaxial specimens tested in the experimental program had height = diameter = 3.8 inches = 9.7 cm. Thus, relatively large specimens with volumes of about 715 cm^3 were tested. Lubricated end plates were used in all tests involving considerable lateral expansion to avoid development of significant shear stresses at the cap and base. The specimens were prepared by placing a pre-weighed amount of dry sand in a uniformly loose condition inside the membrane which was held by a forming jacket. The sand was then densified by vibration produced by light taps with a hammer on the forming jacket until the desired specimen height (=3.8 inches) was obtained. After having applied a small confining pressure (=0.30 kg/cm^2), the dry specimen was saturated using the CO_2-method (Lade & Duncan, 1973). In addition, a back pressure (=4.0 kg/cm^2 in most cases) was applied to the specimen to insure a high degree of saturation. Measured B-values of 0.98 or higher indicated fully saturated specimens.

CD-Tests. - Four consolidated-drained triaxial compression tests were performed with effective confining pressures of 1.00 (1 test), 2.00 (2 tests), and 5.00 kg/cm^2 (1 test). Isotropic compression from 0.30 kg/cm^2 to the respective values of confining pressure was performed in steps such that the relations between vertical strains, volumetric strain, and confining pressure could be determined. The shear stage was then initiated by applying a vertical stress difference $(\sigma_1-\sigma_3)$ to the specimen, while the effective confining pressure was held constant. During application of shear stresses, the vertical load, the vertical deformation, and the volume change were measured such that the relations between stress difference $(\sigma_1-\sigma_3)$, vertical strain ε_1, and volumetric strain ε_v could be established. Following failure of each specimen, an unloading-reloading cycle was performed to enable determination of the unloading-reloading modulus.

Stress differences and volumetric strains are plotted versus vertical strains for confining pressures of 1.00, 2.00 (2 tests), and 5.00 kg/cm^2 on Figs. 2,3,4, and 5, respectively. Two tests were performed with confining pressure of 2.00 kg/cm^2. The results of these two tests are compared on Fig. 6. It may be seen that the differences in stress-strain and volumetric behavior from the two specimens are very small.

In order to compare the results of the CD-tests with different confining pressures, the effective stress ratios σ_1'/σ_3' and the volumetric strains ε_v are plotted versus vertical strain

ε_1 on Fig. 7. It may be seen that the results of the CD-tests form a consistent pattern, as is usually obtained from good quality tests. The initial modulus and the unloading-reloading modulus increase with increasing confining pressure (see Figs. 2,3,4, and 5), the strain-to-failure increases (not pronounced in the present tests), the friction angle decreases, and the volumetric strains become more compressive with increasing confining pressure (Fig. 7). Only the peak point from one of the tests performed with confining pressure of 2.00 kg/cm^2 is shown on Fig. 7. It may be seen that the difference in strength between comparable tests (i.e. the two tests with confining pressure equal to 2.00 kg/cm^2) is much smaller than the differences in strength due to different confining pressures. Thus, for uniform, homogeneous specimens, it is more important to account for the curvature of the failure envelope (i.e. the decrease in friction angle with increasing confining pressure) than to account for differences in test results due to scatter.

CDE-Tests. - Two consolidated-drained triaxial extension tests were performed with effective confining pressures of 2.00 kg/cm^2. Following the isotropic compression from 0.30 kg/cm^2 to 2.00 kg/cm^2, the vertical stress was decreased until failure occurred with $\sigma_1 = \sigma_2 = 2.00$ kg/cm^2 in the horizontal directions and $\sigma_3 (< \sigma_1 = \sigma_3)$ in the vertical direction.

Stress differences and volumetric strains from the two tests are shown on Fig. 8. The volumetric strains compare very well, whereas a small difference in strength is present between the two tests. Whereas this difference in strength corresponds

to slightly more than one degree in the friction angles, this amount of scatter is actually quite small for this type of test.

CU-Tests. - Two consolidated-undrained triaxial compression tests were performed with effective consolidation pressures of 2.00 kg/cm^2. Following the isotropic compression, the vertical stress was increased while the volume of the specimen was held constant by closing the drainage value. Thus, pore pressure changes different from zero were recorded together with vertical stresses and strains.

The results of the two CU-tests are compared on Figs. 9, 10,11, and 12. Figs. 9 and 10 should be examined together. Fig. 9 shows the vertical stress difference plotted against the vertical strain, whereas Fig. 10 shows the pore pressure variation. The stress-strain curves exhibit the characteristic shapes observed for specimens in which the pore pressure reverses at an early stage in the test. The stress difference initially increases, reaches a peak, and then decreases slightly. Since the initial pore pressure increase causes the effective confining pressure to decrease, the specimen reaches a stage at which a tendency for dilation occurs. Since the test is undrained, this tendency is reflected in a decreasing pore pressure, as seen on Fig. 10. This in turn causes the effective confining pressure to increase and the specimen therefore begins to pick up strength again. This results in the upwards concave stress-strain relationships indicated on Fig. 9.

Upon continued straining, the pore pressure continues to

decrease until the cavitation pressure is reached. The cavitation pressure for clean water is close to -1 atmosphere (17 mm Hg), but since the CO_2-method was used to saturate the specimen (gaseous CO_2 dissolves relatively easily in water and also comes out of solution relatively easily), the cavitation pressure is actually increased, as in the cases shown on Fig. 10. The cavitation pressures observed in these tests were between -0.5 and -0.6 atmospheres. Upon cavitation of the pore water, the test becomes a drained test and volume expansion (not measured) occurs. At this stage in the test, the effective stresses are close to the failure envelope, and pore water cavitation causes the effective stress path to change direction towards the failure envelope, as shown on Fig. 12. This results in failure of the specimen almost immediately after cavitation.

The relation between volume changes in drained tests and tendencies for volume changes resulting in changing pore pressures in undrained tests are explained in detail by Lee and Seed (1967) and Seed and Lee (1967).

Fig. 11 shows the effective stress ratio plotted versus the vertical strain. In terms of the effective stress ratio, the specimens both fail at 8-9% vertical strain, whereas failure according to the maximum stress difference occurs at 25-28% vertical strain.

Whereas the stress-strain curves and the pore pressure curves on Figs. 9 and 10 indicate some scatter, the effective stress ratio-strain curves and the effective stress paths on

Figs. 11 and 12 indicate very little scatter. Thus, the effective stress path is consistently reproduced in the two undrained tests. It appears therefore that the scatter is associated with the strains rather than the stresses.

K_o-Test. - A K_o-test was performed in the triaxial apparatus. In this test the lateral deformation was kept at zero (within 0.001 inch). Lubricated ends were not applied in this test, because lateral strains were prevented and undesirable shear stresses did therefore not develop at the cap and base. The test was performed using a π-tape mounted around the middle of the specimen. With increasing, strain-controlled vertical stresses the cell pressure was increased in such a manner that no lateral deformation occurred in the specimen.

The initial state of stress in the specimen was isotropic with $\sigma_3 = 0.30$ kg/cm^2. Thus, the initial value of $K = \sigma_3/\sigma_1$ was 1.00. Upon application of vertical stresses the specimen compressed vertically and tended to expand laterally. This tendency for lateral expansion was indicated on the π- tape and the cell pressure was consequently increased to prevent the lateral expansion. The lateral expansion was controlled within 0.001 inch during the entire test.

The results of the K_o-test are shown on Fig. 13. The upper diagram shows the relation between the vertical and the horizontal stresses, the diagram in the middle indicates the vertical compression, and the lower diagram shows the variation of K_o with horizontal stress. The values of $K_o = 1-\sin\phi$ (Jaky's

formula) in which ϕ is the friction angles from the CD-tests are also shown on the lower diagram. This formula usually indicates the value of K_o with excellent accuracy, and the test results compare very favorably with the calculations from this formula. Note that the variation in friction angle with confining pressure in the CD-tests is included in the calculation of the three K_o-values indicated on Fig. 13.

Cyclic Test. - A consolidated-undrained, slow cyclic triaxial test with increasing pore pressures and 5 cycles was desirable. Following a preliminary test (Test No. Cyc-2.0-1; detailed results not given in this report) in which the cyclic stress was high enough to cause the specimen to fail on the first cycle, the test presented here was performed. Because only very small vertical and lateral strains occur before failure in a cyclic test at low relative densities (Seed and Lee, 1966; Lee and Seed, 1967), lubricated ends were not used in this test.

Following the initial isotropic compression, the drainage valve was closed and the vertical stress was increased (i.e. the test was initiated on the compression side of the cycle as conventially done) slow enough to make several recordings of vertical load, pore pressure and vertical deformation. After the desired vertical stress difference had been reached, the cyclic stress was reversed to cause the specimen to be loaded in extension until the stress difference was precisely equal to that used on the compression side. Stress reversals were continued past the 5 desired cycles and the specimen failed in extension during

the 6th cycle. Since strain-control was used in the test, it was possible to follow the stress-strain and pore pressure relations and the effective stress path during the failure on the 6th cycle.

The results of the cyclic test are shown on Figs. 14, 15, and 16. Fig. 14 shows the stress-strain relation obtained throughout the test. It may be seen that following the initial compression, the specimen continues to move into extension as the test progresses, i.e. increasing negative vertical strains are recorded on consecutive cycles. Upon failure during the 6th cycle the specimen failed in extension and the stress difference which could be sustained continued to decrease until a very low value was reached.

Fig. 15 shows the pore pressure which developed throughout the test. This pore pressure increased on each consecutive cycle, with local decreases within each cycle. It is due to this increasing pore pressure that the specimen eventually fails. If the test had been stress-controlled, the specimen would have liquefied on the 6th cycle, because the stress difference could not be sustained on this cycle. Note that the maximum stress difference reached in extension on the 6th cycle is smaller than that applied on the previous 5 cycles (Fig. 14).

Fig. 16 shows the effective stress path followed during the cyclic loading test. As the specimen is loaded in consecutive cycles the effective stresses gradually approach the static failure surface, and plastic yielding occurs on each new cycle.

Larger amounts of plastic yielding occurs on the extension side than on the compression side, because for equal maximum stress differences in compression and in extension, the effective stress path is closer to the failure surface in extension than it is in compression. It is interesting to note, however, that the effective stress path apparently does not reach the failure surface obtained from static tests (indicated by dashed lines on Fig. 16).

Detailed Test Results

The results of all tests presented and discussed above are given on digital form in Appendix A. All relevant information for each test is listed on the appropriate forms.

Conclusion

A set of stress-strain, pore pressure or volume change, and strength data has been produced for a fine sand prepared in triaxial specimens with the same relative density. Several different types of tests and different stress paths were followed in these tests, but the results are directly comparable and they should form a consistent basis for evaluation of stress-strain models.

References

ASTM (1974) Standard Method of Test for "Specific Gravity of Soils," ASTM Designation: D854-58, Annual Book of ASTM Standards, American Society for Testing and Materials.

Frydman, S., Zeitlen, J.G., and Alpan, I. (1973), "The Membrane Effect in Triaxial Testing of Granular Soils," Journal of Testing and Evaluation, Vol. 1, No. 1, January, pp. 37-41.

Kolbuszewski, J.J. (1948), "An Experimental Study of the Maximum and Minimum Porosities of Sands," Proceedings of the 2nd International Conference on Soil Mechanics and Foundation Engineering, Rotterdam, Vol. I, pp. 158-165.

Lade, P.V., and Duncan, J.M. (1973), "Cubical Triaxial Tests on Cohesionless Soil," Journal of the Soil Mechanics and Foundations Division, ASCE, Vol. 99, No. SM10, Proc. Paper 10057, October, pp. 793-812.

Lade, P.V., and Hernandez, S.B. (1977), "Membrane Penetration Effects in Undrained Tests," Journal of the Geotechnical Engineering Division, ASCE, Vol. 103, No. GT2, Proc. Paper 12758, February, pp. 109-125.

Lee, K.L., and Seed, H.B. (1967), "Cyclic Stress Conditions Causing Liquefaction of Sand," Journal of the Soil Mechanics and Foundations Division, ASCE, Vol. 93, No. SM1, Proc. Paper 5058, January, pp. 47-70.

Lee, K.L., and Seed, H.B. (1967), "Drained Strength Characteristics of Sands," Journal of the Soil Mechanics and Foundations Division, ASCE, Vol. 93, No. SM6, Proc. Paper 5561, November, pp. 117-141.

Martin, G.R., Finn, W.D.L., and Seed, H.B. (1978), "Effects of System Compliance on Liquefaction Tests," Journal of the Geotechnical Engineering Division, ASCE, Vol. 104, No. GT4, Proc. Paper 13667, April, pp. 463-479.

Seed, H.B., and Lee, K.L. (1966), "Liquefaction of Saturated Sands During Cyclic Loading," Journal of the Soil Mechanics and Foundations Division, ASCE, Vol. 92, No. SM6, Proc. Paper 4972, November, pp. 105-134.

Seed, H.B., and Lee, K.L. (1967), "Undrained Strength Characteristics of Cohesionless Soils," Journal of the Soil Mechanics and Foundations Division, ASCE, Vol. 93, No. SM6, Proc. Paper 5618, November, pp. 333-360.

Table 1. Properties of Fine Silica Sand

D_{10} (mm)	0.10
D_{60} (mm)	0.20
$C_u = D_{60}/D_{10}$	2.0
D_{60} (mm)	0.18
Particle Shapes	Angular
Mineral Composition	Mainly quartz with a few black mineral grains
Specific Gravity, G_s	2.66
Max. Void Ratio, e_{max}	0.85
Min. Void Ratio, e_{min}	0.55
Min. Dry Density (g/cm^3)	1.438
Max. Dry Density (g/cm^3)	1.716
Conditions in Tests:	
Void Ratio, e	0.760
Dry Density, γd (g/cm^3)	1.511
Relative Density, D_r (%)	30.0

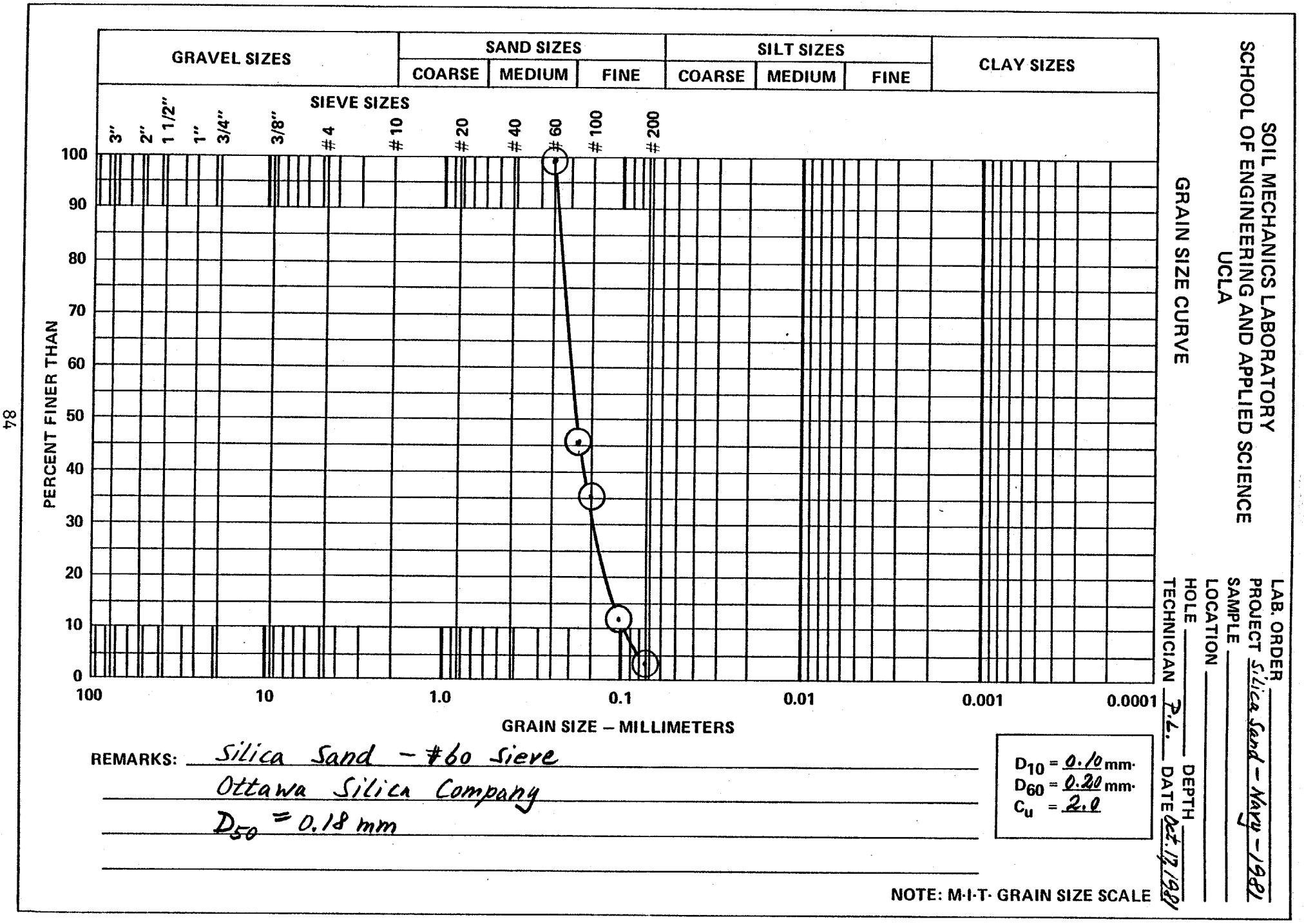

Fig. 1 Grain Size Curve for Fine Silica Sand

Test No. CD-1.0-1

$e = 0.743$; $D_r = 35.7\%$

$\sigma_3' = 1.00\ kg/cm^2$

$\varphi' = 34.1°$

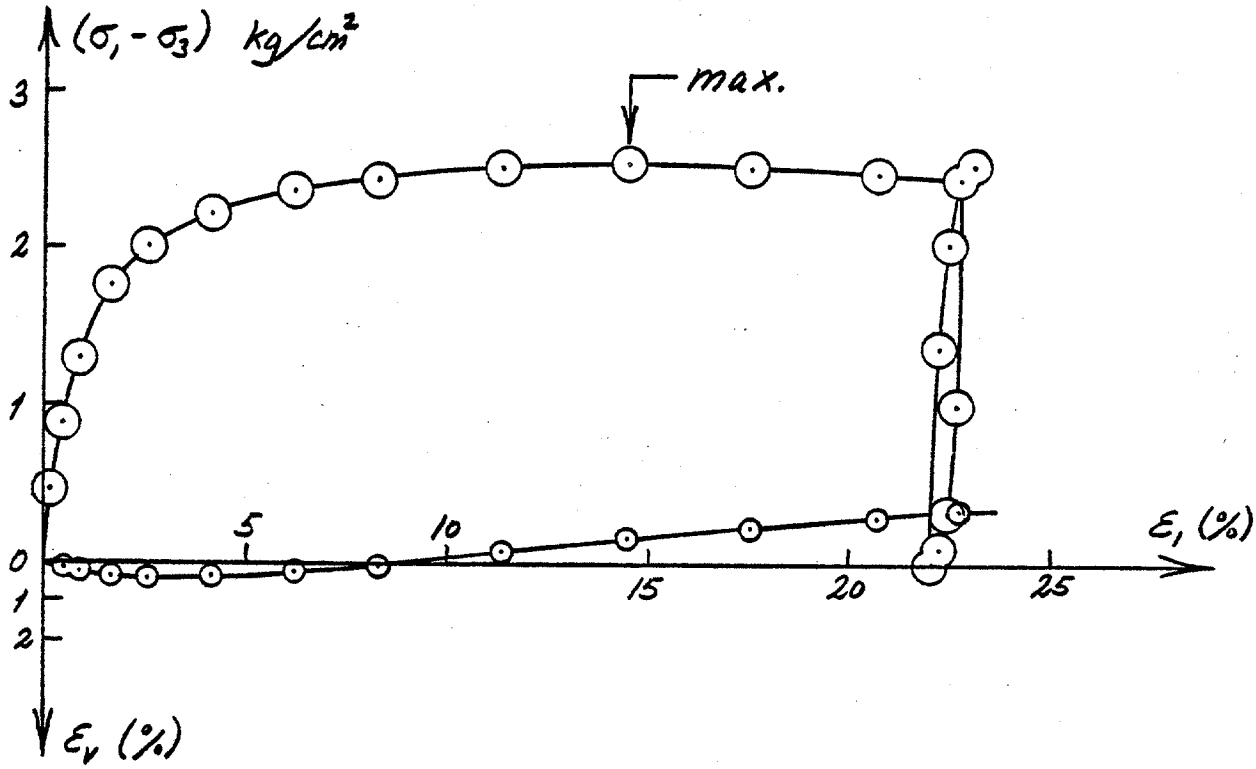

Fig. 2. Stress-Strain and Volumetric Strain Curves From Consolidated-Drained Triaxial Compression Test with $\sigma_{3c}' = 1.00\ kg/cm^2$ on Fine Silica Sand.

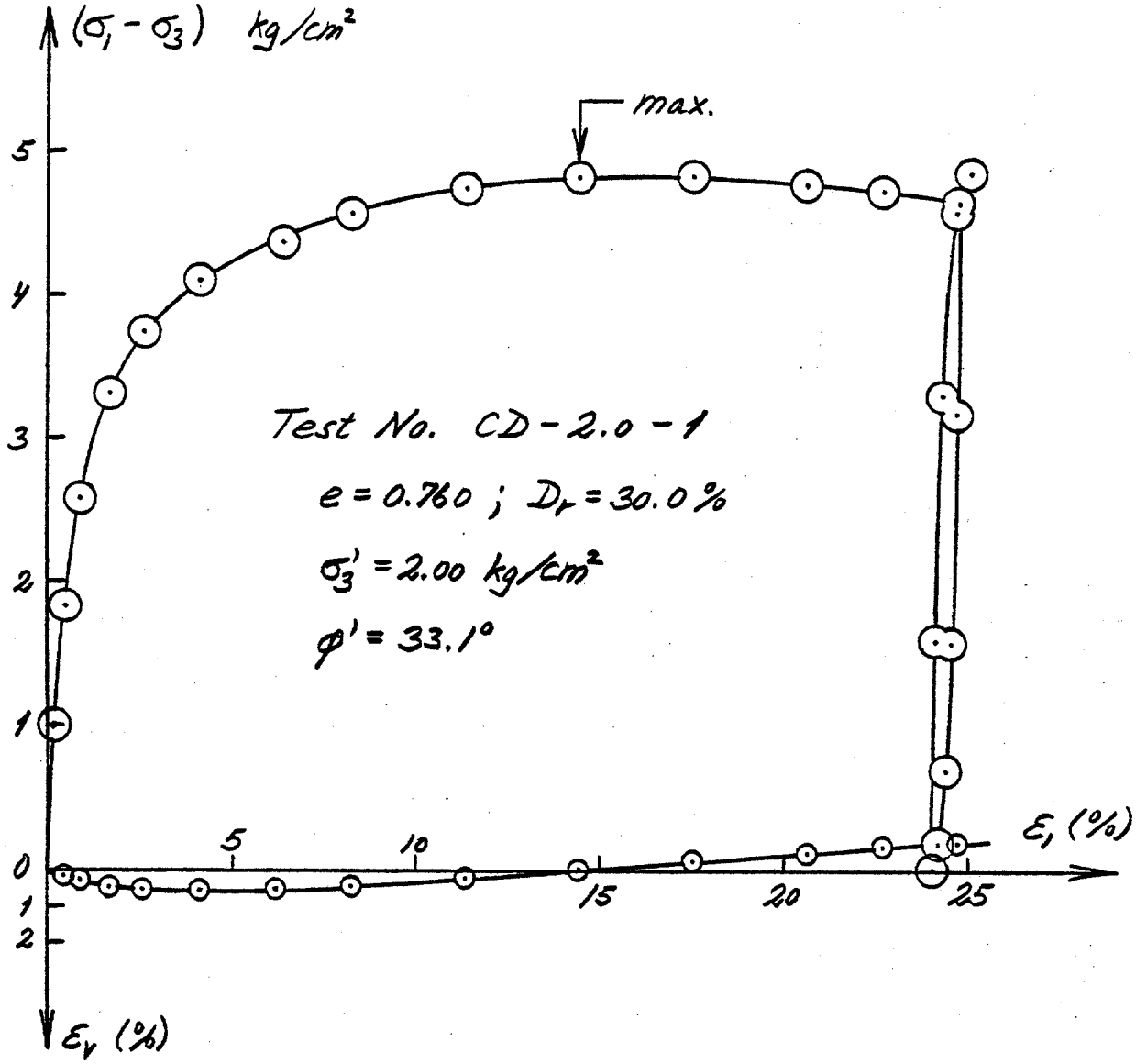

Fig. 3. Stress-Strain and Volumetric Strain Curves from Consolidated-Drained Triaxial Compression Test with $\sigma_{3c}' = 2.00$ kg/cm² on Fine Silica Sand.

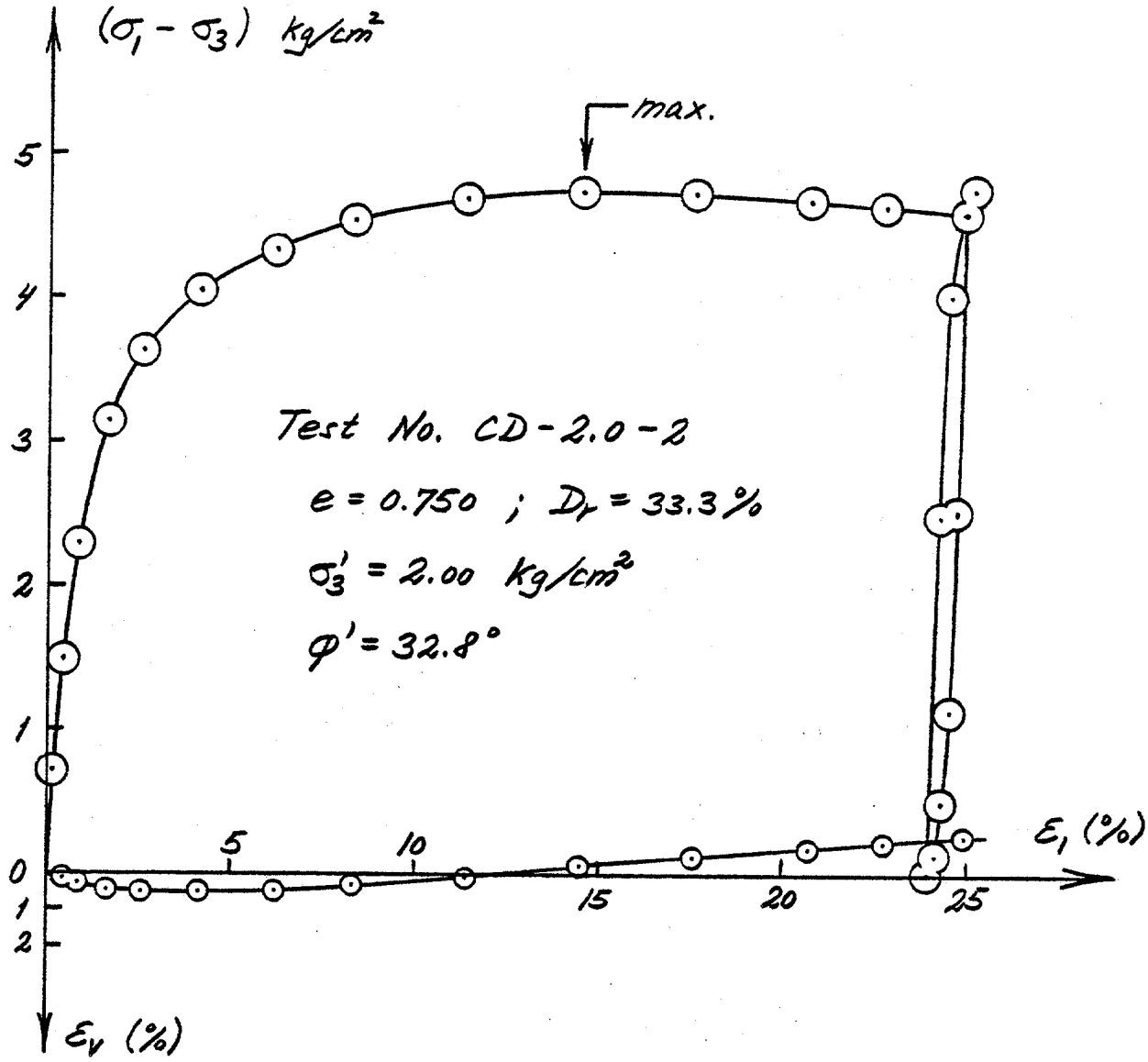

Fig. 4. Stress-Strain and Volumetric Strain Curves from Consolidated-Drained Triaxial Compression Test with $\sigma_{3c}' = 2.00$ kg/cm² on Fine Silica Sand.

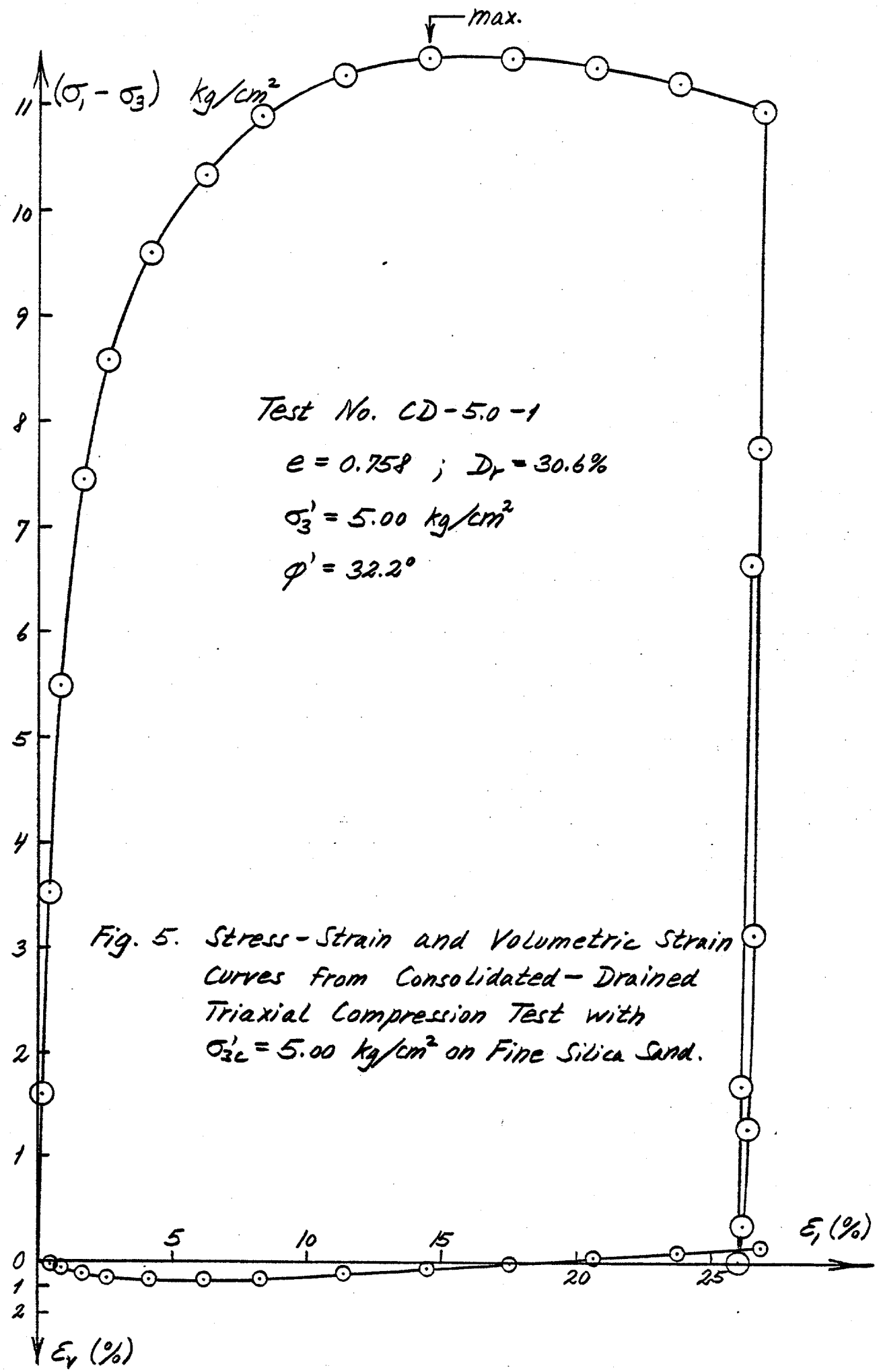

Fig. 5. Stress-Strain and Volumetric Strain Curves from Consolidated-Drained Triaxial Compression Test with σ_{3c}' = 5.00 kg/cm² on Fine Silica Sand.

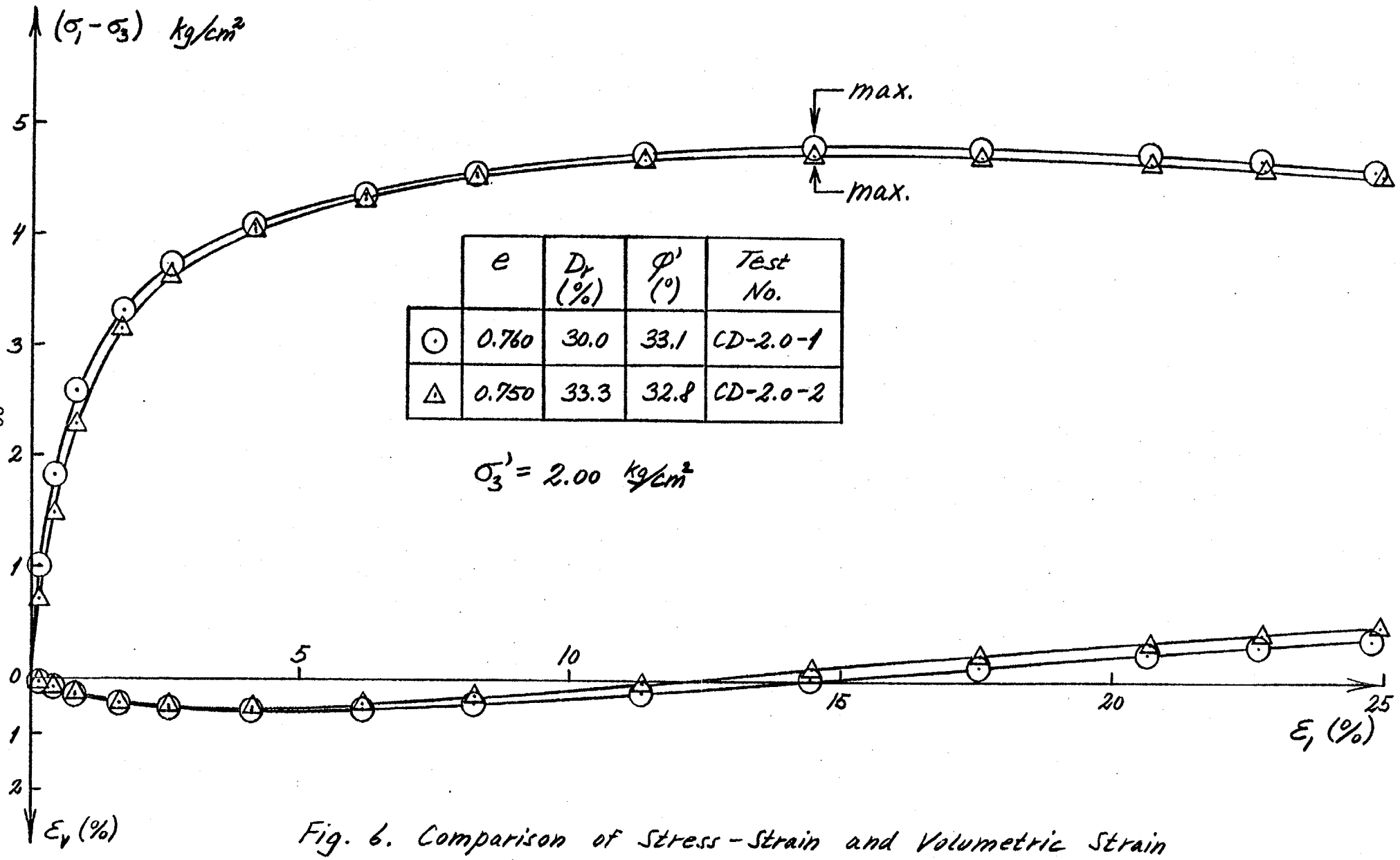

	e	D_r (%)	φ' (°)	Test No.
⊙	0.760	30.0	33.1	CD-2.0-1
△	0.750	33.3	32.8	CD-2.0-2

$\sigma_3' = 2.00$ kg/cm²

Fig. 6. Comparison of Stress-Strain and Volumetric Strain Curves from Consolidated-Drained Triaxial Compression Tests with $\sigma_3' = 2.00$ kg/cm² on Fine Silica Sand.

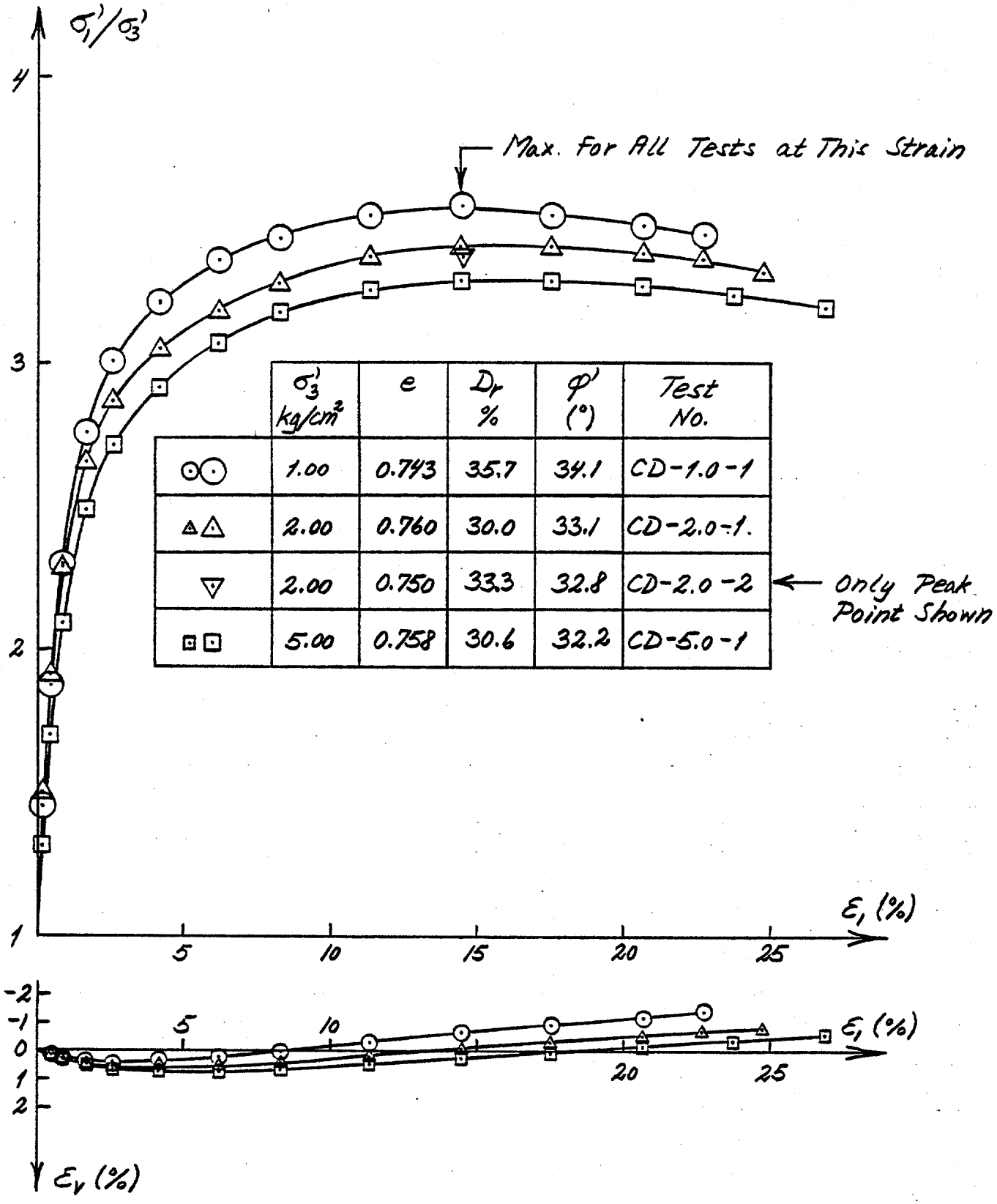

	σ_3' kg/cm²	e	D_r %	φ' (°)	Test No.
⊙⊙	1.00	0.743	35.7	34.1	CD-1.0-1
△△	2.00	0.760	30.0	33.1	CD-2.0-1.
▽	2.00	0.750	33.3	32.8	CD-2.0-2
⊡⊡	5.00	0.758	30.6	32.2	CD-5.0-1

Fig. 7. Comparison of Stress-Strain and Volumetric Strain Curves from Consolidated-Drained Triaxial Compression Tests on Fine Silica Sand.

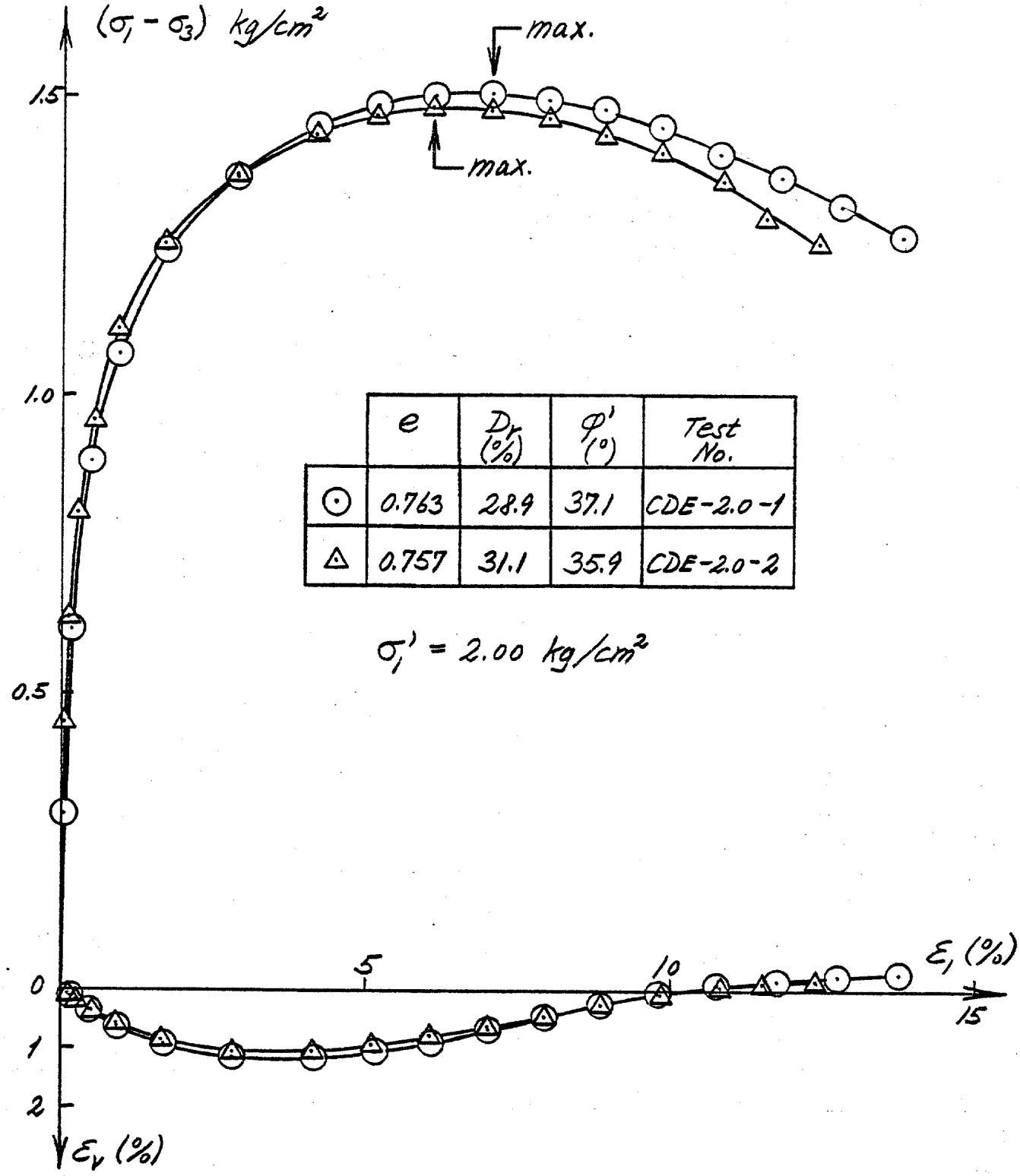

	e	D_r (%)	φ' (°)	Test No.
⊙	0.763	28.9	37.1	CDE-2.0-1
△	0.757	31.1	35.9	CDE-2.0-2

Fig. 8. Comparison of Stress-Strain and Volumetric Strain Curves from Consolidated-Drained Triaxial Extension Tests with $\sigma_1' = 2.00$ kg/cm² on Fine Silica Sand.

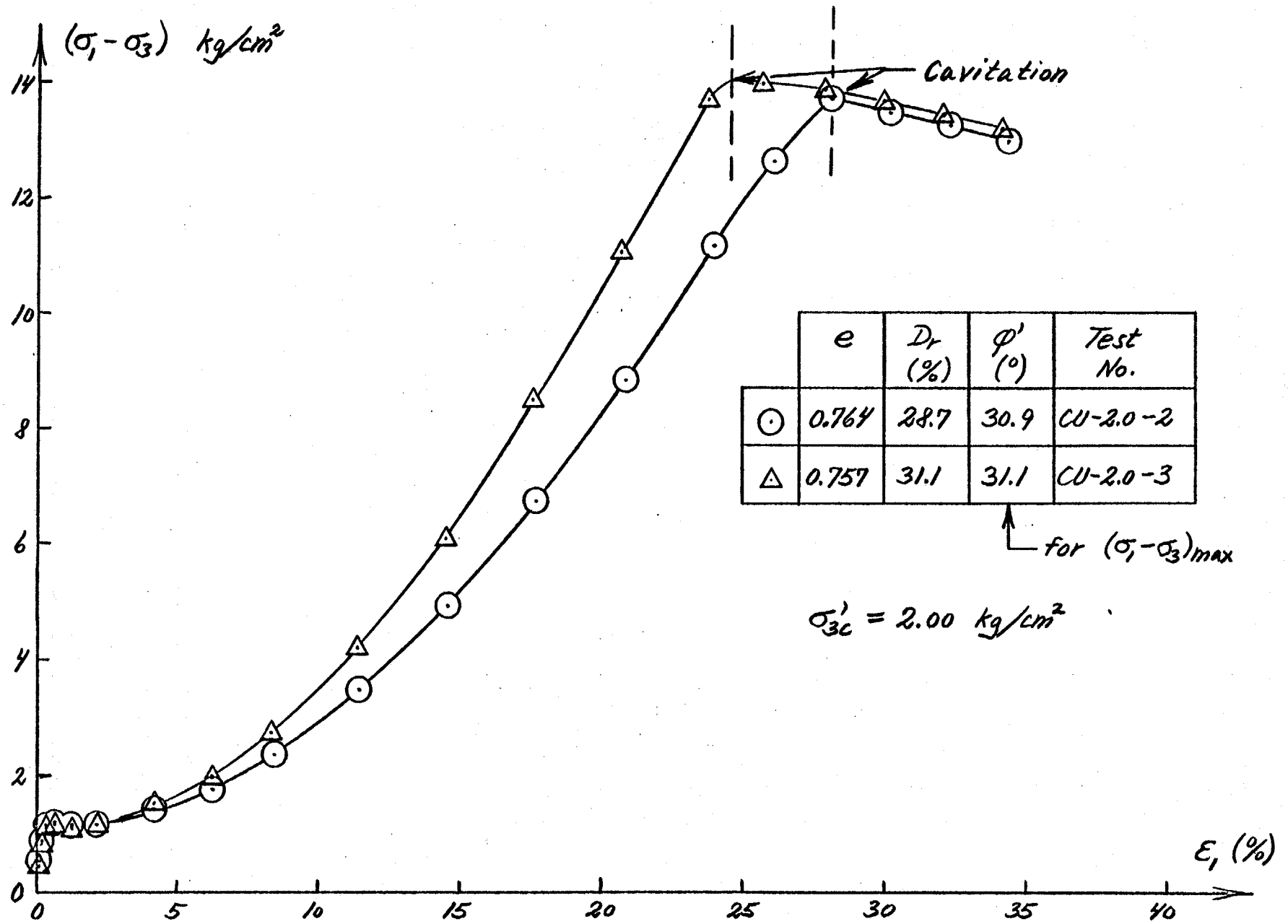

Fig. 9. Comparison of Stress Difference – Strain Curves from Consolidated-Undrained Triaxial Compression Tests on Fine Silica Sand.

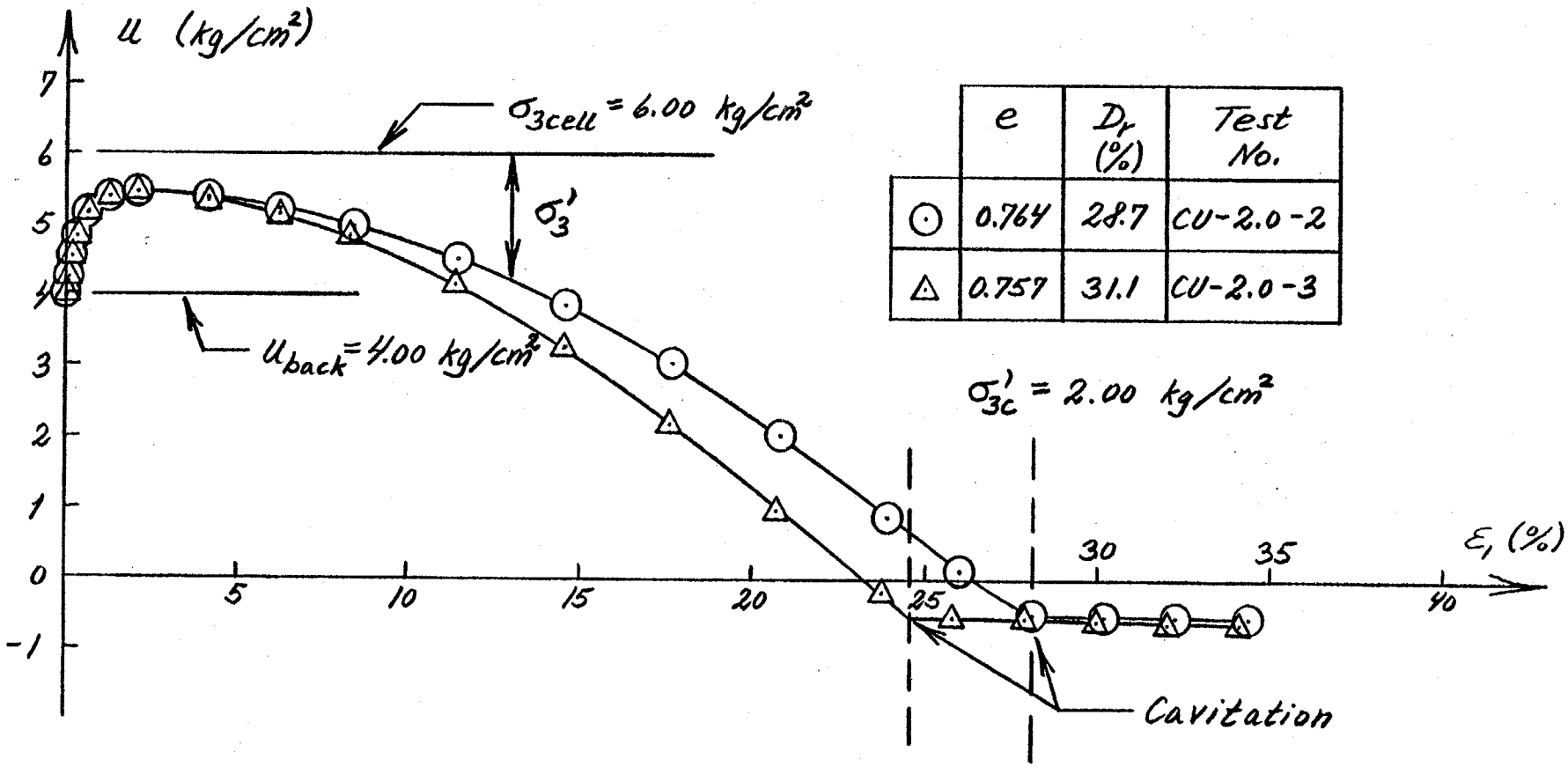

Fig. 10. Comparison of Pore Pressure -Strain Curves from Consolidated -Undrained Triaxial Compression Tests on Fine Silica Sand.

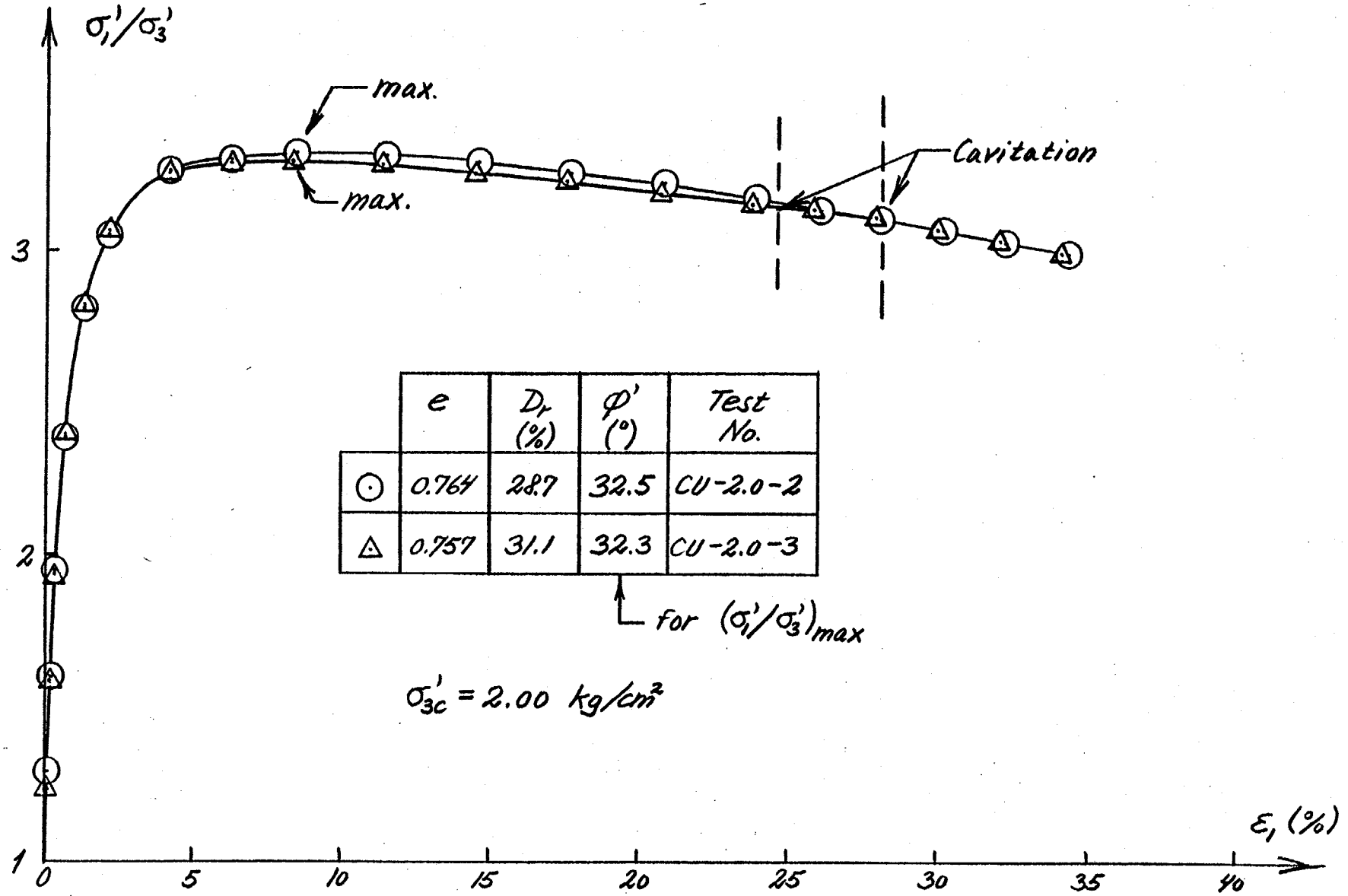

	e	D_r (%)	φ' (°)	Test No.
⊙	0.764	28.7	32.5	CU-2.0-2
△	0.757	31.1	32.3	CU-2.0-3

for $(\sigma_1'/\sigma_3')_{max}$

Fig. 11. Comparison of Effective Stress Ratio – Strain Curves from Consolidated -Undrained Triaxial Compression Tests on Fine Silica Sand.

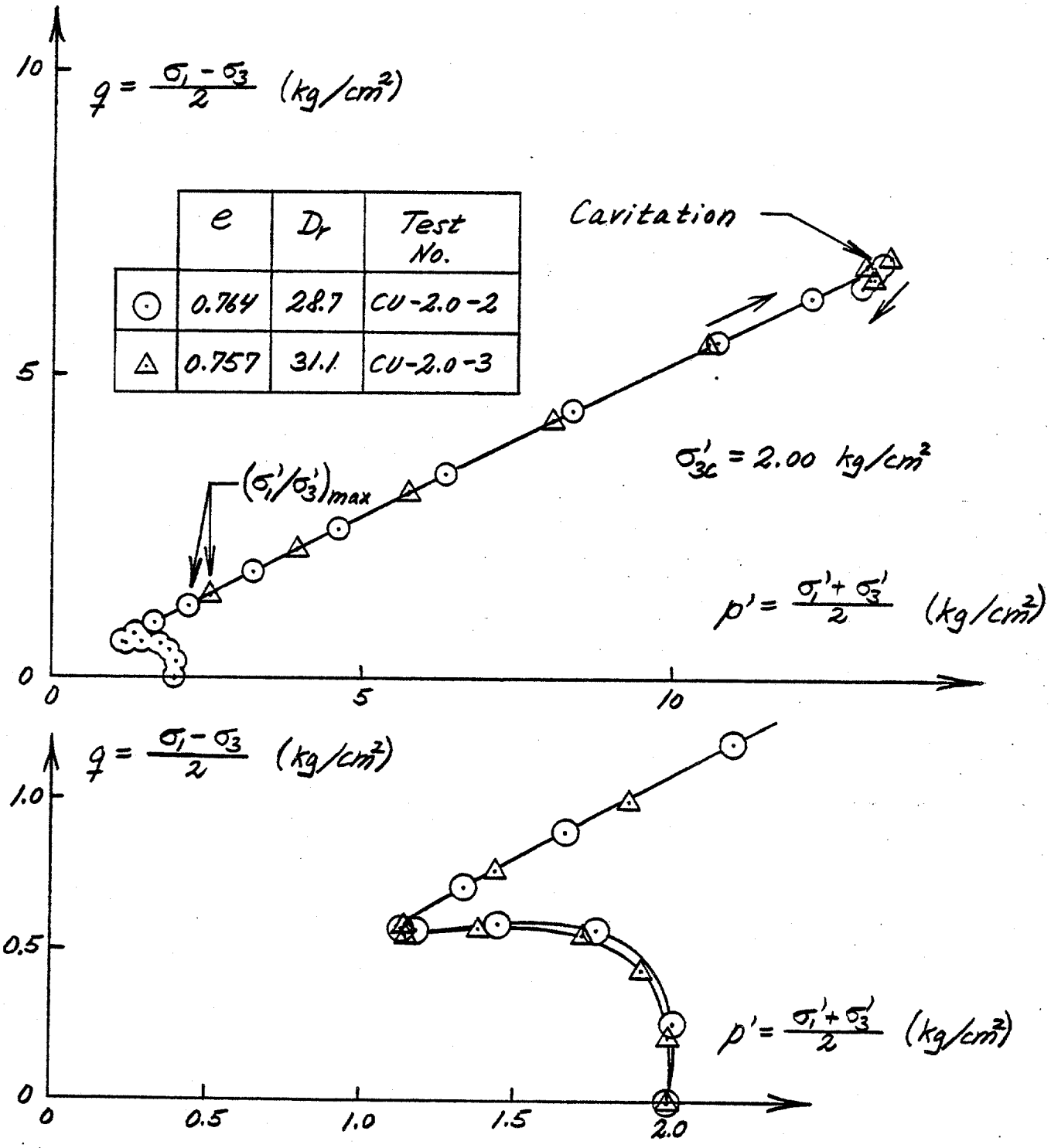

Fig. 12. Comparison of Effective Stress Paths from Consolidated - Undrained Triaxial Compression Tests on Fine Silica Sand.

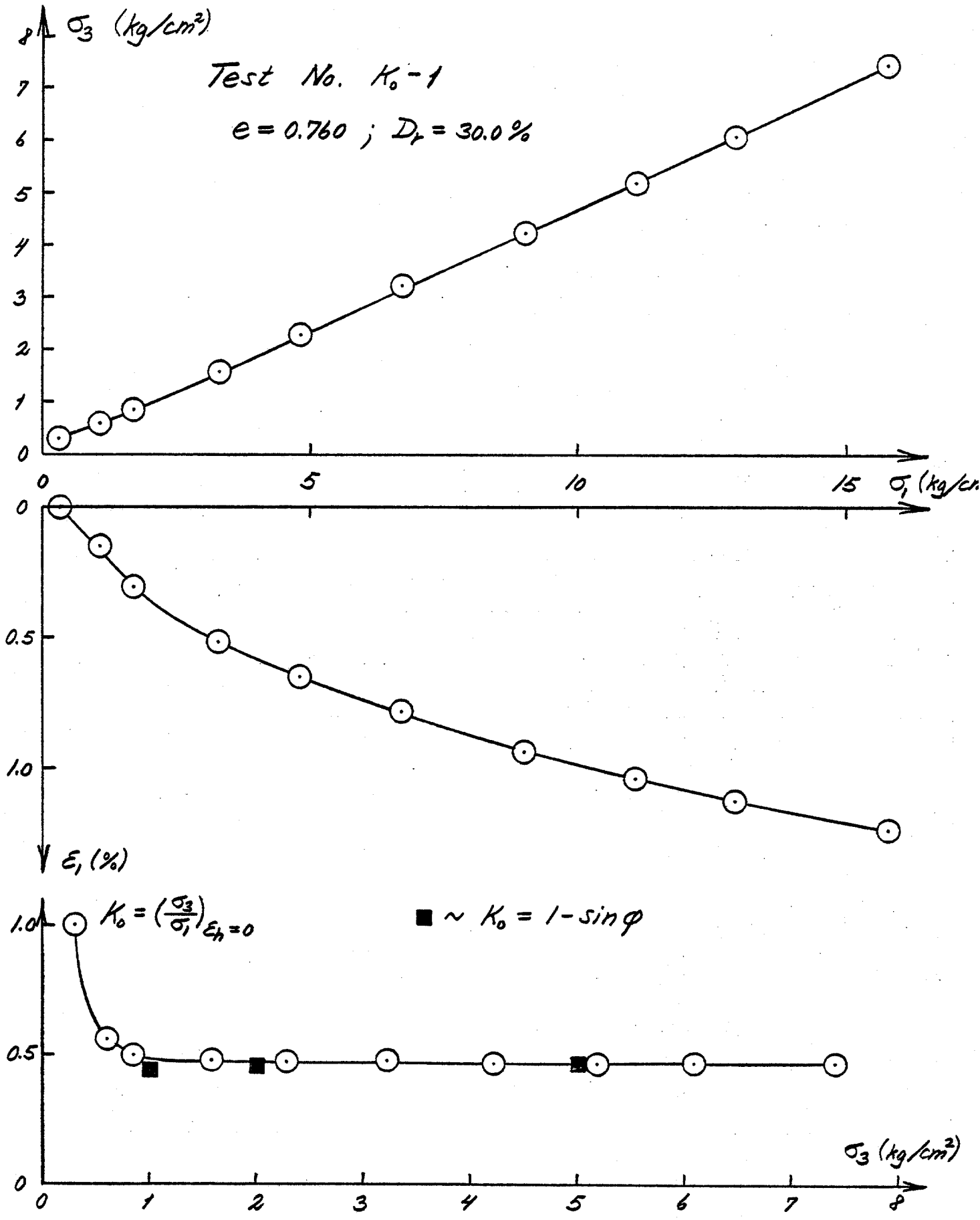

Fig. 13. Relations Between Stresses and Strains in K_0-Test on Fine Silica Sand.

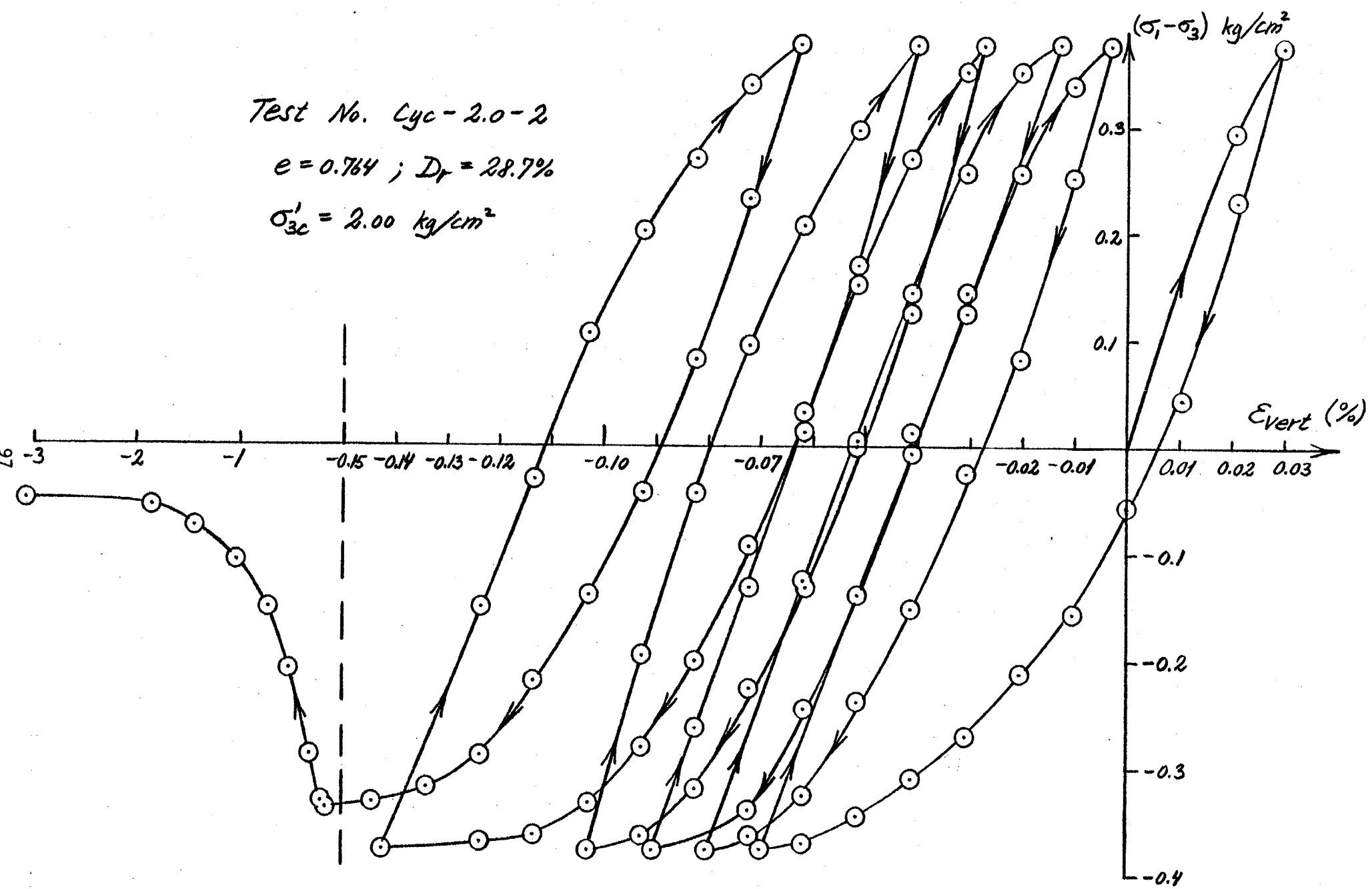

Fig. 14. Stress-Strain Relation from Consolidated-Undrained Cyclic Triaxial Test on Fine Silica Sand.

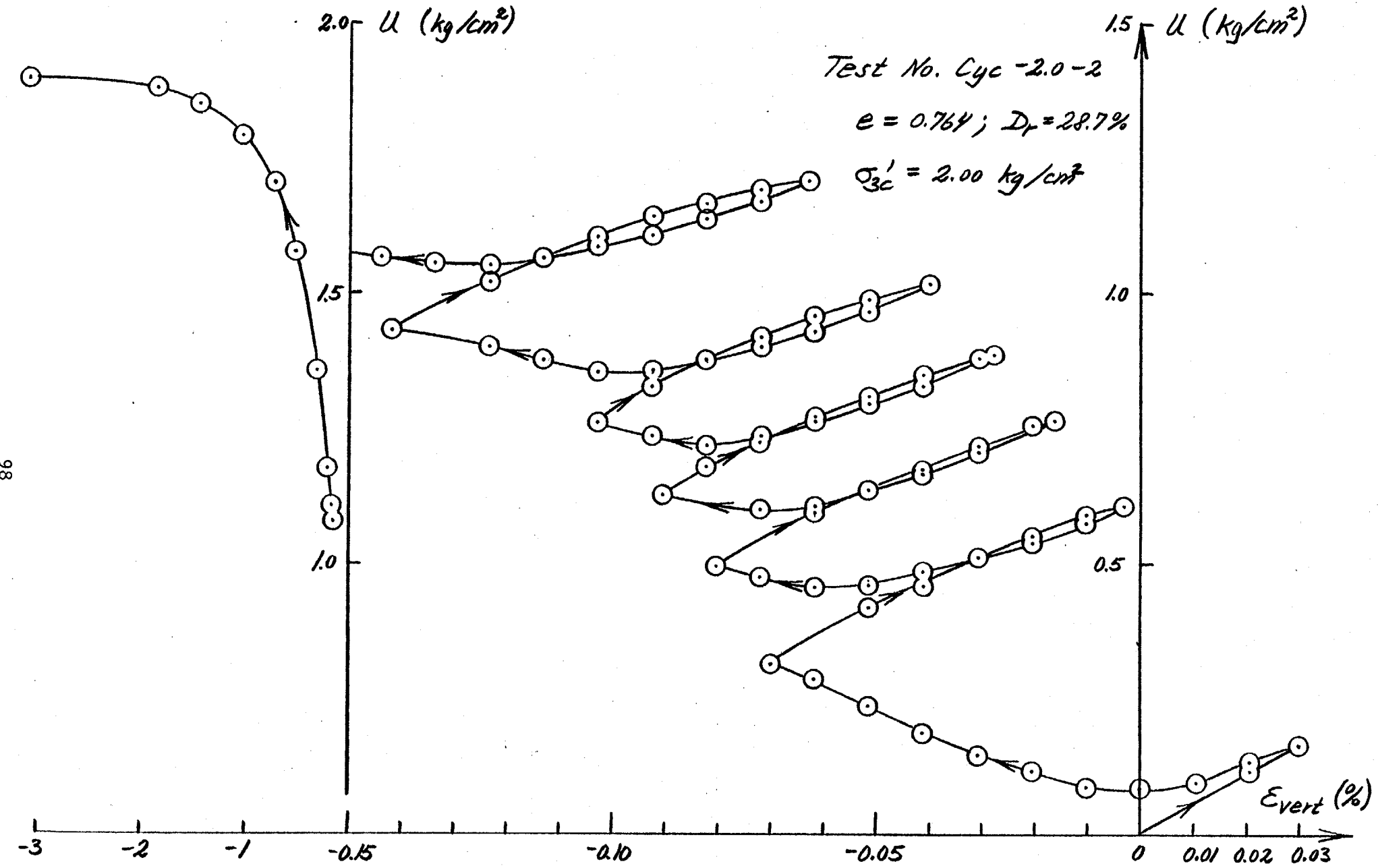

Fig. 15. Pore Water Pressure – Strain Relation from Consolidated-Undrained Cyclic Triaxial Test on Fine Silica Sand.

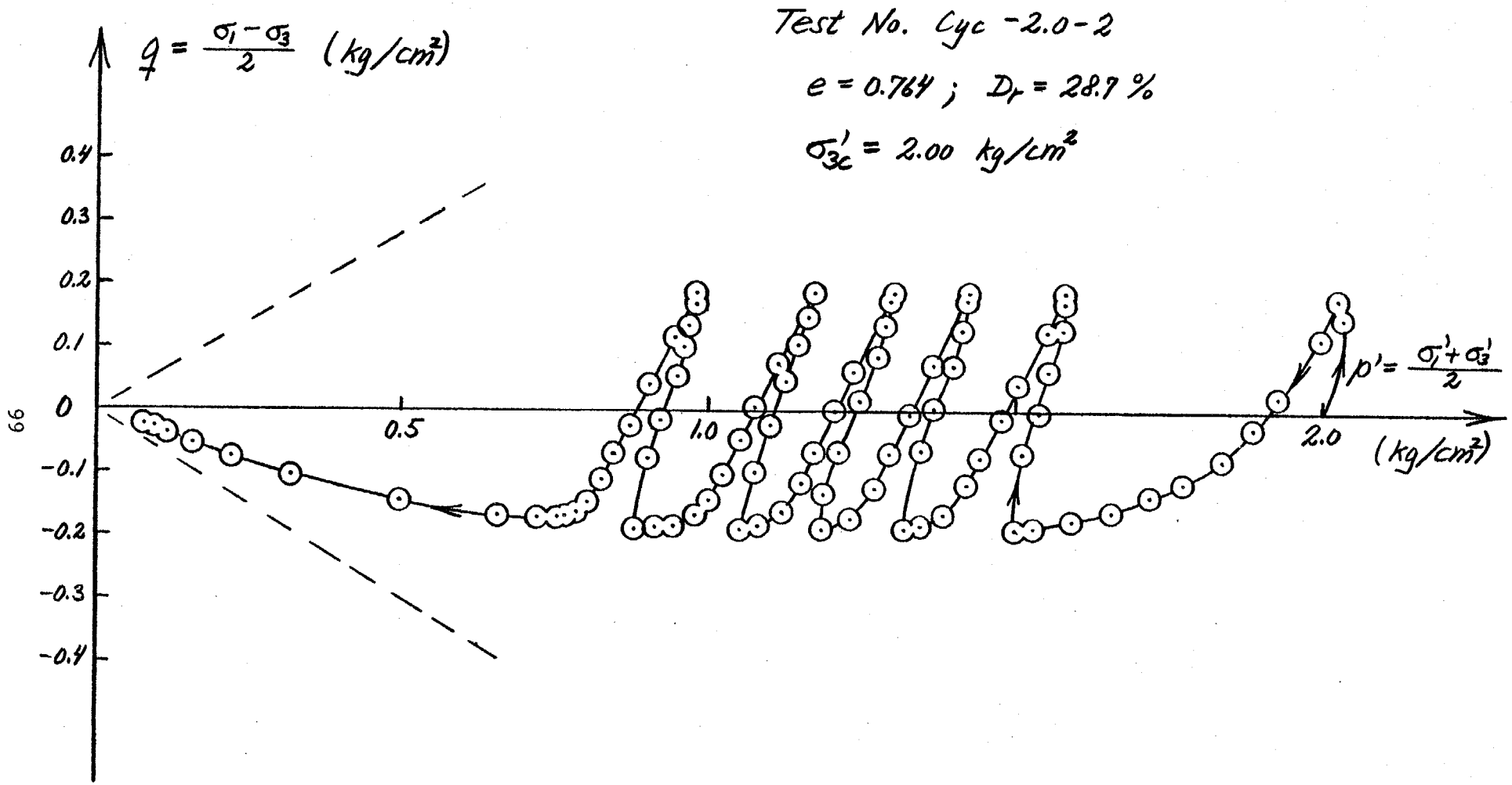

Fig. 16. Effective Stress Path from Consolidated - Undrained Cyclic Triaxial Test on Fine Silica Sand.

UNIVERSITY OF CALIFORNIA, LOS ANGELES
Soil Mechanics Laboratory

Test No. CD-1.0-1 Date: Oct. 29, 1981

H_c = 9.670 cm Silica Sand, -#60 sieve

A_c = 72.90 cm^2 $\varphi' = \text{Arcsin}\frac{3.546-1}{3.546+1} = 34.1°$

σ_3' = 1.000 kg/cm^2 $A = A_o \cdot \frac{1-\varepsilon_v}{1-\varepsilon_1}$

Read No.	δ_1 mm	ε_1 %	ΔV cm^3	ε_v %	A cm^2	P kg	$\sigma_1-\sigma_3$ kg/cm^2	σ_1'/σ_3'	
1	0.00	0.000	0.000	0.000	72.90	0.0	0.000	1.000	
4	0.15	0.155	0.322	0.046	72.98	33.5	0.459	1.459	
7	0.40	0.414	1.047	0.148	73.10	64.2	0.879	1.879	
11	0.80	0.827	1.909	0.271	73.31	95.4	1.302	2.302	
15	1.60	1.655	2.691	0.382	73.84	129.8	1.758	2.758	
18	2.50	2.585	2.875	0.408	74.53	150.0	2.013	3.013	
21	4.00	4.137	2.507	0.356	75.78	167.9	2.216	3.216	
25	6.00	6.205	1.518	0.215	77.56	183.1	2.360	3.360	
28	8.00	8.273	0.150	0.021	79.46	193.6	2.437	3.437	
31	11.00	11.375	-2.070	-0.294	82.50	207.4	2.514	3.514	
34	14.00	14.478	-4.405	-0.625	85.77	218.4	2.546	3.546	
37	17.00	17.580	-6.475	-0.918	89.26	224.4	2.513	3.513	
40	20.00	20.683	-8.349	-1.184	93.00	230.3	2.477	3.477	
42	22.00	22.751	-9.649	-1.369	95.66	234.0	2.446	3.446	
↓ 44	21.90	22.647	-9.442	-1.339	95.51	97.3	1.018		
48	21.70	22.441	-7.556	-1.072	95.00	31.2	0.328		
52	21.50	22.234	-5.359	-0.760	94.46	9.6	0.102		
56	21.32	22.048	-3.634	-0.516	94.00	0.0	0.000		
↑ 58	21.50	22.234	-2.990	-0.424	94.14	128.9	1.369		
60	21.70	22.441	-3.059	-0.434	94.40	192.2	2.036		
63	22.00	22.751	-3.703	-0.525	94.87	232.6	2.452		
66	22.30	23.061	-4.405	-0.625	95.34	242.7	2.546		

$e = 0.743$; $\gamma_d = 1.526\ g/cm^3$; $D_r = 35.7\%$

UNIVERSITY OF CALIFORNIA, LOS ANGELES
Soil Mechanics Laboratory

Test No. CD-2.0-1 Date: Oct. 25, 1981

H_c = 9.692 cm — Silica Sand, -#60 Sieve

A_c = 73.16 cm^2 — $\varphi' = \text{Arcsin}\frac{4.812}{4.812+2\cdot2.0} = 33.1°$

σ_3' = 2.000 kg/cm^2 — $A = A_0 \cdot \frac{1-\varepsilon_v}{1-\varepsilon_1}$

Read No.	δ_1 mm	ε_1 %	ΔV cm^3	ε_v %	A cm^2	P kg	$\sigma_1-\sigma_3$ kg/cm^2	σ_1'/σ_3'	
1	0.00	0.000	0.000	0.000	73.16	0.0	0.000	1.000	
4	0.15	0.155	0.506	0.071	73.22	73.4	1.003	1.502	
7	0.40	0.413	1.208	0.170	73.34	134.4	1.833	1.917	
11	0.80	0.825	2.116	0.298	73.55	189.9	2.583	2.292	
15	1.60	1.651	3.186	0.449	74.05	245.5	3.315	2.658	
18	2.50	2.579	3.761	0.530	74.70	279.0	3.734	2.867	
21	4.00	4.127	4.025	0.568	75.88	311.1	4.099	3.050	
25	6.00	6.191	3.761	0.530	77.58	338.6	4.364	3.182	
28	8.00	8.254	2.990	0.422	79.41	362.0	4.559	3.280	
31	11.00	11.350	1.495	0.211	82.35	390.4	4.741	3.371	
34	14.00	14.445	-0.230	-0.032	85.54	411.5	4.811	3.406	
37	17.00	17.540	-1.932	-0.272	88.96	428.1	4.812	3.406	
40	20.00	20.636	-3.588	-0.506	92.65	440.9	4.759	3.380	
42	22.00	22.699	-4.715	-0.665	95.27	449.6	4.719	3.360	
44	24.02	24.783	-5.612	-0.791	98.04	453.8	4.628	3.314	
↓ 46	23.95	24.711	-5.612	-0.791	97.94	310.6	3.171		
49	23.80	24.556	-5.129	-0.723	97.67	153.7	1.574		e = 0.760
52	23.65	24.402	-3.669	-0.517	97.28	67.4	0.693		γ_d = 1.511 g/cm
55	23.45	24.195	-1.495	-0.211	96.71	18.8	0.195		D_r = 30.0 %
57	23.32	24.061	+0.012	+0.002	96.34	2.3	0.024		
↑ 58	23.38	24.123	+0.506	+0.071	96.35	153.7	1.595		
62	23.55	24.298	+0.702	+0.099	96.55	318.4	3.298		
66	23.90	24.660	+0.150	+0.021	97.09	444.1	4.574		
70	24.30	25.072	-0.667	-0.094	97.73	474.9	4.859		

UNIVERSITY OF CALIFORNIA, LOS ANGELES
Soil Mechanics Laboratory

Test No. CD-2.0-1 Date: Oct. 25, 1981 / July 7, 1982

H_c = 9.692 cm Silica Sand, -#60 Sieve

A_c = 73.16 cm^2 Additional Stress-Strain and

σ_3' = 2.000 kg/cm^2 Volume Change Data

Read No.	δ_1 mm	ε_1 %	ΔV cm^3	ε_v %	A cm^2	P kg	$\sigma_1-\sigma_3$ kg/cm^2	σ_1'/σ_3'	
1	0.00	0.000	0.000	0.000	73.16	0.0	0.000	1.000	
2	0.05	0.052	0.196	0.028	73.18	36.2	0.495	1.247	
3	0.10	0.103	0.357	0.050	73.20	58.3	0.796	1.398	
4	0.15	0.155	0.506	0.071	73.22	73.4	1.003	1.502	
5	0.20	0.206	0.667	0.094	73.24	89.5	1.222	1.611	
6	0.30	0.310	0.943	0.133	73.29	113.8	1.553	1.776	
7	0.40	0.413	1.208	0.170	73.34	134.4	1.833	1.917	
8	0.50	0.516	1.472	0.208	73.39	150.9	2.056	2.028	
9	0.60	0.619	1.702	0.240	73.44	166.5	2.267	2.134	
10	0.70	0.722	1.921	0.271	73.49	179.4	2.441	2.221	
11	0.80	0.825	2.116	0.298	73.55	189.9	2.583	2.292	
12	1.00	1.032	2.461	0.347	73.67	208.8	2.834	2.417	
13	1.20	1.238	2.737	0.386	73.79	223.4	3.027	2.514	
14	1.40	1.444	2.979	0.420	73.92	235.4	3.185	2.592	
15	1.60	1.651	3.186	0.449	74.05	245.5	3.315	2.658	
16	1.80	1.857	3.358	0.474	74.19	254.6	3.432	2.716	
17	2.00	2.064	3.508	0.495	74.33	263.4	3.544	2.772	
18	2.50	2.579	3.761	0.530	74.70	279.0	3.734	2.867	
19	3.00	3.095	3.922	0.553	75.08	291.3	3.880	2.940	
20	3.50	3.611	3.991	0.563	75.47	302.3	4.005	3.003	
21	4.00	4.127	4.025	0.568	75.88	311.1	4.099	3.050	
22	4.50	4.643	4.002	0.564	76.29	318.9	4.180	3.090	

UNIVERSITY OF CALIFORNIA, LOS ANGELES
Soil Mechanics Laboratory

Test No. CD-2.0-1 Date: Oct. 25, 1981 / July 7, 1982

Continued Silica Sand, - #60 Sieve

Read No.	δ_1 mm	ε_1 %	ΔV cm^3	ε_v %	A cm^2	P Kg	$\sigma_1 - \sigma_3$ kg/cm^2	σ_1'/σ_3'	
23	5.00	5.159	3.456	0.558	76.71	325.7	4.246	3.123	
24	5.50	5.675	3.876	0.547	77.14	332.2	4.307	3.153	
25	6.00	6.191	3.761	0.530	77.58	338.6	4.364	3.182	
26	6.50	6.707	3.623	0.511	78.02	345.0	4.422	3.211	
27	7.00	7.222	3.459	0.485	78.47	351.0	4.473	3.236	
28	8.00	8.254	2.990	0.422	79.41	362.0	4.559	3.280	
29	9.00	9.286	2.496	0.352	80.37	372.5	4.635	3.318	
30	10.00	10.318	1.978	0.279	81.35	382.2	4.698	3.349	
31	11.00	11.350	1.495	0.211	82.35	390.4	4.741	3.371	
32	12.00	12.381	0.978	0.138	83.38	397.3	4.765	3.382	
33	13.20	13.619	0.276	0.039	84.66	406.5	4.801	3.401	
34	14.00	14.445	-0.230	-0.032	85.54	411.5	4.811	3.406	

UNIVERSITY OF CALIFORNIA, LOS ANGELES
Soil Mechanics Laboratory

Test No. CD-2.0-2 Date: Oct. 30, 1981

H_c = 9.664 cm Silica Sand, - #60 sieve

A_c = 73.00 cm^2 $\varphi' = \text{Arcsin}\frac{3.370-1}{3.370+1} = 32.8°$

σ_3' = 2.000 kg/cm^2 $A = A_o \cdot \frac{1-\varepsilon_v}{1-\varepsilon_1}$

Read No.	δ_1 mm	ε_1 %	ΔV cm^3	ε_v %	A cm^2	P kg	$\sigma_1-\sigma_3$ kg/cm^2	σ_1'/σ_3'	
1	0.00	0.000	0.000	0.000	73.00	0.0	0.000	1.000	
4	0.15	0.155	0.357	0.051	73.08	51.8	0.709	1.355	
7	0.40	0.414	1.012	0.143	73.20	108.7	1.485	1.743	
11	0.80	0.828	1.875	0.266	73.41	168.4	2.294	2.147	
15	1.60	1.656	2.967	0.421	73.92	233.1	3.153	2.577	
18	2.50	2.587	3.485	0.494	74.57	271.2	3.636	2.818	
21	4.00	4.139	3.554	0.504	75.77	307.4	4.057	3.028	
25	6.00	6.209	3.059	0.434	77.50	335.8	4.333	3.167	
28	8.00	8.278	2.059	0.292	79.36	360.2	4.538	3.269	
31	11.00	11.382	0.299	0.042	82.34	385.9	4.686	3.343	
34	14.00	14.487	-1.587	-0.225	85.56	405.6	4.740	3.370	
37	17.00	17.591	-3.404	-0.483	89.01	420.7	4.727	3.363	
40	20.00	20.695	-5.118	-0.725	92.72	433.1	4.671	3.336	
42	22.00	22.765	-6.314	-0.895	95.36	442.3	4.638	3.319	
44	24.09	24.928	-7.314	-1.037	98.25	450.1	4.581	3.290	
↓ 48	23.90	24.731	-7.268	-1.030	97.98	245.9	2.510		
52	23.70	24.524	-6.429	-0.911	97.60	111.5	1.142		$e = 0.750$
56	23.50	24.317	-4.761	-0.675	97.11	48.2	0.496		$\gamma_d = 1.520$ g/
60	23.30	24.110	-2.875	-0.408	96.58	13.3	0.138		$D_r = 33.3\%$
63	23.17	23.976	-1.484	-0.210	96.22	0.9	0.010		
↑ 65	23.40	24.214	-0.817	-0.116	96.44	239.0	2.479		
68	23.70	24.524	-0.989	-0.140	96.86	389.1	4.017		
71	24.00	24.834	-1.564	-0.222	97.33	446.4	4.587		
74	24.30	25.145	-2.185	-0.310	97.82	465.2	4.756		

MODEL PREDICTIONS

Figure 3 shows model predictions for an undrained axial compression test. Figure 3a shows the shear stress versus shear strain curve, and Fig. 3b shows the corresponding effective stress path (shear stress versus effective mean normal stress). Note that upon unloading, the model predicts that the sand would liquify, due to the extreme (and unrealistic) compactive volumetric behavior observed in the extension test as discussed above. Also, note that the model predicts less pore water pressure build-ups during the compressive phase of the test as compared to the corresponding experiment run by Lade which indicates that the volumetric strain recorded in the drained axial compression test experiment must be too low.

Figure 4 shows the model predictions for a conventional hydrostatic consolidation test, and Fig. 5 the simulation of a simple shear strain loading test. Figure 5 shows the hysteresis loops shear stress versus shear strain generated under 1.5 cycles of loading.

In order to correct for the unrealistic volumetric strains measured in the axial test experiments, the elastic bulk modulus of the material model was divided by 10, and Figures 6 and 7 show the resulting predictions of that "model sand" for cyclic axial undrained strain-controlled experiments. In Figure 6, the axial strain amplitude is 1% and in Figure 7, it is 2%. Note the progressive build-up of pore water pressure as cyclic loading proceeds (due mostly to the extension phase of the loading), and the corresponding softening of the shear-stress versus shear-strain hysteresis loops. Note that the sand liquefies in ten (10) cycles for a cyclic axial strain amplitude of 2% (Figure 7).

All the numerical results presented hereafter were obtained by using the computer programs MUDI and TESTA.

TEST RESULTS

Figure 1 shows the experimental results obtained in conventional drained monotonic axial compression/extension soil tests. Fig. 1a shows the shear stress versus shear strain stress-strain curve, and Fig. 1b shows the shear stress versus volumetric strain stress-strain curve. Note that the sand exhibits first compressive then dilative strains in both compression and extension. This behavior is a characteristic and is typical of loose sand. However, it is important at this stage to point out to an oddity of the test results: namely that the sand exhibits more compaction in extension than in compression. To the knowledge of the author, this has never been observed before. The compactive strains observed in tensile experiments performed by other investigators are always smaller than the one observed in compression. This raises serious doubts about the volumetric accuracy of the present data.

The test data shown in Fig. 1 were fed into the computer program MUDI to generate the corresponding model parameters (see Appendix 1 for the output) and Fig. 2 shows the associated field of yield surfaces plotted in the shear stress versus effective mean normal stress plane. Note that eleven (11) surfaces were generated which is the maximum possible number of surfaces given the number of data points of the experiments.

NUMERICAL SIMULATION OF FINE SILICA SAND BEHAVIOR

by

Jean H. Prevost
Department of Civil Engineering
PRINCETON UNIVERSITY
Princeton, NJ 08544

SCOPE OF INVESTIGATION

A series of conventional soil tests were performed on fine silica sand by Paul V. Lade for the Navy, under Contract N 62583/81 M R-543. The sand, specimen preparation, test procedures and test results have been reported by Paul V. Lade in a separate report. The test data were transmitted to the author last December 1981. This report describes the test results and their analysis.

The constitutive theory used for the numerical simulation of the fine silica sand behavior is described in the appended paper:

"Constitutive Theory for Pressure Sensitive Soils: Theory, Numerical Implementation and Examples,"
by Jean H. Prévost

The Navy has been provided with the computer program MUDI which automatically generates the required material model parameters from the results of conventional axial compression and extension soil test results. Also, the Navy has been provided with the computer program TESTA which is used to test the material model predictions for complex strain paths. Finally, the Navy has been provided with the finite element analysis computer program DYNA-FLOW, in which the above mentioned constitutive model has been implemented.

Appendix B

NUMERICAL SIMULATION OF FINE SILICA SAND BEHAVIOR

by

Jean H. Prevost
Department of Civil Engineering
PRINCETON UNIVERSITY
Princeton, NJ 08544

Report to

Department of the Navy
Civil Engineering Laboratory
Naval Construction Battalion Center
Port Hueneme, California 93043

July 1982

UNIVERSITY OF CALIFORNIA, LOS ANGELES
Soil Mechanics Laboratory

Test No. PL-2 Date: March 21, 1962

H = 8.043 cm Silica Sand, -#30 +#40 Sieve

A = 78.73 cm²

Proportional Loading

Read No.	δ_1 mm	ε_1 %	ΔV cm³	ε_v %	A cm²	P kg	$(\sigma_1 - \sigma_3)$ kg/cm²	σ_3 kg/cm²	σ_1 kg/cm²	σ_1/σ_3
28	0.00	0.000	0.000	0.000	78.73	345.0	4.382	2.000	6.382	3.19
30	0.55	0.615	0.161	0.023	79.20	390.4	4.930	2.272	7.202	3.17
32	1.21	1.353	0.391	0.056	79.77	448.2	5.619	2.608	8.227	3.15
34	1.74	1.946	0.633	0.090	80.22	506.5	6.314	2.943	9.257	3.14
36	2.16	2.415	0.874	0.124	80.58	564.3	7.003	3.279	10.282	3.13
38	2.54	2.840	1.104	0.157	80.90	622.1	7.690	3.614	11.304	3.12
40	2.85	3.187	1.334	0.189	81.17	679.9	8.377	3.949	12.326	3.12
42	3.15	3.522	1.564	0.222	81.42	737.8	9.061	4.285	13.346	3.11
44	3.41	3.813	1.771	0.252	81.65	795.6	9.744	4.620	14.364	3.10
46	3.66	4.093	1.978	0.281	81.86	853.4	10.425	4.956	15.381	3.103
48	3.87	4.327	2.185	0.310	82.04	911.2	11.106	5.291	16.397	3.09
50	4.09	4.573	2.381	0.338	82.22	969.0	11.785	5.626	17.411	3.095
52	4.28	4.786	2.576	0.366	82.39	1026.8	12.463	5.962	18.425	3.090
54	4.47	4.998	2.772	0.394	82.55	1085.1	13.144	6.297	19.441	3.087
57	4.73	5.289	3.048	0.433	82.77	1171.8	14.157	6.800	20.957	3.082

UNIVERSITY OF CALIFORNIA, LOS ANGELES
Soil Mechanics Laboratory

(1)

Test No. PL-2 Date: March 21, 1962

r_c = 9.688 cm Silica Sand - # 60 Sieve

A_c = 72.99 cm^2 Shear Strength 10 Psi

σ_3' = 2.000 kg/cm^2 $K = \frac{\sigma_1'}{\sigma_3'}$ = 3.2

(2)

Read No.	δ_l mm	ε_l %	ΔV cm^3	ε_v %	A cm^2	P Kg	$(\sigma_1 - \sigma_3)$ kg/cm^2	σ_1'/σ_3'	
1	0.00	0.000	0.000	0.000	72.99	0.0	0.000	1.000	
3	0.10	0.103	0.265	0.037	73.04	43.6	0.597	1.298	
5	0.20	0.206	0.564	0.080	73.08	75.2	1.030	1.515	
7	0.40	0.413	1.127	0.159	73.18	120.7	1.649	1.824	
13	1.00	1.032	2.220	0.314	73.52	191.3	2.602	2.301	
16	1.60	1.652	2.921	0.413	73.91	228.0	3.085	2.543	
20	3.00	3.097	3.703	0.524	74.43	273.4	3.649	2.825	
23	4.50	4.645	3.887	0.550	76.13	304.2	3.996	2.998	
26	6.00	6.193	3.611	0.511	77.41	327.6	4.232	3.116	
28	7.45	7.690	3.094	0.437	78.73	345.0	4.382	3.191	
			e =	0.756					
			γ_d =	1.515	g/cm³				
			D_r =	31.4%					

consolidated to 2 kg/cm²
Shear stage only

UNIVERSITY OF CALIFORNIA, LOS ANGELES
Soil Mechanics Laboratory

(2)

Test No. PL-1 Date: March 22, 1982

H = 9.303 cm Silica Sand, - #60 Sieve

A = 76.47 cm²

Proportional Loading

(1)

Read No.	δ_1 mm	ε_1 %	ΔV cm³	ε_v %	A cm²	P kg	$(\sigma_1-\sigma_3)$ kg/cm²	σ_3 kg/cm²	σ_1 kg/cm²	σ_1/σ_3
19	0.00	0.000	0.000	0.000	76.47	51.8	0.678	0.300	0.978	3.2
21	2.40	2.580	1.047	0.147	78.38	101.4	1.294	0.590	1.884	3.1
23	4.00	4.300	1.898	0.267	79.69	159.2	1.998	0.926	2.924	3.1
25	5.10	5.482	2.588	0.364	80.61	217.0	2.692	1.261	3.953	3.13
27	5.92	6.364	3.174	0.446	81.30	274.8	3.380	1.597	4.977	3.11
29	6.60	7.094	3.646	0.512	81.89	332.6	4.062	1.932	5.994	3.10
31	7.06	7.589	4.054	0.575	82.27	390.4	4.746	2.267	7.013	3.0
33	7.45	8.008	4.497	0.632	82.60	448.2	5.427	2.603	8.030	3.08
35	7.80	8.384	4.865	0.684	82.90	506.5	6.110	2.938	9.048	3.08
37	8.13	8.739	5.187	0.729	83.18	564.3	6.784	3.274	10.058	3.07
39	8.39	9.019	5.520	0.776	83.40	622.1	7.460	3.609	11.069	3.06
41	8.67	9.320	5.831	0.820	83.64	679.9	8.129	3.944	12.073	3.06
43	8.92	9.588	6.130	0.862	83.85	737.8	8.798	4.280	13.078	3.05
45	9.16	9.846	6.406	0.900	84.06	795.6	9.464	4.615	14.079	3.05
47	9.39	10.094	6.659	0.936	84.26	853.4	10.128	4.951	15.079	3.04
49	9.61	10.330	6.912	0.972	84.45	911.2	10.790	5.286	16.076	3.04
51	9.82	10.556	7.153	1.005	84.64	969.0	11.448	5.621	17.069	3.03
53	10.04	10.792	7.383	1.038	84.83	1026.8	12.104	5.957	18.061	3.03
55	10.26	11.029	7.613	1.070	85.03	1085.1	12.761	6.292	19.053	3.02
58	10.54	11.330	7.935	1.115	85.28	1171.8	13.740	6.795	20.535	3.02

UNIVERSITY OF CALIFORNIA, LOS ANGELES
Soil Mechanics Laboratory

(1)

Test No. PL-1 Date: March 20, 1962

H_c = 9.703 cm. Silica Sand, - #60 Sieve

A_c = 73.48 cm^2 Shear Stage to Reach

σ_3' = 0.333 kg/cm^2 $K = \frac{\sigma_1'}{\sigma_3'}$ = 3.2

(1)

Read	δ_1	ε_1	ΔV	ε_v	A	P	$(\sigma_1 - \sigma_3)$	σ_1'/σ_3'	
No.	mm	%	cm^3	%	cm^2	kg	kg/cm^2		
1	0.00	0.000	0.000	0.000	73.48	0.0	0.000	1.000	
3	0.10	0.103	0.334	0.047	73.52	18.8	0.256	1.853	
4	0.20	0.206	0.575	0.081	73.57	24.3	0.331	2.102	
6	0.40	0.412	0.886	0.124	73.64	30.7	0.417	2.390	
9	1.00	1.031	1.438	0.202	74.10	39.0	0.526	2.754	
12	1.60	1.649	1.688	0.234	74.54	43.1	0.579	2.929	
15	2.40	2.473	1.771	0.248	75.16	46.8	0.623	3.075	
17	3.20	3.298	1.725	0.242	75.80	49.1	0.648	3.159	
19	4.00	4.122	1.576	0.221	76.47	51.8	0.678	3.260	
			e = 0.758						
			γ_d = 1.513	g/cm^3					
			D_r = 30.6	%					

NOT PLOTTED

Shear plane

RATIO 3.1

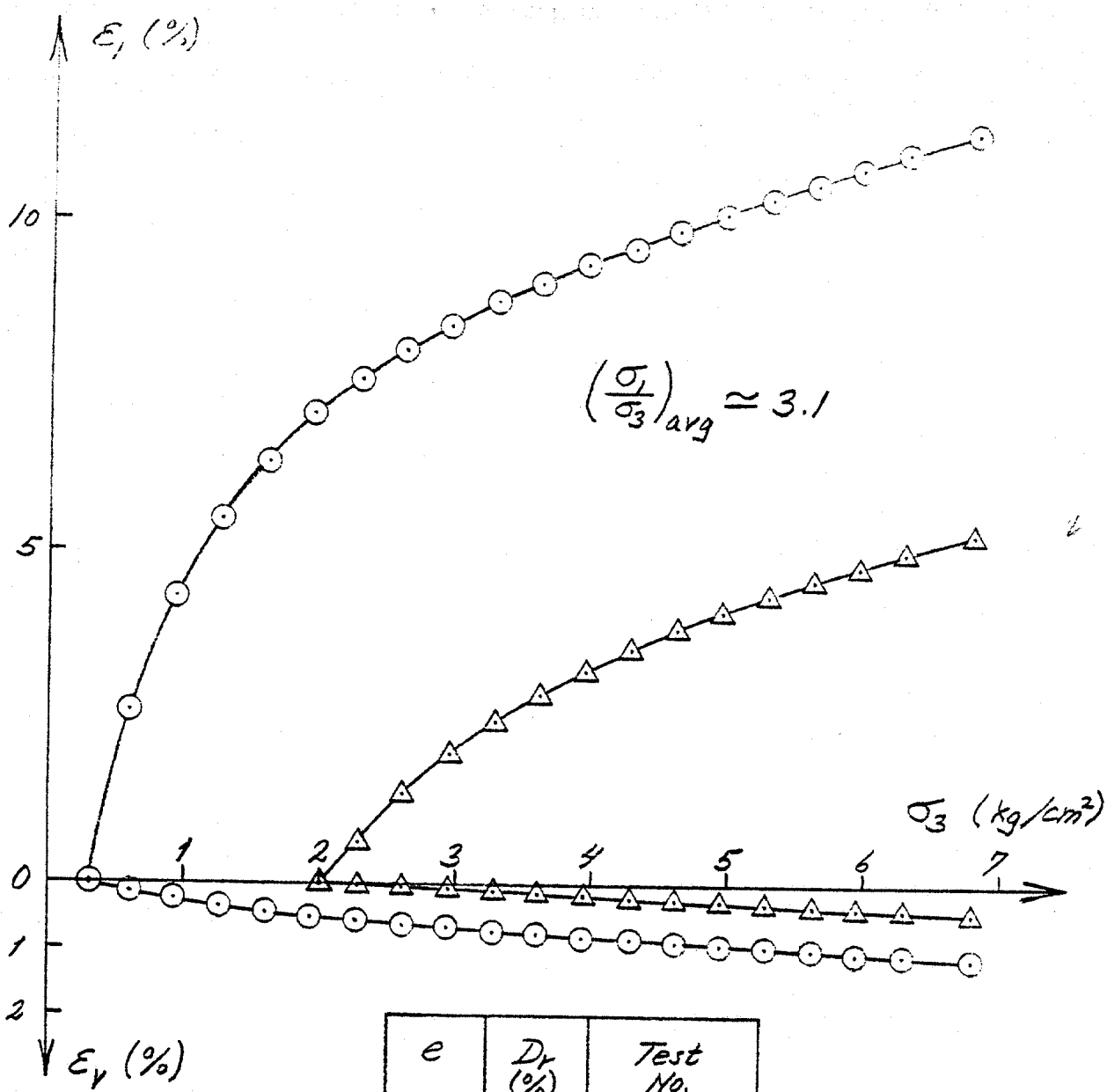

	e	D_r (%)	Test No.
⊙	0.758	30.6	PL-1
△	0.756	31.4	PL-2

Fig. 21. Relations Between Stresses and Strains in Proportional Loading Tests on Fine Silica Sand.

UNIVERSITY OF CALIFORNIA, LOS ANGELES
Soil Mechanics Laboratory

Test No. Cyc-2.0-3 Date: March 18, 1982

Extension

Read No.	δ_1 mm	ε_{vert} %	A cm^2	P kg	$(\sigma_1-\sigma_3)$ kg/cm²	u kg/cm²	σ_3' kg/cm²	σ_1'/σ_3'	$\frac{\sigma_1-\sigma_3}{2}$ kg/cm²	$\frac{\sigma_1+\sigma_3}{2}$ kg/cm²
45	-0.21	-0.2162	72.89	-22.0	-0.302	1.214	0.786	1.624	-0.151	0.63
46	-0.24	-0.2470	72.87	-21.1	-0.290	1.268	0.732	1.655	-0.145	0.5
47	-0.29	-0.2985	72.83	-19.7	-0.271	1.345	0.655	1.706	-0.136	0.5
48	-0.34	-0.3500	72.80	-19.9	-0.246	1.425	0.575	1.750	-0.123	0.4
49	-0.39	-0.4014	72.76	-16.1	-0.221	1.487	0.513	1.760	-0.111	0.4
50	-0.49	-0.5044	72.68	-13.3	-0.183	1.578	0.422	1.766	-0.092	0.3
51	-0.59	-0.6073	72.61	-11.0	-0.152	1.650	0.350	1.769	-0.076	0.2
52	-0.69	-0.7102	72.53	-9.2	-0.127	1.704	0.296	1.750	-0.064	0.2
53	-0.79	-0.8132	72.46	-7.8	-0.108	1.749	0.251	1.757	-0.054	0.1
54	-0.99	-1.0190	72.31	-6.4	-0.089	1.806	0.194	1.848	-0.045	0.1
55	-1.19	-1.2225	72.17	-4.6	-0.064	1.835	0.165	1.628	-0.032	0.1
56	-1.39	-1.431	72.02	-3.7	-0.051	1.858	0.142	1.562	-0.026	0.11
57	-1.59	-1.637	71.87	-3.2	-0.045	1.873	0.127	1.549	-0.023	0.10
58	-1.79	-1.843	71.73	-2.8	-0.038	1.883	0.117	1.486	-0.019	0.09
59	-1.99	-2.048	71.58	-2.3	-0.032	1.892	0.108	1.415	-0.016	0.09
60	-2.49	-2.563	71.22	-2.3	-0.032	1.900	0.100	1.471	-0.016	0.08
61	-2.99	-3.078	70.87	-2.3	-0.032	1.902	0.098	1.479	-0.016	0.08

Test No. Cyc - 2.0 - 3 Date: March 18, 1982

	Read No.	δ_l mm	ε_{vert} %	A cm^2	P kg	$(\sigma_1-\sigma_3)$ kg/cm^2	u kg/cm^2	σ_3' kg/cm^2	σ_1'/σ_3'	$\frac{\sigma_1-\sigma_3}{2}$ kg/cm^2	$\frac{\sigma_1'+\sigma_3'}{2}$ kg/c
Comp.	23	-0.05	-0.0515	73.01	21.6	0.295	0.839	1.162	1.253	0.148	1.31
	24	-0.04	-0.0412	73.02	27.5	0.377	0.874	1.126	1.335	0.189	1.31
	25	-0.045	-0.0463	73.02	0.0	0.000	0.771	1.229	1.000	0.000	1.22
Extension	26	-0.05	-0.0515	73.01	-12.8	-0.176	0.716	1.284	1.159	-0.088	1.19
	27	-0.06	-0.0618	73.00	-21.1	-0.289	0.693	1.307	1.283	-0.145	1.16
	28	-0.073	-0.0751	73.00	-25.7	-0.352	0.709	1.291	1.375	-0.176	1.11
	29	-0.085	-0.0875	72.99	-26.6	-0.365	0.740	1.260	1.407	-0.183	1.07
	30	-0.10	-0.1029	72.97	-27.1	-0.371	0.783	1.217	1.439	-0.186	1.03
	31	-0.122	-0.1256	72.96	-27.5	-0.377	0.845	1.155	1.485	-0.189	0.96
Compression	32	-0.11	-0.1132	72.97	-0.9	-0.013	1.005	0.995	1.013	-0.007	0.98
	33	-0.10	-0.1029	72.97	13.3	0.182	1.085	0.915	1.199	0.091	1.00
	34	-0.09	-0.0926	72.98	20.2	0.277	1.124	0.876	1.317	0.139	1.01
	35	-0.08	-0.0823	72.99	26.2	0.358	1.159	0.841	1.426	0.179	1.02
	36	-0.074	-0.0762	72.99	27.5	0.377	1.167	0.833	1.452	0.189	1.02
Extension	37	-0.08	-0.0823	72.99	5.0	0.069	1.087	0.913	1.076	0.035	0.94
	38	-0.09	-0.0926	72.98	-11.5	-0.157	1.025	0.975	1.161	-0.079	0.89
	39	-0.102	-0.1050	72.97	-20.2	-0.277	1.001	0.999	1.384	-0.139	0.86
	40	-0.11	-0.1132	72.97	-22.5	-0.308	1.006	0.994	1.449	-0.154	0.84
	41	-0.13	-0.1338	72.95	-23.9	-0.327	1.035	0.965	1.512	-0.164	0.80
	42	-0.15	-0.1544	72.94	-23.9	-0.327	1.080	0.920	1.551	-0.164	0.75
	43	-0.17	-0.1750	72.92	-23.4	-0.321	1.119	0.881	1.572	-0.161	0.72
	44	-0.19	-0.1956	72.91	-22.9	-0.315	1.160	0.840	1.601	-0.158	0.68

UNIVERSITY OF CALIFORNIA, LOS ANGELES
Soil Mechanics Laboratory

Test No. Cyc-2.0-3 Date: March 8, 1972

H_c = 9.715 cm Silica Sand - #200 sieve

A_c = 73.05 cm^2

σ_{3c} = 2.000 kg/cm^2 $n = \Delta e / (1 - \varepsilon_{vert})$

	Read No.	δ_l mm	ε_{vert} %	A cm^2	P Kg	$(\sigma_1 - \sigma_3)$ kg/cm^2	u kg/cm^2	σ_3' kg/cm^2	σ_1'/σ_3'	$\frac{\sigma_1 - \sigma_3}{2}$ kg/cm^2	$\frac{\sigma_1'+\sigma_3'}{2}$ kg/cm^2
Compression	1	0.00	0.0000	73.05	0.0	0.000	0.000	2.000	1.000	0.000	2.00
	2	0.006	0.0062	73.05	8.7	0.119	0.050	1.950	1.061	0.060	2.01
	3	0.01	0.0103	73.06	23.4	0.320	0.134	1.866	1.171	0.160	2.03
	4	0.014	0.0144	73.06	27.5	0.377	0.161	1.839	1.205	0.189	2.02
Extension	5	0.012	0.0124	73.06	0.9	0.013	0.075	1.925	1.007	0.007	1.93
	6	0.006	0.0062	73.05	-11.5	-0.157	0.070	1.930	1.089	-0.079	1.85
	7	0.00	0.000	73.05	-16.5	-0.226	0.101	1.899	1.135	-0.113	1.78
	8	-0.01	-0.0103	73.04	-22.0	-0.302	0.173	1.827	1.198	-0.151	1.67
	9	-0.02	-0.0206	73.03	-23.9	-0.327	0.213	1.787	1.224	-0.164	1.62
	10	-0.03	-0.0309	73.03	-25.7	-0.352	0.262	1.738	1.254	-0.176	1.56
	11	-0.04	-0.0412	73.02	-27.1	-0.371	0.307	1.693	1.281	-0.186	1.50
	12	-0.052	-0.0535	73.01	-27.5	-0.377	0.335	1.665	1.293	-0.189	1.47
Compression	13	-0.05	-0.0515	73.01	-10.1	-0.138	0.458	1.542	1.098	-0.069	1.47
	14	-0.042	-0.0432	73.02	0.0	0.000	0.510	1.490	1.000	0.000	1.49
	15	-0.03	-0.0309	73.03	22.0	0.302	0.637	1.363	1.221	0.151	1.51
	16	-0.022	-0.0226	73.03	27.5	0.377	0.672	1.328	1.284	0.189	1.51
Extension	17	-0.028	-0.0288	73.03	0.0	0.000	0.569	1.431	1.000	0.000	1.43
	18	-0.03	-0.0309	73.03	-9.2	-0.126	0.533	1.467	1.094	-0.063	1.40
	19	-0.04	-0.0412	73.02	-19.7	-0.270	0.500	1.500	1.219	-0.135	1.36
	20	-0.05	-0.0515	73.01	-25.2	-0.346	0.511	1.489	1.303	-0.173	1.31
	21	-0.07	-0.0721	73.00	-27.5	-0.377	0.560	1.440	1.355	-0.189	1.25
Comp.	22	-0.062	-0.0638	73.00	0.0	0.000	0.723	1.277	1.000	0.000	1.27

$e = 0.760$; $\gamma_d = 1.511$ g/cm³ ; $D_r = 30.0\%$

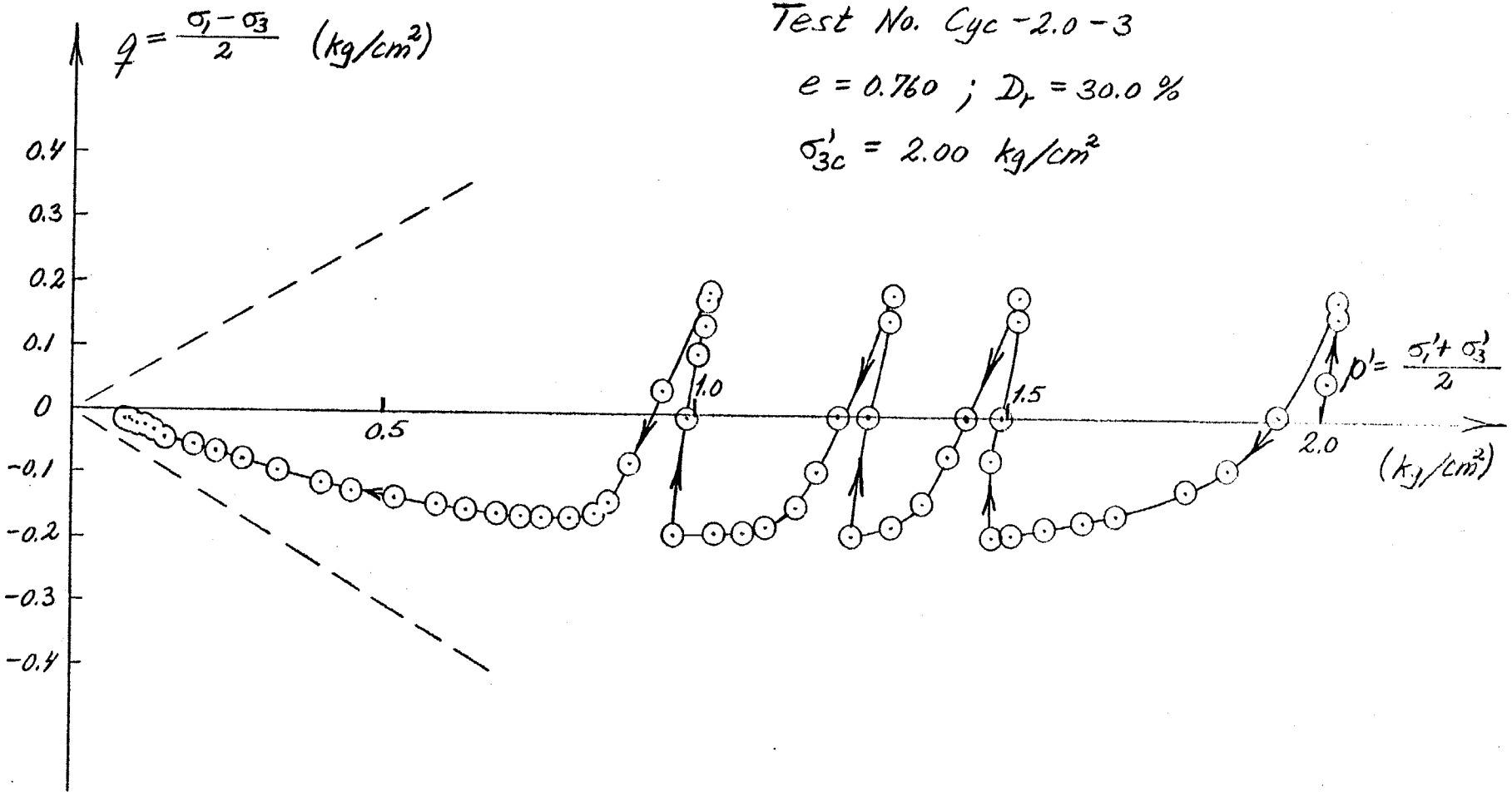

Fig. 20. Effective Stress Path From Consolidated-Undrained Cyclic Triaxial Test on Fine Silica Sand.

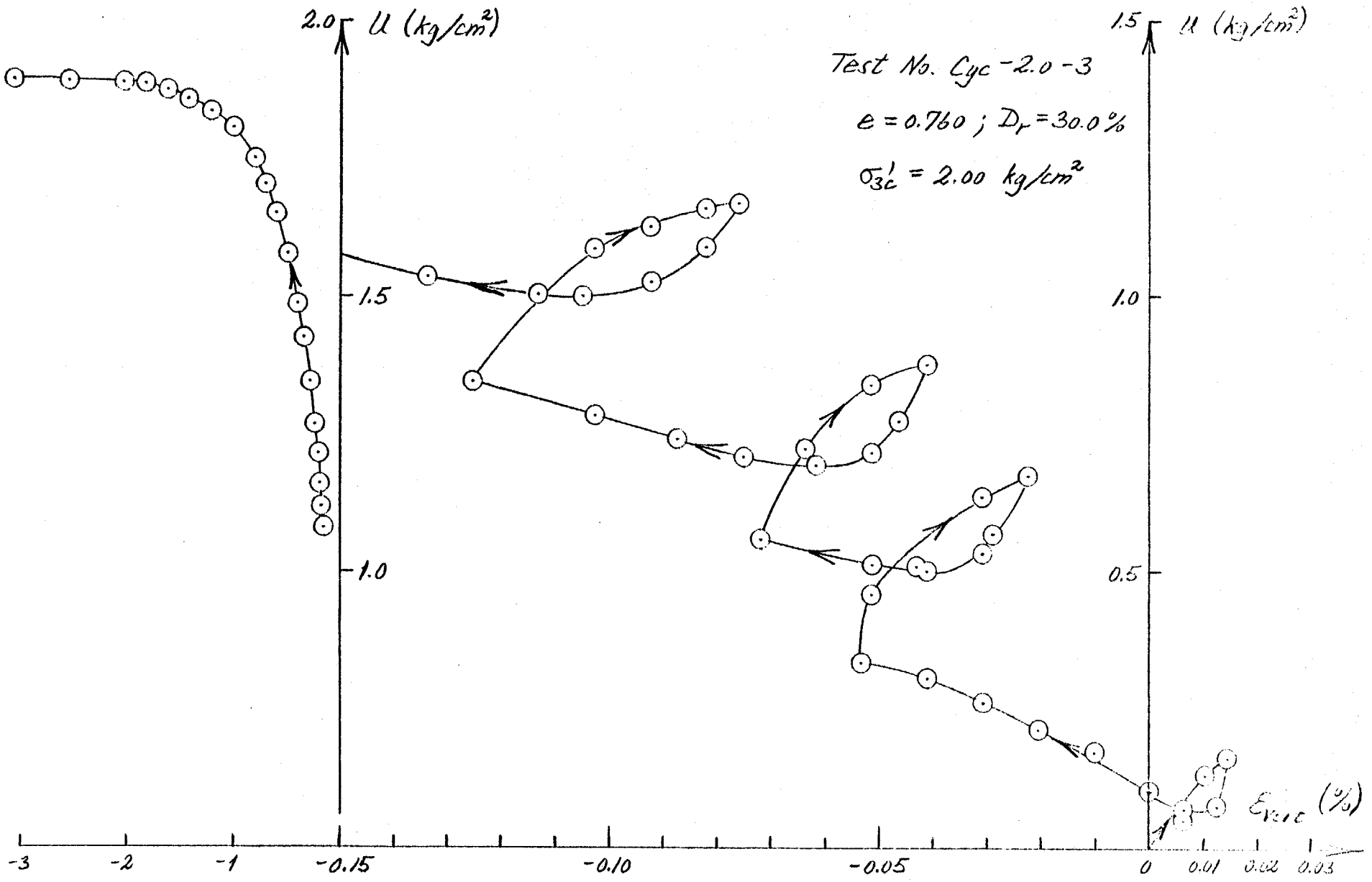

Fig. 19. Pore Water Pressure – Strain Relation From Consolidated-Undrained Cyclic Triaxial Test on Fine Silica Sand.

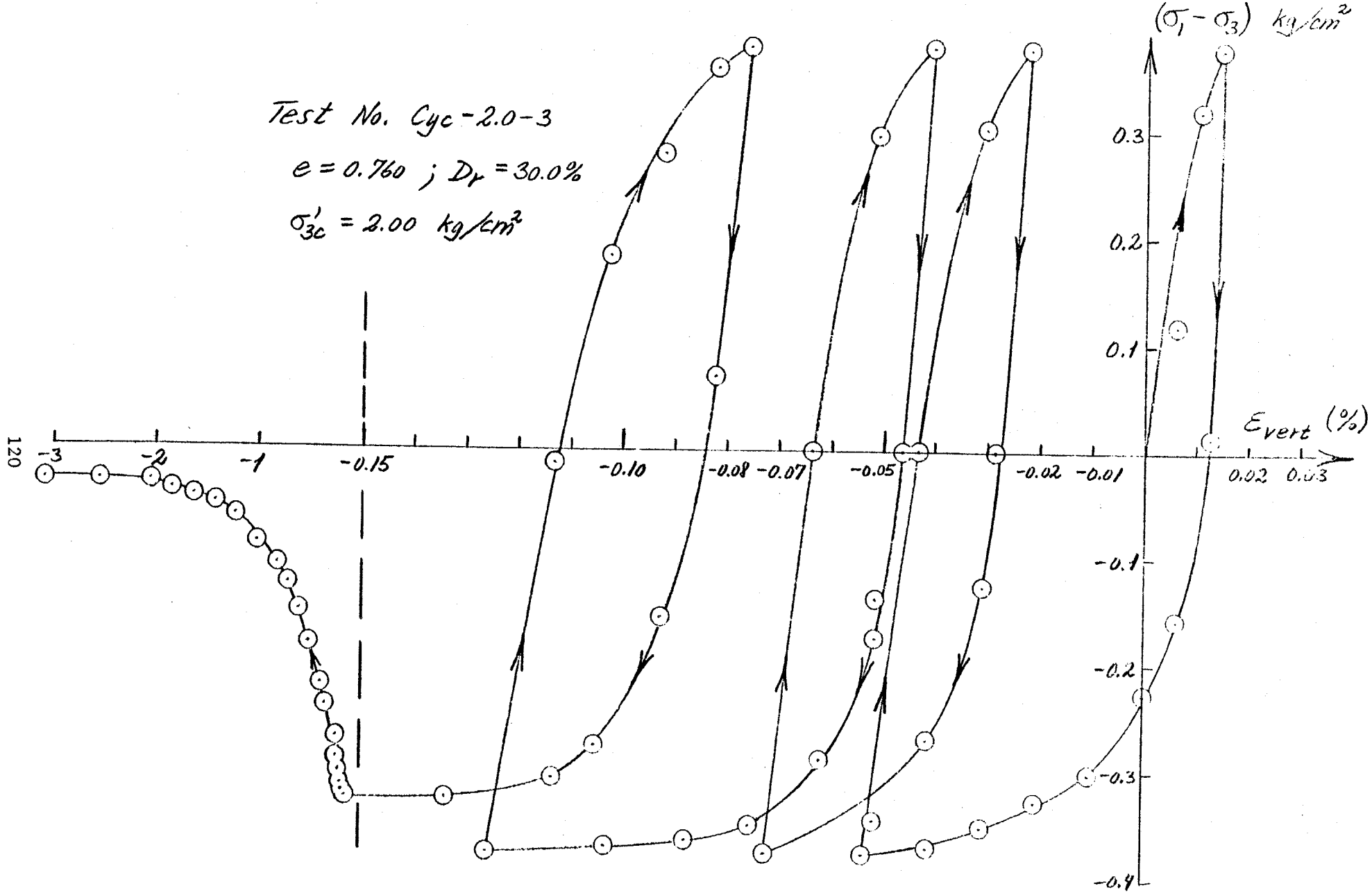

Fig. 18. Stress - Strain Relation from Consolidated - Undrained Cyclic Triaxial Test on Fine Silica Sand.

UNIVERSITY OF CALIFORNIA, LOS ANGELES
Soil Mechanics Laboratory

Test No. K_o-2 Date: March 20, [illegible]

A_o = 73.48 cm^2

H_o = 9.793 cm

V_o = 712.9 cm^3

Read No.	P Kg	$(\sigma_1-\sigma_3)$ kg/cm^2	σ_3 kg/cm^2	$K_o=\frac{\sigma_3}{\sigma_1}$	$\varepsilon_1=\varepsilon_v$ %	σ_1 kg/cm^2			
1	0.0	0.000	0.300	1.000	0.000	0.300			
2	47.7	0.649	0.738	0.532	0.252	1.387			
3	91.8	1.249	1.155	0.480	0.439	2.404			
4	157.4	2.142	2.019	0.485	0.645	4.161			
5	240.4	3.272	2.972	0.476	0.829	6.244			
6	330.3	4.496	4.013	0.472	0.992	8.509			
7	412.0	5.608	5.026	0.469	1.120	10.714			
8	509.3	6.931	6.114	0.469	1.247	13.045			
9	637.7	8.679	7.562	0.466	1.389	16.241			

Test No.	σ_3 kg/cm^2	ϕ'	$K_o=1-\sin\phi$					
CD-1.0-1	1.00	34.1°	0.439			e =	0.759	
CD-2.0-1	2.00	33.1°	0.454			γ_d =	1.512	g/cm^3
CD-2.0-2	2.00	32.8°	0.458			D_r =	30.2%	
CD-5.0-1	5.00	32.2°	0.467					

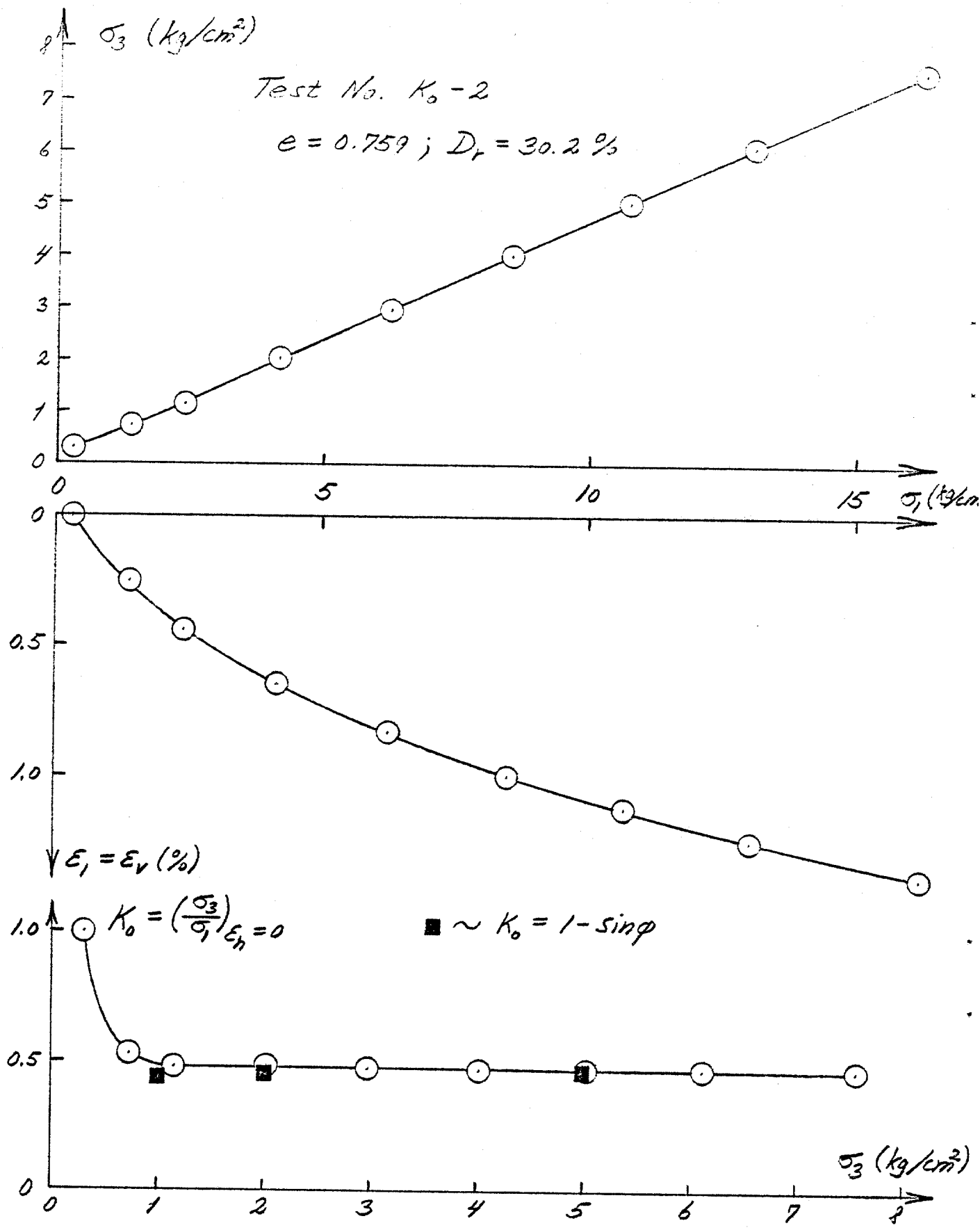

Fig. 17. Relations Between Stresses and Strains in K_o-Test on Fine Silica Sand.

Report on

Additional Tests on Fine Silica Sand

by Poul V. Lade

The tests reported below have been conducted on triaxial specimens of fine Silica Sand. These tests were performed in addition to those reported under Contract No. N62583/81 M R543. The sand, specimen preparation, test procedures, and measurement techniques employed under the present contract are the same as those reported under the previous contract.

The following additional tests were included in the present experimental program:

1 K_0 - Test

1 Consolidated - Undrained, Slow Cyclic Triaxial Test

2 Proportional Loading Tests on Triaxial Specimens

The results of these tests are presented on the following figures 17 to 21, and the test data are presented on digital form on the attached data sheets.

Additional Tests on Fine Silica Sand

by

Poul V. Lade

Report to

Department of the Navy
Civil Engineering Laboratory
Naval Construction Battalion Center
Port Hueneme, California 93043

Under Contract No. N62583/82 M R175

March, 1982

UNIVERSITY OF CALIFORNIA, LOS ANGELES
Soil Mechanics Laboratory

Test No. Cyc -2.0-2 Date: Nov. 22, 1981

Read No.	δ_1 mm	Evert %	A cm^2	P kg	$(\sigma_1-\sigma_3)$ kg/cm^2	u kg/cm^2	σ_3' kg/cm^2	σ_1'/σ_3'	$\frac{\sigma_1-\sigma_3}{2}$ kg/cm^2	$\frac{\sigma_1'+\sigma}{2}$ kg/cm
94	-0.70	-0.7205	72.65	-11.0	-0.152	1.702	0.298	2.043	-0.076	0.22
96	-1.00	-1.0293	72.42	-7.8	-0.108	1.789	0.211	2.056	-0.054	0.157
98	-1.40	-1.4411	72.13	-5.5	-0.076	1.848	0.152	2.001	-0.038	0.11
100	-1.80	-1.8528	71.84	-4.1	-0.057	1.878	0.122	1.877	-0.029	0.09
103	-3.00	-3.0880	70.98	-3.7	-0.052	1.895	0.105	1.982	-0.026	0.07

UNIVERSITY OF CALIFORNIA, LOS ANGELES
Soil Mechanics Laboratory

Test No. Cyc-2.0-2 Date: Nov. 22, 1981

	Read No.	δ_l mm	Evert %	A cm^2	P kg	$(\sigma_1-\sigma_3)$ kg/cm^2	u kg/cm^2	σ_3' kg/cm^2	σ_1'/σ_3'	$\frac{\sigma_1-\sigma_3}{2}$ kg/cm^2	$\frac{\sigma_1'+\sigma_3'}{2}$ kg/cm^2
Extension	67	-0.12	-0.1235	73.08	-27.1	-0.370	0.899	1.101	1.506	-0.185	0.91
	68	-0.138	-0.1420	73.07	-27.5	-0.377	0.931	1.069	1.544	-0.189	0.88
	69	-0.12	-0.1235	73.08	-11.0	-0.151	1.021	0.979	1.183	-0.076	0.90
Compression	70	-0.11	-0.1132	73.09	-2.3	-0.031	1.062	0.938	1.034	-0.016	0.923
	71	-0.10	-0.1029	73.09	7.8	0.107	1.103	0.897	1.119	0.054	0.95
	72	-0.09	-0.0926	73.10	14.7	0.201	1.140	0.860	1.234	0.101	0.96
	73	-0.08	-0.0823	73.11	19.7	0.270	1.166	0.834	1.324	0.135	0.96
	74	-0.07	-0.0721	73.12	24.8	0.339	1.189	0.811	1.418	0.170	0.98
	75	-0.061	-0.0628	73.12	27.5	0.376	1.207	0.793	1.474	0.188	0.98
	76	-0.07	-0.0721	73.12	17.0	0.232	1.169	0.831	1.279	0.116	0.94
	77	-0.08	-0.0823	73.11	6.0	0.082	1.135	0.865	1.094	0.041	0.90
	78	-0.09	-0.0926	73.10	-3.2	-0.044	1.105	0.895	1.052	-0.022	0.87
	79	-0.10	-0.1029	73.09	-10.1	-0.138	1.082	0.918	1.176	-0.069	0.84
Extension	80	-0.11	-0.1132	73.09	-16.1	-0.220	1.062	0.938	1.306	-0.110	0.82
	81	-0.12	-0.1235	73.08	-21.1	-0.289	1.050	0.950	1.437	-0.145	0.80
	82	-0.13	-0.1338	73.07	-23.4	-0.320	1.053	0.947	1.511	-0.160	0.78
	83	-0.14	-0.1441	73.06	-24.3	-0.333	1.065	0.935	1.553	-0.167	0.76
	84	-0.15	-0.1544	73.06	-24.8	-0.339	1.075	0.925	1.578	-0.170	0.75
	86	-0.17	-0.1750	73.04	-24.8	-0.339	1.108	0.892	1.614	-0.170	0.72
	88	-0.20	-0.2059	73.02	-24.3	-0.333	1.174	0.826	1.675	-0.167	0.66
	90	-0.30	-0.3088	72.94	-21.1	-0.289	1.357	0.643	1.815	-0.145	0.49
	92	-0.50	-0.5147	72.80	-15.1	-0.208	1.576	0.424	1.963	-0.104	0.32

UNIVERSITY OF CALIFORNIA, LOS ANGELES
Soil Mechanics Laboratory

Test No. Cyc-2.0-2 Date: Nov. 22, 1981

	Read No.	δ_l mm	Evert %	A cm^2	P Kg	$\sigma_1-\sigma_3$ Kg/cm^2	u Kg/cm^2	σ_3' Kg/cm^2	σ_1'/σ_3'	$\frac{\sigma_1-\sigma_3}{2}$ Kg/cm^2	$\frac{\sigma_1'+\sigma_3'}{2}$ Kg/cm^2
Compression	45	-0.03	-0.0309	73.15	25.7	0.351	0.879	1.121	1.313	0.176	1.297
	46	-0.027	-0.0278	73.15	27.5	0.376	0.885	1.115	1.337	0.188	1.303
	47	-0.04	-0.0412	73.14	9.2	0.125	0.827	1.173	1.107	0.063	1.236
	48	-0.05	-0.0515	73.13	0.0	0.000	0.793	1.207	1.000	0.000	1.207
Extension	49	-0.06	-0.0618	73.12	-9.6	-0.132	0.761	1.239	1.120	-0.066	1.173
	50	-0.07	-0.0721	73.12	-16.5	-0.226	0.735	1.265	1.217	-0.113	1.152
	51	-0.08	-0.0823	73.11	-23.4	-0.320	0.719	1.281	1.334	-0.160	1.121
	52	-0.09	-0.0926	73.10	-26.6	-0.364	0.736	1.264	1.405	-0.182	1.082
	53	-0.10	-0.1029	73.09	-27.5	-0.377	0.760	1.240	1.436	-0.189	1.052
	54	-0.09	-0.0926	73.10	-14.2	-0.196	0.825	1.175	1.200	-0.098	1.077
Compression	55	-0.08	-0.0823	73.11	-3.2	-0.044	0.875	1.125	1.041	-0.022	1.103
	56	-0.07	-0.0721	73.12	6.9	0.094	0.919	1.081	1.087	0.047	1.128
	57	-0.06	-0.0618	73.12	15.1	0.207	0.956	1.044	1.198	0.104	1.148
	58	-0.05	-0.0515	73.13	21.6	0.295	0.986	1.014	1.291	0.148	1.162
	59	-0.039	-0.0401	73.14	27.5	0.376	1.015	0.985	1.382	0.188	1.173
	60	-0.05	-0.0515	73.13	11.0	0.151	0.961	1.039	1.145	0.076	1.115
	61	-0.06	-0.0618	73.12	0.9	0.013	0.929	1.071	1.012	0.007	1.078
Extension	62	-0.07	-0.0721	73.12	-6.9	-0.094	0.899	1.101	1.093	-0.047	1.054
	63	-0.08	-0.0823	73.11	-14.7	-0.201	0.875	1.125	1.218	-0.101	1.025
	64	-0.09	-0.0926	73.10	-20.6	-0.282	0.855	1.145	1.327	-0.141	1.004
	65	-0.10	-0.1029	73.09	-24.3	-0.333	0.852	1.148	1.409	-0.167	0.982
	66	-0.11	-0.1132	73.09	-26.6	-0.364	0.874	1.126	1.477	-0.182	0.944

UNIVERSITY OF CALIFORNIA, LOS ANGELES
Soil Mechanics Laboratory

Test No. Cyc-2.0-2 Date: Nov. 22, 1981

	Read No.	δ_l mm	Event %	A cm^2	P Kg	$(\sigma_1-\sigma_3)$ Kg/cm²	u Kg/cm²	σ_3' Kg/cm²	σ_1'/σ_3'	$\frac{\sigma_1-\sigma_3}{2}$ Kg/cm²	$\frac{\sigma_1'+\sigma_3'}{2}$ Kg/cm²
Extension	23	-0.04	-0.0412	73.14	-11.0	-0.151	0.481	1.519	1.111	-0.076	1.445
	24	-0.05	-0.0515	73.13	-17.4	-0.238	0.459	1.541	1.183	-0.119	1.423
	25	-0.06	-0.0618	73.12	-23.9	-0.326	0.454	1.546	1.268	-0.163	1.383
	26	-0.07	-0.0721	73.12	-26.6	-0.364	0.473	1.527	1.313	-0.182	1.345
	27	-0.078	-0.0803	73.11	-27.5	-0.377	0.493	1.507	1.334	-0.189	1.319
Compression	28	-0.06	-0.0618	73.12	-9.2	-0.125	0.592	1.408	1.097	-0.063	1.346
	29	-0.05	-0.0515	73.13	0.5	0.006	0.634	1.366	1.004	0.003	1.369
	30	-0.04	-0.0412	73.14	10.6	0.144	0.672	1.328	1.108	0.072	1.400
	31	-0.03	-0.0309	73.15	18.8	0.257	0.716	1.284	1.200	0.129	1.413
	32	-0.02	-0.0206	73.15	25.7	0.351	0.753	1.247	1.281	0.176	1.423
	33	-0.016	-0.0165	73.16	27.5	0.376	0.763	1.237	1.304	0.188	1.425
	34	-0.03	-0.0309	73.15	10.6	0.144	0.703	1.297	1.111	0.072	1.369
Extension	35	-0.04	-0.0412	73.14	-0.9	-0.013	0.666	1.334	1.010	-0.007	1.328
	36	-0.05	-0.0515	73.13	-10.1	-0.138	0.636	1.364	1.112	-0.069	1.295
	37	-0.06	-0.0618	73.12	-17.9	-0.245	0.607	1.393	1.213	-0.123	1.271
	38	-0.07	-0.0721	73.12	-24.8	-0.339	0.599	1.401	1.319	-0.170	1.232
	39	-0.088	-0.0906	73.10	-27.5	-0.377	0.626	1.374	1.377	-0.189	1.186
Compression	40	-0.08	-0.0823	73.11	-19.3	-0.264	0.679	1.321	1.250	-0.132	1.189
	41	-0.07	-0.0721	73.12	-9.6	-0.132	0.721	1.279	1.115	-0.066	1.213
	42	-0.06	-0.0618	73.12	2.3	0.031	0.770	1.230	1.025	0.016	1.246
	43	-0.05	-0.0515	73.13	12.4	0.169	0.808	1.192	1.142	0.085	1.277
	44	-0.04	-0.0412	73.14	19.7	0.270	0.847	1.153	1.234	0.135	1.288

UNIVERSITY OF CALIFORNIA, LOS ANGELES
Soil Mechanics Laboratory

Test No. Cyc-2.0-2 Date: Nov. 22, 1981

H_c = 9.715 cm Silica Sand, -#60 Sieve

A_c = 73.17 cm^2

σ_{3c} = 2.000 kg/cm^2 $A = A_c/(1-\varepsilon_{vert})$

	Read No.	d_l mm	ε_{vert} %	A cm^2	P kg	$(\sigma_1-\sigma_3)$ kg/cm^2	u kg/cm^2	σ_3' kg/cm^2	σ_1'/σ_3'	$\frac{\sigma_1-\sigma_3}{2}$ kg/cm^2	$\frac{\sigma_1'+\sigma_3'}{2}$ kg/cm^2
Compression	1	0.00	0.0000	73.17	0.0	0.000	0.000	2.000	1.000	0.000	2.000
	2	0.02	0.0206	73.19	21.6	0.295	0.117	1.883	1.156	0.148	2.031
	3	0.029	0.0299	73.19	27.5	0.376	0.164	1.836	1.205	0.188	2.021
	4	0.02	0.0206	73.19	17.0	0.232	0.131	1.869	1.124	0.116	1.985
	5	0.01	0.0103	73.18	3.2	0.044	0.094	1.906	1.023	0.022	1.928
	6	0.00	0.0000	73.17	-4.1	-0.056	0.084	1.916	1.030	-0.028	1.888
Extension	7	-0.01	-0.0103	73.16	-11.5	-0.157	0.086	1.914	1.089	-0.079	1.836
	8	-0.02	-0.0206	73.15	-16.5	-0.226	0.114	1.886	1.136	-0.113	1.773
	9	-0.03	-0.0309	73.15	-19.7	-0.270	0.146	1.854	1.170	-0.135	1.719
	10	-0.04	-0.0412	73.14	-23.4	-0.320	0.183	1.817	1.214	-0.160	1.657
	11	-0.05	-0.0515	73.13	-25.2	-0.345	0.235	1.765	1.243	-0.173	1.593
	12	-0.06	-0.0618	73.12	-27.1	-0.370	0.285	1.715	1.275	-0.185	1.530
	13	-0.068	-0.0700	73.12	-27.5	-0.376	0.312	1.688	1.287	-0.188	1.500
	14	-0.05	-0.0515	73.13	-10.1	-0.138	0.419	1.581	1.096	-0.069	1.512
Compression	15	-0.04	-0.0412	73.14	-0.5	-0.006	0.459	1.541	1.004	-0.003	1.538
	16	-0.03	-0.0309	73.15	9.2	0.125	0.510	1.490	1.084	0.063	1.553
	17	-0.02	-0.0206	73.15	18.8	0.257	0.550	1.450	1.177	0.129	1.579
	18	-0.01	-0.0103	73.16	24.8	0.339	0.589	1.411	1.240	0.170	1.581
	19	-0.003	-0.0031	73.17	27.5	0.376	0.607	1.393	1.270	0.188	1.581
Extension	20	-0.01	-0.0103	73.16	18.4	0.251	0.574	1.426	1.151	0.126	1.552
	21	-0.02	-0.0206	73.15	6.0	0.082	0.537	1.463	1.056	0.041	1.504
	22	-0.03	-0.0309	73.15	-1.8	-0.025	0.510	1.490	1.017	-0.013	1.478

e = 0.764 ; γ_d = 1.508 g/cm^3 ; D_r = 28.7%

UNIVERSITY OF CALIFORNIA, LOS ANGELES
Soil Mechanics Laboratory

Test No. K_o - 1 Date: Nov. 17, 1981

A_o = 73.36 cm^2 Silica Sand, - #60 sieve

H_o = 9.728 cm

V_o = 713.6 cm^3

Read No.	P Kg	$(\sigma_1 - \sigma_3)$ kg/cm^2	σ_3 kg/cm^2	σ_1 kg/cm^2	$K_o = \frac{\sigma_3}{\sigma_1}$	δ_1 mm	ε_1 %	ΔV cm^3	ε_v %
1	0.0	0.000	0.300	0.300	1.000	0.00	0.000	0.000	0.000
2	34.4	0.469	0.599	1.068	0.561	0.15	0.154	1.369	0.192
3	62.4	0.851	0.849	1.700	0.500	0.30	0.308	2.335	0.327
4	125.7	1.714	1.583	3.297	0.480	0.50	0.514	4.060	0.569
5	185.4	2.527	2.289	4.816	0.475	0.63	0.648	5.210	0.730
6	256.0	3.490	3.222	6.712	0.480	0.76	0.781	6.348	0.890
7	351.0	4.784	4.226	9.010	0.469	0.91	0.935	7.487	1.049
8	433.1	5.904	5.190	11.094	0.468	1.01	1.038	8.326	1.167
9	504.2	6.873	6.084	12.957	0.470	1.09	1.120	8.982	1.259
10	614.8	8.380	7.411	15.791	0.469	1.20	1.234	9.890	1.386
11	210.1	2.864	6.071	8.935	0.679	1.13?		9.384	1.315
12	82.1	1.119	4.558	5.677	0.803	1.11?		8.821	1.236
13	10.6	0.144	3.525	3.669	0.961	1.09?		8.372	1.173
14	0.0	0.000	2.816	2.816	1.000	1.16?		8.062	1.130

Test No.	σ_3' kg/cm^2	ϕ'	$K_o = 1 - \sin\phi$
CD-1.0-1	1.00	34.1	0.439
CD-2.0-1	2.00	33.1	0.454
CD-2.0-2	2.00	32.8	0.458
CD-5.0-1	5.00	32.2	0.467

e = 0.760

γ_d = 1.511 g/cm^3

D_r = 30.0 %

UNIVERSITY OF CALIFORNIA, LOS ANGELES
Soil Mechanics Laboratory

Test No. CU-2.0-3 Date: Nov. 1, 1981

H_c = 9.664 cm — Silica Sand, - #60 sieve

A_c = 73.16 cm^2 — $\phi' = \text{Arcsin}\frac{3.295-1}{3.295+1} = 32.3$

σ_{3c} = 2.000 kg/cm^2 — $A = A_o/(1-\varepsilon_1)$

Read No.	δ_1 mm	ε_1 %	A cm^2	P Kg	$(\sigma_1-\sigma_3)$ kg/cm^2	u kg/cm^2	σ_3' kg/cm^2	σ_1'/σ_3'	$\frac{\sigma_1-\sigma_3}{2}$ kg/cm^2	$\frac{\sigma_1'+\sigma_3'}{2}$ kg/cm^2
1	0.00	0.000	73.16	0.0	0.000	0.000	2.000	1.000	0.000	2.00
2	0.05	0.052	73.20	31.2	0.426	0.213	1.787	1.238	0.213	2.00
4	0.15	0.155	73.27	63.3	0.864	0.525	1.475	1.586	0.432	1.90
7	0.30	0.310	73.39	80.7	1.100	0.830	1.170	1.940	0.550	1.72
13	0.60	0.621	73.62	84.0	1.140	1.186	0.814	2.400	0.570	1.38
* 18	1.20	1.242	74.08	81.2	1.096	1.399	0.601	2.824	0.548	1.14
22	2.00	2.070	74.71	86.7	1.161	1.437	0.563	3.062	0.581	1.14
26	4.00	4.139	76.32	116.1	1.521	1.325	0.675	3.253	0.761	1.43
29	6.00	6.209	78.00	155.1	1.988	1.130	0.870	3.285	0.994	1.86
31	8.00	8.278	79.76	218.4	2.738	0.807	1.193	3.295	1.369	2.56
34	11.00	11.382	82.56	347.3	4.207	0.158	1.842	3.284	2.104	3.94
37	14.00	14.487	85.55	521.7	6.098	-0.704	2.704	3.255	3.049	5.75
40	17.00	17.591	88.78	753.8	8.491	-1.806	3.806	3.231	4.246	8.05
43	20.00	20.695	92.25	1017.2	11.026	-3.030	5.030	3.192	5.513	10.54
46	23.00	23.800	96.01	1314.9	13.696	-4.360	6.360	3.153	6.848	13.20
48	25.00	25.869	98.69	1377.3	13.956	-4.528	6.528	3.138	6.978	13.5
50	27.00	27.939	101.52	1408.1	13.870	-4.568	6.568	3.112	6.935	13.5
52	29.00	30.008	104.53	1429.6	13.677	-4.595	6.595	3.074	6.839	13.4
54	31.00	32.078	107.71	1448.0	13.443	-4.612	6.612	3.033	6.722	13.33
56	33.00	34.147	111.10	1464.5	13.182	-4.622	6.622	2.991	6.591	13.21
		e =	0.757;	γ_d = 1.514 g/cm³;			D_r =	31.1%		

UNIVERSITY OF CALIFORNIA, LOS ANGELES
Soil Mechanics Laboratory

Test No. CU-2.0-2 Date: Oct. 23, 1981

H_c = 9.692 cm Silica Sand, −#60 Sieve

A_c = 73.30 cm^2 $\phi' = \text{Arcsin}\frac{3.323-1}{3.323+1} = 32.5°$

σ_{3c} = 2.000 kg/cm^2 $A = A_0/(1-\varepsilon_1)$

Read No.	δ_1 mm	ε_1 %	A cm^2	P Kg	$(\sigma_1-\sigma_3)$ kg/cm^2	u kg/cm^2	σ_3' kg/cm^2	σ_1'/σ_3'	$\frac{\sigma_1-\sigma_3}{2}$ kg/cm^2	$\frac{\sigma_1'+\sigma_3'}{2}$ kg/cm
1	0.00	0.000	73.30	0.0	0.000	0.000	2.000	1.000	0.000	2.00
2	0.06	0.062	73.35	37.6	0.513	0.248	1.752	1.293	0.257	2.00
4	0.17	0.175	73.43	64.7	0.881	0.535	1.465	1.601	0.441	1.90
7	0.30	0.310	73.53	83.5	1.136	0.802	1.198	1.948	0.568	1.76
13	0.60	0.619	73.76	87.2	1.182	1.147	0.853	2.386	0.591	1.44
19	1.20	1.238	74.23	83.5	1.125	1.378	0.622	2.809	0.563	1.18
24	2.00	2.064	74.86	85.8	1.146	1.442	0.558	3.053	0.573	1.13
34	4.00	4.127	76.49	108.3	1.416	1.375	0.625	3.266	0.708	1.33
44	6.00	6.191	78.19	139.0	1.778	1.229	0.771	3.306	0.889	1.66
51	8.10	8.357	80.06	189.5	2.367	0.981	1.019	3.323	1.184	2.20
57	11.00	11.350	82.79	287.7	3.475	0.501	1.499	3.318	1.738	3.23
63	14.00	14.445	85.82	421.6	4.913	-0.143	2.143	3.293	2.457	4.60
69	17.00	17.540	89.08	598.7	6.721	-0.976	2.976	3.258	3.361	6.33
75	20.00	20.636	92.60	817.6	8.829	-1.970	3.970	3.224	4.415	8.38
81	23.00	23.731	96.41	1075.0	11.150	-3.121	5.121	3.177	5.575	10.69
85	25.00	25.794	99.12	1249.3	12.604	-3.894	5.894	3.138	6.302	12.19
89	27.00	27.858	102.00	1397.5	13.701	-4.504	6.504	3.107	6.851	13.35
93	29.00	29.922	105.05	1414.9	13.469	-4.508	6.508	3.070	6.735	13.24
97	31.00	31.985	108.28	1431.9	13.224	-4.520	6.520	3.028	6.612	13.13
101	33.00	34.049	111.72	1448.4	12.965	-4.526	6.526	2.987	6.483	13.00
		e = 0.764 ;		γ_d =	1.508 g/cm^3 ;		D_r =	28.7%		

UNIVERSITY OF CALIFORNIA, LOS ANGELES
Soil Mechanics Laboratory

Test No. CDE-2.0-2 Date: Nov. 20, 1981

H_c = 9.689 cm — Silica Sand, -#60 Sieve

A_c = 73.08 cm^2 — $\varphi' = \text{Arcsin}\frac{3.843-1}{3.843+1} = 35.9°$

$\sigma_1' = 2.000\ kg/cm^2$ — $A = A_c \cdot \frac{1-\varepsilon_v}{1-\varepsilon_3}$; $\varepsilon_1 = \frac{1}{2}\cdot(\varepsilon_v - \varepsilon_3)$

Read No.	δ_3 mm	ε_3 %	ΔV cm^3	ε_v %	A cm^2	P kg	$\sigma_1-\sigma_3$ kg/cm^2	σ_1'/σ_3'	ε_1 %
1	0.00	0.000	0.000	0.000	73.08	0.0	0.000	1.000	0.000
3	0.05	-0.052	0.069	0.010	73.04	33.0	0.452	1.292	0.031
5	0.15	-0.155	0.541	0.076	72.91	45.9	0.629	1.459	0.116
8	0.30	-0.310	1.311	0.185	72.72	58.3	0.801	1.668	0.248
11	0.63	-0.650	2.553	0.361	72.35	69.3	0.958	1.919	0.505
16	1.20	-1.239	4.048	0.572	71.77	79.4	1.106	2.237	0.905
21	2.40	-2.477	6.026	0.851	70.71	88.5	1.252	2.675	1.664
26	4.50	-4.644	7.372	1.041	69.11	94.5	1.368	3.162	2.843
31	7.00	-7.225	7.349	1.038	67.45	96.8	1.435	3.541	4.131
35	9.00	-9.289	6.636	0.937	66.24	97.3	1.468	3.762	5.113
38	11.00	-11.353	5.555	0.784	65.12	96.3	1.480	3.843	6.069
40	13.00	-13.417	4.278	0.604	64.05	94.5	1.476	3.814	7.011
42	15.00	-15.481	2.933	0.414	63.02	92.2	1.463	3.727	7.948
44	17.00	-17.546	1.599	0.226	62.03	89.0	1.435	3.539	8.886
46	19.00	-19.610	0.472	0.067	61.06	85.8	1.405	3.362	9.838
48	21.00	-21.674	-0.207	-0.029	60.08	81.7	1.359	3.122	10.822
50	23.00	-23.738	-0.725	-0.102	59.12	76.6	1.296	2.841	11.507
52	25.00	-25.802	-1.012	-0.143	58.17	72.9	1.254	2.681	12.395
		e = 0.757;		γ_d = 1.514 g/cm^3; D_r = 31.1 %					

σ_3 = 0.52 kg/cm

UNIVERSITY OF CALIFORNIA, LOS ANGELES
Soil Mechanics Laboratory

Test No. CDE-2.0-1 Date: Nov. 19, 1981

H_c = 9.717 cm — Silica Sand, - #60 Sieve

A_c = 73.08 cm^2 — $\varphi' = \text{Arcsin}\frac{4.0\%_0 - 1}{4.0\%_0 + 1} = 37.1°$

σ_1' = 2.000 kg/cm^2 — $A = A_c \cdot \frac{1-\varepsilon_v}{1-\varepsilon_3}$; $\varepsilon_1 = \frac{1}{2}\cdot(\varepsilon_v - \varepsilon_3)$

Read No.	δ_3 mm	ε_3 %	ΔV cm^3	ε_v %	A cm^2	P kg	$\sigma_1-\sigma_3$ kg/cm^2	σ_1'/σ_3'	ε_1 %
1	0.00	0.000	0.000	0.000	73.08	0.0	0.000	1.000	0.000
3	0.05	-0.051	0.023	0.003	73.04	21.6	0.295	1.173	0.027
6	0.20	-0.206	0.840	0.118	72.84	44.0	0.605	1.433	0.162
11	0.60	-0.617	2.542	0.358	72.37	64.2	0.888	1.798	0.488
16	1.20	-1.235	4.336	0.611	71.75	76.6	1.068	2.146	0.923
22	2.40	-2.470	6.544	0.921	70.66	87.6	1.240	2.632	1.696
32	4.40	-4.528	8.119	1.143	69.12	94.5	1.367	3.161	2.836
42	7.00	-7.204	8.257	1.163	67.38	97.7	1.450	3.639	4.184
46	9.00	-9.262	7.533	1.061	66.18	98.2	1.484	3.873	5.162
50	11.00	-11.320	6.302	0.887	65.07	97.7	1.502	4.015	6.104
54	13.00	-13.379	4.853	0.683	64.02	96.3	1.505	4.040	7.031
56	15.00	-15.437	3.324	0.468	63.01	94.1	1.493	3.942	7.953
58	17.00	-17.495	1.771	0.249	62.04	91.8	1.479	3.839	8.872
60	19.00	-19.553	0.322	0.045	61.10	88.5	1.449	3.631	9.799
62	21.00	-21.612	-0.644	-0.091	60.15	84.4	1.403	3.353	10.761
64	23.00	-23.670	-1.208	-0.170	59.19	80.7	1.364	3.146	11.750
66	25.00	-25.728	-1.610	-0.227	58.26	76.6	1.315	2.920	12.751
68	27.00	-27.786	-1.932	-0.272	57.35	72.5	1.264	2.717	13.757
		e = 0.763 ;	γ_d =	1.509 g/cm^3 ;	D_r =	28.9%			

σ_3 = 0.49 kg/cm^2

UNIVERSITY OF CALIFORNIA, LOS ANGELES
Soil Mechanics Laboratory

Test No. CD-5.0-1 Date: Oct. 27, 1981

H_c = 9.679 cm Silica Sand, − # 60 sieve

A_c = 72.77 cm^2 $\varphi' = \text{Arcsin}\frac{3.285-1}{3.285+1} = 32.2°$

σ_3' = 5.000 kg/cm^2 $A = A_o \cdot \frac{1-\varepsilon_v}{1-\varepsilon_1}$

Read No.	δ_1 mm	ε_1 %	ΔV cm^3	ε_v %	A cm^2	P kg	$\sigma_1-\sigma_3$ kg/cm^2	σ_1'/σ_3	
1	0.00	0.000	0.000	0.000	72.77	0.0	0.000	1.000	
4	0.15	0.155	0.391	0.056	72.84	116.5	1.600	1.320	
7	0.40	0.413	1.150	0.163	72.95	256.9	3.522	1.704	
11	0.80	0.827	2.220	0.315	73.15	401.0	5.482	2.096	
15	1.60	1.653	3.588	0.509	73.62	548.3	7.447	2.489	
18	2.50	2.583	4.405	0.625	74.23	636.4	8.573	2.715	
21	4.00	4.133	4.957	0.704	75.37	722.2	9.581	2.916	
25	6.00	6.199	4.945	0.702	77.04	796.0	10.333	3.067	
28	8.00	8.265	4.485	0.637	78.82	858.0	10.885	3.177	
31	11.00	11.365	3.255	0.462	81.72	920.8	11.268	3.254	
34	14.00	14.464	1.771	0.251	84.86	969.4	11.424	3.285	
37	17.00	17.564	0.265	0.038	88.24	1008.0	11.423	3.285	
40	20.00	20.663	-1.242	-0.176	91.88	1041.0	11.330	3.266	
43	23.00	23.763	-2.714	-0.385	95.82	1071.3	11.180	3.236	
46	26.00	26.862	-4.129	-0.586	100.080	1094.7	10.938	3.188	
↓ 48	25.90	26.759	-4.129	-0.586	99.939	774.9	7.754		
52	25.70	26.552	-3.381	-0.480	99.552	311.5	3.129		
56	25.50	26.346	-1.840	-0.261	99.058	126.6	1.278		
60	25.30	26.139	-0.161	-0.023	98.546	34.9	0.354		
63	25.16	25.994	+1.139	+0.162	98.171	0.0	0.000		
↑ 65	25.25	26.087	+1.323	+0.188	98.268	165.2	1.681		
69	25.60	26.449	+1.783	+0.253	98.688	655.6	6.643		

$e = 0.758$; $\gamma_d = 1.513\ g/cm^3$; $D_r = 30.6\%$

CONSTITUTIVE EQUATIONS

The constitutive equations for the solid skeleton are written in one of the following forms:

$$\underset{\sim}{C} : \overset{\bullet}{\underset{\sim}{\varepsilon}} = \begin{cases} \overset{\bullet}{\underset{\sim}{\sigma}}' & \text{small deformations} \\ \overset{\nabla}{\underset{\sim}{\sigma}}' + \underset{\sim}{\sigma}' \operatorname{div} \underset{\sim}{v} & \text{finite deformations} \end{cases} \tag{1}$$

in which $\underset{\sim}{\sigma}'$ = effective (Cauchy) stress tensor; $\underset{\sim}{v}$ = (spatial) velocity of solid phase; $\overset{\bullet}{\underset{\sim}{\varepsilon}}$ = rate of deformation tensor for the solid phase (= symmetric part of the spatial solid velocity gradient); a dot denotes the material derivative; and $\overset{\nabla}{\underset{\sim}{\sigma}}'$ = Jaumann derivative [5], viz.

$$\overset{\nabla}{\underset{\sim}{\sigma}}' = \overset{\bullet}{\underset{\sim}{\sigma}}' + \underset{\sim}{\sigma}' \cdot \underset{\sim}{w} - \underset{\sim}{w} \cdot \underset{\sim}{\sigma}' \tag{2}$$

where $\underset{\sim}{w}$ = spin tensor for the solid phase (= skew-symmetric part of the spatial solid velocity gradient). In Eq. 1, C_{abcd} is an (objective) tensor valued function of, possibly, $\underset{\sim}{\sigma}'$ and the solid deformation gradients. Many nonlinear material models of interest can be put in the above form (e.g., <u>all</u> nonlinear elastic materials, and many elasto-plastic materials). The finite deformation form of the constitutitve equation above was first proposed by Hill [1] within the context of plasticity theory.

For soil media, the form of the $\underset{\sim}{C}$ tensor is given as follows [10],

$$\underset{\sim}{C} = \underset{\sim}{E} - \frac{(\underset{\sim}{E}:\underset{\sim}{P})\ (\underset{\sim}{Q}:\underset{\sim}{E})}{H' + \underset{\sim}{Q}:\underset{\sim}{E}:\underset{\sim}{P}} \tag{3}$$

As for notation, boldface letters denote vectors, second and fourth-order tensors in three-dimensions. All stresses are effective stresses [24].

CONSTITUTIVE EQUATIONS FOR PRESSURE SENSITIVE SOILS: THEORY, NUMERICAL IMPLEMENTATION, AND EXAMPLES

Jean H. Prevost[1]

INTRODUCTION

Soil consists of an assemblage of particles with different sizes and shapes which form a skeleton whose voids are filled with various fluids. The stresses carried by the soil skeleton are conventionally termed "effective stresses" [24] in the soil mechanics literature, and those in the fluids are called "pore-fluid pressures". It is observed experimentally that the stress-strain behavior of the soil skeleton is strongly nonlinear, anisotropic and hysteretic. In order to relate the changes in effective stresses carried by the soil skeleton to the skeleton rate of deformation, a general analytical model which describes the nonlinear, anisotropic, elastoplastic, path-dependent, stress-strain-strength properties of the soil skeleton when subjected to complicated three-dimensional, and in particular to cyclic loading paths [8] is presented. A brief summary of the model's basic principles [10] is included and the constitutive equations are provided. It is shown that the model parameters required to characterize the behavior of any given soil can be derived entirely from the results of conventional soil tests. The model's accuracy is evaluated by applying it to represent the behavior of both cohesive and cohesionless soils. Implementation of the proposed formulation in a general finite element program for solution of boundary value problems is discussed.

(1) Associate Professor, Department of Civil Engineering, Princeton University, Princeton, NJ 08544

CONSTITUTIVE EQUATIONS FOR PRESSURE SENSITIVE SOILS: THEORY, NUMERICAL IMPLEMENTATION, AND EXAMPLES

Jean H. Prevost[1]

ABSTRACT

A general analytical model which describes the nonlinear, anisotropic, path-dependent, stress-strain-strength properties of the soil skeleton when subjected to complicated three-dimensional, and in particular to cyclic loading paths is presented. A brief summary of the model's basic principles is included and the constitutive equations are provided. It is shown that the model parameters required to characterize the behavior of any given soil can be derived entirely from the results of conventional soil tests. The model's accuracy is evaluated by applying it to represent the behavior of both cohesive and cohesionless soils. Implementation of the proposed model in a general finite element program for solution of boundary value problems is discussed.

[1] Associate Professor, Department of Civil Engineering, Princeton University, Princeton, NJ 08544.

```
0    9
 -9.24E-01 -2.90E+00 -9.24E-01  0.0        0.0        0.0        3.23E+00  3.23E+00  4.34E+00  8.00E-01 -5.68E-01 -2.09E-01
0    10
 -8.62E-01 -2.87E+00 -8.62E-01  0.0        0.0        0.0        3.41E+00  1.22E+00  1.68E+00  8.00E-01 -5.53E-01 -1.32E-02
0    11
 -8.31E-01 -2.83E+00 -8.31E-01  0.0        0.0        0.0        3.51E+00  1.73E-02  2.43E-02  8.00E-01 -5.02E-01  4.28E-02
```

0	4	1.198E+00	1.822E+00	1.731E+00	6.525E+01	7.580E+01	7.999E-01	1.000E+00	-2.274E-01	-7.282E-01
0	5	1.525E+00	1.763E+00	2.237E+00	2.906E+01	3.531E+01	8.000E-01	1.000E+00	-3.371E-01	-8.958E-01
0	6	1.668E+00	1.695E+00	2.583E+00	1.417E+01	1.782E+01	8.000E-01	1.000E+00	-4.246E-01	-7.182E-01
0	7	1.802E+00	1.643E+00	2.872E+00	7.385E+00	9.563E+00	7.999E-01	1.000E+00	-4.831E-01	-4.828E-01
0	8	1.873E+00	1.587E+00	3.113E+00	5.282E+00	7.051E+00	8.000E-01	1.000E+00	-5.339E-01	-3.395E-01
0	9	1.977E+00	1.583E+00	3.228E+00	3.231E+00	4.344E+00	7.999E-01	1.000E+00	-5.685E-01	-2.091E-01
0	10	2.009E+00	1.531E+00	3.415E+00	1.223E+00	1.685E+00	7.999E-01	1.000E+00	-5.530E-01	-1.316E-02
0	11	2.004E+00	1.499E+00	3.508E+00	1.734E-02	2.427E-02	8.000E-01	1.000E+00	-5.022E-01	4.282E-02

1 NAVY PROJECT - FINE SILICA SAND - RAW DATA

C O N T R O L I N F O R M A T I O N

NUMBER OF YIELD SURFACES.....(NYS) = 11

TYPE OF TRIAXIAL TEST.....(ID) = 0

ID=0, DRAINED TEST

ID=1, UNDRAINED TEST

0 XLAM ARRAY

	D1	DU	C	P1	LAMDA	PF	BF	POROSITY
0	0.0	0.0	1.000E+00	0.0	0.0	0.0	0.0	0.0

0 FM ARRAY

	M											
	A11	A22	A33	A12	A23	A31	KM	HC	HE	SC	AMC	AME
0	1											
	-2.00E+00	-2.00E+00	-2.00E+00	0.0	0.0	0.0	2.53E+02	5.07E+02	6.75E+02	5.00E-01	0.0	0.0
0	2											
	-1.78E+00	-2.25E+00	-1.78E+00	0.0	0.0	0.0	6.69E-01	4.61E+02	4.96E+02	8.00E-01	-1.64E-01	-2.22E+00
0	3											
	-1.61E+00	-2.49E+00	-1.61E+00	0.0	0.0	0.0	1.18E+00	1.72E+02	1.91E+02	8.00E-01	-9.69E-02	-8.52E-01
0	4											
	-1.42E+00	-2.62E+00	-1.42E+00	0.0	0.0	0.0	1.73E+00	6.52E+01	7.58E+01	8.00E-01	-2.27E-01	-7.28E-01
0	5											
	-1.25E+00	-2.78E+00	-1.25E+00	0.0	0.0	0.0	2.24E+00	2.91E+01	3.53E+01	8.00E-01	-3.37E-01	-8.96E-01
0	6											
	-1.14E+00	-2.81E+00	-1.14E+00	0.0	0.0	0.0	2.58E+00	1.42E+01	1.78E+01	8.00E-01	-4.25E-01	-7.18E-01
0	7											
	-1.04E+00	-2.84E+00	-1.04E+00	0.0	0.0	0.0	2.87E+00	7.39E+00	9.56E+00	8.00E-01	-4.83E-01	-4.83E-01
0	8											
	-9.62E-01	-2.84E+00	-9.62E-01	0.0	0.0	0.0	3.11E+00	5.28E+00	7.05E+00	8.00E-01	-5.34E-01	-3.40E-01

1 NAVY PROJECT - FINE SILICA SAND - RAW DATA

C O N T R O L I N F O R M A T I O N

PRESSURE SENSITIVE MATERIAL

NUMBER OF YIELD SURFACES.....(NYS) = 100

EXECUTION MODE.....(MODE) = 1

MODE=0, DATA CHECK

MODE=1, EXECUTION

PLOTTING CODE.....(IPLOT) = 2

IPLOT=0, NO PLOTS

IPLOT=1, PLOT Q-E, P-EV, Q-EV, AND Q-P

IPLOT=2, PLOT YIELD SURFACES

IPLOT=3, PLOT BOTH 1 & 2 ABOVE

PUNCH CODE.....(IPUNCH) = 0

IPUNCH=0, NO PUNCH OUTPUT

IPUNCH=1, PUNCH OUTPUT

YIELD SURFACES DETERMINATION CODE .....(ITEST) = 0

ITEST=0, USE AXIAL COMPRESSION DATA

ITEST=1, USE AXIAL EXTENSION DATA

YIELD SURFACES AXIS RATIO ..... (C) = 1.000E+00

POWER EXPONENT ..... (XN) = 5.000E-01

VOLUMETRIC EXPONENT ..... (XL) = 0.0

TOLERANCE ..... (TOL) = 1.000E+00

1 NAVY PROJECT - FINE SILICA SAND - RAW DATA

	M	ALPHA	BETA	XKM	HPC	HPE	SC	SE	AMC	AME
0	1	0.0	2.000E+00	2.533E+02	5.066E+02	6.754E+02	5.000E-01	0.0	0.0	0.0
0	2	4.683E-01	1.933E+00	6.686E-01	4.606E+02	4.956E+02	7.997E-01	1.000E+00	-1.638E-01	-2.220E+00
0	3	8.873E-01	1.902E+00	1.182E+00	1.718E+02	1.913E+02	7.998E-01	1.000E+00	-9.692E-02	-8.521E-01

PORT HUENEME PROJECT - FINE SILICA SAND - DATA MODIFIED

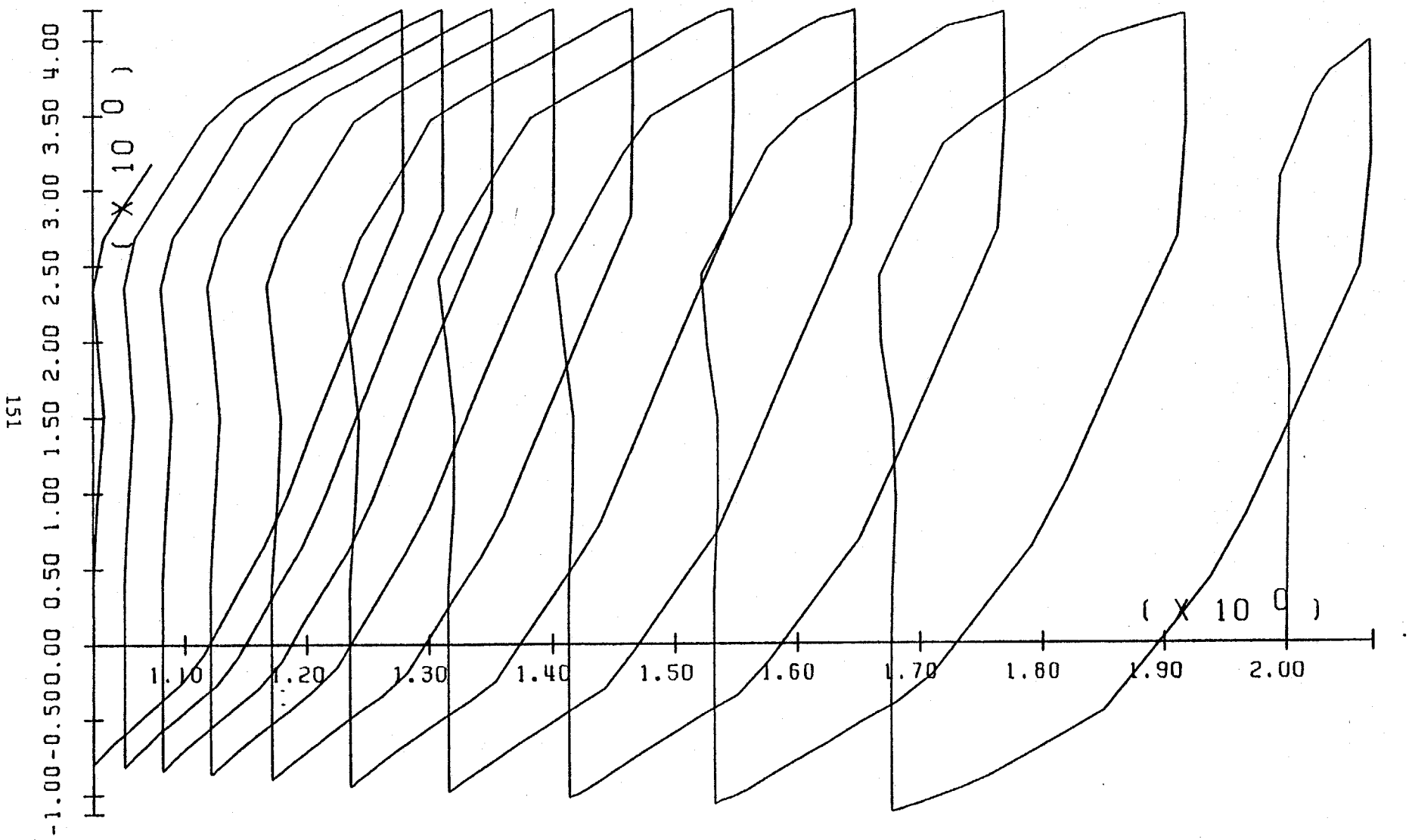

S11 - S22 VS P

FIG 10b

PORT HUENEME PROJECT - FINE SILICA SAND - DATA MODIFIED

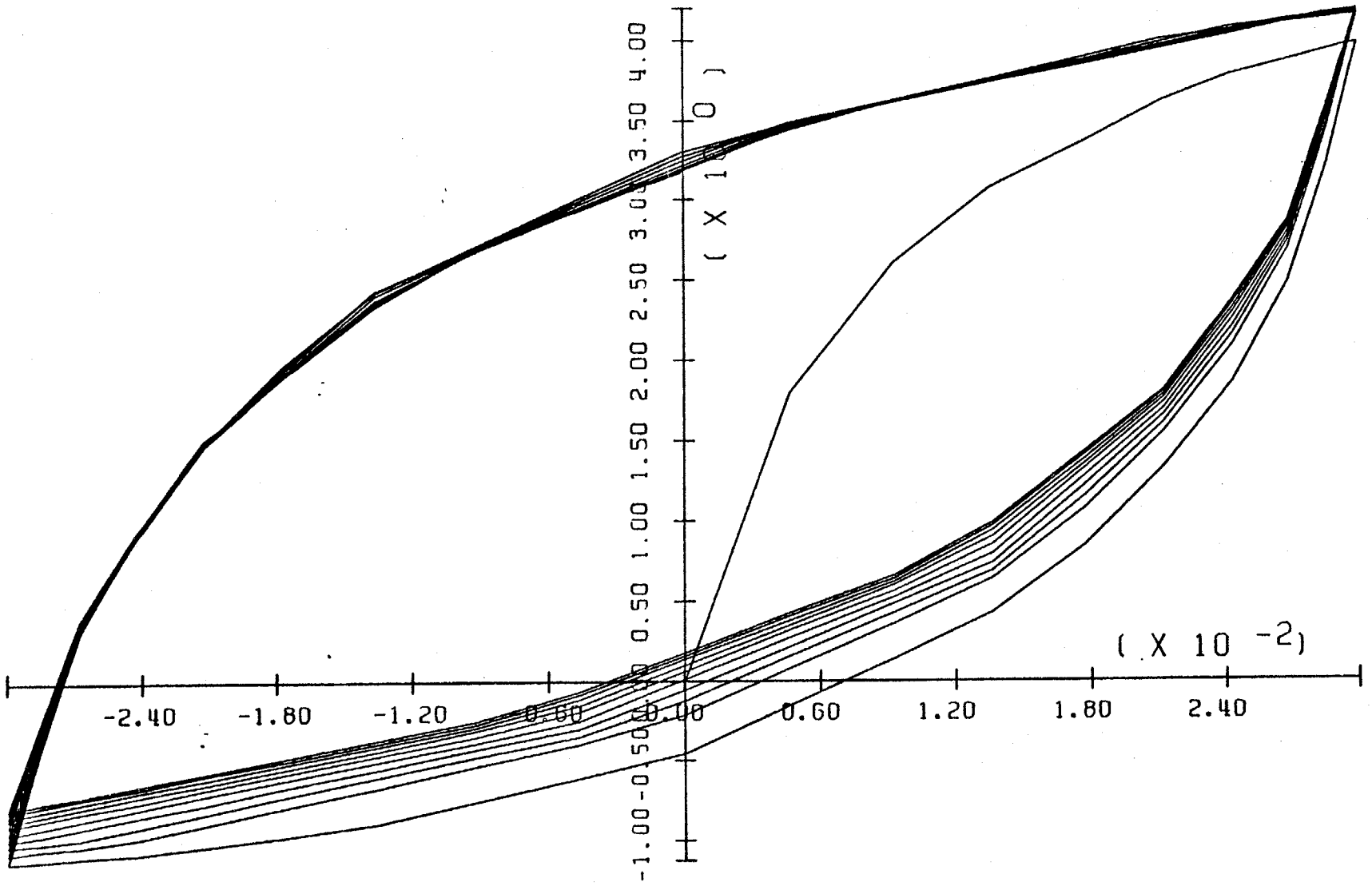

S11 - S22 VS E11 - E22

FIG 102

PORT HUENEME PROJECT - FINE SILICA SAND - DATA MODIFIED

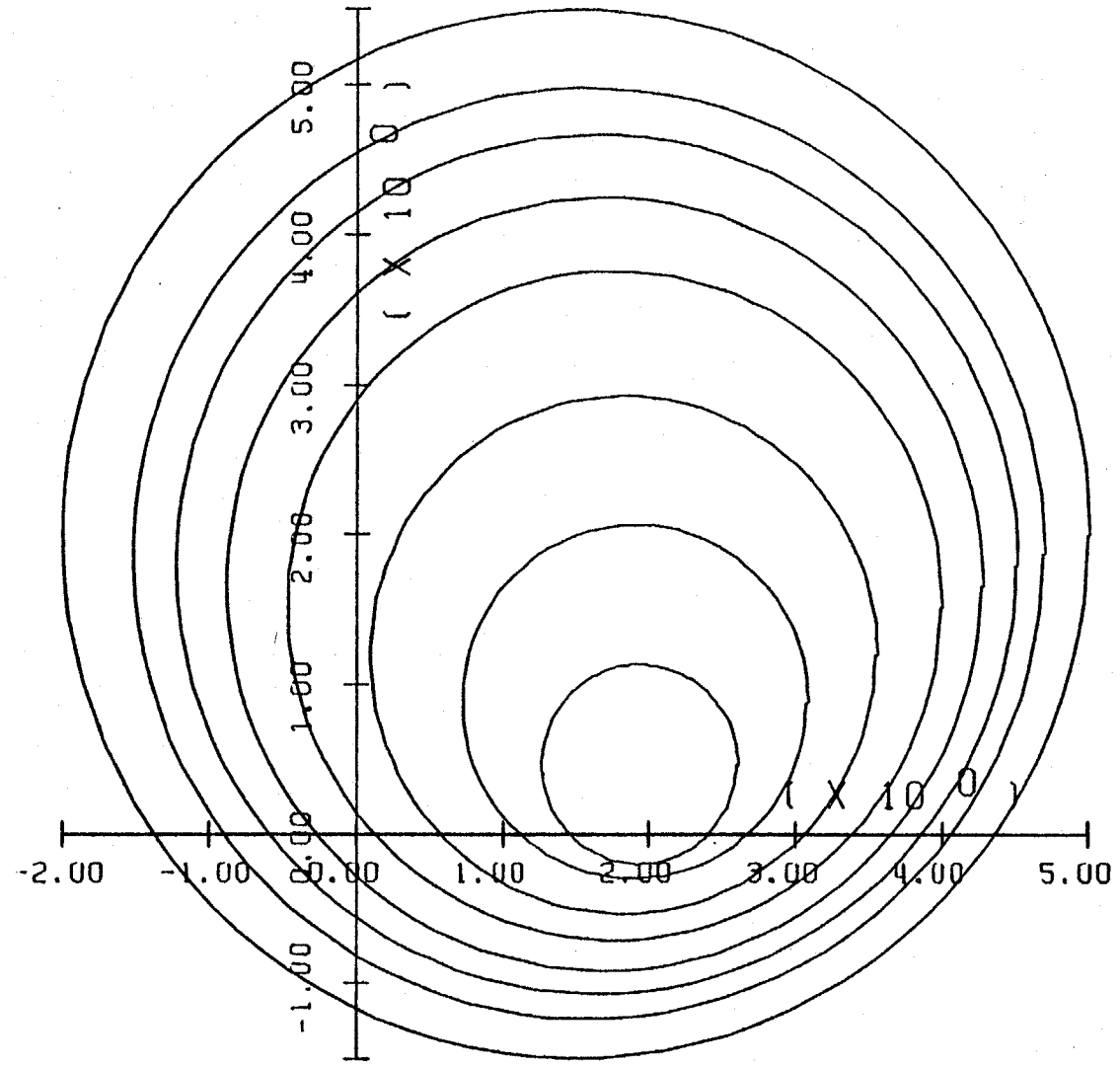

YIELD SURFACES

AXIAL TESTS DATA

FIG 9

PORT HUENEME PROJECT - FINE SILICA SAND - DATA MODIFIED

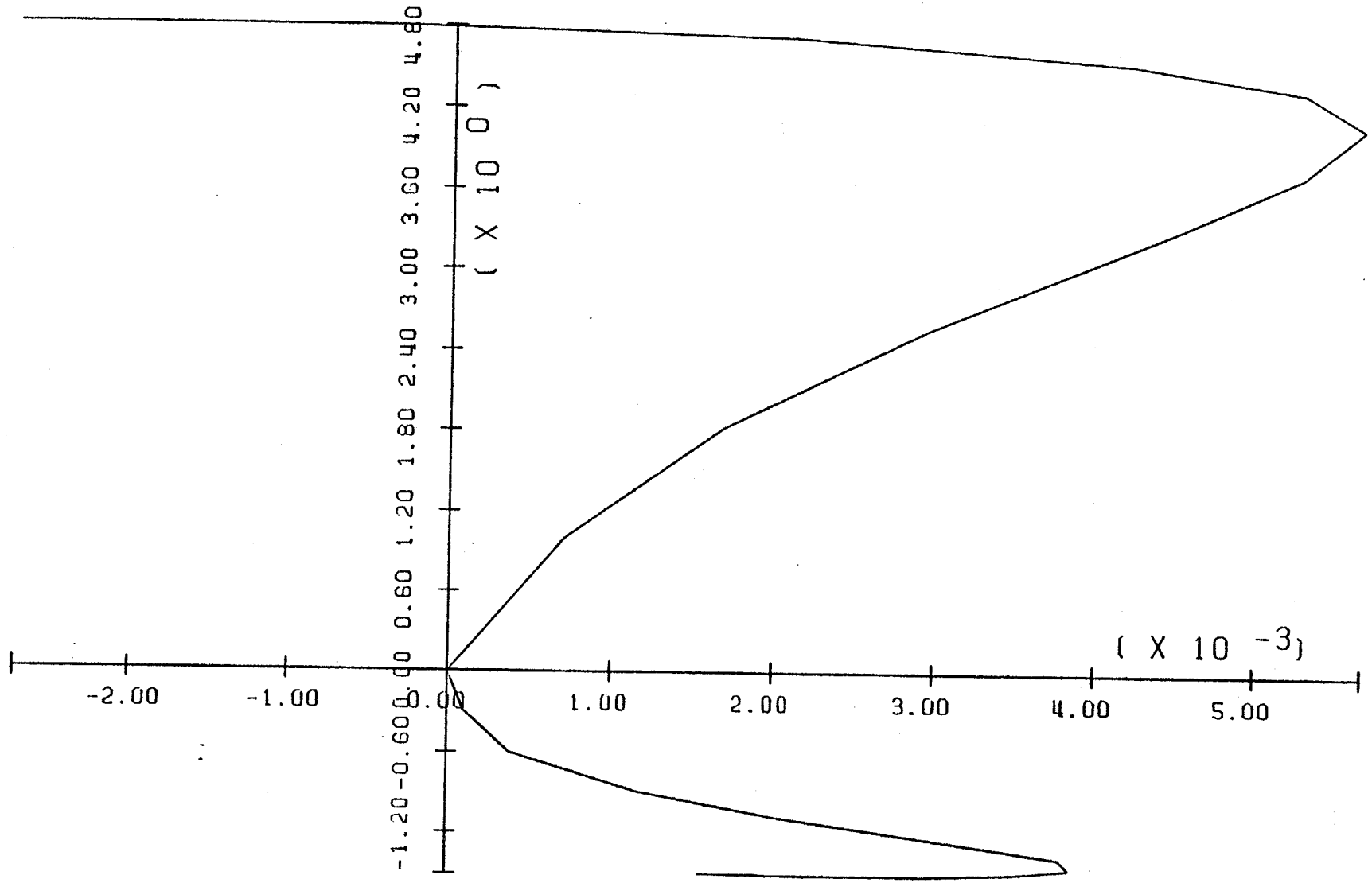

148

Q VS EV

AXIAL TESTS DATA

FIG 8b

PORT HUENEME PROJECT - FINE SILICA SAND - DATA MODIFIED

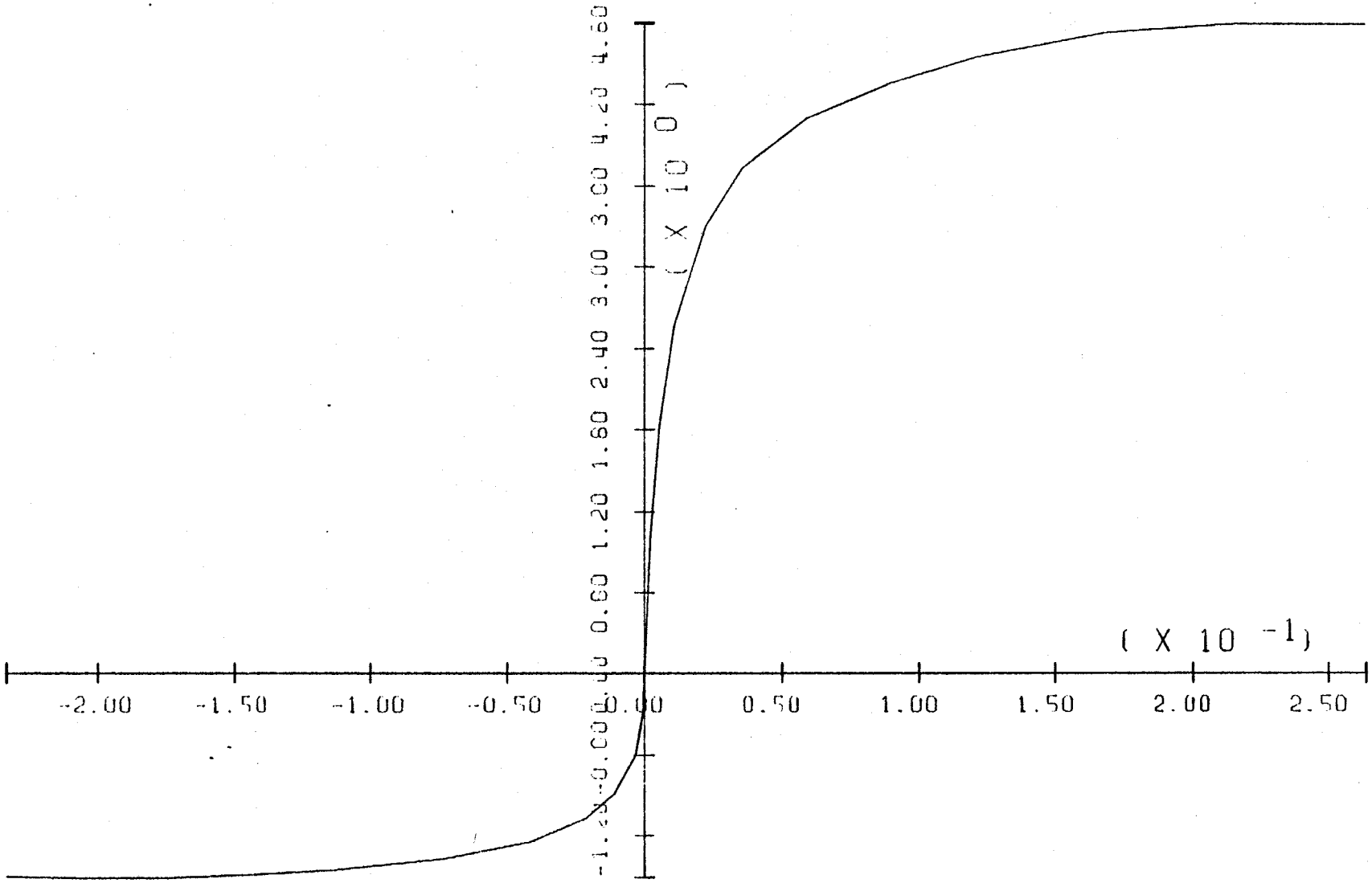

S11 - S22 VS E11 - E22

AXIAL TESTS DATA

Fig 3a

NAVY SAND - UNDRAINED AXIAL CYCLIC TEST - 10 CYCLES, E = 3.0 % (MODIFIED DATA)

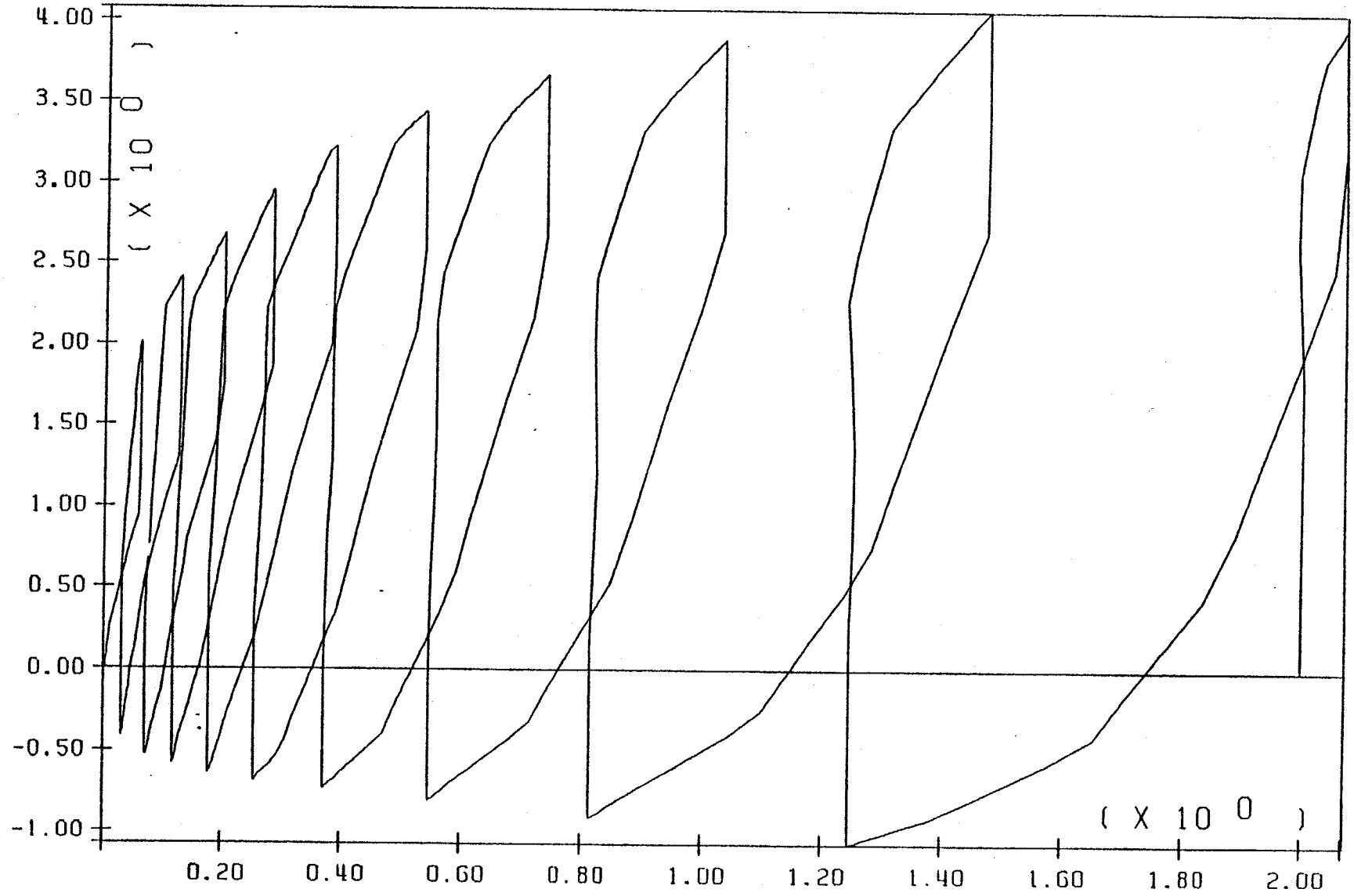

S11 - S22 VS P

FIG 76

NAVY SAND - UNDRAINED AXIAL CYCLIC TEST - 10 CYCLES, E = 3.0 % (MODIFIED DATA)

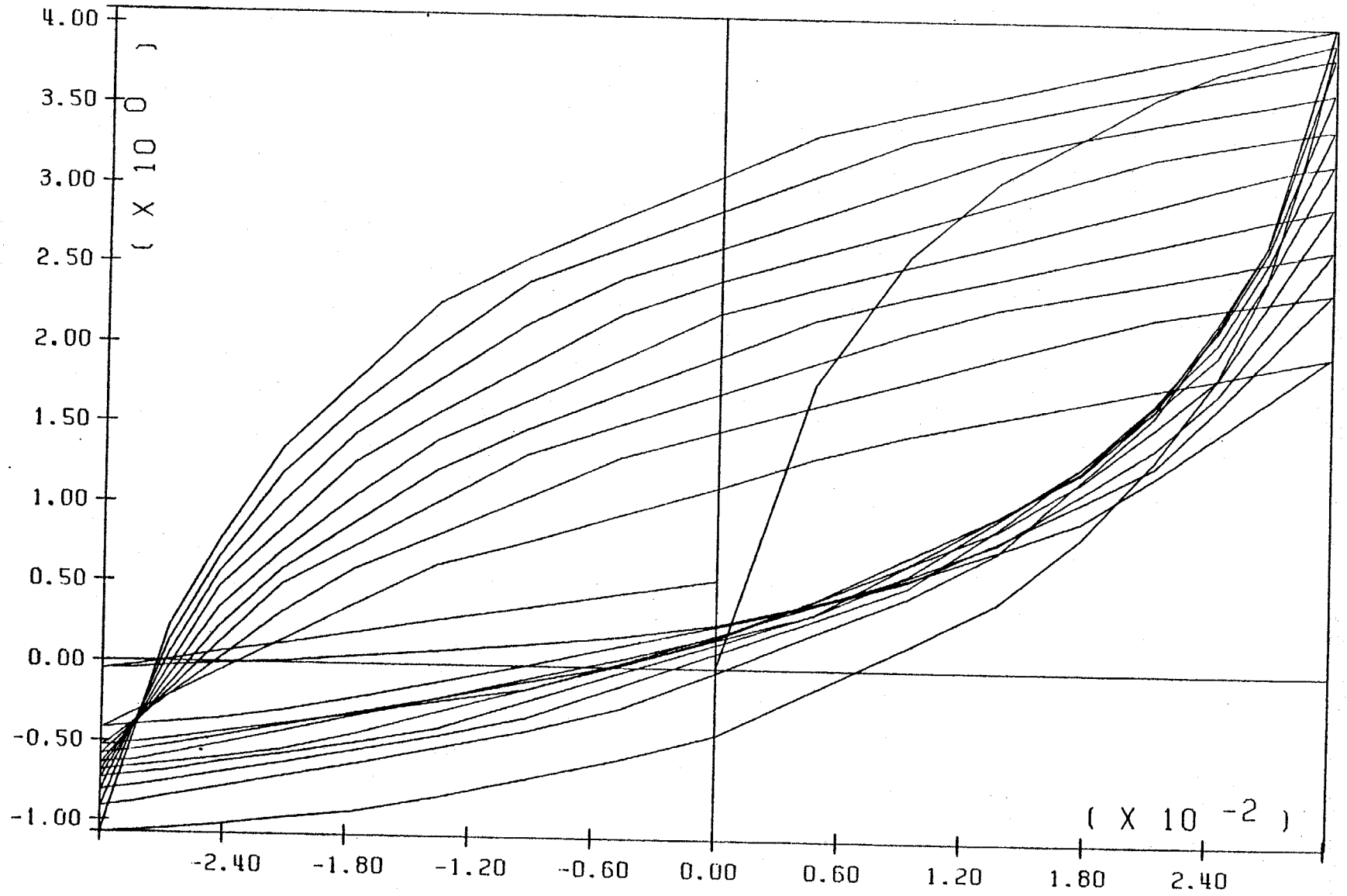

S11 - S22 VS E11 - E22

FiG 7a

NAVY SAND - UNDRAINED AXIAL CYCLIC TEST - 10 CYCLES, E = 1.5 % (MODIFIED DATA)

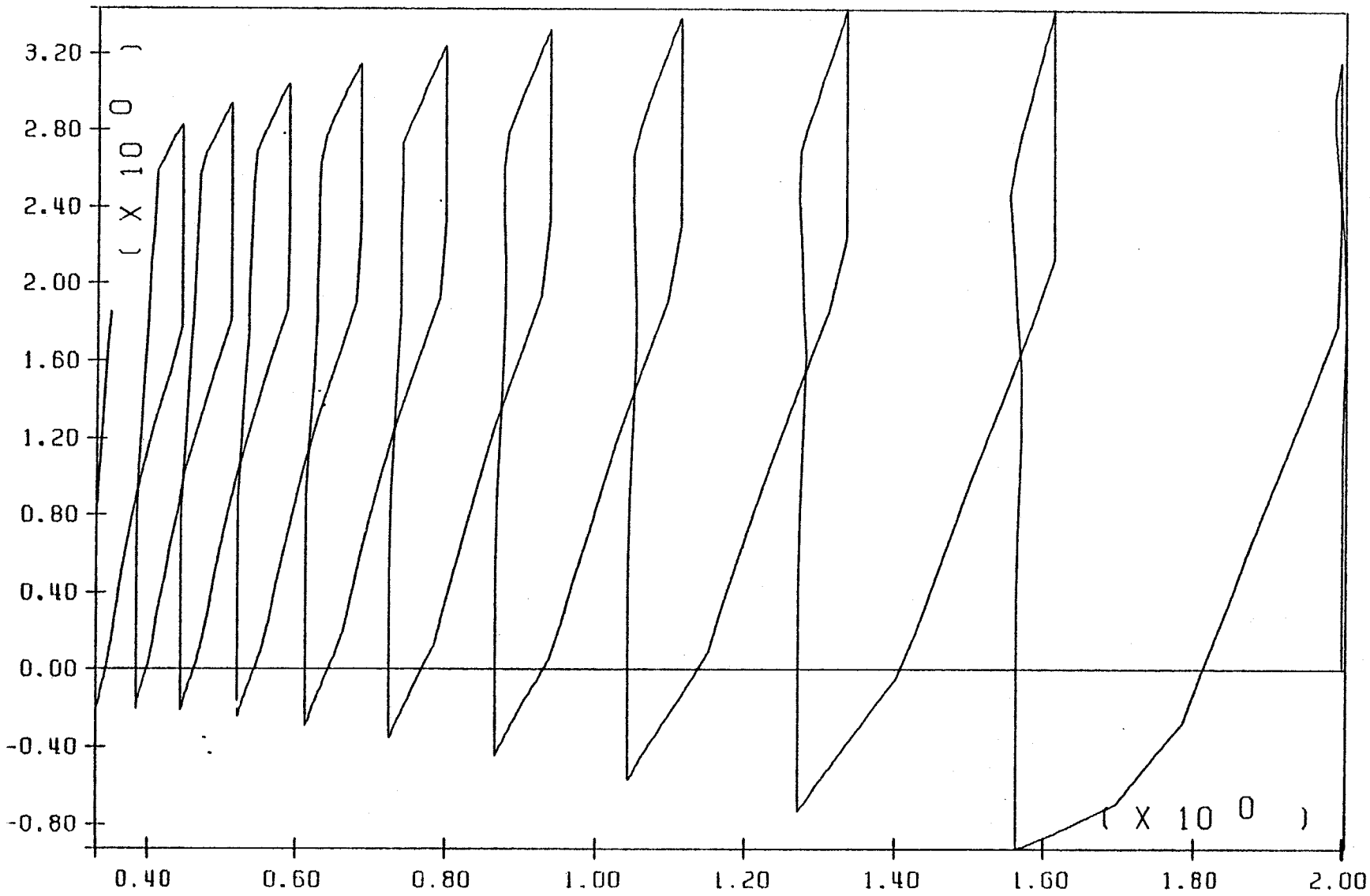

S11 - S22 VS P

FIG. 6b

NAVY SAND - UNDRAINED AXIAL CYCLIC TEST - 10 CYCLES, E = 1.5 % (MODIFIED DATA)

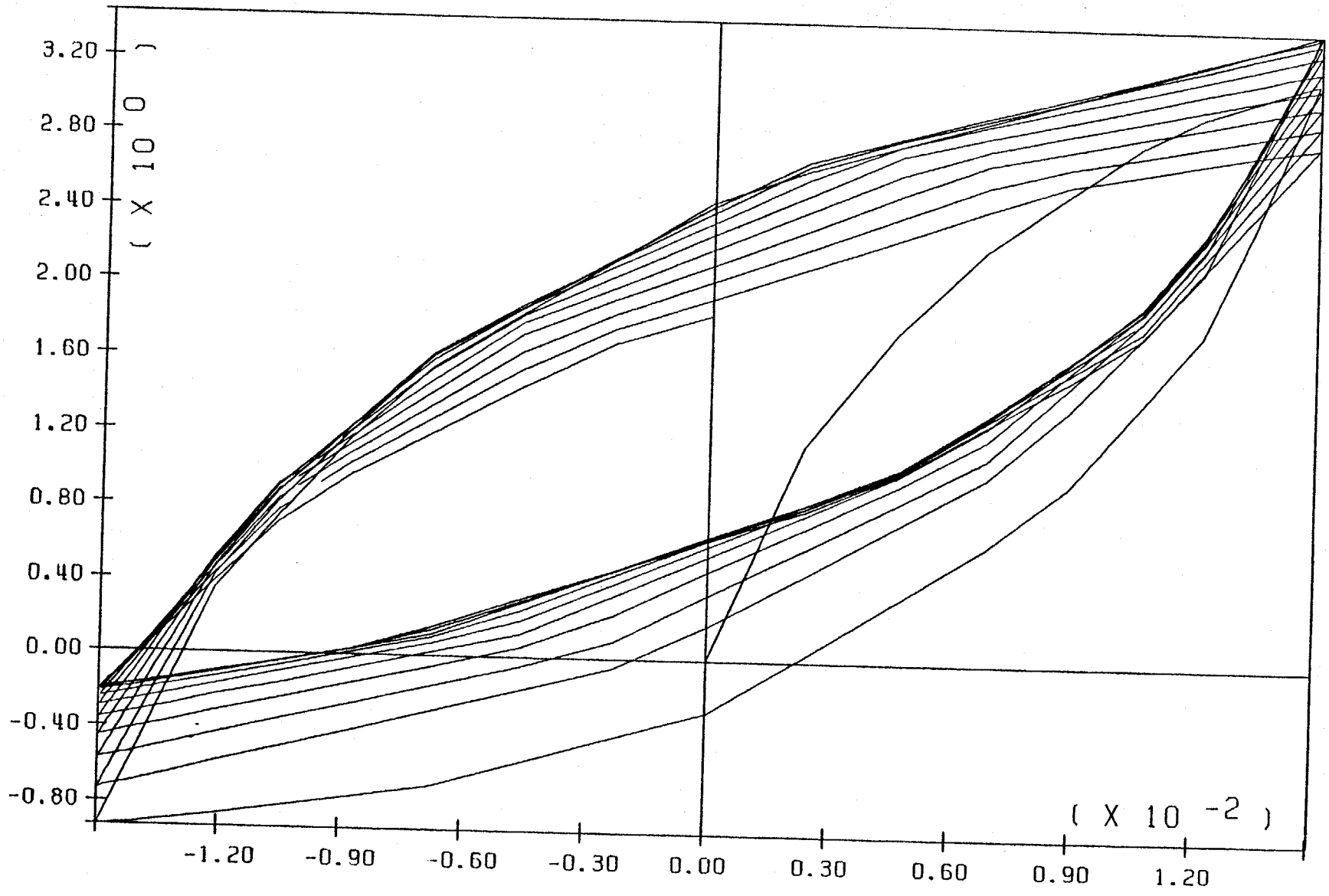

S11 - S22 VS E11 - E22

Fig 6a

NAVY SAND - SIMPLE SHEAR TEST - PO = 2 KG/CM2 (RAW DATA)

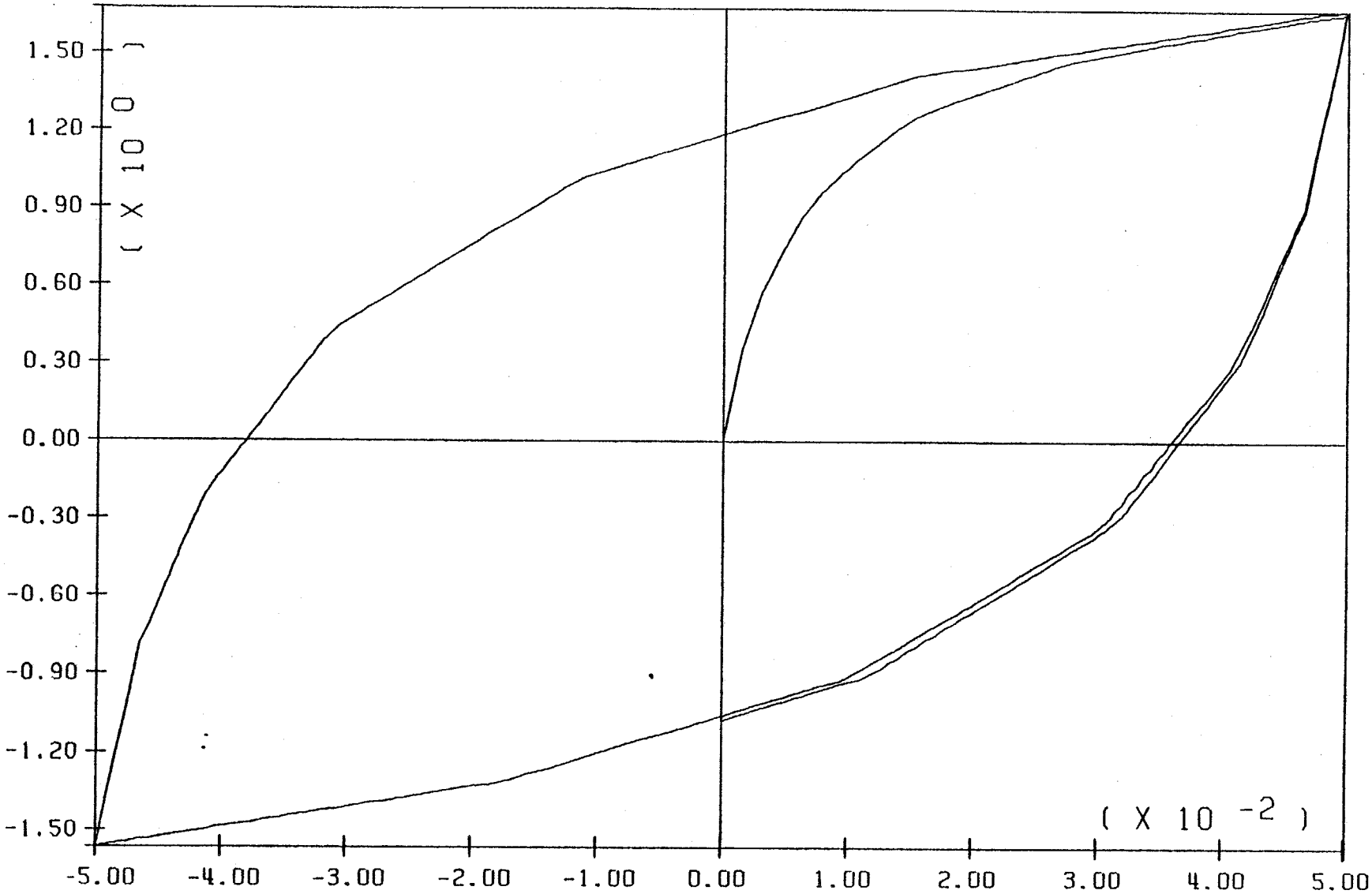

T12 VS G12

FIG. 5

NAVY SAND - ISOTROPIC CONSOLIDATION TEST - PO = 2 KG/CM2 (RAW DATA)

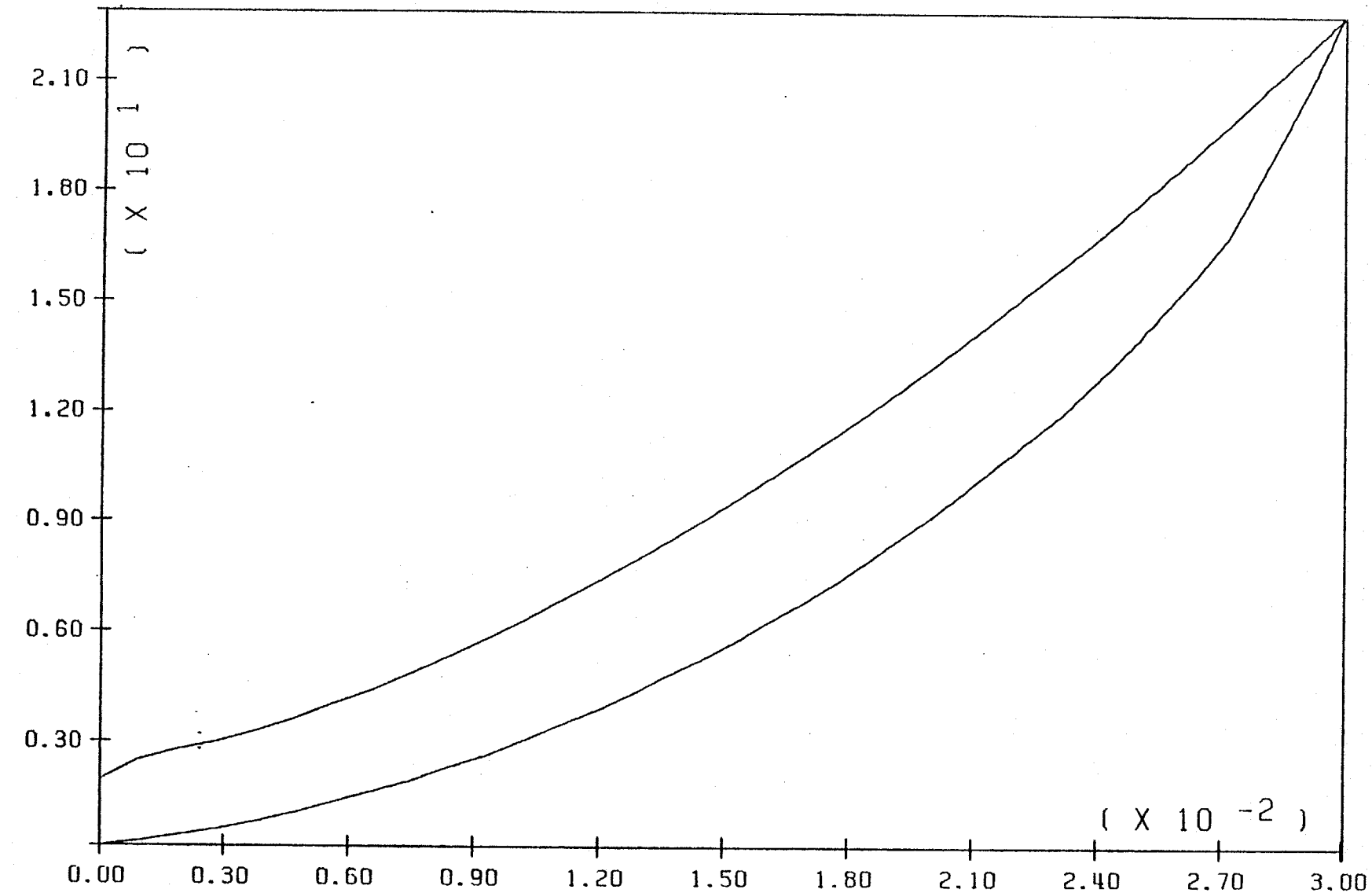

P VS EV

FIG. 4

NAVY SAND - UNDRAINED AXIAL COMPRESSION TEST - PO = 2.0 KG/CM2 (RAW DATA)

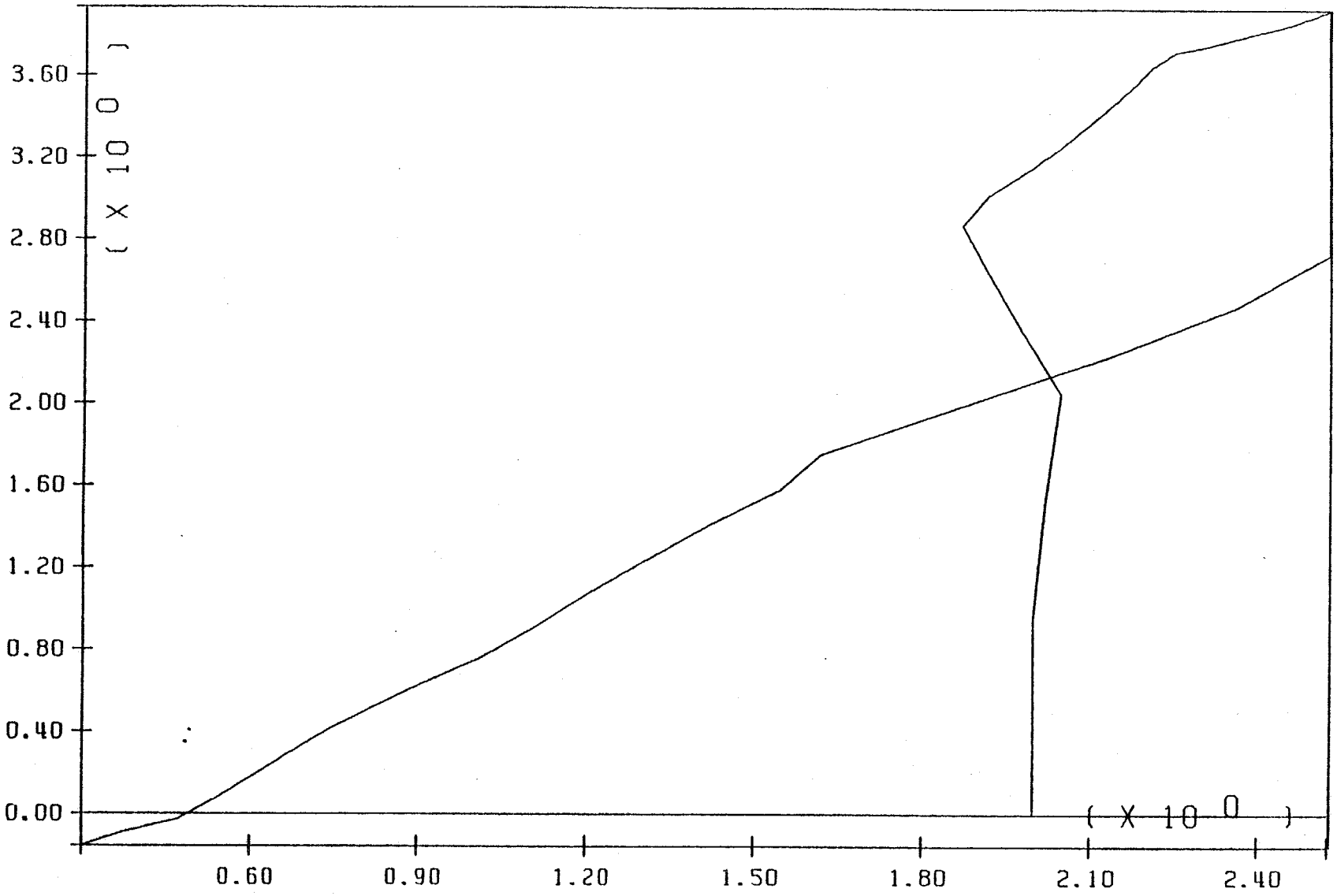

S11 - S22 VS P

FIG 3b

NAVY SAND - UNDRAINED AXIAL COMPRESSION TEST - PO = 2.0 KG/CM2 (RAW DATA)

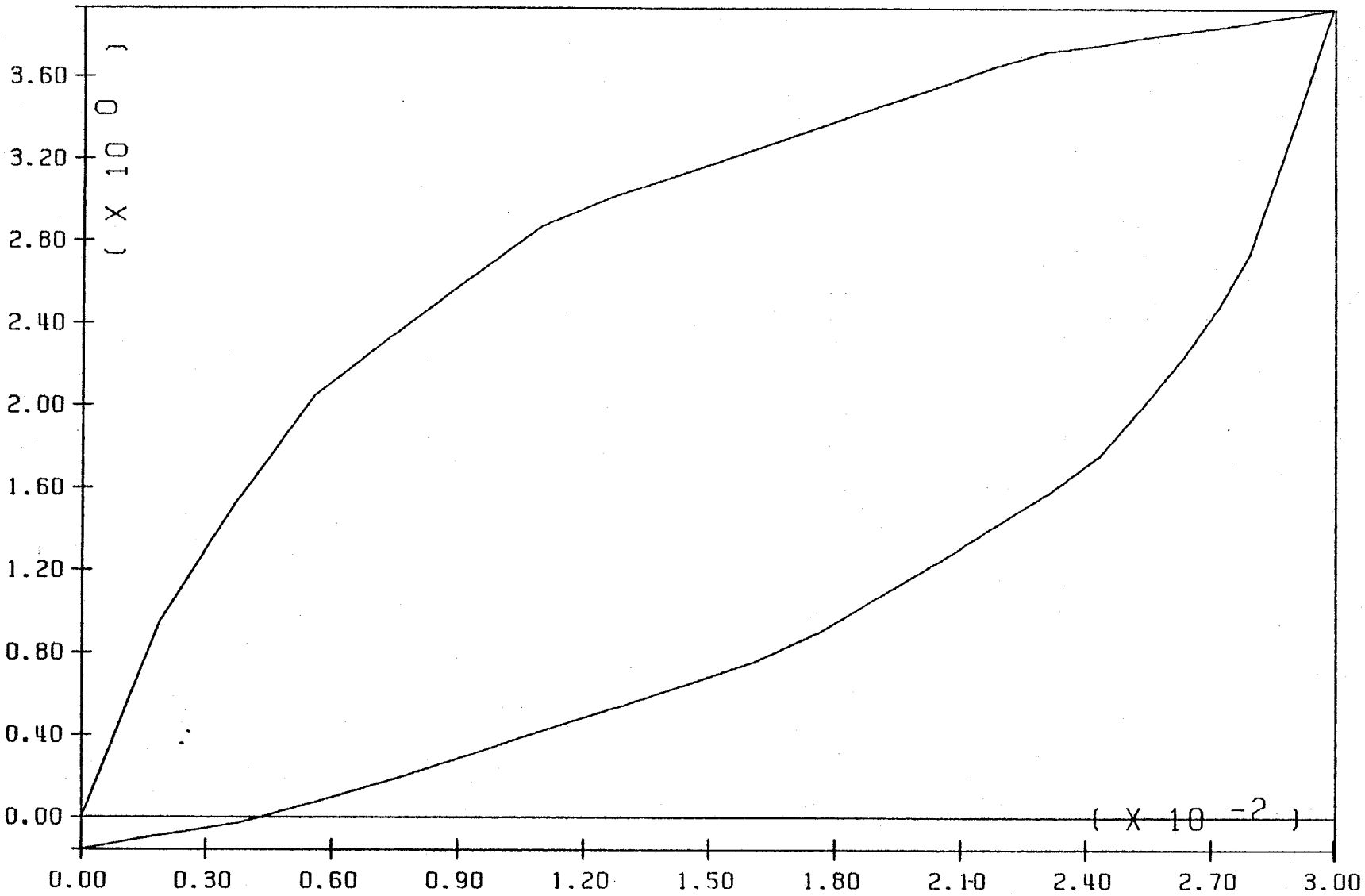

S11 - S22 VS E11 - E22

FIG 3a

NAVY PROJECT - FINE SILICA SAND - RAW DATA

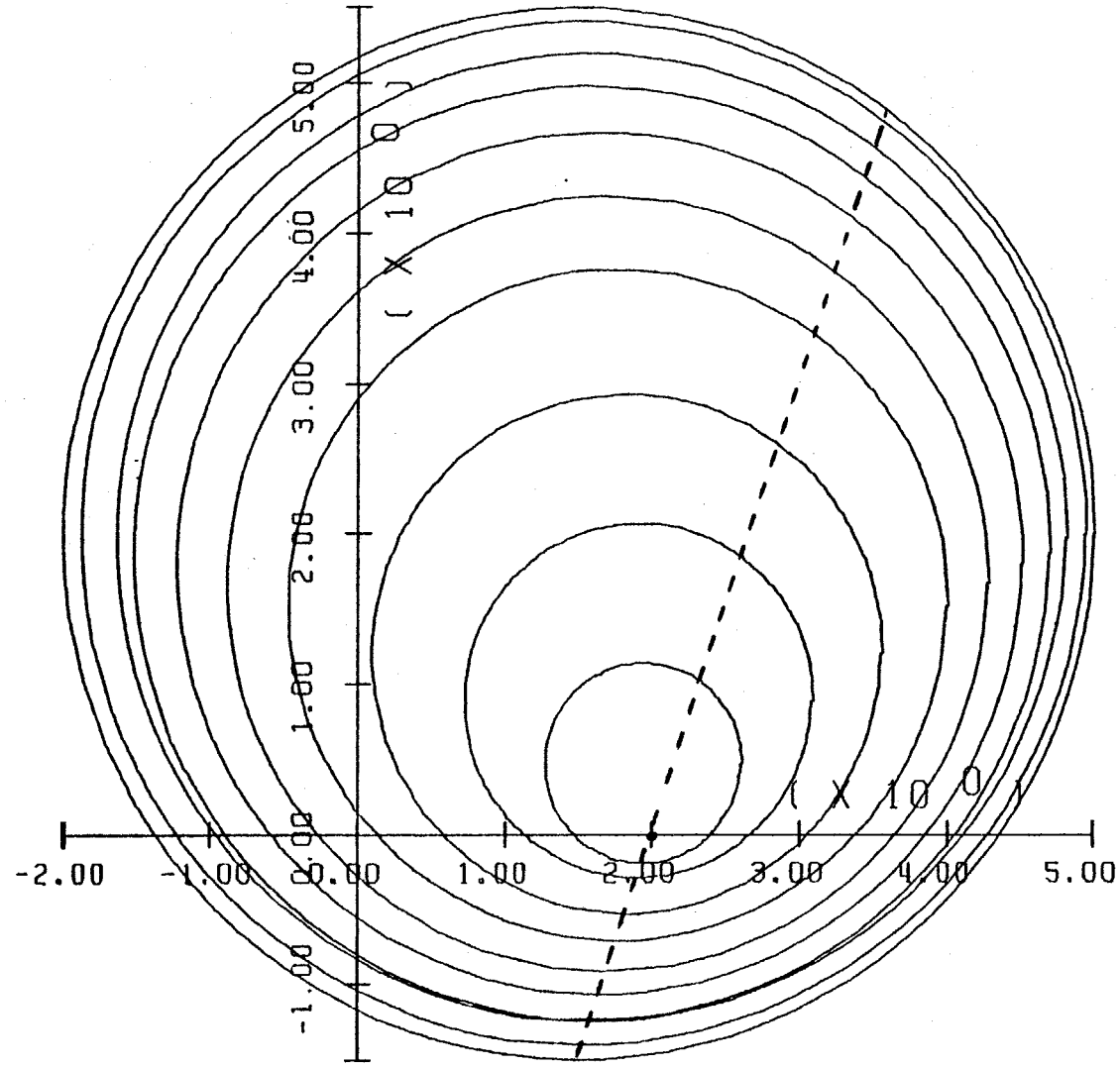

YIELD SURFACES

AXIAL TESTS DATA

Fig. 2

NAVY PROJECT - FINE SILICA SAND - RAW DATA

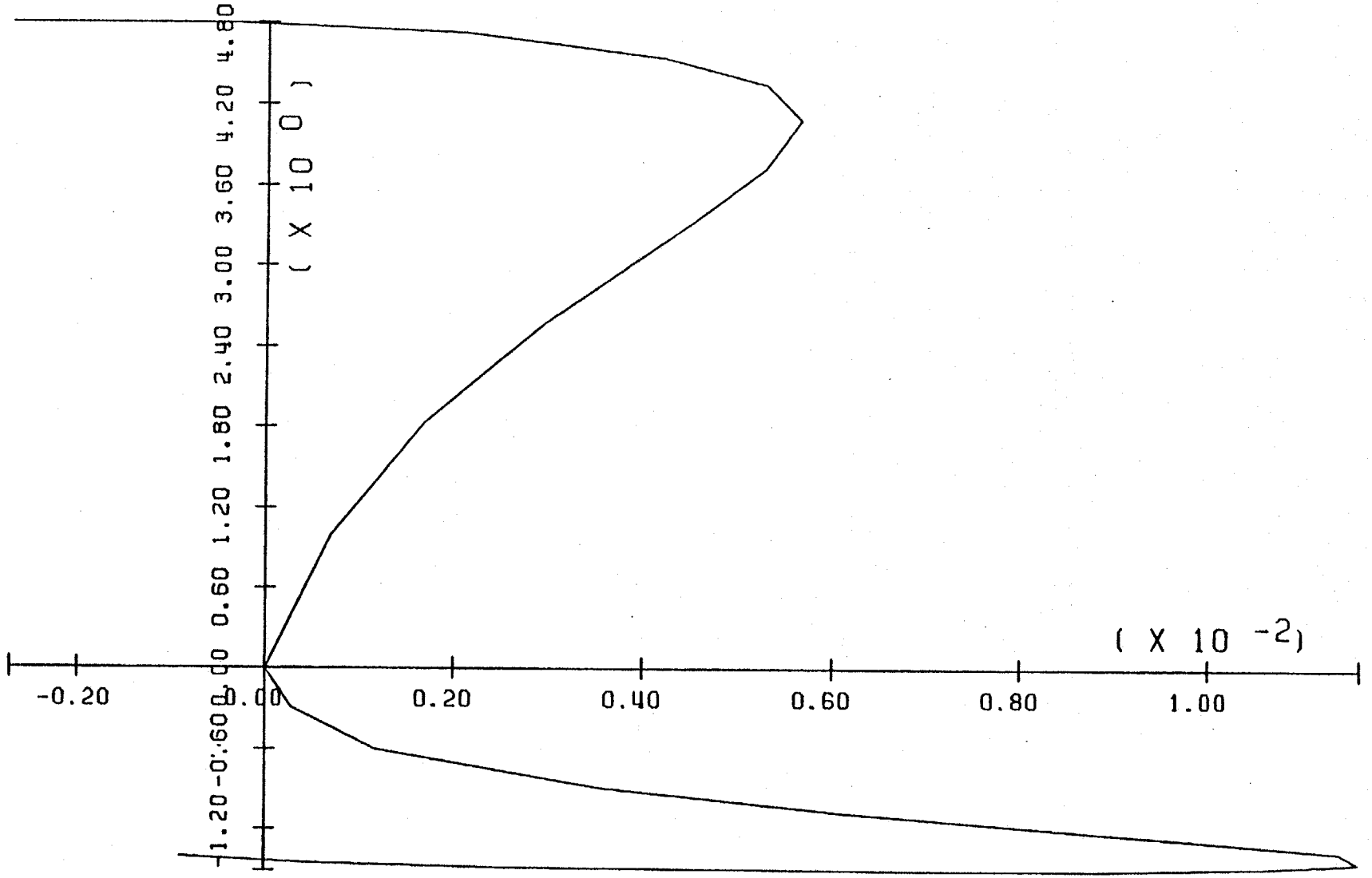

Q VS EV

AXIAL TESTS DATA

FIG 16

NAVY PROJECT - FINE SILICA SAND - RAW DATA

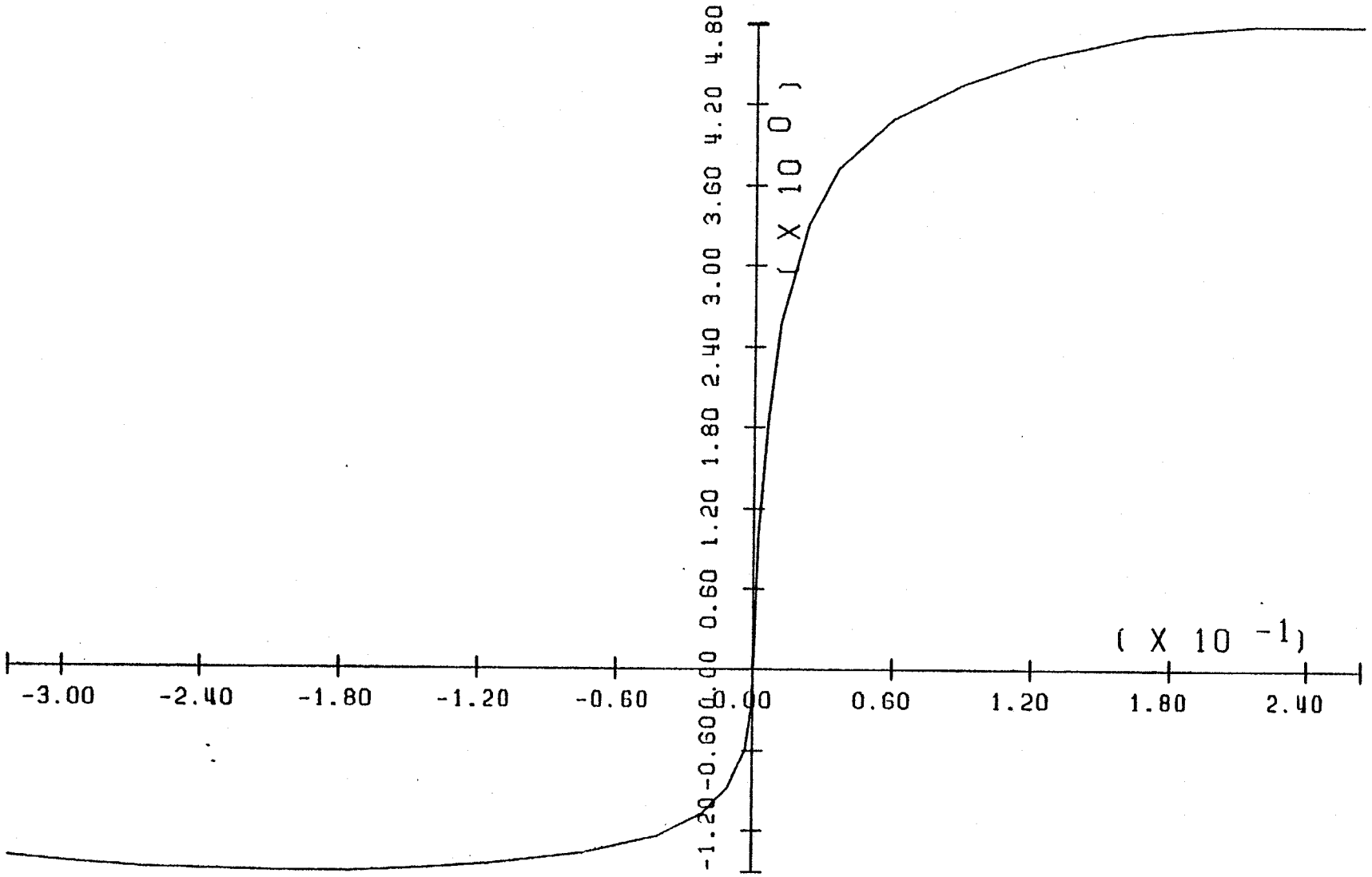

S11 - S22 VS E11 - E22

AXIAL TESTS DATA

FIG. 13

In order to investigate the effects of more realistic volumetric strains, the volumetric data were modified, and the new set of experimental data assumed data assumed is shown in Figure 8. Figure 9 shows the associated field of yield surfaces. Figure 10 shows the model predictions for a cyclic axial undrained, strain-controlled test with axial strain amplitude = 2%.

Note again the progressive build-up of pore water pressure as cyclic loading proceeds and that the rate of pore-water pressure build up decreases significantly with the number of cycles, in that case.

in which H' is the plastic modulus; $\underset{\sim}{P}$ and $\underset{\sim}{Q}$ are symmetric second-order tensors, such that $\underset{\sim}{P}$ gives the direction of plastic deformations and $\underset{\sim}{Q}$ the outer normal to the active yield surface; and $\underset{\sim}{E}$ is the fourth-order tensor of elastic moduli, assumed isotropic, viz.,

$$E_{abcd} = \Lambda\, \delta_{ab}\delta_{bc} + G(\delta_{ac}\delta_{bd} + \delta_{ad}\delta_{bc}) \tag{4}$$

where Λ and G = Lame's constants; δ_{ab} = Kronecker delta. The yield function is selected of the following form

$$f = \frac{3}{2}(\underset{\sim}{S} - \underset{\sim}{\alpha}) : (\underset{\sim}{S} - \underset{\sim}{\alpha}) + C^2(p' - \beta)^2 = k^2 \tag{5}$$

where $\underset{\sim}{S} = \underset{\sim}{\sigma}' - p'\underset{\sim}{1}$ = deviatoric stress tensor; $p' = \frac{1}{3}\,\mathrm{tr}\,\underset{\sim}{\sigma}'$ = effective mean normal stress; $\underset{\sim}{\alpha}$ and β are the coordinates of the center of the yield surface in the deviatoric stress subspace and along the hydrostatic stress axis, respectively; k = size of the yield surface; C = material parameter called the yield surface axis ratio. From Eq. 5

$$\mathrm{grad}\, f = \frac{\partial f}{\partial \underset{\sim}{\sigma}'} = 3(\underset{\sim}{S} - \underset{\sim}{\alpha}) + \frac{2}{3} C^2 (p' - \beta)\, \underset{\sim}{1} \tag{6}$$

and

$$|\mathrm{grad}\, f|^2 = 6k^2 + 6C^2(\tfrac{2}{9} C^2 - 1)(p' - \beta)^2 \tag{7}$$

It is convenient to decompose $\underset{\sim}{P}$ and $\underset{\sim}{Q}$ into their deviatoric and dilatational components, and in the following

$$\underset{\sim}{P} = \underset{\sim}{P}' + P''\,\underset{\sim}{1} \qquad\qquad \underset{\sim}{Q} = \underset{\sim}{Q}' + Q''\,\underset{\sim}{1} \tag{8}$$

where

$$P'' = \frac{1}{3}\ \mathrm{tr}\ \underset{\sim}{P} \qquad\qquad Q'' = \frac{1}{3}\ \mathrm{tr}\ \underset{\sim}{Q} \tag{9}$$

and

$$\underset{\sim}{Q} = \mathrm{grad}\ f / |\mathrm{grad}\ f| \tag{10}$$

The plastic potential is selected such that the plastic rate of deformation vector remains normal to the projection of the yield surface onto the deviatoric stress subspace, viz.,

$$\underset{\sim}{P}' = \underset{\sim}{Q}' \tag{11a}$$

and

$$3P'' = Q'' + A\ \mathrm{tr}\ (\underset{\sim}{Q}')^3 / \mathrm{tr}(\underset{\sim}{Q}')^2 \tag{11b}$$

where

$$\begin{aligned} \mathrm{tr}(\underset{\sim}{Q}')^2 &= \underset{\sim}{Q}' : \underset{\sim}{Q}' = Q'_{ab}\ Q'_{ab} \\ \mathrm{tr}(\underset{\sim}{Q}')^3 &= 3\ \det(\underset{\sim}{Q}') = Q'_{ab}\ Q'_{bc}\ Q'_{ca} \end{aligned} \tag{12}$$

and A is a material parameter which measures the departure from an associative plastic flow rule. When A=0, the principal directions of $\underset{\sim}{P}$ and $\underset{\sim}{Q}$ coincide and consequently the $\underset{\sim}{C}$ tensor possesses the major symmetry and leads to a symmetric material tangent stiffness. On the other hand, when A≠0, the principal directions of $\underset{\sim}{P}$ and $\underset{\sim}{Q}$ do not coincide, and $\underset{\sim}{C}$ does not possess the major symmetry.

From Eqs. 4, 8 and 9,

$$\underset{\sim}{Q} : \underset{\sim}{\sim}\underset{\sim}{E} : \underset{\sim}{P} = B\ \mathrm{tr}\ \underset{\sim}{P}\ \mathrm{tr}\ \underset{\sim}{Q} + 2G\ \underset{\sim}{P}' : \underset{\sim}{Q}' \tag{13}$$

where $B = \Lambda + 2G/3$ and G are the elastic bulk and shear moduli, respectively.

Remarks

1. Under the assumptions spelled above Eqs. 1 and 3 write in expanded form as (small deformation case)

$$\dot{\underset{\sim}{\sigma}}' = 2G\,\dot{\underset{\sim}{\varepsilon}} + (B - \frac{2G}{3})\,\dot{\varepsilon}_v\,\underset{\sim}{1}$$

$$-(2G\,\underset{\sim}{Q}' + B\,3P''\,\underset{\sim}{1})\,\frac{2G\,\underset{\sim}{Q}':\dot{\underset{\sim}{\varepsilon}} + B3Q''\,\dot{\varepsilon}_v}{H' + 2G\,\underset{\sim}{Q}':\underset{\sim}{Q}' + B3Q''3P''} \qquad (14)$$

where $\dot{\varepsilon}_v = \mathrm{tr}\,\dot{\underset{\sim}{\varepsilon}}$. Or equivalently, in terms of deviatoric and dilatational components:

$$\dot{\underset{\sim}{S}} = 2G\,\dot{\underset{\sim}{e}} - 2G\,\underset{\sim}{Q}'\,\frac{2G\,\underset{\sim}{Q}':\dot{\underset{\sim}{e}} + B\,3Q''\,\dot{\varepsilon}_v}{H' + 2G\,\underset{\sim}{Q}':\underset{\sim}{Q}' + B\,3Q''3P''} \qquad (15a)$$

$$\dot{p}' = B\,\dot{\varepsilon}_v - B\,3P''\,\frac{2G\,\underset{\sim}{Q}':\dot{\underset{\sim}{e}} + B\,3Q''\dot{\varepsilon}_v}{H' + 2G\,\underset{\sim}{Q}':\underset{\sim}{Q}' + B\,3Q''\,3P''} \qquad (15b)$$

where $\dot{\underset{\sim}{e}} = \dot{\underset{\sim}{\varepsilon}} - \dot{\varepsilon}_v\,\underset{\sim}{1}$ = deviatoric rate of deformation tensor.

When $\underset{\sim}{Q}' = 0$, $3Q''^2 = 1$ and Eq. 15b simplifies to

$$\dot{p} = (\frac{1}{B} + \frac{1}{H'})^{-1}\,\dot{\varepsilon}_v \qquad (16)$$

and the plastic modulus H' thus plays the role of a <u>plastic bulk modulus.</u> Similarly, when Q"=0, $\underset{\sim}{Q}':\underset{\sim}{Q}' = 1$ and Eq. 15a yields

$$\underset{\sim}{Q}':\dot{\underset{\sim}{S}} = (\frac{1}{2G} + \frac{1}{H'})^{-1}\,\underset{\sim}{Q}':\dot{\underset{\sim}{e}} \qquad (17)$$

and the plastic modulus H' thus plays the role of a <u>plastic shear modulus.</u>

2. When C=0, the yield surface plots in stress space as a cylinder (translated Von-Mises yield surface) whose axis is parallel to the space diagonal, and the model reduces to the one used in [8,9]. When C≠0, the yield surface plots in stress space as an ellipsoidal surface of revolution whose axis is parallel to the space diagonal.

In order to allow for the adjustment of the plastic hardening rule to any kind of experimental data, for example data obtained from axial or simple shear soil tests, a collection of nested yield surfaces is used. Much pros and cons have been said about multi-surface versus two-surface plasticity theories and a critical assessment of their relative merits and shortcomings is reported in [16]. The surfaces are all similar, i.e., the axis ratio C (Eq. 5) is the same for all yield surfaces. The yield surfaces, in general, may translate and change in size, but never rotate. The model therefore combines properties of isotropic and kinematic plasticity. In order to avoid overlappings of the surfaces (which would lead to a non-unique definition of the constitutive theory) the isotropic/kinematic hardening rule couples the simultaneous deformation/translation of all yield surfaces. This is further discussed and explained in [10].

A plastic modulus $H'^{(m)}$ and a nonassociative parameter $A^{(m)}$ are associated with each yield surface. In general, both $A^{(m)}$ and $H'^{(m)}$ are allowed to take different values at different locations on any given yield surface, i.e., both $A^{(m)}$ and $H'^{(m)}$ are functions of position. That much degree of complexity and generality is required in order to be able to accommodate any given soil.

Remarks

Several levels of sophistication (and complexity but versatility) of the model can be achieved by appropriate selection of $A^{(m)}$ and $H'^{(m)}$. Up to this date, the following rules have been used:

cohesive soils [11, 14] $A^{(m)}$ constant on each surface, and

$$H'^{(m)} = h'^{(m)} + \frac{\text{tr } \underset{\sim}{Q}^{(m)}}{\sqrt{3}} B'^{(m)} \tag{18}$$

where $h'^{(m)}$ plays the role of a plastic shear modulus and $(h'^{(m)} \pm B'^{(m)})$ play the role of plastic bulk moduli.

cohesionless soils: Both $A^{(m)}$ and $H'^{(m)}$ are allowed to vary on each yield surface;

$$A^{(m)} = A_i^{(m)} \qquad \begin{cases} i=1 & \text{if } \text{tr}(\underset{\sim}{Q}'^{(m)})^3 > 0 \\ i=2 & \text{if } \text{tr}(\underset{\sim}{Q}'^{(m)})^3 < 0 \end{cases} \tag{19}$$

and

$$H'^{(m)} = h_i'^{(m)} \left| \frac{\text{tr}(\underset{\sim}{Q}'^{(m)})^3}{\underset{\sim}{A}_i} \right| + B_i'^{(m)} \left| 1 - \frac{\text{tr}(\underset{\sim}{Q}'^{(m)})^3}{\underset{\sim}{A}_i} \right| \tag{20}$$

$$\begin{cases} i=1 & \text{if } \text{tr } \underset{\sim}{Q}^{(m)} > 0 \\ i=2 & \text{if } \text{tr } \underset{\sim}{Q}^{(m)} < 0 \end{cases}$$

where $h_i'^{(m)}$ and $B_i'^{(m)}$ play the role of plastic shear and bulk moduli, respectively.

The yield surfaces' initial positions and sizes reflect the past stress-strain history of the soil skeleton, and in particular their initial positions are a direct expression of the material's "memory" of its past loading history. Because the $\underset{\sim}{\alpha}$'s are not necessarily all equal to zero, the yielding of the material is anisotropic. Direction is therefore of importance and the physical reference axes (x,y,z) are fixed with respect to the material element and specified to coincide with the reference axes of consolidation. For a soil element whose anisotropy initially exhibits rotational symmetry about the y-axis, $\alpha_x = \alpha_z = -\alpha_y/2$, and Eq. 5 simplifies to

$$[(\sigma'_y - \sigma'_x) - \alpha]^2 + C^2(p' - \beta)^2 - k^2 = 0 \tag{21}$$

in which $\alpha = 3\alpha_y/2$. The yield surfaces then plot as ellipses in the axisymmetric stress plane ($\sigma'_x = \sigma'_z$) as shown in Fig. 1a. Points C and E on the outermost yield surface define the critical state conditions (i.e., H' = 0) for axial compression and extension loading conditions, respectively [2]. It is assumed that the slopes of the critical state lines OC and OE remain constant during yielding.

The yield surfaces are allowed to change in size as well as to be translated by the stress point. Their associated plastic moduli are also allowed to vary and in general both k and H' are functions of the plastic strain history. They are conveniently taken as functions of invariant measures of the amount of plastic volumetric strains and/or plastic shear distortions, respectively [8, 10, 14].

Complete specification of the model parameters requires the determination of

(i) the initial positions and sizes of the yield surfaces together with their associated plastic moduli;

(ii) their size and/or plastic modulus changes as loading proceeds, and finally,

(iii) the elastic shear G and bulk B(= Λ + 2G/3) moduli.

Remarks

1. The yield surface $f^{(1)}$ is chosen as a degenerate yield surface of size $k^{(1)}=0$ which coincides with the stress point. Further, in order to get a smooth transition from the elastic into the plastic regime, $A^{(1)} = 0$ and $H'^{(1)} = \infty$, so that the material behavior inside $f^{(2)}$ is purely elastic.

2. The dependence of the model parameters upon the effective mean normal stress and volumetric strain are assumed of the following form

$$x = x_1 \left(\frac{p'}{p'_1}\right)^n \qquad y = y_1 \exp(\lambda \varepsilon_v)$$

respectively, where x =B, G and $H'^{(m)}$, and y = $\alpha_{ab}^{(m)}$, $\beta^{(m)}$ and $k^{(m)}$; n is an experimental parameters (n=0.5 for most cohesionless soils [22], and n=1 for most cohesive soils); p'_1 = reference effective mean normal stress (i.e., at $\varepsilon_v = 0$ when $p' = p'_1$). It is assumed that when the soil is in a "normally consolidated" state, the consolidation soil text results plot (1) as a straight line parallel to the projections of the critical state lines in the Ln p'/p'_1 vs ε_v diagram [23], and (2) as a straight line in the axial stress plane. The parameter λ is then

simply determined from the results of K_o-consolidation soil test results, viz.,

$$\lambda = \frac{1}{p'_K} \frac{\dot{p}'_K}{\dot{\varepsilon}^K_v} \tag{22}$$

where the subscript/superscript K refers to K_o-loading conditions.

The soil's anisotropy originally develops during its deposition and subsequent consolidation which, in most practical cases, occurs under no lateral deformations. In the following, the y-axis is vertical and coincides with the direction of consolidation, the horizontal xz-plane is thus a plane of material's isotropy and the material's anisotropy initially exhibits rotational symmetry about the vertical y-axis. The model parameters required to characterize the behavior of any given soil can then be derived entirely from the results of conventional monotonic axial and cyclic strain-controlled simple shear soil texts [8, 14]. This is explained and further discussed in the following.

DETERMINATION OF MODEL PARAMETERS

In order to follow common usage in soil mechanics, compressive stresses and strains are considered positive in the following. All stresses are effective stresses unless otherwise specified.

As explained previously, for a material which initially exhibits cross-anisotropy about the vertical y-axis, the initial position in stress space of the yield surfaces are defined by the sole determination of the two parameters $\alpha^{(m)}$ and $\beta^{(m)}$ (m=1,...,p) and Eq. 5 simplified to

$$[q - \alpha^{(m)}]^2 + C^2[p' - \beta^{(m)}]^2 - [k^{(m)}]^2 = 0 \tag{23}$$

for axial loading conditions (i.e., $\sigma'_x = \sigma'_z$ and $\tau_{xy} = \tau_{yz} = \tau_{zx} = 0$), where $q = (\sigma'_y - \sigma'_x)$. The yield surfaces then plot as circles in the q versus Cp' plane (referred to as the axial stress plane hereafter) as shown in Fig. 1b. When the stress point reaches the yield surface $f^{(m)}$,

$$q = \alpha^{(m)} + k^{(m)} \sin\theta \tag{24a}$$

$$p' = \beta^{(m)} + \frac{k^{(m)}}{C} \cos\theta \tag{24b}$$

where θ is defined in Fig. 16, and Eq. 15 simplifies to:

$$\frac{\dot{\varepsilon}}{\dot{q}} = \frac{1}{2G} + \frac{1}{H'^{(m)}} \frac{\sin\theta(\sin\theta + C\gamma \cos\theta)}{\sin^2\theta + \frac{2}{9}C^2\cos^2\theta} \tag{25a}$$

$$\frac{\dot{\varepsilon}_v}{\dot{p}'} = \frac{1}{B} + \frac{1}{H'^{(m)}} \frac{(\frac{2C}{3}\cos\theta + A^{(m)}\sin\theta)\frac{1}{3\gamma}(\sin\theta + C\gamma\cos\theta)}{\sin^2\theta + \frac{2}{9}C^2\cos^2\theta} \tag{25b}$$

in which

$$\dot{\varepsilon}_v = \dot{\varepsilon}_y + 2\dot{\varepsilon}_x \tag{26}$$

$$\dot{\varepsilon} = (\dot{\varepsilon}_y - \dot{\varepsilon}_x) \tag{27}$$

$$\gamma = \frac{\dot{p}'}{\dot{q}} \tag{28}$$

(i) Interpretation of Monotonic Drained Axial Compression and Extension Soil Test Results

Let θ_C and θ_E denote the values of θ when the stress point reaches the yield surface $f^{(m)}$ in axial compression and extension loading conditions, respectively. Combining Eqs. 24-28 one finds that:

$$\tan(\theta_C + \theta_E) = \frac{-2R}{1 - R^2} \tag{29}$$

$$\frac{1}{\tan\theta_C} = \frac{3}{2C}\left[3\gamma_C \frac{x_C}{y_C} - A_C^{(m)}\right] \tag{30a}$$

$$\frac{1}{\tan\theta_E} = \frac{3}{2C}\left[3\gamma_E \frac{x_E}{y_E} - A_E^{(m)}\right] \tag{30b}$$

in which

$$R = C\,\frac{p'_C - p'_E \exp\left[\lambda(\varepsilon_v{}^C - \varepsilon_v{}^E)\right]}{q_C - q_E \exp\left[\lambda(\varepsilon_v{}^C - \varepsilon_v{}^E)\right]} \tag{31}$$

and

$$\frac{1}{x_C} = \left(\frac{p'_C}{p'_1}\right)^n \frac{\dot{\varepsilon}}{\dot{q}} - \frac{1}{2G_1} \tag{32}$$

$$\frac{1}{y_C} = \left(\frac{p'_C}{p'_1}\right)^n \frac{\dot{\varepsilon}_v}{\dot{p}'} - \frac{1}{B_1} \tag{33}$$

and similarly for x_E and y_E, where the subscript C and E refer to axial compression and extension loading conditions, respectively. Further,

$$H'^{(m)}_C = x_C \sin\theta_C \frac{\sin\theta_C + C\gamma_C \cos\theta_C}{\sin^2\theta_C + \frac{2}{9}C^2\cos^2\theta_C} \tag{34}$$

and similarly for $H'^{(m)}_E$.

The smooth experimental stress-strain curves obtained in axial tests are approximated by linear segments along which the tangent (or secant) modulus is constant. Evidently, the degree of accuracy achieved by such a representation of the experimental curves is directly dependent upon the number of linear segments used. The model parameters associated with the yield surface $f^{(m)}$ are determined by the condition that the slopes $\dot{q}/\dot{\bar{\varepsilon}}$ are to be the same in axial compression and extension tests when the stress point has reached the yield surface $f^{(m)}$ [8,9,10,14]. The corresponding values of θ_C and θ_E are determined by combining Eqs. 29 and 30 once a rule has been adopted for $A^{(m)}$ (see previous discussion). The case $A^{(m)}$ = constant is discussed in detail in [14]. Once θ_C and θ_E have been determined, the model parameters associated with $f^{(m)}$ are simply obtained from Eqs. 24-25 (see e.g., [14]).

(ii) Interpretation of Monotonic Drained Axial Compression and Extension Soil Test Results

In undrained tests, $\dot{\varepsilon}_v = 0$, and (from Eq. 33) $y_C = y_E = -B_1$ in that case. The model parameters associated with the yield surface $f^{(m)}$ are again determined by the condition that the slopes $\dot{q}/\dot{\bar{\varepsilon}}$ are to be the same in axial compression and extension tests when the stress point has reached the yield surface $f^{(m)}$. As previously, the corresponding values θ_C and θ_E are determined from Eqs. 29 and 30, in which

$$R = C \frac{p'_C - p'_E}{q_C - q_E} . \qquad (35)$$

Knowing θ_C and θ_E, the model parameters associated with $f^{(m)}$ are computed from Eqs. 24 and 25, in which $\varepsilon_v^C = \varepsilon_v^E = 0$.

(iii) Interpretation of Simple Shear Soil Test Results

In simple shear soil tests, $\dot{\varepsilon}_x = \dot{\varepsilon}_y = \dot{\varepsilon}_z = 0$. The necessary algebra for the determination of the model parameters is considerably simplified in that case if the elastic contributions to the normal strains is neglected. Eq. 15 then yields: $\sigma'_x = \sigma'_z$,

$$\frac{\dot{\gamma}_{xy}}{\dot{\tau}_{xy}} = \frac{1}{G} + \frac{2}{h'_m} \tag{36}$$

$$\alpha^{(m)} = (\sigma'_y - \sigma'_x) \tag{37}$$

$$\beta^{(m)} = \sigma'_y - \frac{2}{3}(\sigma'_y - \sigma'_x) \tag{38}$$

$$k^{(m)} = \sqrt{3}\ \tau_{xy} \tag{39}$$

The model parameters associated with the yield surface $f^{(m)}$ are then simply determined from the above equations and a piecewise linear representation of the shear stress-strain curves obtained in a simple shear test. Note that the sole use of simple shear test results does not allow the determination of the parameters $B'^{(m)}$ and $A^{(m)}$. On the other hand, it is apparent from Eqs. 36 and 39 that the degradation of the mechanical properties of the material under cyclic shear loading conditions, i.e.,

$$k^{(m)}(\bar{e}) \quad \text{and} \quad h'^{(m)}(\bar{e}) \tag{40}$$

with

$$\bar{e} = \int \{\frac{2}{3}\, \dot{\underset{\sim}{e}}' : \dot{\underset{\sim}{e}}'\} \qquad \dot{\underset{\sim}{e}} = \dot{\underset{\sim}{\varepsilon}} - \frac{1}{3}\,(\mathrm{tr}\ \dot{\underset{\sim}{\varepsilon}})\ \underset{\sim}{1} \tag{41}$$

where the integration is carried along the strain path, are most conveniently determined from the results of cyclic strain-controlled simple shear tests

($\bar{e} = \int \frac{1}{\sqrt{3}}\, |\dot{\gamma}|$ in that case). This is explained and further discussed in [8].

MODEL EVALUATION

1. Laboratory Prepared Kaolinite Clay

The soil data to be used in this section are part of the ones which were collected by the organizing committee of the NSF/NSERC North American Workshop on plasticity and generalized stress-strain applications in soil engineering held May 28-30, 1980 at McGill University, Montreal, Canada. Laboratory axial test data on a laboratory-prepared kaolinite clay had then been transmitted to the author. Predictions about the constitutive behavior of the soil subjected to loading stress paths not identified in the data had been requested by the organizing committee. This section describes the test results, their analysis, and compares the model predictions [11] with observed behavior in the tests.

The experimental tests had been conducted on cyclindrical samples in a torsional shear testing device. All samples had first been K_o-consolidated with a cell pressure of 58 psi and a backpressure of 18 psi, and then left to rebound to an equal-all-around cell pressure of 58 psi, and a backpressure of 18 psi (in other words, the excess axial load necessary for K_o-consolidation

was then released). All the tests were stress-controlled and performed under constant volume conditions (i.e., undrained).

Fig. 2 shows in dashed-lines the experimental results obtained in conventional undrained monotonic axial compression/extension soil tests, and in solid-lines the design curves used to determine the model parameters for that clay. Note that some data points close to failure have been ignored when selecting the design curves because they are not consistent with the rest of the data. This inconsistency may be due to experimental difficulties in capturing failure states in stress-controlled testing devices.

Fig. 3 shows model predictions for a shear test in which the major principal stress is inclined at $\theta = 15°$ relative to the vertical axis of the soil specimen. Fig. 3 also shows a comparison between predicted (solid lines) and observed (dashed-lines) behavior of the soil in these tests. Note that all the model predictions agree well with the experimental test results.

2. Dilating Sand

"Dilating sand" is a synthesized data set generated from real sand data. Fig. 4 shows the corresponding conventional drained axial compression/extension test data. As shown in Fig. 4, the sand is assumed to exhibit first volumetric compaction than dilation in both compression and extension loading conditions.

Figs. 5 and 6 show the computed hysteresis loops and effective stress paths for undrained cyclic strain-controlled tests performed at axial strain amplitudes of 1% and 2%, respectively. Note the progressive build-ups of pore-fluid pressures as cyclic loading proceeds (due to the extension phase of the loading), and corresponding softening of the shear-stress vs shear-strain hysteresis loops.

COMPUTATIONAL ASPECTS

The soil model described above has been coded and incorporated into the finite element program DYNA-FLOW [12] for use in analysis of boundary value problems of interest in soil mechanics. DYNA-FLOW is a finite element analysis program for the static and transient response of linear and nonlinear two- and three-dimensional systems. DYNA-FLOW is an expanded version of DIRT II [3]. In particular, DYNA-FLOW offers transient analysis capabilities for both parabolic and hyperbolic initial value problems in both solid and fluid mechanics. There are no restrictions on the number of elements, the number of load cases and the number or bandwidth of the equations. Despite large system capacity, no loss of efficiency is encountered in solving small problems. In both static and transient analyses, an implicit-explicit predictor-multicorrector scheme [2] is used. Some features which are available in the program area:

- Selective specification of high- and low-speed storage allocations;
- Both symmetric and non-symmetric matrix equations solvers;
- Eigenvalue/vector solution solver;
- Reduced/selective integration procedures, for effective treatment of incompressibility constraints;
- Coupled field equation capabilities for treatment of thermoelastic and saturated porous media;
- Isoparametric data generation schemes;
- Mesh optimization options;
- Plotting options;
- Interactive options.

The element and material model libraries are modularized and may be easily expanded without alteration of the main code.

The element library contains a two-dimensional element with plane stress/ plane strain and axisymmetric options, and full finite deformations may be accounted for. A three-dimensional element is also included. A contact element, a slide-line element, a truss element and a beam element are available for two- and three-dimensional analysis.

The material library contains a linear elastic model, a linear thermo-elastic model, a Newtonian fluid model, and a family of elasto-plastic models developed by the author.

Accuracy and versatility of the computer code DYNA-FLOW in applications of interest in geotechnical engineering have been demonstrated in examples reported in a number of papers (see e.g., [13,15,17-21].

Use of elastic-plastic equations of the above type in analysis of boundary value problems requires that an efficient, "sturdy" and accurate numerical integration procedure of the plasticity equations at the stress point level be available. Substantial efforts have thus been devoted to designing a computational procedure with the best balance of accuracy and computational speed. The integration algorithm presently used in the stress routine is a generalization of the conventional radial return technique [6,7]. Numerical results which demonstrate the accuracy of the stress-point algorithm are presented in this section. All simulations reported here were performed with the "dilating sand" model described previously. A number of monotonic and cyclic, axial and simple shear strain-experiment simulations are reported hereafter. Each simulation was performed for various load step numbers, and the computed stress-strain curves are shown on the same plot for comparison and evaluation of the stress routine accuracy. The results for 100 steps may be viewed as converged in the following calculations.

1. Simple shear strain loading condition

In that case the only nonzero strain component is $\gamma_{xy} = 2\varepsilon_{xy}$. Calculated results are presented in Fig. 7.

2. Hydrostatic strain loading condition

In that case, $\varepsilon_x = \varepsilon_y = \varepsilon_z$ and $\varepsilon_{xy} = \varepsilon_{yz} = \varepsilon_{zx} = 0$. Calculated results are presented in Fig. 8.

SUMMARY AND CONCLUSIONS

A general analytical model which describes the nonlinear, anisotropic, elastoplastic, stress-strain-strength properties of the soil skeleton when subjected to complicated three-dimensional loading paths is proposed. A brief summary of the model's basic principle is included and the constitutive equations are provided. It is shown that the model parameters required to characterize the behavior of any given soil can be derived entirely from the results of conventional soil tests. The model's accuracy is evaluated by applying it to represent the behavior of both cohesive and cohesionless soils. Implementation of the proposed model in a general finite element program for solution of boundary value problems is discussed.

ACKNOWLEDGMENTS

This work was supported in part by grants from the Naval Civil Engineering Laboratory, Port Heuneme, CA, and the National Science Foundation (CEE-8120757). These supports are most gratefully acknowledged. Computer time was provided by Princeton University Computer Center.

REFERENCES

[1] Hill, R., "A General Theory of Uniqueness and Stability in Elastic-Plastic Solids," J. Mech. Phys. Solids, Vol. 6, 1958, pp. 236-249.

[2] Hughes, T.J.R., Pister, K.S., and Taylor R.L., "Implicit-Explicit Finite Elements in Nonlinear Transient Analysis," Comp. Meth. Appl. Mech. Eng., Vol. 17/18, 1979, pp. 159-182.

[3] Hughes, T.J.R., and Prevost, J.H., "DIRT II: A Nonlinear Quasi-Static Finite Element Analysis Program," California Institute of Technology, Pasadena, California, 1979.

[4] Hvorslev, M.J., "Uber die Festigkeitseigenschaften gestorler bindiger boden," Ingeniozvidenskabelige Skrifter, A. no. 45, Copenhagen, 1937.

[5] Jaumann, G., Gzundlagen der Bewegungolehze, Leipzig, 1903.

[6] Kzieg, R.D., and Key, S.W., "Implementation of a Time Independent Plasticity Theory Into Structural Computer Programs," in Constitutive Equations in Viscoplasticity Theory: Computational and Engineering Aspects, AMD-Vol. 20, ASME, New York, 1976.

[7] Krieg, R.D., and Krieg, D.B., "Accuracies of Numerical Solution Methods for the Elastic-Perfectly Plastic Model," J. of Pressure Vessel Technology, ASME, Vol. 99, No. 4, 1977, pp. 510-515.

[8] Prevost, J.H., "Mathematical Modeling of Monotonic and Cyclic Undrained Clay Behavior," Int. J. Num. Analyt. Methods in Geomechanics, Vol. 1, No. 2, 1977, pp. 196-216.

[9] Prevost, J.H., "Anisotropic Undrained Stress-Strain Behavior of Clays," J. Geotech. Eng. Div., ASCE, Vol. 104, No. GT8, 1978, pp. 1075-1090.

[10] Prevost, J.H., "Plasticity Theory for Soil Stress-Strain Behavior," J. Eng. Mech. Div., ASCE, Vol. 104, No. EM5, 1978, pp. 1177-1194.

[11] Prevost, J.H., "Constitutive Theory for Soil," Proceedings, NSF/NSERC North American Workshop on Plasticity and Generalized Stress-Strain Applications in Soil Engineering, Montreal, Canada, May 1980.

[12] Prevost, J.H., "DYNA-FLOW: A Nonlinear Transient Finite Element Analysis Program," Department of Civil Engineering, Report 81-SM-1, Princeton University, January 1981.

[13] Prevost, J.H., "Consolidation of Anelastic Porous Media," ASCE, Vol. 107, No. EM1, February, 1981, pp. 169-186.

[14] Prevost, J.H., "Nonlinear Anisotropic Stress-Strength Behavior of Soils," in ASTM STP 740 on Shear Strength of Soils, 1982, pp. 431-455.

[15] Prevost, J.H., "Nonlinear Transient Phenomena in Saturated Porous Media," Comp. Meth. Appl. Mech., Vol. 30, No. 1, 1982, pp. 3-18.

[16] Prevost, J.H., "Two-Surface vs. Multi-Surface Plasticity Theories," Int. J. Num. Anal. Meth. Geomechanics. (1982) (to appear).

[17] Prevost, J.H., "Nonlinear Transient Phenomena in Elastic-Plastic Solids," J. Eng. Mech. Div., ASCE,1982 (to appear).

[18] Prevost, J.H. and Hughes, T.J.R., "Analysis of Gravity Offshore Structure Foundations Subjected to Cyclic Wave Forces," Proceedings, 1978 Offshore Technology Conference, Houston, Texas, Vol. 1 (May 1978), pp. 1809-1818.

[19] Prevost, J.H. and Hughes, T.J.R., "Finite Element Solution of Boundary Value Problems in Soil Mechanics," Proceedings, International Symposium on Soils under Cyclic and Transient Loading, Swansea, U.K., (January 1980), pp. 263-276.

[20] Prevost, J.H., Cuny, B., Hughes, T.J.R. and Scott, R.F., "Foundations of Offshore Gravity Structures: Analysis," J. Geotech. Eng. Div., ASCE, Vol. 107, No. GT2, February, 1981, pp. 143-165.

[21] Prevost, J.H. and Hughes, T.J.R., "Finite Element Solution of Elastic-Plastic BVP," J. Appl. Mech., ASME, Vol. 48, No. 1, March, 1981, pp. 69-34.

[22] Richard, R.E., Woods, R.D. and Hall, J.R., Vibrations of Soils and Foundations, Prentice-Hall, Inc., Englewood Cliffs, New Jersey, 1970.

[23] Roscoe, K.H. and Burland, J.B., "On the Generalized Stress-Strain Behavior of 'Wet' Clay," in Engineering Plasticity, Heymand and Leckis, eds., Cambridge University Press, Cambridge, England, 1968, pp. 535-609.

[24] Terzaghi, K., Theoretical Soil Mechanics, Wiley, New York, 1943.

LIST OF FIGURES

List of Figures (cont)

Figure No.

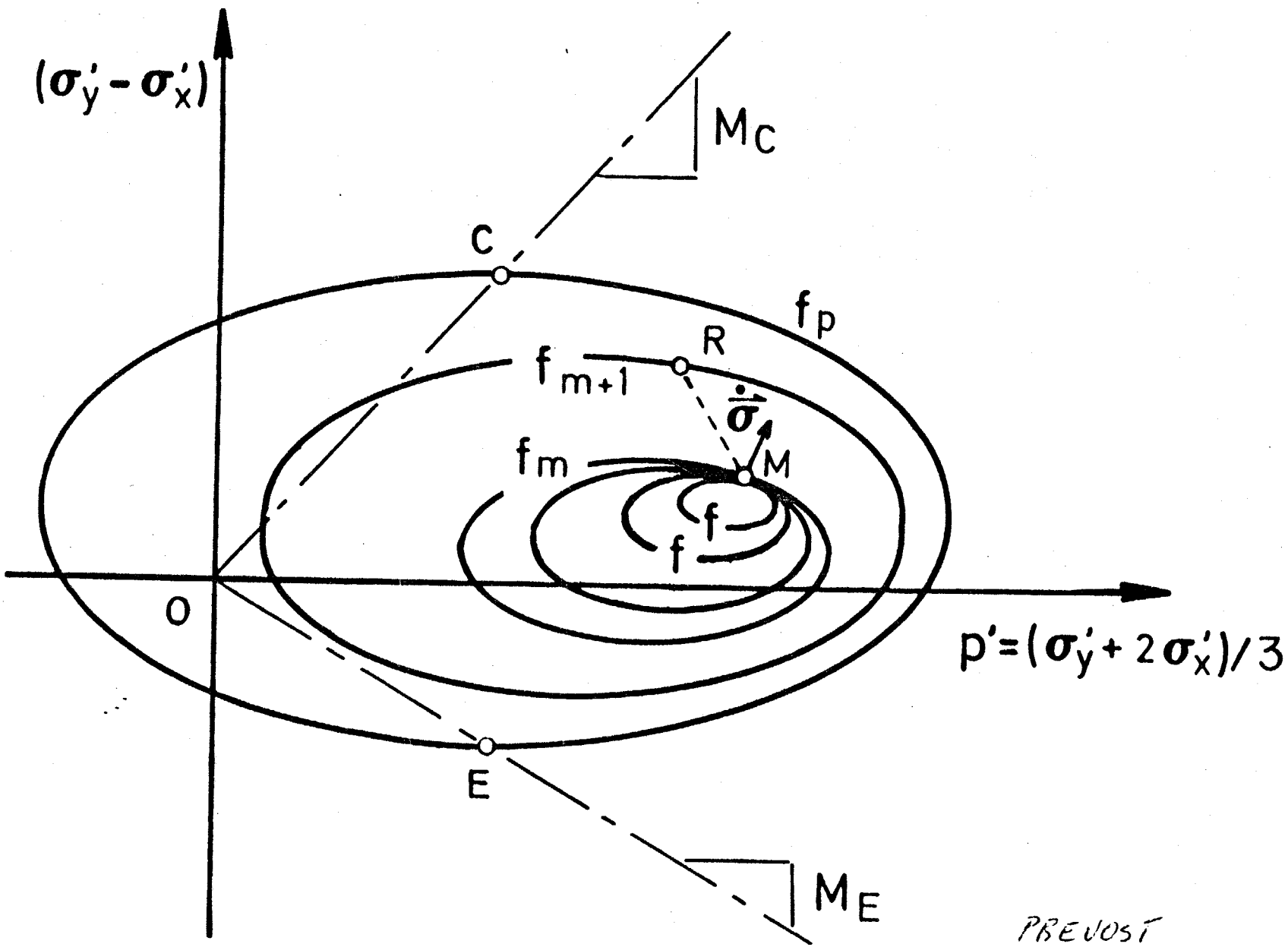

PREVOST

FIG. 1a

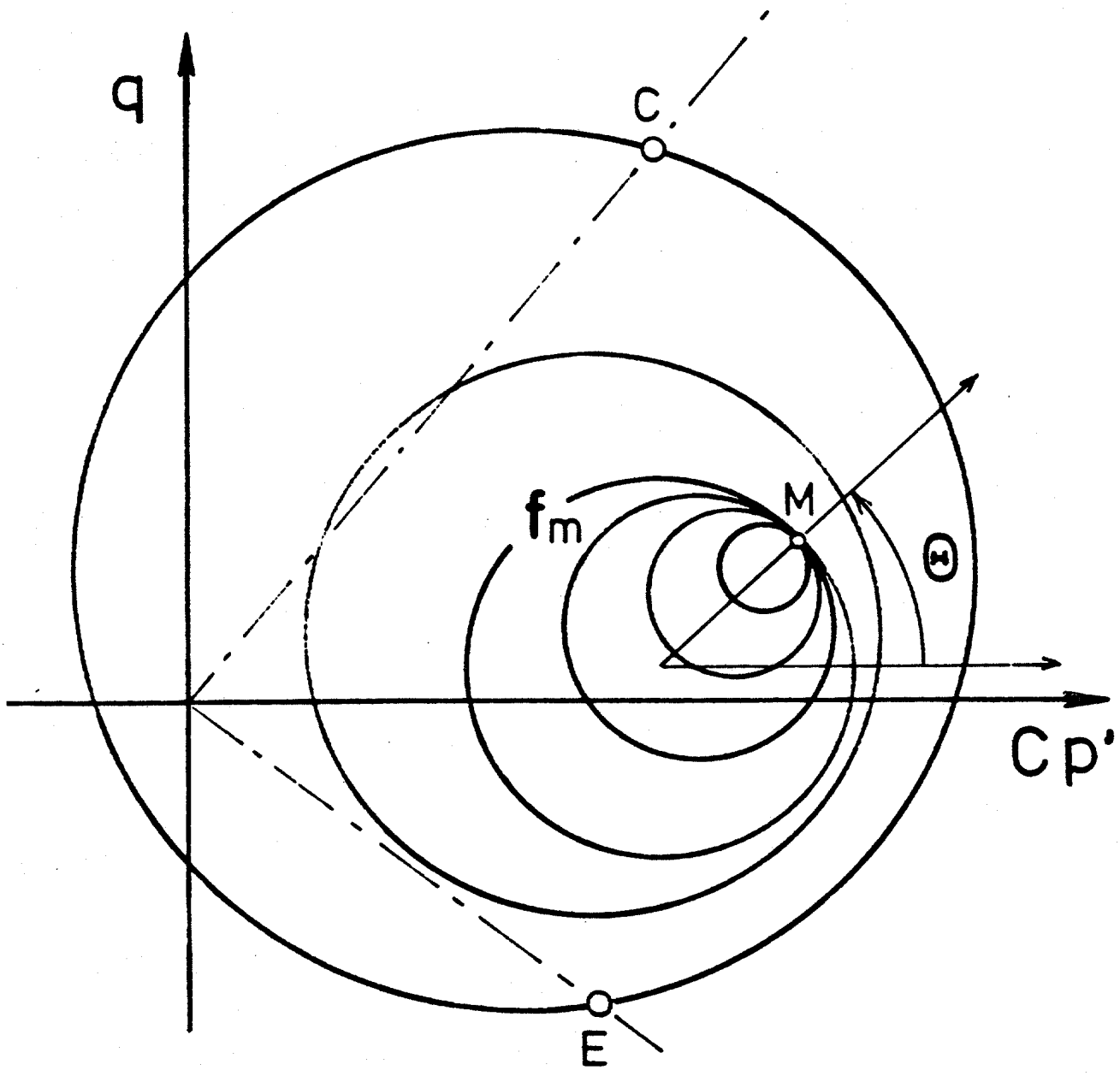

PREVOST
FIG. 1b

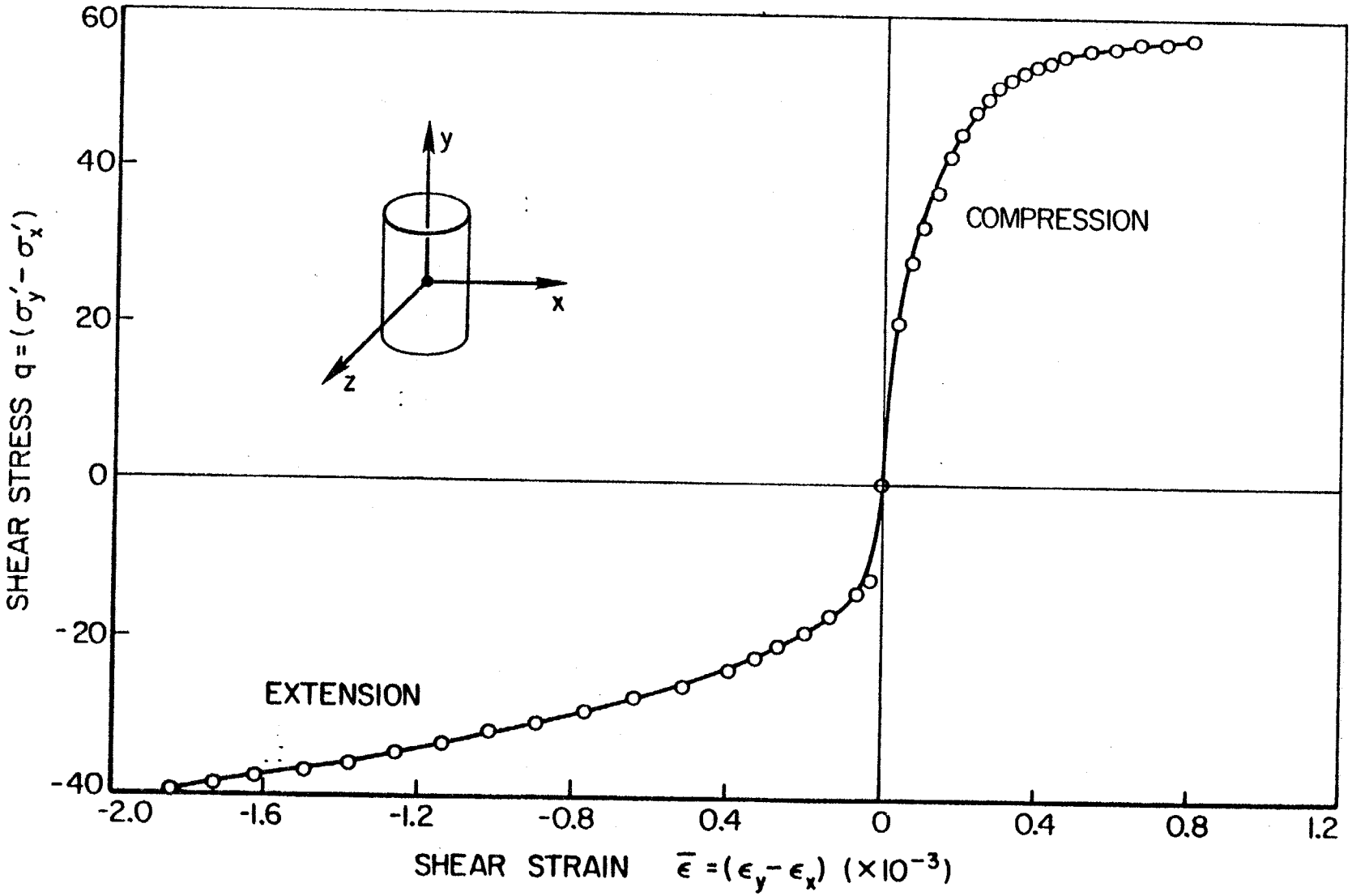

PREVOST

FIG 2a

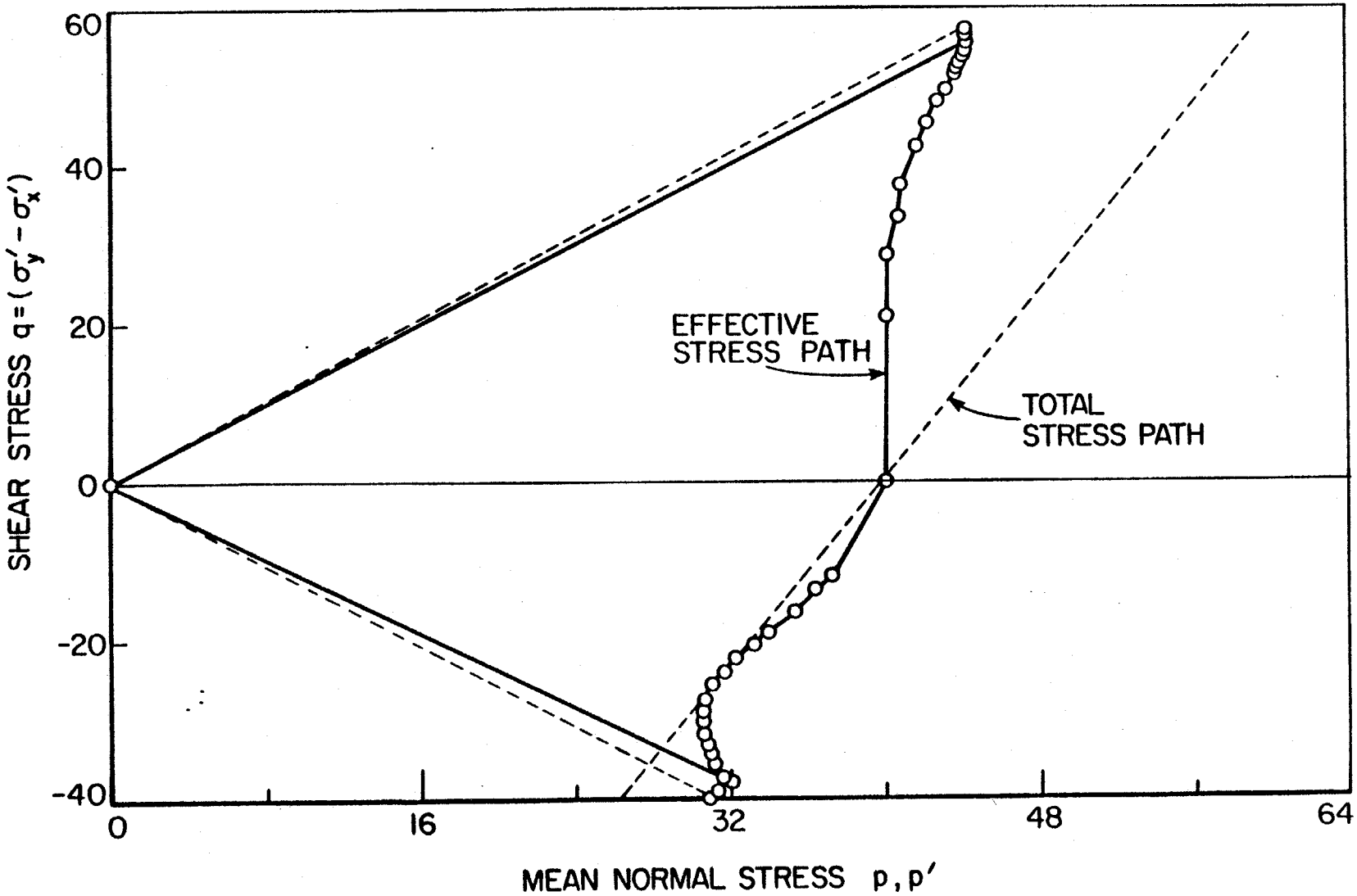

PREVOST

FIG. 2b

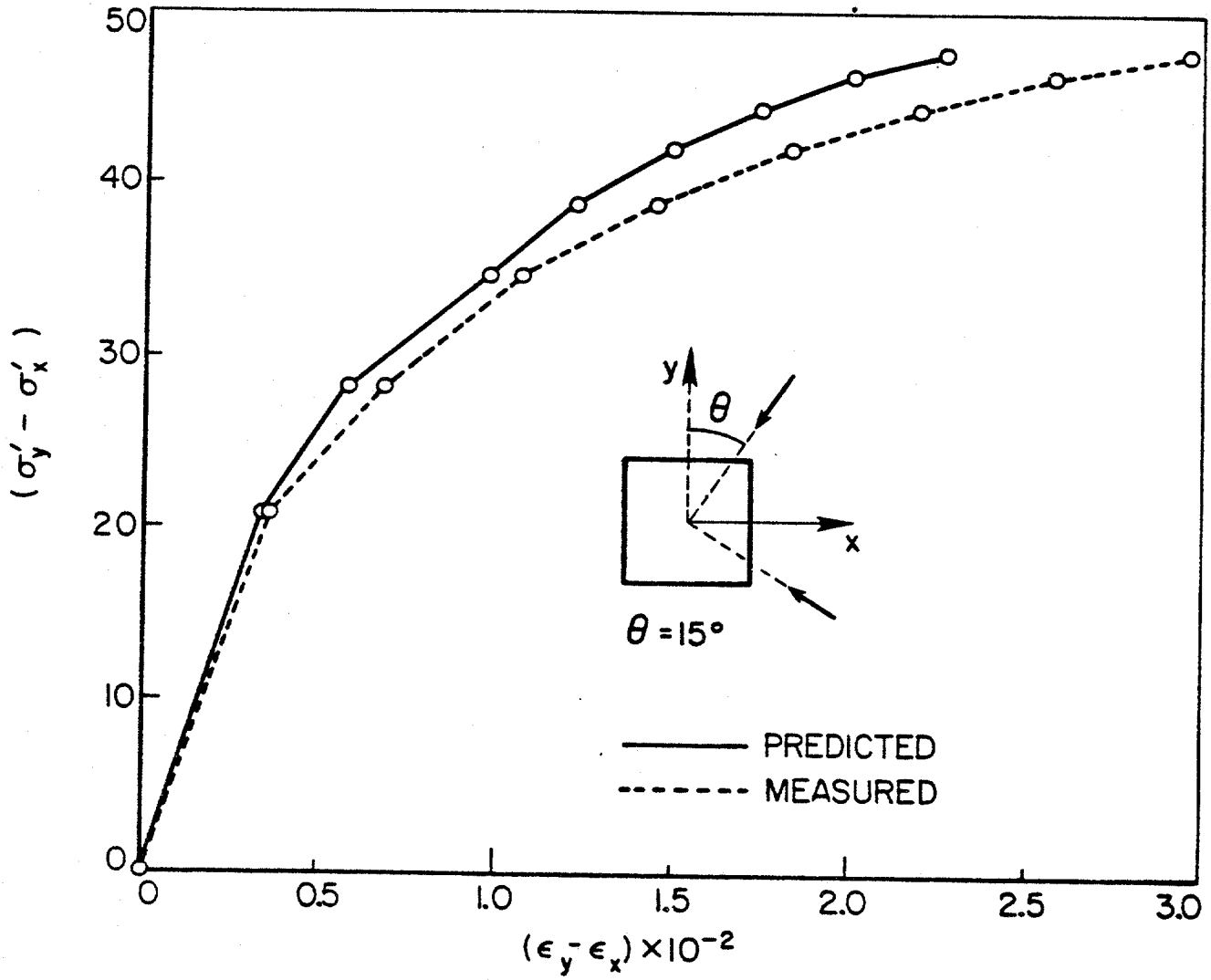

PRELIST
FIG. 3a

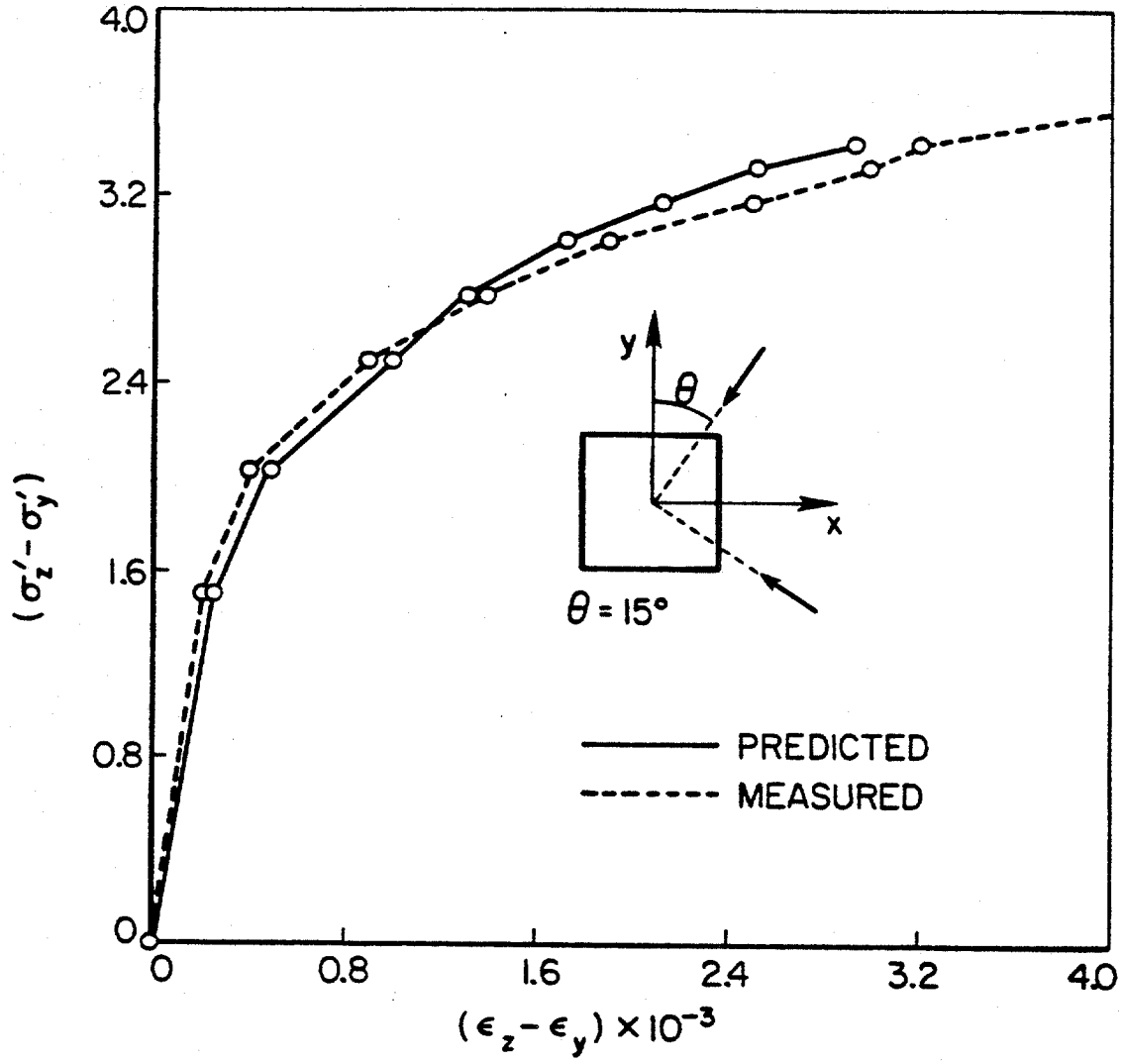

PREVOST
FIG. 3b

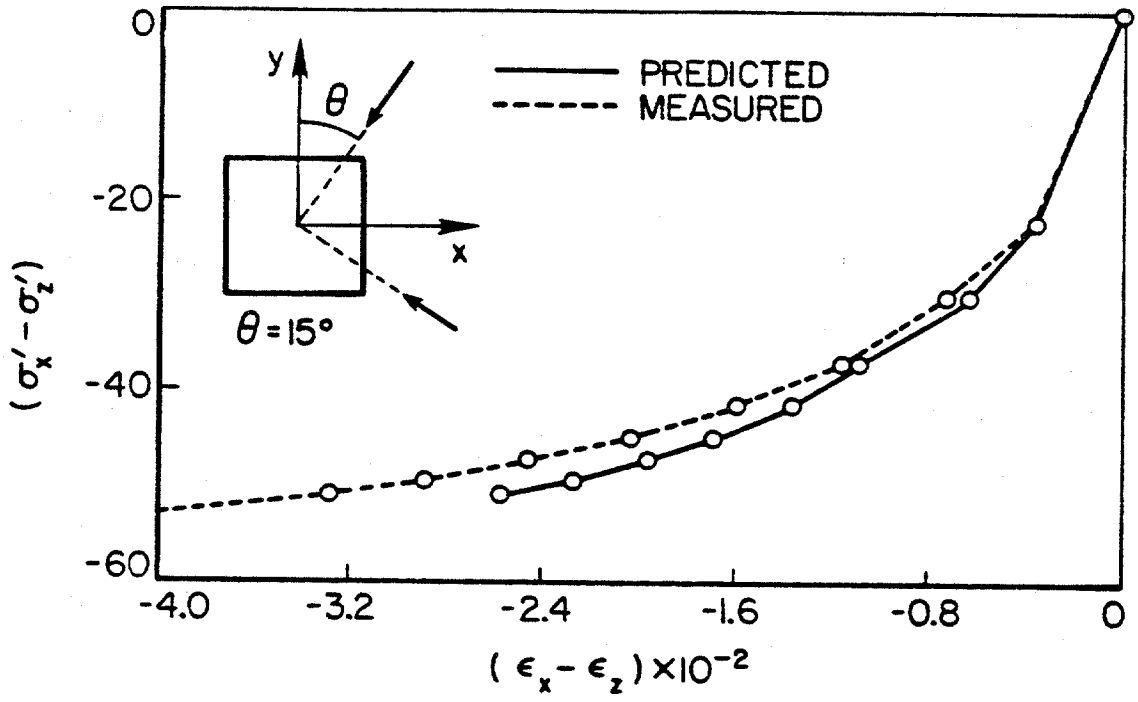

PREVOST
FIG. 3C

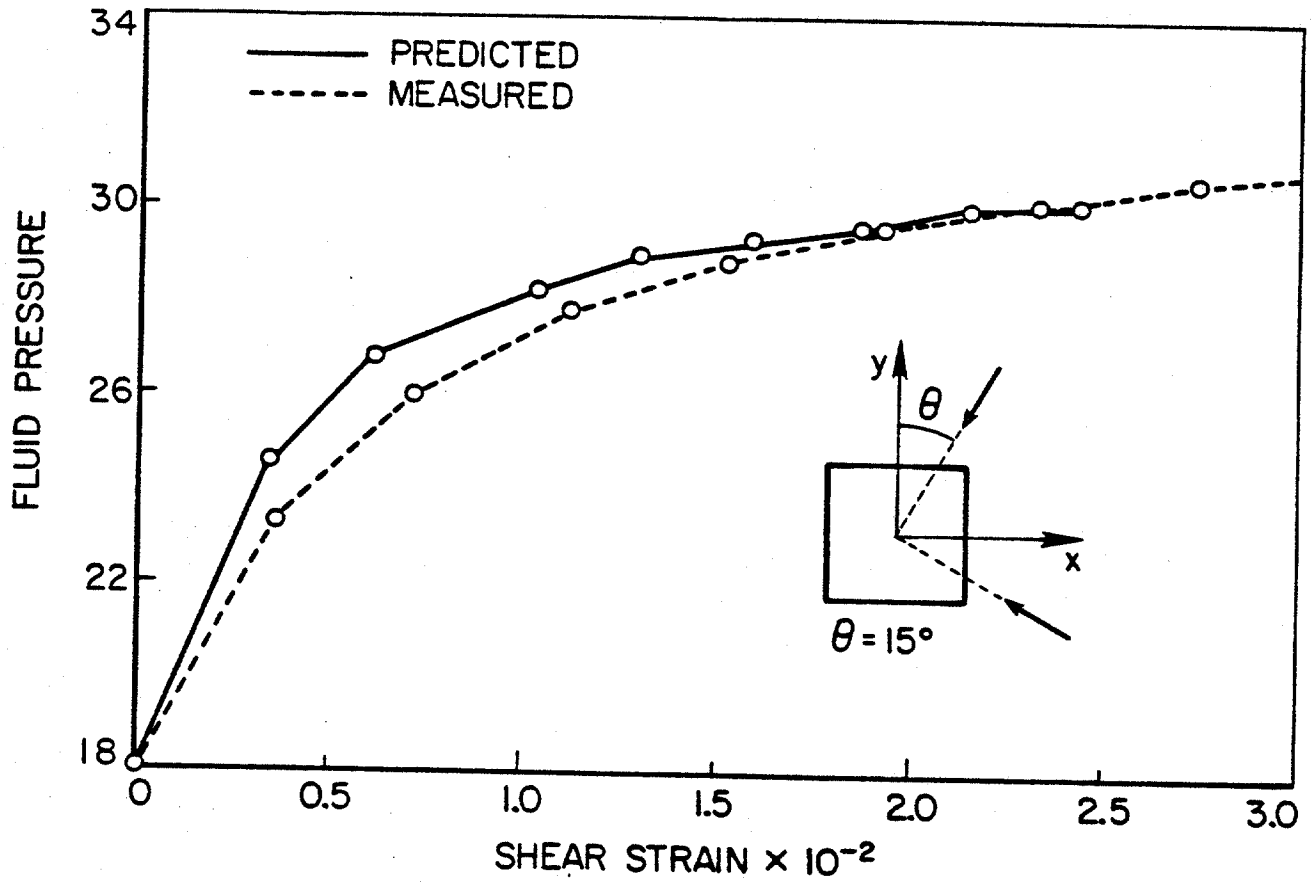

PREVOST
FIG. 3d

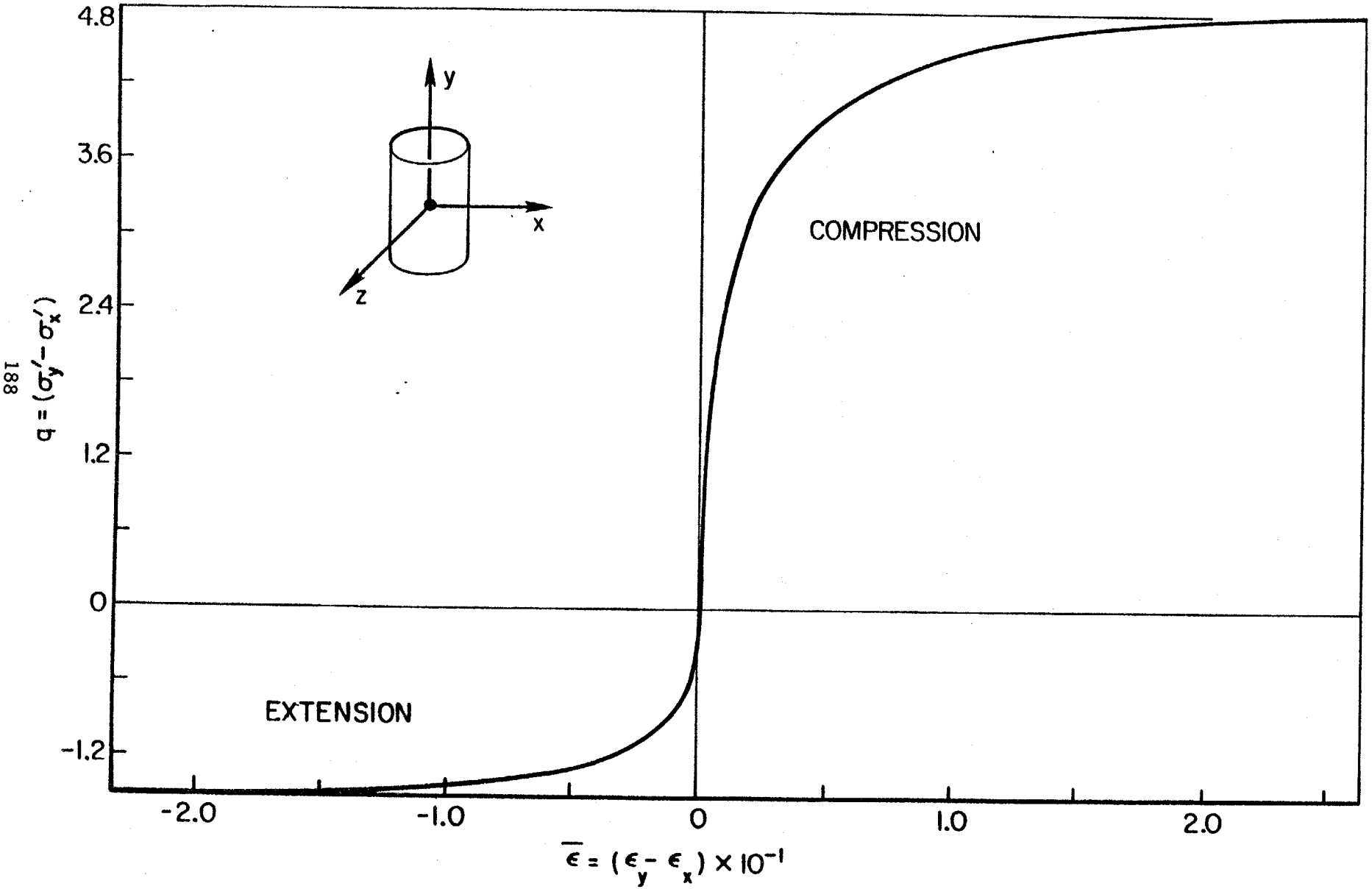

PREVOST
FIG. 4a

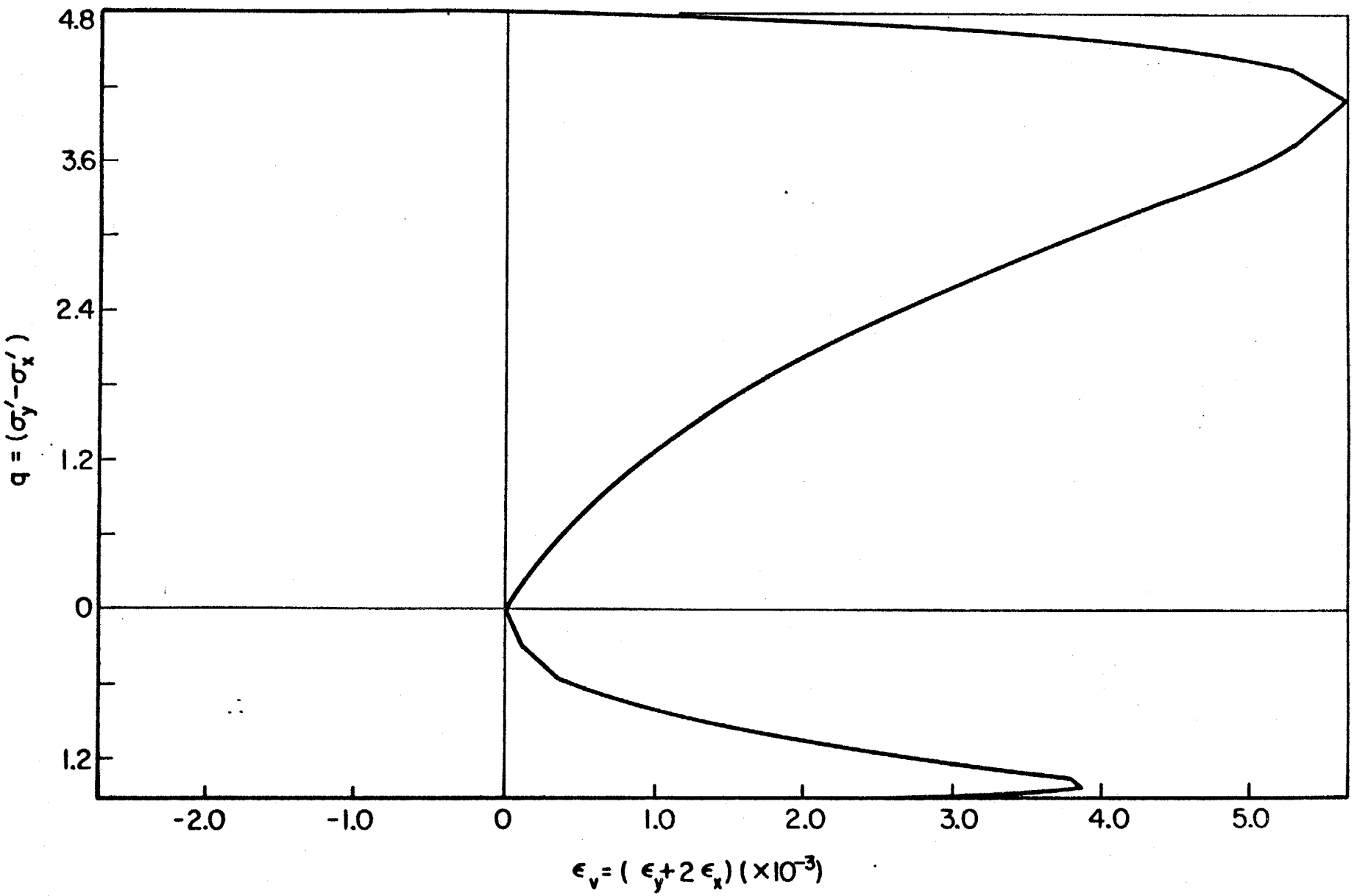

PREVOST

FIG. 4b

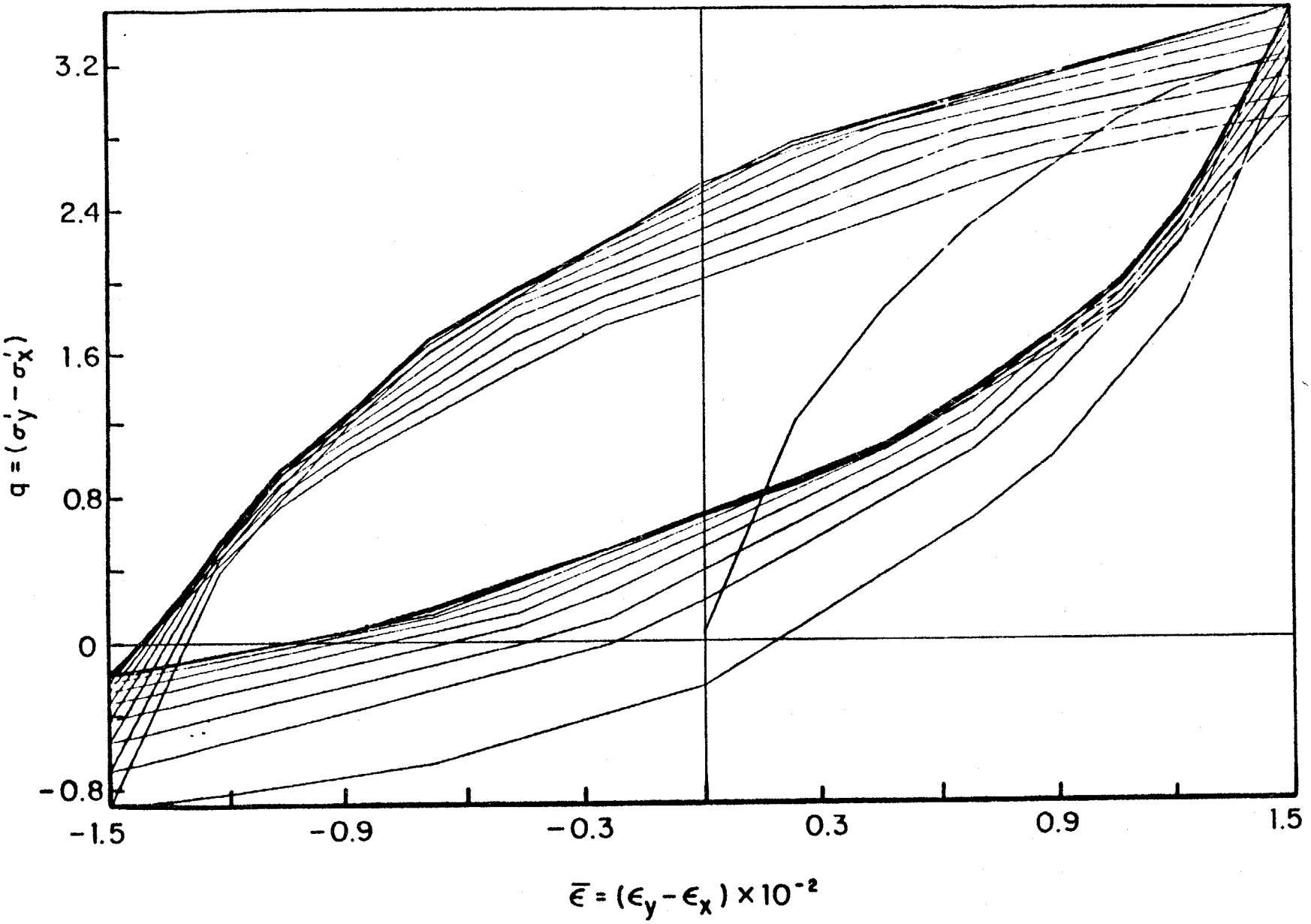

PREVOST
FIG. 5a

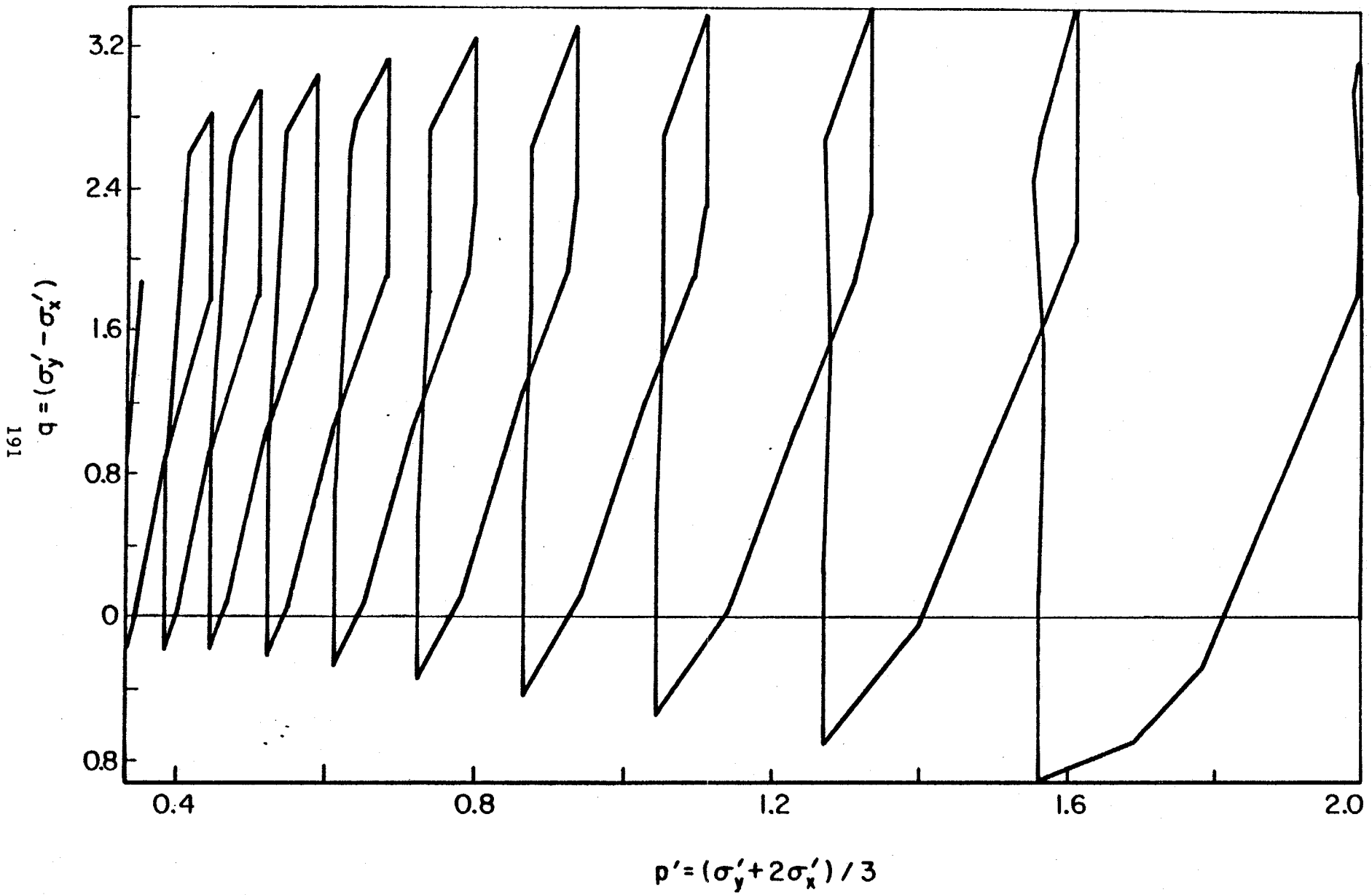

PREVOST
FIG. 5b

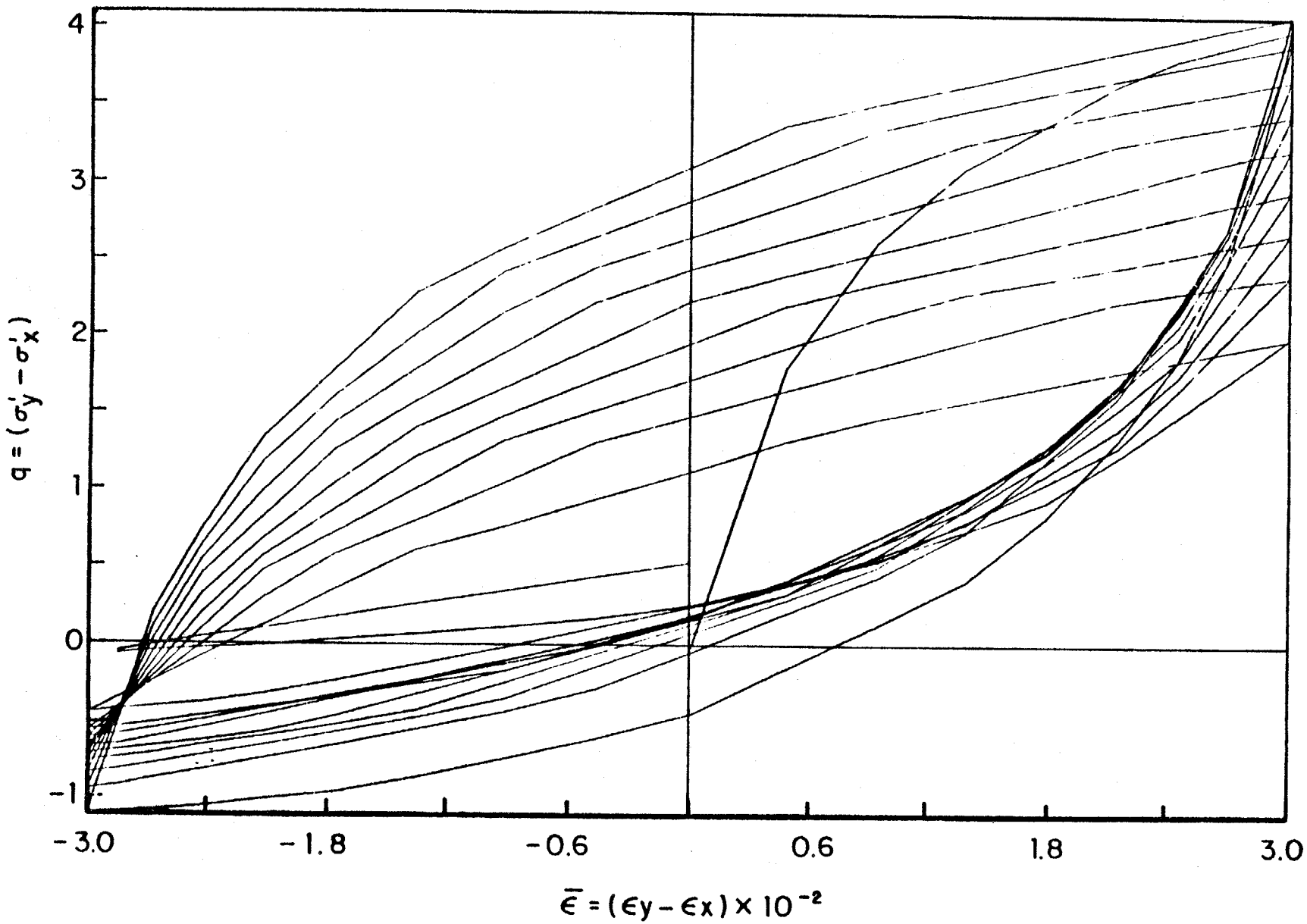

PREVOST
FIG. 62

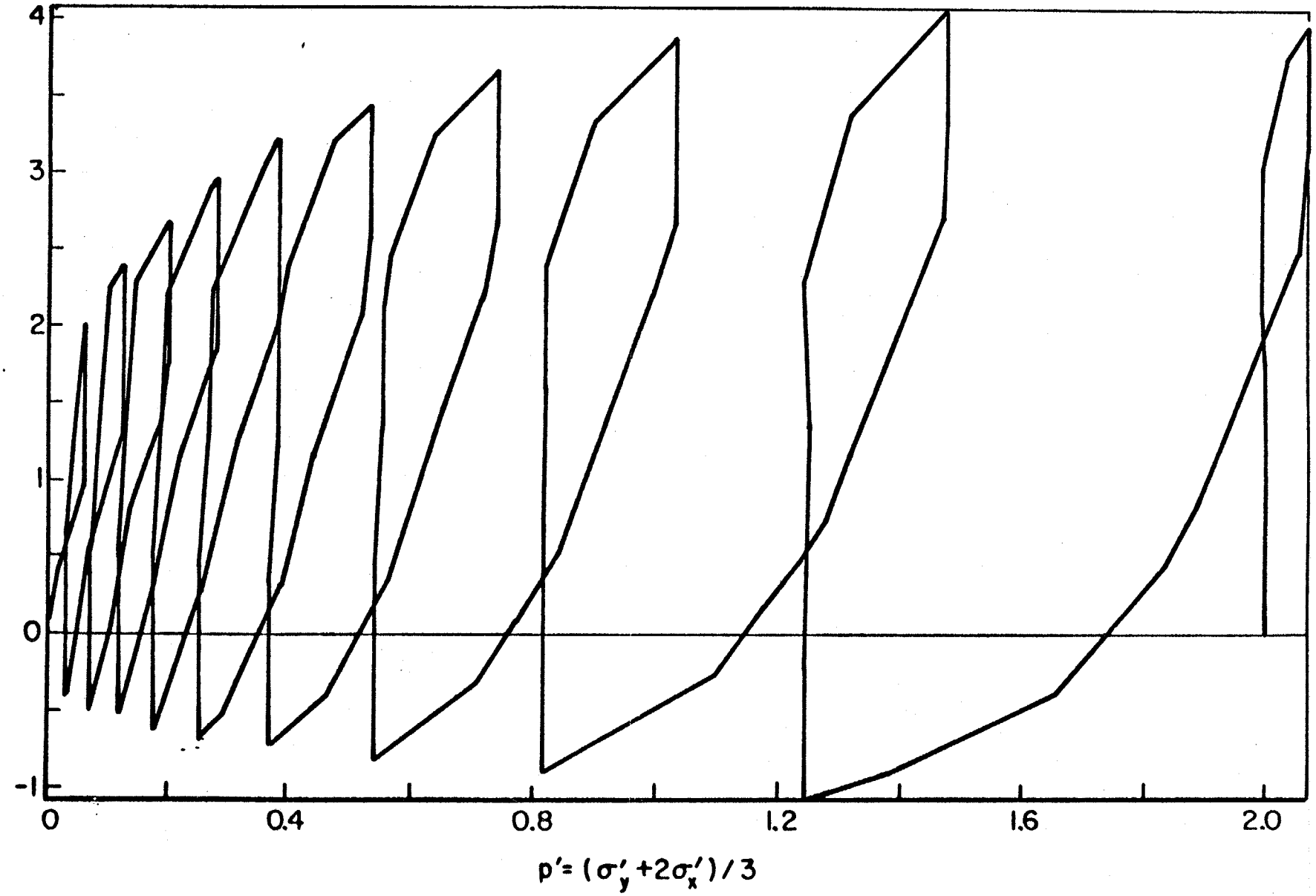

PREVOST
FIG. 6b

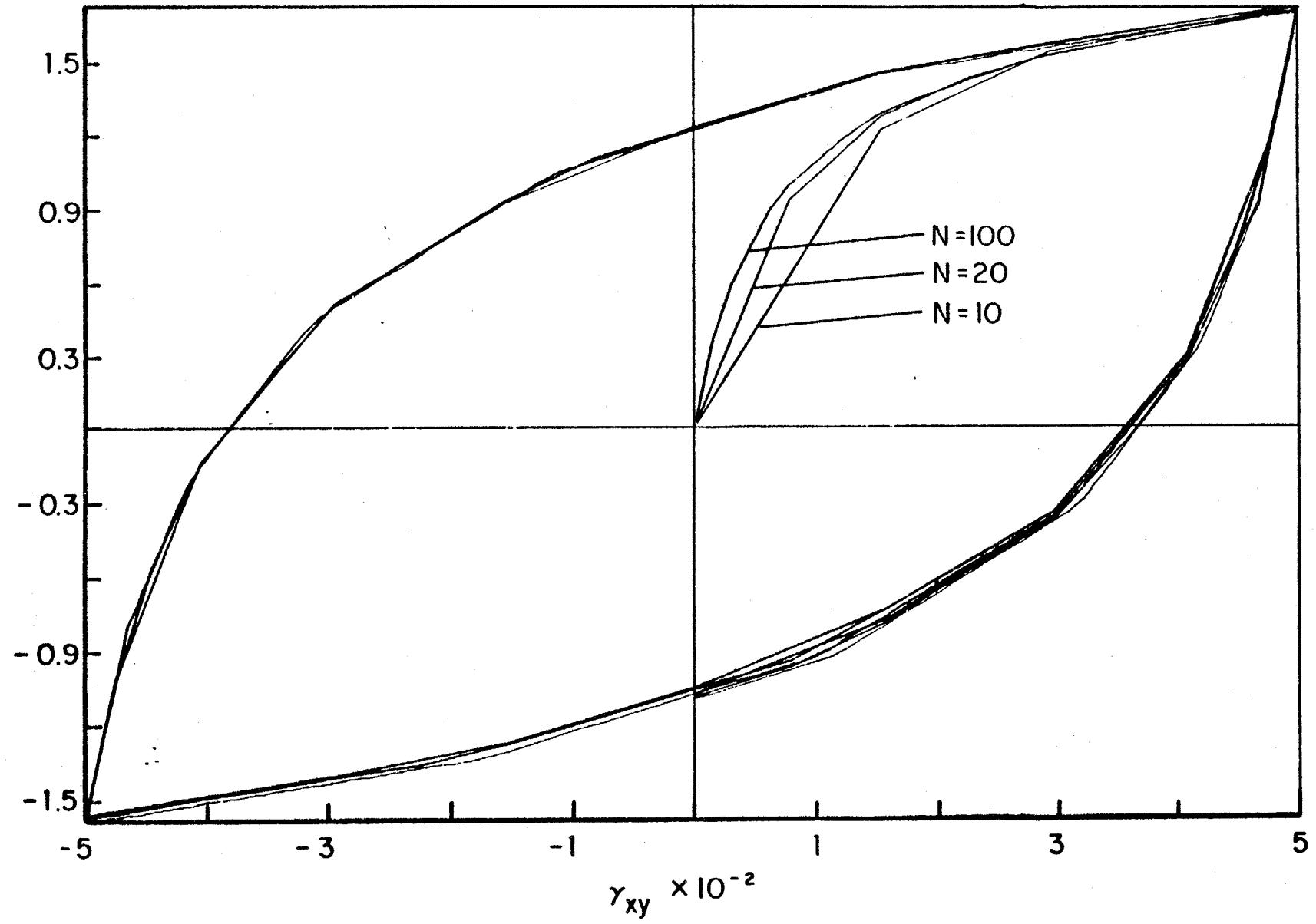

PREVOST
FIG 7a

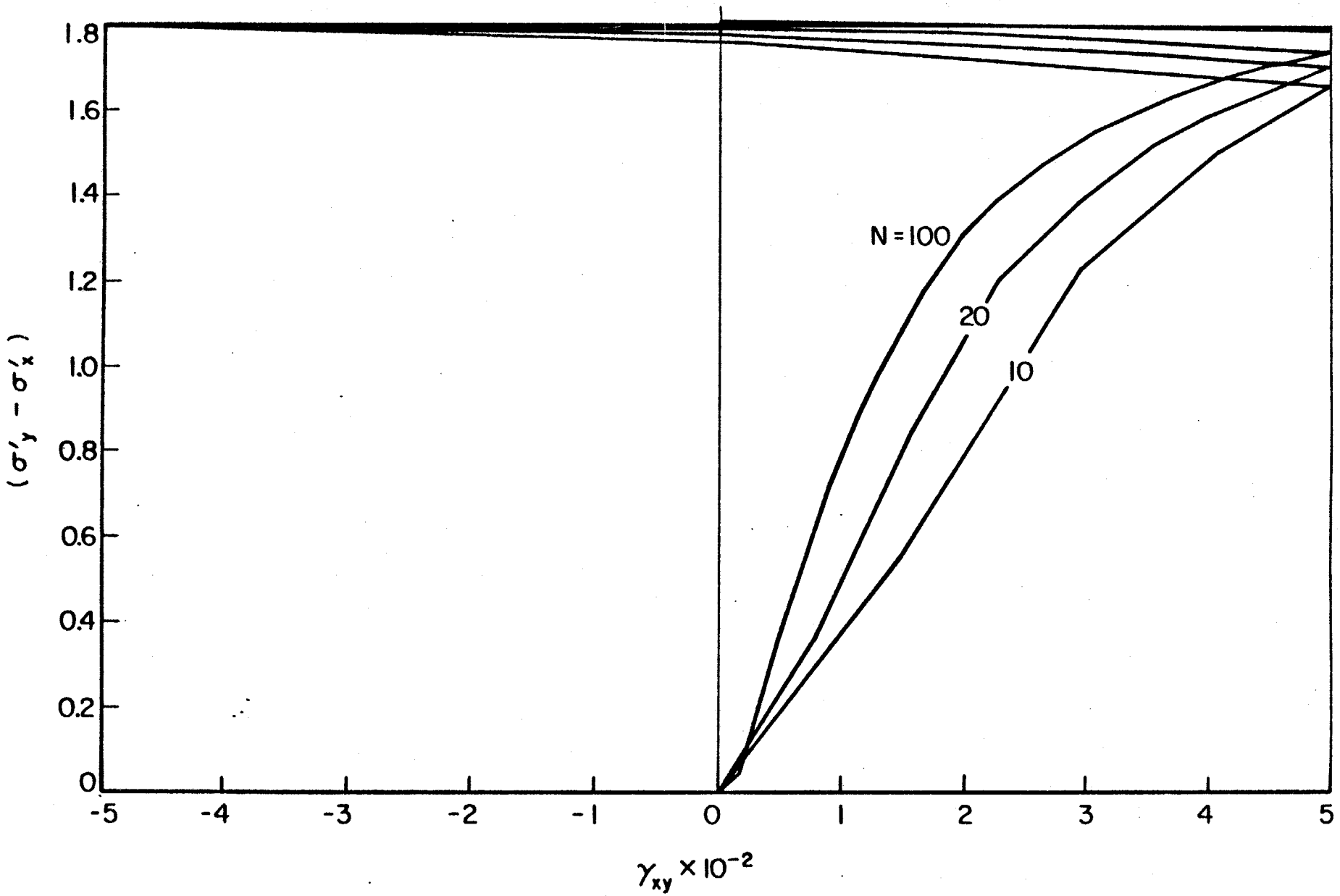

PREVOST
FIG. 7b

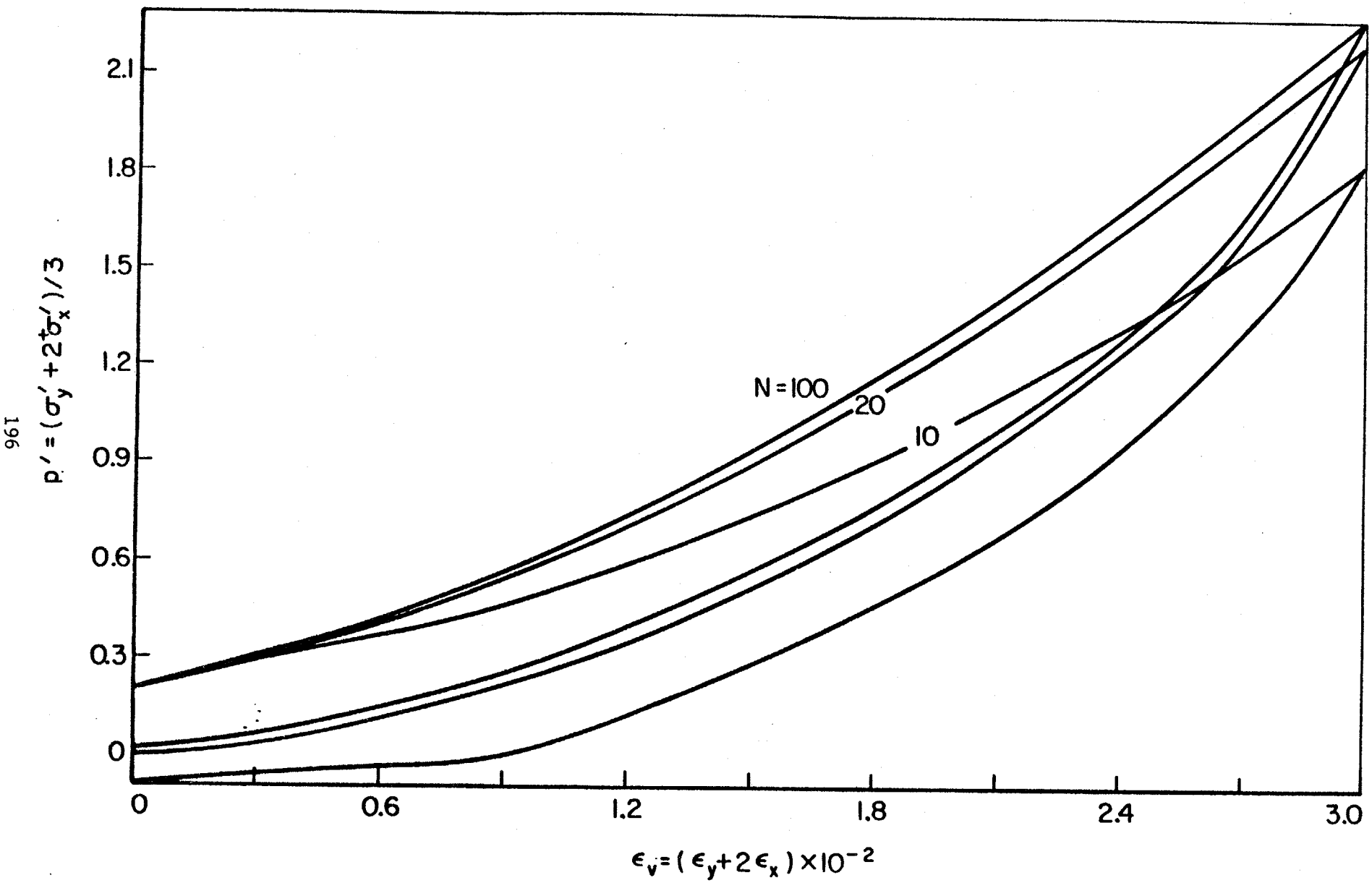

PREVOST
FIG. 8